

Solution-Processed Metal Oxide
Dielectrics and Semiconductors
for Thin Film Transistor Applications



Dimitrios Afouxenidis

MSc Materials Physics and Technology

A thesis submitted in partial fulfilments for the degree of

Doctor of Philosophy

Engineering Department, Lancaster University, UK

October 2018

Abstract

Transparent thin film transistors (TFTs) have been the subject of extensive scientific research over the last couple of decades, for applications in displays and imaging, as their implementation in active-matrix liquid crystal displays backplanes is expected to improve their performance in terms of switching times and stability. To this end, several material systems have emerged as contenders to address this need for a high performance, low power, large-area electronics i.e. thin film silicon, organic semiconductors and metal oxides. The electronic limitations of thin film silicon are well documented, and although organic semiconductors have seen significant improvements in recent years, their persistent low mobility and instability means that they are unlikely to progress beyond niche applications.

This thesis is focused on the investigation of the physical properties of metal oxides and their implementation in TFTs. Metal oxide based TFTs were fabricated by spray pyrolysis, a simple and large-area-compatible deposition technique.

More precisely, the implementation of titanium-aluminate and niobium-aluminate both wide band gap and high- k gate dielectric metal oxides in solution processed ZnO-based TFTs was studied and high performance, low operational voltage devices were fabricated. ZnO-based TFTs employing stoichiometric $\text{Al}_2\text{O}_3\text{-TiO}_2$ ($k\sim 13$, $E_g\sim 4.5$ eV) or $\text{Nb}_2\text{O}_5\text{-Al}_2\text{O}_3$ ($k\sim 13.5$, $E_g\sim 5.1$ eV) as gate dielectric exhibited low leakage currents, high on-off current modulation ratios, high field-effect mobilities and low subthreshold voltage swings.


Furthermore, the implementation of solution-processed crystalline indium-zinc oxide (c-IZO) as active channel material in TFTs was equally investigated and high-performance c-IZO-based TFTs employing Al_2O_3 were fabricated. The effects of metal cation doping in c-IZO matrix were investigated in particular, and c-IZO:X (X:Ga,Y,Zr,Nb) based TFTs were fabricated and their properties were assessed for each dopant. Amongst them, Yttrium doped c-IZO (c-YIZO)-based TFTs exhibited the best performance in terms of low off-state currents, high field-effect mobilities and low subthreshold voltage swings.

Declaration

I declare that this thesis is my own work and has not been submitted in substantially the same form for the award of a higher degree elsewhere

Dimitrios Afouxenidis

Date:.....**Monday, 1 October 2018**.....

Signature:..........

Acknowledgments

First and foremost, I would like to thank my academic supervisor, Dr George Adamopoulos, for his unconditional support, constructive criticism and academic guidance throughout the years. Besides great scientist and source of inspiration, I consider him a good friend as well.

I would like to thank Prof Anthony Krier and Prof Claudio Paoloni, for their valuable feedbacks during my research. I would like to express my acknowledgments to Prof Oleg Kolosov and his research group members, for familiarising me with the atomic force microscopy. I would also like to thank the senior lab technician, Mr. Peter Jones, for always having time for me; familiarising me with experimental equipment, answering my queries and helping me to tackle technical problems during experiments.

To that point, I should express my deeply acknowledgements to my friends and colleagues for their help, for inspiring me, and for all the good time we had together; Dr George Polymeris, Dr Lefteris Danos, Dr Emmanouil Papaioannou, Dr Ioannis Tsitsimpelis, Dr Eleftherios Kastis, Dr Anna Karapiperi, Dr Angelo Greco, Tilly Alton, Mazran Esro, Mohamed Milad, Armin Yousefi Kanani, Chiemela Victor Amaechi, Ryan Smith, Finn Redman, Gareth Ellis, Apostolis Akritidis, Nikolaos Gkountas, Kostas Tarpanis, Vassiliki Markoulaki, Epaminondas Patiris, Stavroula Lappa, Vasileios Mantaras, Athina Kommata, Sophia Anastasia Rattan and Zoi Kalou.

I would like to thank my family for their continuing support. Moreover, I would like to thank my cousin Petros Platis for his support, especially during the last year. Last but not least, I am more than grateful to my beloved partner in life miss Sofia Bourelaki, for the vast emotional support and encouragement she has provided me with.

Dedicated to my mentor,

Prof George Kitis

Table of Contents

Abstract	2
Declaration	3
Acknowledgments	4
List of Figures	10
List of Tables	18
1. Introduction	20
1.1 Functional Metal Oxides for Electronic Devices	21
1.2 Deposition Techniques: A Brief Overview	27
1.2.1 Vacuum Based Deposition Techniques.....	27
1.2.2 Solution Based Deposition Techniques.....	29
1.3 Thesis Outline	31
1.4 References	32
2. Solution Processed Metal Oxides: An Overview.....	39
2.1 Solution Processed Transparent Oxide (Semi)Conductors.....	40
2.1.1 Binary Oxides	40
2.1.2 Multicomponent Oxides	49
2.2 Solution Processed Metal Oxide Dielectrics.....	68
2.2.1 Low- <i>k</i> Dielectrics	68
2.2.2 High- <i>k</i> Dielectrics.....	68
2.3 References	79
3. Theory and Operational Characteristics.....	99
3.1 Introduction	100
3.2 MIM Devices	101
3.2.1 Impedance Characteristics.....	103
3.2.2 Leakage Current and Conduction Mechanisms	107
3.3 Metal Oxide Semiconductor (MOS).....	113
3.3.1 Accumulation	114
3.3.2 Depletion	115
3.3.3 Inversion	116
3.4 Metal Oxide Semiconductor Field Effect Transistors (MOSFETs)	117

3.4.1	TFT Operating Characteristics	119
3.5	References	123
4.	Experimental Methods.....	128
4.1	Introduction	129
4.2	Deposition Techniques	129
4.2.1	Thermo-Chemical Spray Coating	129
4.2.2	Thermal Evaporation	131
4.3	Characterisation techniques	132
4.3.1	Simultaneous thermal analysis (STA)	133
4.3.2	X-Ray Diffraction (XRD).....	134
4.3.3	Atomic Force Microscopy (AFM)	135
4.3.4	Ultraviolet-Visible-near IR absorption spectroscopy (UV-Vis-NIR).....	136
4.3.5	Fourier Transformed Infrared Spectroscopy (FT-IR)	138
4.3.6	Ellispometry	139
4.3.7	Impedance spectroscopy	140
4.3.8	Current Voltage Measurements	141
4.4	References	143
5.	Aluminum Titanate $Ti_{1-x}Al_{2x}O_y$ Thin Films.....	147
5.1	Introduction	148
5.2	Experimental.....	150
5.2.1	Precursor Solution Chemistry	150
5.2.2	Device Fabrication	151
5.2.3	Thin Film & Device Characterisation Techniques	152
5.3	Results and Discussion.....	153
5.3.1	Precursor thermal properties.....	153
5.3.2	X-Ray Diffraction (XRD).....	155
5.3.3	Atomic Force Microscopy (AFM)	156
5.3.4	UV-Vis-NIR Spectroscopy	157
5.3.5	Spectroscopic Ellipsometry	159
5.3.6	Impedance Spectroscopy	161
5.3.7	I-V characteristics and leakage currents	163
5.3.8	I-V Characteristics of TFTs	165

5.4	Conclusions	168
5.5	References	169
6.	Niobium Aluminate $Nb_{1-x}Al_xO_y$ Thin Films	174
6.1	Introduction	175
6.2	Experimental.....	176
6.2.1	Precursor and Solutions.....	176
6.2.2	Device Fabrication	177
6.2.3	Thin Film & Device Characterisation Techniques	178
6.3	Results and Discussion.....	179
6.3.1	Precursor thermal properties.....	179
6.3.2	UV-Vis-NIR Spectroscopy	180
6.3.3	FTIR Spectroscopy	182
6.3.4	X-Ray Diffraction (XRD).....	183
6.3.5	Atomic Force Microscopy (AFM)	184
6.3.6	Impedance Spectroscopy	185
6.3.7	Leakage Currents.....	187
6.3.8	Field effect measurements	195
6.4	Summary.....	199
6.5	References	200
7.	Solution Processed Crystalline Indium Zinc Oxide (c-IZO) for High Performance Thin Film Transistors	208
7.1	Introduction	209
7.2	Experimental.....	214
7.2.1	Precursor Solution Chemistry	214
7.2.2	Device Fabrication	214
7.2.3	Thin Film & Device Characterisation Techniques	215
7.3	Results	216
7.3.1	Thermal Analysis of Precursor Compounds	216
7.3.2	Solution Processed Indium Oxide (In_2O_3)	218
7.3.3	Solution Processed Indium Zinc Oxide (IZO)	224
7.4	Summary.....	240
7.5	References	243

7.6 Appendix.....	251
8. High-Performance TFTs based on Indium Zinc Oxide (c-IZO:X) TFTs.....	252
8.1 Introduction	253
8.2 Experimental.....	254
8.2.1 Precursor Solution Chemistry	254
8.2.2 Device Fabrication	255
8.2.3 Thin Film & Device Characterisation Techniques	255
8.3 Results	255
8.3.1 Thermal Analysis of Precursor Compounds	255
8.3.2 Optical & structural properties of c-IZO:X thin films	258
8.3.3 Field effect measurements	271
8.3.4 Detailed study of IZO:Y.....	277
8.4 Summary & Discussion	286
8.5 References	288
9. Conclusions and Further Work	292
9.1 Conclusions	293
9.2 Further Work.....	296

List of Figures

Figure 1-1: Schematic design of a LCD. (Reproduced from)	22
Figure 1-2: Schematic orbital drawings for the carrier transport paths (that is, conduction band bottoms) in crystalline and amorphous semiconductors, reproduced from [10].	25
Figure 2-1: Side and top view of hexagonal wurtzite crystal structure of ZnO, after [2]	41
Figure 2-2: Band structure of hexagonal wurtzite ZnO obtained from density-functional theory calculations (DFT), after [3].	42
Figure 2-3: Crystal structure of cubic (bixbyite) In_2O_3 , after [26].	45
Figure 2-4: Band structure of In_2O_3 , after [31].	46
Figure 2-5: The mobility and hysteresis of solution deposited IZO TFTs annealed at 550 °C by Banger et al. [70].	50
Figure 2-6: Variation of band gap and dielectric constant for various oxides, reproduced from [194].	69
Figure 2-7: Calculated band offset of some dielectrics. The values are normalised to the VBM of ZnO. The thinner line indicates the minimum of 1 eV for CBO. Reproduced from [196].	70
Figure 3-1: Metal-insulator-metal (MIM) structure used to assess the properties of the insulator.	101
Figure 3-2: Equivalent circuit of a MIM capacitor.	102
Figure 3-3: Impedance vector plane representation.	103
Figure 3-4: Frequency response of the equivalent circuit (inset) used to describe impedance characteristics of a MIM device.	105
Figure 3-5: Frequency dependence of the real and imaginary parts of the dielectric constant, reproduced from.	106
Figure 3-6: Classification of conduction mechanisms in dielectric films reproduced from [16]	107
Figure 3-7: Schematic energy-band diagram of Schottky emission in a MIM structure.	108
Figure 3-8: Schematic energy-band diagram of Fowler-Nordheim tunnelling in a MIM structure.	110
Figure 3-9: Schematic energy-band diagram of direct tunnelling in MIM structure.	111
Figure 3-10: Schematic energy-band diagram of Poole-Frenkel (PF) emission in MIM structure.	112
Figure 3-11: Typical metal-oxide-semiconductor field effect transistor (MOSFET) structure.	113

Figure 3-12: Energy band diagram for ideal MOS capacitor employing n-type semiconductor at equilibrium ($V_{app}=0$). (1) $q\phi_m$: ϕ_m is the metal work function, (2) $q\chi_i$: χ_i is the electron affinity of the insulator, (3) $q\chi$: χ is the electron affinity of the semiconductor, (4) $E_g/2$: E_g is the band gap of the semiconductor, (5) $q\phi_n$: ϕ_n is the Fermi potential with respect to conduction band edge, (6) $q\psi_{Bn}$: ψ_{Bn} is the Fermi potential with respect to midgap edge.	114
Figure 3-13: Schematic energy-band diagram MOS capacitor employing n-type semiconductor under positive voltage bias ($V_{app}>0$).	115
Figure 3-14: Schematic energy-band diagram MOS capacitor employing n-type semiconductor under small negative voltage bias ($V_{app}<0$).	116
Figure 3-15: Schematic energy-band diagram MOS capacitor employing n-type semiconductor under high negative voltage bias ($V_g=V_{app}<<0$).	117
Figure 3-16: Family tree of Field-Effect Transistors (FETs). Reproduced from [10] ..	118
Figure 3-17: Schematics showing some of the most conventional TFT structures, according to the position of the gate electrode and the distribution of the electrodes relative to the semiconductor, reproduced from [40].	118
Figure 3-18: Schematic of a thin-film transistor showing the source, drain and gate contacts, dielectric layer and semiconductor with a graphic representation of the charge accumulation and depletion regions. The device is shown in the saturation regime where $V_D > V_G - V_T$, reproduced from[41]	119
Figure 3-19: Typical a) output and b) transfer characteristics of a n-type oxide TFT, reproduced from[40]	121
Figure 4-1: Schematic diagram of spray pyrolysis equipment configuration, reproduced from [6].	130
Figure 4-2: Schematic of evaporation system used to deposit metallic contacts.	132
Figure 4-3: Schematic design of x-ray diffraction from a periodic atom structure. ...	134
Figure 4-4: Schematic representation of an atomic force microscope setup.	136
Figure 4-5:Tauc plot and linear fit for analysis of the Tauc-gap.	137
Figure 4-6: Schematic of the operational principles of a UV-Vis spectrophotometer.	138
Figure 4-7: Schematic of an FT-IR experimental setup.	139
Figure 4-8: Single wavelength ellipsometer setup.....	140
Figure 5-1:(a) MIM capacitor and (b) Bottom gate-top contact (BG-TC) ZnO-based TFT structures used in this study, implementing $Ti_{1-x}Al_{2x}O_y$ thin film dielectric.	152
Figure 5-2: TGA and DSC data of aluminium (III) chloride powder. TGA and DSC measurements conducted under nitrogen at a heating rate of 10 K/min.	154

Figure 5-3: TGA and DSC data of titanium (IV) butoxide. TGA and DSC measurements conducted under nitrogen at a scan rate of 10K/min.	154
Figure 5-4: GIXRD patterns of selected $Ti_{1-x}Al_{2x}O_y$ films deposited by spray pyrolysis on c-Si substrates.	155
Figure 5-5: AFM topography images (RMS roughness inset) of spray deposited Al_2O_3 , stoichiometric Al_2TiO_y , and (c) TiO_2 films on silicon substrate.	156
Figure 5-6: Tauc plots of selected $Ti_{1-x}Al_{2x}O_y$ films as function of the $[Ti^{4+}]/([Ti^{4+}]+2[Al^{3+}])$ ratio.	157
Figure 5-7: Optical band gap of $Ti_{1-x}Al_{2x}O_y$ thin films as a function of the $[Ti^{4+}]/([Ti^{4+}]+2[Al^{3+}])$ ratio. The solid line is a guide to the eye.	158
Figure 5-8: Urbach tail energy (E_u) as a function of the $[Ti^{4+}]/([Ti^{4+}]+2[Al^{3+}])$ ratio. The solid line guides the eye.	159
Figure 5-9: Schottky barrier pinning factor S of solution processed (SP) Al_2O_3 , TiO_2 , and stoichiometric in the solution dielectrics as well as a wide range of dielectrics grown by vacuum-based deposition techniques as well as solutions.	161
Figure 5-10: Static dielectric constant (k) dispersions of selected $Ti_{1-x}Al_{2x}O_y$ films deposited by spray pyrolysis.	162
Figure 5-11: Dielectric constant (estimated at 10 kHz) of $Ti_{1-x}Al_{2x}O_y$ films as a function of the $[Ti^{4+}]/([Ti^{4+}]+2[Al^{3+}])$ ratio. The solid line guides the eye.	162
Figure 5-12: Static dielectric constant versus band gap of $Ti_{1-x}Al_{2x}O_y$ gate dielectrics deposited by spray pyrolysis. The solid line is a guide to the eye.	163
Figure 5-13: Current-Voltage characteristics of selected $Ti_{1-x}Al_{2x}O_y$ spray deposited dielectrics with different $[Ti^{4+}]/([Ti^{4+}]+2[Al^{3+}])$ ratio.	164
Figure 5-14: Leakage current density of solution processed $Ti_{1-x}Al_{2x}O_y$ gate dielectrics at 2 and 3 MV/cm as a function of the $[Ti^{4+}]/([Ti^{4+}]+2[Al^{3+}])$ ratio. The solid lines guide the eye.	164
Figure 5-15: a) Transfer and b) output characteristics of ZnO-based TFTs employing spray coated Al_2O_3 gate dielectric.	166
Figure 5-16: a) Transfer and b) output characteristics of ZnO-based TFTs employing $Ti_{1-x}Al_{2x}O_y$ gate dielectric ($[Ti^{4+}]/([Ti^{4+}]+2[Al^{3+}]) \sim 45\%$).	166
Figure 5-17: Band diagrams of ZnO, Al_2O_3 and TiO_2 and estimated conduction and valence band offsets on ZnO.	167
Figure 6-1: (a) MIM capacitor and (b) Bottom gate-top contact (BG-TC) ZnO-based TFT structures used in this study, implementing $Nb_{1-x}Al_xO_y$ thin film dielectric.	178
Figure 6-2: TGA and DSC data of niobium (V) chloride. TGA and DSC measurements conducted under nitrogen at a scan rate of 10K/min.	179
Figure 6-3: Tauc plots of selected $Nb_{1-x}Al_xO_y$ films of different $[Nb^{5+}]/([Nb^{5+}]+[Al^{3+}])$ ratios.	180

Figure 6-4: Optical band gap of $\text{Nb}_{1-x}\text{Al}_x\text{O}_y$ thin films as a function of the $[\text{Nb}^{5+}]/([\text{Nb}^{5+}]+[\text{Al}^{3+}])$ ratio. The solid line is a guide to the eye.	181
Figure 6-5: Urbach tail energy (E_u) as a function of the $[\text{Nb}^{5+}]/([\text{Nb}^{5+}]+[\text{Al}^{3+}])$ ratio. The solid line guides the eye.....	181
Figure 6-6: FTIR spectra of selected $\text{Nb}_{1-x}\text{Al}_x\text{O}_y$ films and NbCl_5 and AlCl_3 precursors deposited on KBr substrates.	182
Figure 6-7: GIXRD patterns of selected $\text{Nb}_{1-x}\text{Al}_x\text{O}_y$ films of different $[\text{Nb}^{5+}]/([\text{Nb}^{5+}]+[\text{Al}^{3+}])$ ratios.....	183
Figure 6-8: Friction and topography (inset) images (RMS roughness inset) of solution-processed AlO_x , stoichiometric $\text{Nb}_{0.5}\text{Al}_{0.5}\text{O}_y$, and (c) NbO_x films on silicon substrates.....	184
Figure 6-9: Static dielectric constant (k) dispersion of selected $\text{Nb}_{1-x}\text{Al}_x\text{O}_y$ films in the frequency range of 1 kHz-10 MHz	185
Figure 6-10: Dielectric constant of $\text{Nb}_{1-x}\text{Al}_x\text{O}_y$ films as a function of the $[\text{Nb}^{5+}]/([\text{Nb}^{5+}]+[\text{Al}^{3+}])$ ratio. The solid line is a guide to the eye.	186
Figure 6-11: Static dielectric constant (k) vs band gap for $\text{Nb}_{1-x}\text{Al}_x\text{O}_y$ dielectrics grown by spray pyrolysis. The solid line is a guide to the eye.	186
Figure 6-12: Leakage current density-electric field characteristics of selected $\text{Nb}_{1-x}\text{Al}_x\text{O}_y$ spray deposited dielectrics as a function of the $[\text{Nb}^{5+}]/([\text{Nb}^{5+}]+[\text{Al}^{3+}])$ atomic ratio (in the solution).	187
Figure 6-13: Leakage current density of solution processed $\text{Nb}_{1-x}\text{Al}_x\text{O}_y$ gate dielectrics at 0.5 and 1 MV/cm as a function of the $[\text{Nb}^{5+}]/([\text{Nb}^{5+}]+[\text{Al}^{3+}])$ atomic ratio in the solutions. The solid lines are guides to the eye.....	188
Figure 6-14: Schottky emission (SE) plots of selected $\text{Nb}_{1-x}\text{Al}_x\text{O}_y$ films.	189
Figure 6-15: Fowler-Nordheim (FN) plots of selected $\text{Nb}_{1-x}\text{Al}_x\text{O}_y$ films.	190
Figure 6-16: Poole-Frenkel (PF) plots of selected $\text{Nb}_{1-x}\text{Al}_x\text{O}_y$ films.....	191
Figure 6-17: Schematic energy-band diagram of Schottky emission in a MIM structure.	192
Figure 6-18: a) Electron effective mass in the $\text{Nb}_{1-x}\text{Al}_x\text{O}_y$ and b) barrier height at the $\text{Au}/\text{Nb}_{1-x}\text{Al}_x\text{O}_y$ interface as a function of the $[\text{Al}^{3+}]/([\text{Nb}^{5+}]+[\text{Al}^{3+}])$ ratio. The lines are guides to the eye.	193
Figure 6-19: Energy band diagrams of selected $\text{Nb}_{1-x}\text{Al}_x\text{O}_y$ films. The conduction bands (black solid lines) are presented in respect to gold's fermi energy (E_F). The calculated effective masses included as well.....	193
Figure 6-20: Fowler-Norheim plot of the stoichiometric $\text{Nb}_{1-x}\text{Al}_x\text{O}_y$ film.	194
Figure 6-21: a) Transfer and b) output characteristics of ZnO-based TFTs employing spray coated AlO_y gate dielectric.	195
Figure 6-22: a) Transfer and b) output characteristics of ZnO-based TFTs employing stoichiometric $\text{Nb}_{0.5}\text{Al}_{0.5}\text{O}_y$ gate dielectric.	196

Figure 6-23: Field effect mobility (left Y-axis) and on/off current modulation ratio (right Y-axis) of ZnO-based TFTs employing spray coated $Nb_{1-x}Al_xO_y$ gate dielectrics.	197
Figure 6-24: Conduction band offsets (ΔE_c) of spray coated $Nb_{1-x}Al_xO_y$ gate dielectrics with ZnO.	198
Figure 6-25: Band diagrams of conduction band offsets for dielectric (a) without gap states, (b) with gap states close to conduction band minimum. (E_{c1} : conduction band minimum of zinc oxide, E_{v1} : valence band maximum of ZnO, E_{F1} : Fermi level of ZnO, E_{c2} : Conduction band minimum of a dielectric, $E_{F2}(=E_g/2)$: Fermi level of dielectric assuming no gap states in its band gap, E'_{F2} : Fermi level of dielectric assuming gap states in its band gap, ΔE_{F2} : the transposition (in eV) of Fermi level from midgap, ΔE_c : conduction band offset for dielectrics without gap states, $\Delta E'_c = \Delta E_c - \Delta E_{F2}$: conduction band offset for dielectrics with gap states).	199
Figure 7-1: Schematic orbital contours for charge transport pathways in the conduction band of crystalline a) covalent semiconductor, b) metal oxide semiconductor, disorder c) covalent semiconductor and d) metal oxide semiconductor.	210
Figure 7-2: (a) Single-crystal $InGaZnO_4$, (b) plane, and (c) cross-section transmission electron microscopy (TEM) images of a c-axis-aligned indium gallium zinc oxide (CAAC IGZO) thin film ($In:Ga:Zn=1:1:1$). The InO_2 layer has a compositional ratio of $In:O=1:2$ and the $(Ga,Zn)O$ layer has a compositional ratio of $Ga:Zn:O=0.5:0.5:1$. In: Indium. Ga: Gallium. Zn: Zinc. O: Oxygen. Reprinted from [49]	212
Figure 7-3: TFT fabrication routine followed in this study: a) ultrasonically clean glass/ITO substrate, b) heated glass/ITO substrates were spray coated with the Al_2O_3 precursor solution, c) deposition of IZO semiconducting channel by spray pyrolysis and d) deposition of source and drain electrodes by thermal evaporation.	215
Figure 7-4: TGA (black line) and weight loss rate (red line) and DSC (right Y axis) data of 30 mg indium (III) chloride powder. TGA and DSC measurements conducted under nitrogen at a heating rate of 10 K/min.....	216
Figure 7-5: TGA (black line) and weight loss rate (red line) and DSC (right Y axis) data of 15 mg zinc acetate dihydrate powder. TGA and DSC measurements conducted under nitrogen at a heating rate of 10 K/min.....	217
Figure 7-6: Tauc plots of spray deposited In_2O_3 films, for different deposition temperatures.	218
Figure 7-7: Variation of band gap (left Y axis) and Urbach tail energy (right Y axis) with deposition temperature of In_2O_3 films.	219
Figure 7-8: FT-IR spectra of spray deposited In_2O_3 thin films at different substrate temperatures.	220
Figure 7-9: Molecular structure of In_2O_3 [66].	221

Figure 7-10: I_{DS} (left axis) and $I_{DS}^{1/2}$ (right axis) versus V_{GS} curves of spray deposited In_2O_3 -based TFTs for different In_2O_3 deposition temperatures (a) 350°C, (b) 400°C, (c) 450°C and (d) 500°C. The channel length (L) and width (W) were 100 and 1000 μm respectively.	222
Figure 7-11: Extracted operational characteristics of spray deposited In_2O_3 -based TFTs for different deposition temperatures. a) threshold voltage, b) off-state current, c) field effect mobility in saturation regime and d) subthreshold swing. (The lines are guides to the eyes)	223
Figure 7-12: Optical transmittance of IZO thin films deposited by spray pyrolysis on fused silica substrates	225
Figure 7-13: Tauc Plots of selected IZO spray deposited thin films.....	226
Figure 7-14: Urbach tail energy E_u (left axis) and optical band gap energy (right axis) of spray deposited IZO thin films as a function of $[Zn^{2+}]/([Zn^{2+}]+[In^{3+}])$ in the solution. The lines are guides to the eye.	226
Figure 7-15: FTIR spectra of spray deposited IZO films on KBr substrates for different wavenumber regions.	228
Figure 7-16: X-ray diffraction of spray deposited IZO films on Si substrates for different $[Zn^{2+}]/([Zn^{2+}]+[In^{3+}])$	229
Figure 7-17: (a) average crystallite size, calculated from (222) diffraction peaks, (b) interplanar spacing d_{hkl} calculated for (222) plane, (c) lattice parameter a calculated from the (222) diffraction peak and (d) the corresponding lattice volume assuming the cubic bixbyite cubic In_2O_3 structure.	231
Figure 7-18: Representation of In_2O_3 lattice structure assuming a) Zn^{2+} interstitials and b) Zn^{2+} interstitials and substitutions in In^{3+} site.....	232
Figure 7-19: Atomic force images of spray deposited IZO films on Si substrates for different $[In^{3+}]:[Zn^{2+}]$ ratios.....	236
Figure 7-20: Transfer characteristics ($I_{DS}-V_{GS}$), in saturation regime ($V_{DS}=20$ V), of the spray deposited IZO thin films for different $[In]:[Zn]$ atomic ratios. (a) Indium rich region, (b) zinc rich region.	237
Figure 7-21: (a) off-state current, (b) current modulation, (c) field effect mobility, (d) subthreshold voltage swing. The lines are guides to the eye.....	238
Figure 7-22: Transfer (left) and output (right) characteristics of the spray deposited IZO based thin film transistor possessing a $[In^{3+}]:[Zn^{2+}]=6:4$ stoichiometry.	240
Figure 7-23: FTIR spectra of IZO thin films and the $InCl_3$ and $Zn(O_2C_2H_3)_2 \cdot 2H_2O$ precursors demonstrating the complete decomposition of the precursors.	251
Figure 8-1: TGA (black line) and weight loss rate (red line) and DSC (right Y axis) data of 20 mg yttrium (III) acetylacetonate hydrate powder. TGA and DSC measurements conducted under nitrogen flow at a heating rate of 10 K/min.....	256

Figure 8-2: TGA (black line) and weight loss rate (red line) and DSC (right Y axis) data of 15 mg zirconium (IV) acetylacetonate powder. TGA and DSC measurements conducted under nitrogen flow at a heating rate of 10 K/min.....	257
Figure 8-3: TGA (black line) and weight loss rate (red line) and DSC (right Y axis) data of 15 mg gallium (III) chloride powder. TGA and DSC measurements conducted under nitrogen flow at a heating rate of 10 K/min.....	258
Figure 8-4: a) Transmittance spectra and b) Tauc plots of the IZO:Ga thin films for different Ga doping concentration.	259
Figure 8-5: Optical band gap and Urbach tail energy of IZO:Ga films as a function of Ga doping levels. Lines are guides to the eye.	260
Figure 8-6: FTIR absorption spectra of Ga -doped IZO, at two different spectra regions, on KBr substrates for thin films of varying Ga doping ratios.....	261
Figure 8-7: GIXRD diffraction patterns of Ga-doped c-IZO films for varying Ga doping ratios.	262
Figure 8-8: a) Transmittance spectra and b) Tauc plots of the IZO:Y thin films for different Y doping concentration.....	263
Figure 8-9: Optical band gap and Urbach tail energy of IZO:Y thin films as a function of Y fraction. Lines are guides to the eye.	263
Figure 8-10: GIXRD diffraction patterns of Y-doped c-IZO films for varying Y doping ratios.	264
Figure 8-11: (a) average crystal size and (b) lattice strain calculated from (222) plane of IZO:Y thin films as a function of Y fraction. The lines are guides to the eye.....	265
Figure 8-12: a) Transmittance spectra and b) Tauc plots of the IZO:Zr thin films for different Zr doping concentration	266
Figure 8-13: Optical band gap and Urbach tail energy of IZO:Zr thin films as a function of Zr content. The lines are guides to the eye.	267
Figure 8-14: FTIR absorption spectra of Zr-doped IZO on KBr substrates for thin films of varying Zr doping ratios.	267
Figure 8-15: a) Transmittance spectra and b) Tauc plots of the IZO:Nb thin films for different Nb doping concentration	269
Figure 8-16: Optical band gap and Urbach tail energy of IZO:Nb thin films as function of Nb ⁵⁺ content. The lines are guides to the eye.	269
Figure 8-17: FTIR absorption spectra of Nb-doped IZO on KBr substrates for thin films of varying Nb doping ratios.....	270
Figure 8-18: Transfer characteristic of (a) Ga -doped IZO, (b) Y -doped IZO, (c) Zr -doped IZO, (d) Nb -doped c-IZO thin films with different doping ratios.....	272
Figure 8-19: Off-state current (I_{off}) of c-IZO:X, (X=Ga, Y, Zr, Nb) based TFTs as a function of X content in the films.....	274

Figure 8-20: Field effect mobility (μ) of c-IZO:X, (X=Ga, Y, Zr, Nb) based TFTs as a function of X content in the films.	275
Figure 8-21: Subthreshold slope (SS) of c-IZO:X, (X=Ga, Y, Zr, Nb) based TFTs as a function of X content in the films.	276
Figure 8-22: (a) Tauc plots of selected c-IZO:Y films, (b) optical band gap and Urbach energy as a function of the $[Y^{3+}]/([In^{3+}]+[Zn^{2+}])$ atomic ratio. The solid lines are guides to the eye.....	277
Figure 8-23: GIXRD diffraction patterns of Y-doped c-IZO films with different $[Y^{3+}]/([In^{3+}]+[Zn^{2+}])$ ratios.	278
Figure 8-24: (a) Average grain size ($\langle d \rangle$) and (b) interplanar spacing (d_{hkl}) calculated from the (222) diffraction peak as a function of $[Y^{3+}]:[In^{3+}]$ atomic ratio (in the solution).	279
Figure 8-25: Lattice parameter a for Y-doped c-IZO thin films as a function of $[Y^{3+}]/([In^{3+}]+[Zn^{2+}])$ atomic ratio.....	280
Figure 8-26: Channel formation at grain boundaries and carrier transport pathway [34].	281
Figure 8-27: AFM (topography and friction) images of selected c-IZO:Y thin films. .	282
Figure 8-28: Field effect mobility of c-IZO:Y based TFTs as a function of $[Y^{3+}]/([In^{3+}]+[Zn^{2+}])$ atomic ratio.....	284
Figure 8-29: Off-state current of c-IZO:Y based TFTs as a function of $[Y^{3+}]/([In^{3+}]+[Zn^{2+}])$ atomic ratio.	285
Figure 8-30: a) Transfer and b) output characteristics of 10% Y-doped c-IZO TFT....	286

List of Tables

Table 1-1: Thin film deposition techniques.	27
Table 2-1: Selected previous work on solution processed ZnO semiconductors based on the number of citations. (SC: spin-coating, SP: spray pyrolysis, CBD: chemical bath deposition, Zn(OAc) ₂ : zinc acetate, ATO: Al ₂ O ₃ /TiO ₂ , superlattice, LAO: lanthanum aluminate, AlTiO: Aluminum titanate, ITO: tin doped indium oxide, T _{dep} : deposition temperature, t _{ox} : gate dielectric thickness, SD: source drain, I _{on} /I _{off} : current modulation, μ _{FE} : field effect mobility).	43
Table 2-2: Selected previous work on solution processed In ₂ O ₃ semiconductors based on the number of citations. (SC: spin-coating, USP: ultrasonic spray pyrolysis, ITO: tin doped indium oxide, T _{dep} : deposition temperature, SD: source drain, I _{on} /I _{off} : current modulation, μ _{FE} : field effect mobility, iXsenic: precursor solution developed by Evonik, FUV: far ultraviolet, FLA: flash lamp annealing, VisLzr: visible laser, UV-O ₃ : Ultraviolet-ozone), SAND: self-assembled nanodielectric.	48
Table 2-3: Selected previous work on solution processed multicomponent metal oxide-based semiconductors. (IJP: ink-jet printing, SC: spin-coating, ITO: indium-tin oxide, T _{dep} : deposition temperature, SD: source drain, I _{on} /I _{off} : current modulation, μ _{FE} : field effect mobility, IZO: indium-zinc oxide, ZTO: zinc-tin oxide, IGZO: indium-gallium-zinc oxide, YIZO: yttrium-indium-zinc oxide, LIZO: lanthanum-indium-zinc oxide, ZITO: zinc-indium-tin oxide, MIZO: magnesium-indium-zinc oxide, SrIZO: strontium-indium-zinc oxide, SiIZO: silicon-indium-zinc oxide, ZIZO: zirconium-indium-zinc oxide, GSIZO: gallium-silicon-indium-zinc oxide, LZTO: lanthanum-zinc-tin oxide, L-YIZO: lithium-yttrium-indium-zinc oxide, AIZO: aluminum-indium-zinc oxide, HIZO: hafnium-indium-zinc oxide, GeIZO: germanium-indium-zinc oxide, WIZO: tungsten-indium-zinc oxide, BIZO: borium-indium-zinc oxide).....	56
Table 2-4 Dielectric constant (<i>k</i>) and band gap (<i>E_g</i>) values of some gate oxides, reproduced from [202]	71
Table 2-5: Literature review of solution processed aluminum oxide gate dielectrics used in various TFTs. (SC: Spin coating, SP: spray pyrolysis, 2-ME: 2-methoxyethanol, AN: acetonitrile, EG: ethyleneglycol, MeOH: methanol, EtOH: ethanol, acac: acetylacetone, DIW: deionised water, DMF: N,N-dimethylformamide, GPTMS: (3-glycidoxy- propyl)trimethoxysilane, ZGO: zinc-gallium oxide, ZTO: zinc-tin oxide, GZTO: gallium-zinc-tin oxide, IGZO: indium-gallium-zinc oxide, ITZO: indium-tin-zinc oxide, IWO: indium-tungsten oxide, IZO: indium-zinc oxide, T _{dep} : maximum deposition temperature, k: dielectric constant, J _{leak} : leakage current density, μ _{FE} : field-effect mobility, SS: subthreshold slope, V _{TH} : threshold voltage, I _{on} /I _{off} : on-off current ratio).	73
Table 2-6: Literature review of solution processed metal aluminate gate dielectrics. (SC: Spin coating, SP: spray pyrolysis, 2-ME: 2-methoxyethanol, AN:	

acetonitrile, EG: ethyleneglycol, MeOH: methanol, acac: acetylacetone, n-buto: n-butoxide, DIW: deionised water, DMF: N,N-dimethylformamide, IGZO: indium-gallium-zinc oxide, ITZO: indium-tin-zinc oxide, IZO: indium-zinc oxide, T_{dep} : maximum deposition temperature, k : dielectric constant, J_{leak} : leakage current density, E_b : dielectric strength, μ_{FE} : field-effect mobility, SS: subthreshold slope, V_{TH} : threshold voltage, I_{on}/I_{off} : on-off current ratio, HAO: hafnium aluminate, ZAO: zirconium aluminate, TAO: titanium aluminate, LAO: lanthanum aluminate, *: no available data). .. 78

Table 4-1: Summary of the conduction mechanisms used to assess the conductivity of thin insulating films.....	142
Table 7-1: Operational characteristics of spray deposited In_2O_3 based TFTs, for different deposition temperatures.....	222
Table 7-2: Summary of operational characteristics of the spray deposited IZO thin films for different [In]:[Zn] atomic ratios.....	238
Table 8-1: Summary of c-IZO:X TFT parameters.....	271
Table 8-2: TFT operational characteristics of spray deposited c-IZO:Y based devices	283

1. Introduction

1.1 Functional Metal Oxides for Electronic Devices

Modern transparent electronics require wide band gap conductors, semiconductors and dielectrics which are transparent in the visible range of the electromagnetic spectrum for the fabrication of electronic devices and circuits. These fundamental requirements are fulfilled by metal oxides.

Generally, the term metal-oxide refers to compounds which are formed with metal and oxygen in the form of oxide ion (O^{2-}). Metal oxides constitute an important class of materials due to their ability to demonstrate novel and tunable properties. There are metal oxides that are insulators, semiconductors, conductors or either superconductors. These macroscopic properties strongly depend on their composition.

The most well-studied class of the metal oxides are the transparent conductive oxides (TCOs). Their applications include smart windows applications, flat panel displays (FPDs) and photovoltaic cells. Regarding the usage of TCOs for low emission windows, fluorine doped tin oxide (FTO) has been used for energy efficient windows, due to their low radiative heat loss because of their low thermal emittance [1]. For FPDs, TCOs such as crystalline indium tin oxide (ITO) and amorphous indium zinc oxide (a-IZO) has been used as transparent electrodes. The a-IZO is a relatively new entry in the FPD industry. It is of amorphous structure and can be deposited at room temperature by vacuum-based deposition techniques. TCOs are also a very important class of materials for PV applications [2], [3]. In PV industry ITO has been implemented as the front side electrode in thin film solar cells because of its high conductivity and transparency at the same time. Because of ITO's manufacturing cost (indium is scarce and consequently expensive), alternative indium-free metal oxides have been considered as potential replacements. Fluorine and antimony doped tin oxide (FTO, ATO) have been considered as low-cost alternatives to ITO [4], [5].

Besides the aforementioned applications of TCOs, electrochromic windows and oxide based thin film transistors (TFTs) are two more areas of high interest. In electrochromic windows, TCOs are vital for their performance. In such applications the highly transparency is a prerequisite.

The most interesting field of metal oxides is that of high performance, fully transparent TFTs. The necessity of high performance and highly transparent TFTs has originated from the FPD market. The most common technology in FPD industry is the liquid crystal displays (LCDs). A schematic of a LCD is shown in Figure 1-1. As the light source is located on the back of the TFT backplane, enhanced optical transparency of the TFT would enhance the optical performance of the display. Additionally, metal-oxide based TFTs exhibit higher electron mobility than amorphous silicon (a-Si) which is currently in use, increasing the performance of the devices. Furthermore, the implementation of high-k metal oxide based dielectric materials in the TFT structure as gate dielectrics, could reduce the operational voltage which leads to low power consumption. The low power electronic devices are of particular interest nowadays because of the market interest on portable devices such as high performance and ultra-portable notebooks, tablets and smartphones.

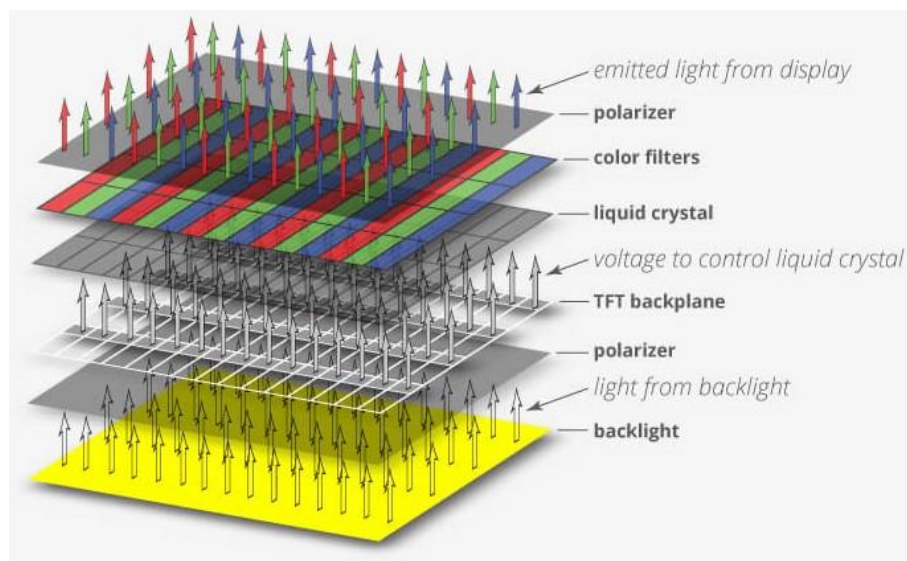


Figure 1-1: Schematic design of a LCD. (Reproduced from¹)

For low voltage and high-performance transparent metal oxide based TFTs several metal oxides with different electrical properties have been studied [6]. As metallic like contacts, indium-tin oxide (ITO), indium-zinc oxide (IZO), gallium-zinc oxide (GZO), aluminum-zinc oxide (AZO) are the most well studied metal oxides that

¹ <http://www.ignisinnovation.com/about-emissive-displays/>

they have been implemented in TFT structures acting as gate and source-drain electrodes. A number of high- k , wide band gap metal oxides have been extensively studied as gate dielectrics. Aluminum oxide (Al_2O_3), hafnium oxide (HfO_2), yttrium oxide (Y_2O_3), zirconium oxide (ZrO_2) are characteristic metal oxides that have been implemented as gate dielectrics in fully transparent TFTs. Binary metal oxides such as aluminum-titanium oxide (TAO), hafnium-aluminum oxide (HAO), lanthanum-aluminum oxide (LAO) have equally been studied as potential gate dielectrics.

Finally, the most extensively studied field towards high performance TFTs is the field of metal oxides. Metal-oxide based semiconductors are in general degenerated TCOs. Transparent conductive oxides exhibit a free carrier concentration (N_c) in excess of 10^{20} cm^{-3} ($N_c > 10^{20} \text{ cm}^{-3}$) while, transparent oxide semiconductors (TSOs) are metal oxides possessing a free carrier concentration typically in the range of 10^{14} - 10^{18} cm^{-3} [7]. Thus, the conductivity of the TSOs can be tuned by using proper setups like field effect transistors, where by applying a voltage to the gate electrode the current flow from source to drain electrode can be controlled.

Zinc oxide (ZnO) is maybe one of the most extensively studied TSO. There is a very high volume of research papers, dealing with the deposition methods of ZnO and how these affect the physical properties of the deposited ZnO thin films. Hoffman et al. in 2003 were prepared a fully transparent ZnO based TFT [8]. They deposited the ZnO active layer on top of a glass/ITO/ATO stack via sputtering resulting in a glass/ITO/TAO/ZnO stack. ITO was serving as gate electrode while ATO (alternating layers of Al_2O_3 and TiO_2) was serving as gate dielectric. Finally, ITO was deposited by sputtering through shadow masks acting as source-drain electrodes. The device exhibited an effective channel mobility of 0.35 - $0.45 \text{ cm}^2/\text{Vs}$, a threshold voltage of 10 - 15 V and a high current on-to-off ratio of about 10^7 .

In the last decade another TSO, a ternary metal oxide composite of indium, gallium and zinc (IGZO) attracted high scientific research interest. In 2003 Nomura et al., developed a TFT implementing single crystalline IGZO as active channel material [9]. They deposited IGZO on an yttria-stabilised zirconia substrate with ITO acting as gate and source-drain electrodes while Al_2O_3 served as the gate dielectric. The device

showed impressive operational characteristics such as a field effect mobility of 80 cm^2/Vs , a turn on voltage of -0.5 V and an on-off current modulation ratio of 10^6 .

In 2004, Nomura et al. introduced for first time a flexible metal oxide-based thin film transistor, deposited at room temperature by PLD, implementing amorphous IGZO (a-IGZO) as semiconducting layer [10]. In their device Y_2O_3 was serving as the gate dielectric while ITO was serving as gate and source-drain electrode.

Nomura's work opened a whole new era for metal oxide based electronic devices. Since then extensive studies for amorphous oxide semiconductors (AOSs) were conducted to replace the amorphous hydrogenated silicon (a-Si:H).

AOSs, in contrast to a-Si:H, are not affected by the degree of disorder. In covalent semiconductors such as a-Si:H the carrier transport pathways consist of hybrid sp^3 orbitals. So, the bonds, which are the main carrier transport pathway, in covalent semiconductors are highly sensitive to structural disorder. So, any kind of structural disorder significantly alters the electronic properties of such semiconductors. On the other hand, oxide-based semiconductors, especially for the transitional metal oxide-based ones with electronic structure of $(n-1)d^{10}ns^0$, ($n \geq 4$), the carrier transport pathways are the bottom of conduction band or conduction band minima (CBM). The CBM of most metal oxides consists of spatially spread spherical metal s-type molecular orbitals, ns orbitals. In contrast, the maximum of the valence band (VBM) is formed of oxygen $2p$ orbitals [11]. Figure 1-2 shows a schematic for the carrier transport paths in crystalline and amorphous semiconductors.

Because of the unique electronic structure of the oxide based semiconductors, they exhibit similar carrier transport properties both in crystalline and amorphous phase. In other words, structural disorder in oxide semiconductors does not significantly alter the carrier transport properties because of the overlapping nature of ns orbitals. So, the electronic properties of oxide semiconductors are immune to structural disorder. Thus, in contrast to the case of a-Si where the mobility is more than two orders of magnitude less than that of poly-Si, amorphous oxide semiconductors are of a mobility that is two to five times lower than that of their crystalline counterparts [12].

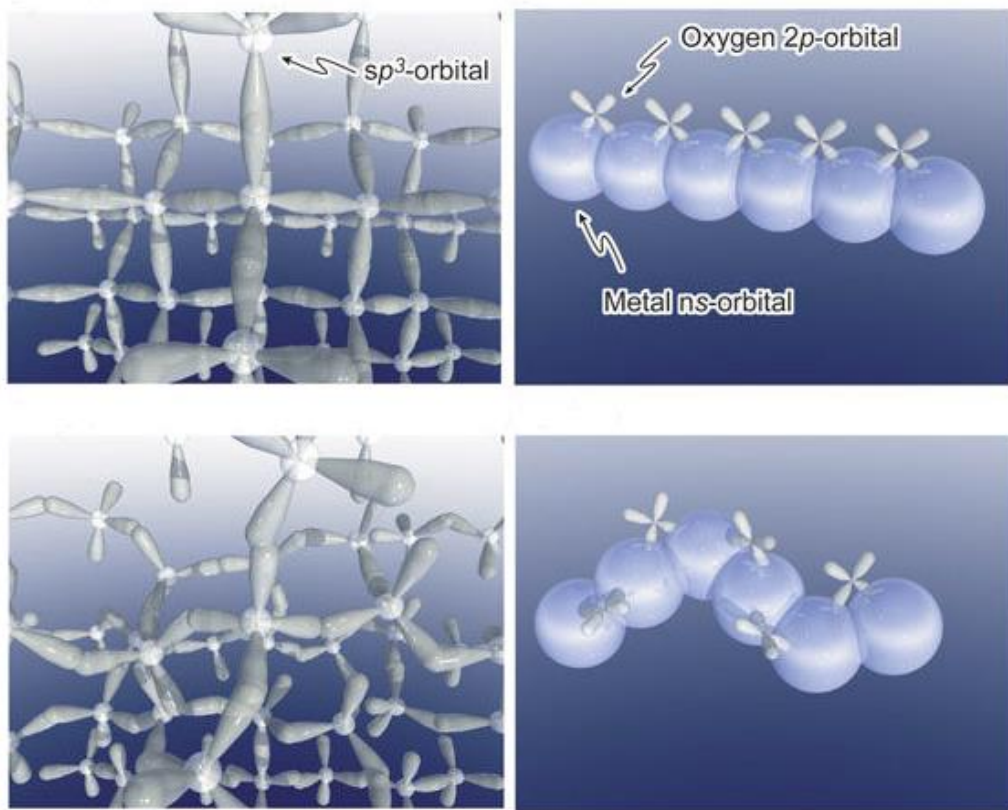


Figure 1-2: Schematic orbital drawings for the carrier transport paths (that is, conduction band bottoms) in crystalline and amorphous semiconductors, reproduced from [10].

The majority of reported AOSs are based on the binary systems of indium oxide (In_2O_3), zinc oxide (ZnO) and tin oxide (SnO_2). Such materials satisfy the criterion of $(n-1)d^{10}ns^0$, ($n \geq 4$), for high performance oxide semiconductors. However, these oxides are of polycrystalline nature. To form amorphous metal oxide semiconductors, blending such binary oxides has been proposed. The combination of indium oxide and the zinc oxide (IZO) results to an amorphous structure, under a particular stoichiometry ($0.25 < [\text{In}]:[\text{Zn}] < 0.8$), which results in enhanced TFT operational characteristics such as high carrier mobility and low hysteresis [13]. Taking the advantage of its structure, a-IZO exhibits a wide range of conductivity depending on the $[\text{In}]:[\text{Zn}]$ atomic ratio and the deposition conditions. A number of TFTs have been reported by various research groups based on a-IZO [14]–[20]. Despite the fact that a-IZO based TFTs have been reported, the control of carrier concentration still remains an issue. Amorphous IZO films exhibit high carrier concentration ($N_c > 10^{17} \text{ cm}^{-3}$) which results in high off-state currents and low current modulation. To control the

carrier concentration the inclusion of various metal cations such as Ga^{3+} [10], [21]–[25], Zr^{4+} [26]–[29], Hf^{4+} [30]–[34], Y^{3+} [35]–[38], La^{3+} [39], [40], have been studied. Among these, Ga^{3+} is the most studied after Nomura’s pioneering work [10]. It has been reported that metal cations such as Ga^{3+} , could effectively suppress the carrier concentration down to $N_c < 10^{17} \text{ cm}^{-3}$, as a result of gallium’s high ionic potential. Because of the high ionic potential of Ga^{3+} metal cations, Ga^{3+} attracts oxygen ions and binds them, suppressing the formation of oxygen vacancies.

Besides the advantages of AOSs, instability issues such as threshold voltage shift (ΔV_{th}) and deterioration of subthreshold voltage swing (ΔSS) under negative (NBS) or positive (PBS) bias, or illumination (NBIS, PBIS) conditions have been reported [6], [41]–[47]. The stability of the TFTs under gate bias and illumination conditions is of significant importance for their implementation in transparent circuit applications. For instance, a shift in threshold voltage could result in an undesirable change of luminance in an OLED pixel resulting in a significant change of the brightness and contrast of the OLED based displays. The origin of such instability issues, is attributed, in general, to charge trapping, defect creation, vacancy ionisation and environmental conditions [12], [48]. Bias stress has been considered as responsible for carrier generation or carrier trapping at the dielectric-semiconductor interface or at the semiconductor itself. Illumination has been found that is responsible for vacancies ionisation resulting in carrier generation shifting the threshold voltage [49].

Different approaches have been followed to tackle the reliability issues of AOSs. Very recently, Yamazaki et al., introduced crystalline IGZO or more precisely c-axis aligned crystalline IGZO (CAAC-IGZO) and they showed that it provides higher reliability than the amorphous counterparts [50]. Besides CAAC-IGZO, nanocrystalline IGZO (nc-IGZO), In-Sn-Zn oxide either as nanocrystalline (nc-ITZO) or c-axis aligned crystalline (CAAC-ITZO) have been considered as channel materials for backplane TFTs in LCD panels [51]. Such materials, developed by Yamazaki’s group exhibit high performance such as ultra-low off currents ($10^{-24} \text{ A}/\mu\text{m}$)[52], and high stability [53].

1.2 Deposition Techniques: A Brief Overview

Metal oxide films have been deposited on various substrates by using a variety of deposition techniques, divided into two main groups, i) vacuum and ii) solution-based deposition ones. Both the techniques show advantages and disadvantages over each other.

In Table 1-1 a summary of the most common used vacuum and solution-based deposition techniques is presented.

Table 1-1: Thin film deposition techniques.

Vacuum Deposition Techniques	Solution Deposition Techniques
Thermal Evaporation (TE)	Chemical Bath
Electron Beam Evaporation (EBE)	Spin Coating
Molecular Beam Epitaxy (MBE)	Dip Coating
Sputtering	Doctor Blade
Plasma Enhanced- Chemical Vapour Deposition (PECVD)	Spray Pyrolysis
Pulsed Laser Deposition (PLD)	Inkjet Printing
Atomic Layer Deposition (ALD)	

1.2.1 Vacuum Based Deposition Techniques

Vacuum-based deposition techniques include physical vapour deposition (PVD) as well as chemical vapour deposition (CVD). Physical vapour deposition (PVD) include among others, thermal (TE) and electron beam evaporation (EBE), molecular beam epitaxy (MBE), sputtering and the pulsed layer deposition (PLD). On the other hand, the vacuum-based chemical vapour (CVD) deposition techniques include metal organic chemical vapour deposition (MOCVD), plasma enhanced chemical vapour deposition (PECVD) and atomic layer deposition (ALD).

Deposition of thin films by vacuum-based techniques requires high vacuum including low and high vacuum pumps, and vacuum chambers. The deposited material

(source/target) is either a metal or metal-oxide material which pulverised to ions or vapours and it deposited on the substrate.

In thermal evaporation (TE) or resistance heating technique, the source material is heated by an electrical current through a filament or a resistance heated boat under high vacuum ($<10^{-5}$ mbar). The source solid material is turned into vapour which travels in the chamber and is deposited on the substrate to form a thin film. In contrast, in the electron beam evaporation (EBE) instead of a heated filament or a resistance heated boat, the source material is tuned into vapours by high energy electron beam bombardment on the material to be deposited. An electron gun is used to generate the electron beam by thermionic emission of electrons from a filament and the electrons are accelerated by an electric field.

In molecular beam epitaxy (MBE) the thin films are being epitaxial grown. This combines both the physical and chemical vapour deposition methods. The source material is heated to its evaporation point, turns into gaseous form and the beams of atoms or molecules are forwarded toward a heated monocrystalline substrate [54]. In this technique the crystalline substrate is very important, and the properties of the deposited film strongly depend on it. The deposition rate is low, but the films are of high crystalline quality.

The most widely used technique for thin films deposition is the sputtering. In its simplest configuration, it consists of a vacuum chamber which is filled with an inert gas such as argon and a metallic anode and cathode to produce a glow discharge. Sputtering is the process that atoms from the target's surface is physically vaporised by momentum transfer from bombarding energetic atomic sized particles [55]. There are two common types of sputtering process: direct current (DC) and radio frequency (RF) sputtering.

In plasma enhanced chemical vapour deposition (PECVD) gaseous precursors are used to deposit the requested materials. The gaseous precursors are turned into reactive ions, atoms, molecules by plasma.

Another vacuum-based thin film deposition technique, is the pulsed laser deposition (PLD) [56]–[58]. In PLD pulses of laser are used to ablate atoms from the

surface of the source material. The ablated, from a pulsed laser, atoms are deposited on the substrate. PLD is a deposition technique that in general does not require an ultra-high vacuum, as other vacuum-based techniques. A major drawback of PLD is the large area incompatibility [59].

Atomic layer deposition (ALD) is a chemical vapour deposition technique. In ALD two or more gaseous precursors are used sequentially. Firstly, the deposition chamber is vacuumed to remove any kind of unwanted air molecules. The first gaseous chemical is then introduced into the reaction chamber by a carrier gas and it reacts with the substrate to form the first layer of the film. Then the reaction chamber is evacuated again, and the second gaseous precursor is introduced. ALD is a sequential deposition technique. It is a slow deposition technique, but it can run even at lower temperatures.

1.2.2 Solution Based Deposition Techniques

Solution based deposition techniques include among others, the chemical bath deposition, the spin and dip coating technique, the so-called doctor blade technique the spray pyrolysis or spray coating deposition technique and the inkjet printing. Among them, spin coating and spray pyrolysis are the two more frequently used techniques for the deposition of metal oxide films.

The chemical bath deposition (CBD) technique has been extensively used to deposit metal chalcogenide thin films [60]–[62]. Chemical bath deposition requires simple instrumentation; just a hot plate with a magnetic stirrer. In CBD the deposition of the films takes place on a substrate immersed in the precursor solution by chemical reactions. With CBD, a large number of substrates can be coated in a single run with a proper jig design.

The dip coating technique consists of the withdrawal of a substrate from a fluid sol: gravitational draining and solvent evaporation, accompanied by further condensation reactions, result in the deposition of a solid film [63]. In dip coating technique there is no solution waste, however this deposition technique offers a

relatively fair thickness control. The drawback of film thickness control is due to the difficulty to homogeneously wet a substrate [64].

Doctor blade and inkjet printing are both printing techniques that they have been used in the field of thin films. Doctor blade (or tape casting) is a rotogravure printing technique [65]. A blade removes the excess of the solution deposited on the desired substrate. The substrate is heated then to the desired temperature to convert the precursor to the metal oxide. Doctor blade is a deposition technique that is mainly used in the field of organic electronics.

Inkjet printing has been considered as one of the cost-effective direct write techniques for films manufacturing. The use of this technique in electronics manufacturing, where interconnects and other conductive features are required is an area of increasing relevance to the fields of electronics manufacturing, packaging and assembly [66].

Among the widely used solution processed thin film deposition techniques, spin coating is the most popular ones. Spin coating is the technique that a precursor solution is deposited onto a rotating substrate. For the deposition of thin films, the spin coater is accelerated to uniformly spread the solution and let the solvent to be evaporated. The substrate is then heated up to let the solvent be evaporated. This step is repeated several times until the desired film thickness is reached. The thickness of the film depends on several parameters, i.e. the chemistry of the solution, the nature of the substrate, the speed and the time of the spinning process. Finally, to enhance the properties of the as deposited thin film a post deposition annealing at higher temperatures is usually occurred.

Finally spray pyrolysis (or spray coating) is a versatile thin film deposition technique [67], [68]. In the spray deposition process, a precursor solution is atomised by a gas such as nitrogen, which also acts as a carrier gas that delivers the atomised solution on a heated substrate in the form of very fine droplets. The constituents react to form a chemical compound onto the substrate.

In this research, thin films were deposited by spray pyrolysis. The parameters that influence the deposition of metal oxides are presented in a following chapter with an extended description of spray pyrolysis instrumentation.

1.3 Thesis Outline

In this thesis the physical properties of solution processed metal oxides are reported. Aiming to develop low cost, high performance and low power consumption transparent thin film transistors (TFTs) for large area compatible applications, metal oxide thin films were deposited on glass substrates by chemical spray coating or as it is widely known spray pyrolysis. Metal oxide thin films were deposited on various substrates, such as fused silica, KBr, Si, glass/ITO.

To investigate the physical properties of metal oxide thin films, several analytical techniques were used. Thermal analysis (STA), UV-Vis-NIR spectroscopy, Fourier-transform infrared (FTIR) spectroscopy, atomic force microscopy (AFM), single wavelength ellipsometry (SWE), impedance spectroscopy (IS) and electrical characterisation measurements were carried out at Lancaster University by the author. X-ray diffraction (XRD) measurements were carried out by Dr. Georgios Vourlias at Aristotle University of Thessaloniki (AUTH) and the raw data were further analysed by the author. Spectroscopic ellipsometry measurements were carried out at Queen Mary University of London and were analysed by Dr. George Adamopoulos.

The thesis presented here is organised in four parts. The first part includes an overview of solution processed metal oxide thin films, *chapter 3* in which the theory governing the operation and operational characteristics of thin metal oxide film-based devices is presented.

The second part includes the deposition and characterisation methods. A brief demonstration of spray pyrolysis technique and the features that governing this technique are included.

The third part includes the investigation of high-*k* dielectrics for low power, high performance thin film transistors (TFTs). The implementation of titanium

aluminate (TAO) as gate dielectric in all-solution processed ZnO based TFTs is studied. Another metal aluminate, the niobium aluminate (NAO) as high- k wide band gap dielectric was also studied. ZnO based TFTs employing NAO as gate dielectric are also reported.

The forth part investigated the solution processed wide band gap semiconductors. While amorphous semiconductors attracted to much of the scientific interest over the last decades, their crystalline counterparts reconsidered after the pioneering work of Shupnei Yamazaki [49]. The optical structural and electronic properties of crystalline indium-zinc-oxide (c-IZO) thin films and c-IZO based TFTs are presented. Furthermore, the performance of metal cation doped c-IZO thin films, is studied.

1.4 References

- [1] C. G. Granqvist, 'Transparent conductors as solar energy materials: A panoramic review', *Sol. Energy Mater. Sol. Cells*, vol. 91, no. 17, pp. 1529–1598, Oct. 2007.
- [2] F. U. Hamelmann, 'Transparent Conductive Oxides in Thin Film Photovoltaics', *J. Phys. Conf. Ser.*, vol. 559, no. 1, p. 012016, Nov. 2014.
- [3] A. E. Delahoy and S. Guo, 'Transparent Conducting Oxides for Photovoltaics', in *Handbook of Photovoltaic Science and Engineering*, 2011, pp. 716–796.
- [4] M. Esro, S. Georgakopoulos, H. Lu, G. Vourlias, A. Krier, W. I. Milne, W. P. Gillin, and G. Adamopoulos, 'Solution processed SnO₂:Sb transparent conductive oxide as an alternative to indium tin oxide for applications in organic light emitting diodes', *J. Mater. Chem. C*, vol. 4, no. 16, pp. 3563–3570, 2016.
- [5] E. Elangovan and K. Ramamurthi, 'A study on low cost-high conducting fluorine and antimony-doped tin oxide thin films', *Appl. Surf. Sci.*, vol. 249, no. 1–4, pp. 183–196, Aug. 2005.
- [6] H. Frenzel, A. Lajn, and M. Grundmann, 'One decade of fully transparent oxide thin-film transistors: fabrication, performance and stability', *Phys. status solidi - Rapid Res. Lett.*, vol. 7, no. 9, pp. 605–615, Sep. 2013.
- [7] M. Grundmann, H. Frenzel, A. Lajn, M. Lorenz, F. Schein, and H. von Wenckstern, 'Transparent semiconducting oxides: materials and devices', *Phys. status solidi*, vol. 207, no. 6, pp. 1437–1449, May 2010.

-
- [8] R. L. Hoffman, B. J. Norris, and J. F. Wager, 'ZnO-based transparent thin-film transistors', *Appl. Phys. Lett.*, vol. 82, no. 5, pp. 733–735, Feb. 2003.
- [9] K. Nomura, 'Thin-Film Transistor Fabricated in Single-Crystalline Transparent Oxide Semiconductor', *Science (80)*, vol. 300, no. 5623, pp. 1269–1272, May 2003.
- [10] K. Nomura, H. Ohta, A. Takagi, T. Kamiya, M. Hirano, and H. Hosono, 'Room-temperature fabrication of transparent flexible thin-film transistors using amorphous oxide semiconductors.', *Nature*, vol. 432, no. November, pp. 488–492, Nov. 2004.
- [11] H. Hosono, 'Recent progress in transparent oxide semiconductors: Materials and device application', *Thin Solid Films*, vol. 515, no. 15 SPEC. ISS., pp. 6000–6014, 2007.
- [12] J. F. Conley, 'Instabilities in Amorphous Oxide Semiconductor Thin-Film Transistors', *IEEE Trans. Device Mater. Reliab.*, vol. 10, no. 4, pp. 460–475, Dec. 2010.
- [13] K. K. Banger, Y. Yamashita, K. Mori, R. L. Peterson, T. Leedham, J. Rickard, and H. Siringhaus, 'Low-temperature, high-performance solution-processed metal oxide thin-film transistors formed by a "sol-gel on chip" process', *Nat. Mater.*, vol. 10, no. 1, pp. 45–50, 2011.
- [14] Kyung-Bae Park, Jong-Baek Seon, Gun Hee Kim, Mino Yang, Bonwon Koo, Hyun Jae Kim, Myung-Kwan Ryu, and Sang-Yoon Lee, 'High Electrical Performance of Wet-Processed Indium Zinc Oxide Thin-Film Transistors', *IEEE Electron Device Lett.*, vol. 31, no. 4, pp. 311–313, Apr. 2010.
- [15] P. Barquinha, A. Pimentel, A. Marques, L. Pereira, R. Martins, and E. Fortunato, 'Influence of the semiconductor thickness on the electrical properties of transparent TFTs based on indium zinc oxide', *J. Non. Cryst. Solids*, vol. 352, no. 9–20, pp. 1749–1752, Jun. 2006.
- [16] Y.-L. Wang, F. Ren, W. Lim, D. P. Norton, S. J. Pearton, I. I. Kravchenko, and J. M. Zavada, 'Room temperature deposited indium zinc oxide thin film transistors', *Appl. Phys. Lett.*, vol. 90, no. 23, p. 232103, Jun. 2007.
- [17] E. Fortunato, P. Barquinha, G. Gonçalves, L. Pereira, and R. Martins, 'High mobility and low threshold voltage transparent thin film transistors based on amorphous indium zinc oxide semiconductors', *Solid. State. Electron.*, vol. 52, no. 3, pp. 443–448, Mar. 2008.
- [18] J.-I. Song, J.-S. Park, H. Kim, Y.-W. Heo, J.-H. Lee, J.-J. Kim, G. M. Kim, and B. D. Choi, 'Transparent amorphous indium zinc oxide thin-film transistors fabricated at room temperature', *Appl. Phys. Lett.*, vol. 90, no. 2, p. 022106, Jan. 2007.

- [19] C. G. Choi, S.-J. Seo, and B.-S. Bae, 'Solution-Processed Indium-Zinc Oxide Transparent Thin-Film Transistors', *Electrochem. Solid-State Lett.*, vol. 11, no. 1, p. H7, 2008.
- [20] N. L. Dehuff, E. S. Kettenring, D. Hong, H. Q. Chiang, J. F. Wager, R. L. Hoffman, C.-H. Park, and D. A. Keszler, 'Transparent thin-film transistors with zinc indium oxide channel layer', *J. Appl. Phys.*, vol. 97, no. 6, p. 064505, Mar. 2005.
- [21] H. Yabuta, M. Sano, K. Abe, T. Aiba, T. Den, H. Kumomi, K. Nomura, T. Kamiya, and H. Hosono, 'High-mobility thin-film transistor with amorphous InGaZnO₄ channel fabricated by room temperature rf-magnetron sputtering', *Appl. Phys. Lett.*, vol. 89, no. 11, p. 112123, Sep. 2006.
- [22] P. Barquinha, L. Pereira, G. Gonçalves, R. Martins, E. Fortunato, G. Goncalves, R. Martins, and E. Fortunato, 'Toward High-Performance Amorphous GIZO TFTs', *J. Electrochem. Soc.*, vol. 156, no. 3, pp. H161–H168, 2009.
- [23] G. H. Kim, H. S. J. Kim, H. S. Shin, B. Du Ahn, K. H. Kim, and H. S. J. Kim, 'Inkjet-printed InGaZnO thin film transistor', *Thin Solid Films*, vol. 517, no. 14, pp. 4007–4010, May 2009.
- [24] M. Kim, J. H. Jeong, H. J. Lee, T. K. Ahn, H. S. Shin, J.-S. Park, J. K. Jeong, Y.-G. Mo, and H. D. Kim, 'High mobility bottom gate InGaZnO thin film transistors with SiO_x etch stopper', *Appl. Phys. Lett.*, vol. 90, no. 21, p. 212114, May 2007.
- [25] J. H. J. K. Jeong, J. H. J. K. Jeong, H. W. Yang, J.-S. Park, Y.-G. Mo, and H. D. Kim, 'High performance thin film transistors with cosputtered amorphous indium gallium zinc oxide channel', *Appl. Phys. Lett.*, vol. 91, no. 11, p. 113505, Sep. 2007.
- [26] Y.-W. Chung, F.-C. Chen, Y.-P. Chen, Y.-Z. Chen, and Y.-L. Chueh, 'High-performance solution-processed amorphous ZrInZnO thin-film transistors', *Phys. status solidi - Rapid Res. Lett.*, vol. 6, no. 9–10, pp. 400–402, Oct. 2012.
- [27] T. H. Jeong, S. J. Kim, D. H. Yoon, W. H. Jeong, D. L. Kim, H. S. Lim, and H. J. Kim, 'Study on the Effects of Zr-Incorporated InZnO Thin-Film Transistors Using a Solution Process', *Jpn. J. Appl. Phys.*, vol. 50, no. 7, p. 070202, Jul. 2011.
- [28] P. T. Tue, T. Miyasako, J. Li, H. T. C. Tu, S. Inoue, E. Tokumitsu, and T. Shimoda, 'High-Performance Solution-Processed ZrInZnO Thin-Film Transistors', *IEEE Trans. Electron Devices*, vol. 60, no. 1, pp. 320–326, Jan. 2013.
- [29] J.-S. Park, K. Kim, Y.-G. Park, Y.-G. Mo, H. D. Kim, and J. K. Jeong, 'Novel ZrInZnO Thin-film Transistor with Excellent Stability', *Adv. Mater.*, vol. 21, no. 3, pp. 329–333, Jan. 2009.
- [30] W. H. Jeong, G. H. Kim, D. L. Kim, H. S. Shin, H. J. Kim, M.-K. Ryu, K.-B. Park, J.-B. Seon, and S.-Y. Lee, 'Effects of Hf incorporation in solution-processed Hf-InZnO TFTs', *Thin Solid Films*, vol. 519, no. 17, pp. 5740–5743, Jun. 2011.

- [31] C.-J. Kim, S. S. S. Kim, J.-H. J. J.-H. Lee, J. J.-S. J. Park, S. S. S. Kim, J. J.-S. J. Park, E. Lee, J.-H. J. J.-H. Lee, Y. Park, J. H. Kim, S. T. Shin, and U.-I. Chung, 'Amorphous hafnium-indium-zinc oxide semiconductor thin film transistors', *Appl. Phys. Lett.*, vol. 95, no. 25, p. 252103, Dec. 2009.
- [32] X. Li, E. Xin, and J. Zhang, 'Effects of Hf incorporation on indium zinc oxide thin-film transistors using solution process', *Electron. Mater. Lett.*, vol. 11, no. 1, pp. 143–148, Jan. 2015.
- [33] E. Chong, K. C. Jo, and S. Y. Lee, 'High stability of amorphous hafnium-indium-zinc-oxide thin film transistor', *Appl. Phys. Lett.*, vol. 96, no. 15, p. 152102, Apr. 2010.
- [34] Y. Gao, X. Li, L. Chen, J. Shi, X. W. Sun, and J. Zhang, 'High mobility solution-processed hafnium indium zinc oxide TFT with an Al-Doped ZrO₂ gate dielectric', *IEEE Electron Device Lett.*, vol. 35, no. 5, pp. 554–556, May 2014.
- [35] H. S. Shin, G. H. Kim, W. H. Jeong, B. Du Ahn, and H. J. Kim, 'Electrical Properties of Yttrium–Indium–Zinc-Oxide Thin Film Transistors Fabricated Using the Sol–Gel Process and Various Yttrium Compositions', *Jpn. J. Appl. Phys.*, vol. 49, no. 3, p. 03CB01, Mar. 2010.
- [36] C.-C. Ting, S.-P. Chang, W.-Y. Li, and C.-H. Wang, 'Enhanced performance of indium zinc oxide thin film transistor by yttrium doping', *Appl. Surf. Sci.*, vol. 284, pp. 397–404, Nov. 2013.
- [37] Y.-J. Lee, J.-H. Kim, B.-Y. Oh, and K.-Y. Kim, 'Electrical and Optical Properties of Y-Doped Indium Zinc Oxide Films Grown by RF Magnetron Sputtering', *J. Nanosci. Nanotechnol.*, vol. 13, no. 9, pp. 6296–6299, Sep. 2013.
- [38] Y.-J. Lee, J.-H. Kim, and J. Kang, 'Characteristics of Y₂O₃-doped indium zinc oxide films grown by radio frequency magnetron co-sputtering system', *Thin Solid Films*, vol. 534, pp. 599–602, May 2013.
- [39] J. C. Park, S. W. Kim, C. J. Kim, and H.-N. Lee, 'Low-Temperature Fabrication and Characteristics of Lanthanum Indium Zinc Oxide Thin-Film Transistors', *IEEE Electron Device Lett.*, vol. 33, no. 5, pp. 685–687, May 2012.
- [40] D. N. Kim, D. L. Kim, G. H. Kim, S. J. Kim, Y. S. Rim, W. H. Jeong, and H. J. Kim, 'The effect of La in InZnO systems for solution-processed amorphous oxide thin-film transistors', *Appl. Phys. Lett.*, vol. 97, no. 19, p. 192105, Nov. 2010.
- [41] J. S. Park, W.-J. Maeng, H.-S. Kim, and J.-S. Park, 'Review of recent developments in amorphous oxide semiconductor thin-film transistor devices', *Thin Solid Films*, vol. 520, no. 6, pp. 1679–1693, Jan. 2012.
- [42] J. F. Wager, B. Yeh, R. L. Hoffman, and D. A. Keszler, 'An amorphous oxide semiconductor thin-film transistor route to oxide electronics', *Current Opinion in Solid State and Materials Science*, vol. 18, no. 2, pp. 53–61, Apr-2014.

- [43] A. Nathan, S. Lee, S. Jeon, and J. Robertson, 'Amorphous Oxide Semiconductor TFTs for Displays and Imaging', *J. Disp. Technol.*, vol. 10, no. 11, pp. 917–927, Nov. 2014.
- [44] B. Ryu, H.-K. Noh, E.-A. Choi, and K. J. Chang, 'O-vacancy as the origin of negative bias illumination stress instability in amorphous In–Ga–Zn–O thin film transistors', *Appl. Phys. Lett.*, vol. 97, no. 2, p. 022108, Jul. 2010.
- [45] H. Kim, D. Choi, S. Park, K. Park, H.-W. Park, K.-B. Chung, and J.-Y. Kwon, 'Impact of bias stability for crystalline InZnO thin-film transistors', *Appl. Phys. Lett.*, vol. 110, no. 23, p. 232104, Jun. 2017.
- [46] J.-Y. K. Kyung Park, Hyun Soo Shin, Jonguk Bae, 'A Study on the Characteristics of Crystalline Indium-Gallium-Zinc-Oxide TFTs', *SID Symp. Dig. Tech. Pap.*, pp. 1162–1165, 2015.
- [47] K. Park, H. W. Park, H. S. Shin, J. Bae, K. S. Park, I. Kang, K. B. Chung, and J. Y. Kwon, 'Reliability of Crystalline Indium-Gallium-Zinc-Oxide Thin-Film Transistors under Bias Stress with Light Illumination', *IEEE Trans. Electron Devices*, vol. 62, no. 9, pp. 2900–2905, Sep. 2015.
- [48] J. K. Jeong, H. Won Yang, J. H. Jeong, Y.-G. Mo, and H. D. Kim, 'Origin of threshold voltage instability in indium-gallium-zinc oxide thin film transistors', *Appl. Phys. Lett.*, vol. 93, no. 12, p. 123508, Sep. 2008.
- [49] J.-Y. Kwon, D.-J. Lee, and K.-B. Kim, 'Review paper: Transparent amorphous oxide semiconductor thin film transistor', *Electron. Mater. Lett.*, vol. 7, no. 1, pp. 1–11, 2011.
- [50] S. Yamazaki, H. Suzawa, K. Inoue, K. Kato, T. Hirohashi, K. Okazaki, and N. Kimizuka, 'Properties of crystalline In–Ga–Zn-oxide semiconductor and its transistor characteristics', *Jpn. J. Appl. Phys.*, vol. 53, no. 4S, p. 04ED18, Jan. 2014.
- [51] T. Takasu, N. Ishihara, M. Oota, Y. Ishiguro, Y. Kurosawa, K. Dairiki, and S. Yamazaki, 'Relationship between crystallinity and device characteristics of In-Sn-Zn oxide', *J. Soc. Inf. Disp.*, vol. 23, no. 12, pp. 593–599, 2015.
- [52] Y. Sekine, K. Furutani, Y. Shionoiri, K. Kato, J. Koyama, and S. Yamazaki, 'Success in Measurement the Lowest Off-state Current of Transistor in the World', in *ECS Transactions*, 2011, vol. 37, no. 1, pp. 77–88.
- [53] S. Yamazaki, T. Atsumi, K. Dairiki, K. Okazaki, and N. Kimizuka, 'In-Ga-Zn-Oxide Semiconductor and Its Transistor Characteristics', *ECS J. Solid State Sci. Technol.*, vol. 3, no. 9, pp. Q3012–Q3022, Jul. 2014.
- [54] J. R. Arthur, 'Molecular beam epitaxy', *Surf. Sci.*, vol. 500, no. 1–3, pp. 189–217, 2002.

- [55] D. M. Mattox, 'Physical Sputtering and Sputter Deposition (Sputtering)', in *Handbook of Physical Vapor Deposition (PVD) Processing*, Elsevier, 2010, pp. 237–286.
- [56] H. Krebs, M. Weisheit, J. Faupel, E. Süske, T. Scharf, C. Fuhse, M. Störmer, K. Sturm, M. Seibt, H. Kijewski, D. Nelke, E. Panchenko, and M. Buback, 'Pulsed Laser Deposition (PLD) -- A Versatile Thin Film Technique', in *Advances in Solid State Physics SE - 36*, 2003, pp. 505–518.
- [57] I. W. Boyd, 'Thin film growth by pulsed laser deposition', *Ceram. Int.*, vol. 22, no. 5, pp. 429–434, 1996.
- [58] D. H. Lowndes, D. B. Geohegan, A. A. Puretzky, D. P. Norton, and C. M. Rouleau, 'Synthesis of Novel Thin-Film Materials by Pulsed Laser Deposition', *Science (80)*, vol. 273, no. 5277, pp. 898–903, 1996.
- [59] J. A. Greer, M. D. Tabat, and C. Lu, 'Future trends for large-area pulsed laser deposition', *Nucl. Instruments Methods Phys. Res. Sect. B Beam Interact. with Mater. Atoms*, vol. 121, no. 1–4, pp. 357–362, Jan. 1997.
- [60] C. D. Lokhande, 'Chemical deposition of metal chalcogenide thin films', *Mater. Chem. Phys.*, vol. 27, no. 1, pp. 1–43, Jan. 1991.
- [61] P. K. Nair, M. T. T. S. Nair, V. M. Garcia, O. L. Arenas, Y. Peña, A. Castillo, I. T. Ayala, O. Gomezdaza, A. Sánchez, J. Campos, H. Hu, R. Suárez, M. E. Rincón, V. García, O. L. Arenas, Y. Peña, A. Castillo, I. T. Ayala, O. Gomezdaza, A. Sánchez, J. Campos, H. Hu, R. Suárez, and M. E. Rincón, 'Semiconductor thin films by chemical bath deposition for solar energy related applications', *Sol. Energy Mater. Sol. Cells*, vol. 52, no. 3–4, pp. 313–344, Apr. 1998.
- [62] S. M. Pawar, B. S. Pawar, J. H. Kim, O.-S. Joo, and C. D. Lokhande, 'Recent status of chemical bath deposited metal chalcogenide and metal oxide thin films', *Curr. Appl. Phys.*, vol. 11, no. 2, pp. 117–161, Mar. 2011.
- [63] C. J. Brinker, G. C. Frye, A. J. Hurd, and C. S. Ashley, 'Fundamentals of sol-gel dip coating', *Thin Solid Films*, vol. 201, no. 1, pp. 97–108, Jun. 1991.
- [64] D. Grosso, 'How to exploit the full potential of the dip-coating process to better control film formation', *J. Mater. Chem.*, vol. 21, no. 43, p. 17033, 2011.
- [65] A. Berni, M. Mennig, and H. Schmidt, 'Doctor Blade', in *Sol-Gel Technologies for Glass Producers and Users*, Boston, MA: Springer US, 2004, pp. 89–92.
- [66] G. Cummins and M. P. Y. Desmulliez, 'Inkjet printing of conductive materials: a review', *Circuit World*, vol. 38, no. 4, pp. 193–213, Nov. 2012.
- [67] P. S. Patil, 'Versatility of chemical spray pyrolysis technique', *Mater. Chem. Phys.*, vol. 59, no. 3, pp. 185–198, Jun. 1999.

- [68] D. Perednis and L. J. Gauckler, 'Thin film deposition using spray pyrolysis', *J. Electroceramics*, vol. 14, pp. 103–111, 2005.

2. Solution Processed Metal Oxides: An Overview

2.1 Solution Processed Transparent Oxide (Semi)Conductors

The introduction of solution processed metal oxides either as transparent front contacts to several devices like displays or solar cells, or as channel material in thin film transistors (TFT), is expected to reduce the production cost of the next generation electronic devices. As it was previously reported, metal oxides based on the primary system of indium-zinc-tin have been considered as potential replacements of a-Si:H. Thin films based on binary metal oxides such as ZnO, In_2O_3 , SnO_2 have already been deposited by various deposition techniques. Among the various deposition techniques, the solution-based ones (spray coating, spin coating, chemical bath deposition or inkjet printing) are the most studied techniques. Here a brief report on the solution processed metal oxides used as channel material in TFTs is presented.

2.1.1 Binary Oxides

Binary metal oxides such as In_2O_3 , ZnO and SnO_2 have been considered as potential materials to replace the a-Si:H in some applications as metal oxides are benefited due to their high transparency and their electrical conductivity. Thin films of metal oxides based on the indium, zinc and tin have been deposited by solution processed techniques, mainly by the spin coating. Other solution-based deposition techniques such as spray pyrolysis and chemical bath deposition have also been considered as large area compatible.

In this section a review on the solution processed binary metal oxides ZnO and In_2O_3 is given. To that point it should be noted that the review is mainly based on the highly cited, up to dated, reports and on reports published the last 2 years (between 2015-2017).

2.1.1.1 Zinc Oxide (ZnO)

Zinc oxide (ZnO) has been considered as a very promising metal oxide in the semiconductor industry. It is a wide band gap (~ 3.37 eV) oxide semiconductor with large exciton energy of 60 meV at room temperature [1]. It is crystallised in three polymorphs (wurtzite, cubic zinc blende and cubic rocksalt). Among those three polymorphs, wurtzite is the thermodynamically stable one. It belongs to the $P6_3mc$ or to the C_{6v}^4 space group. The primitive unit-cell of hexagonal wurtzite crystal structure of ZnO, contains two formula units, which each zinc ion surrounded by four oxygen ions in a tetrahedral coordination and vice versa. In Figure 2-1 the side and top view of the hexagonal wurtzite crystal structure of ZnO is presented.

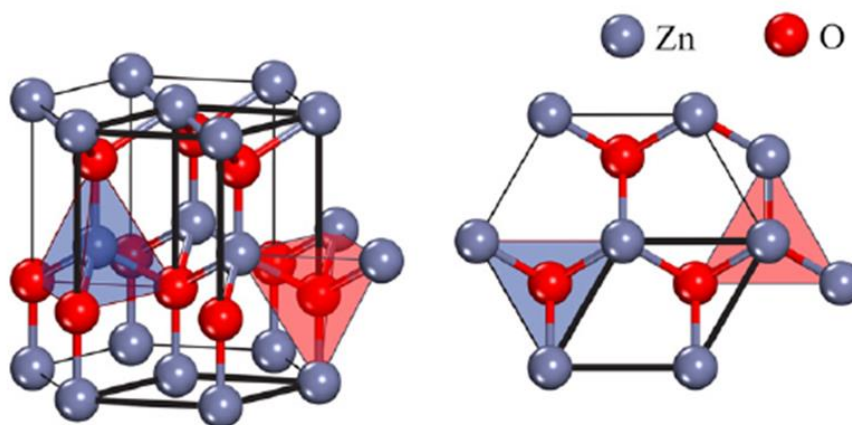


Figure 2-1: Side and top view of hexagonal wurtzite crystal structure of ZnO, after [2]

The lattice parameters of hexagonal wurtzite crystal structure of ZnO are $a=3.23$ Å and $c=5.20$ Å and they exhibit a ratio of $c/a=1.6$.

The band structure along with the electronic states of ZnO, have been subject in a plethora of theoretical and experimental studies. In Figure 2-2 the band structure of hexagonal wurtzite ZnO as it is calculated from density functional theory (DFT) using the local density approximation (LDA) along with atomic self-interaction corrected pseudopotentials (SIC-PP) is illustrated.

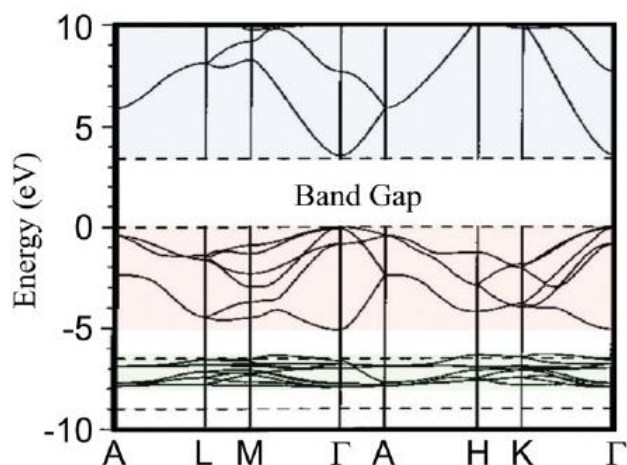


Figure 2-2: Band structure of hexagonal wurtzite ZnO obtained from density-functional theory calculations (DFT), after [3].

The top of the valence band (valence band maxima-VBM) in ZnO is mainly consisted by oxygen (O) $2p$ orbitals and, the bottom of the conduction band (conduction band minima-CBM) by empty zinc (Zn) $4s$ orbitals. Both the VBM and CBM are located at the centre of Brillouin zone (Γ -point) resulting to a direct band gap of about 3.2-3.4 eV depending on the variation of lattice parameters.

The first solution processed ZnO based TFT was reported in 2001 by Ohya et al. [4]. They deposited ZnO by using the dip-coating method, from a starting solution containing zinc acetate dihydrate ($\text{Zn}(\text{COOCH}_3)_2 \cdot 2\text{H}_2\text{O}$) in a mixture of 2-propanol and diethanolamine (DEA). They deposited the solution on a Si/SiO₂ (130 nm) substrate, where the Si was acting as the gate electrode and the SiO₂ as the gate dielectric. On top of the ZnO (40 nm) they deposited gold (Au), as source and drain electrodes by vacuum evaporation, resulting in a TFT geometry of 25 μm channel length (L) and 0.83 mm channel width (W). Prior to the deposition of gold contacts, the ZnO layer was annealed at 600 °C to 900 °C in air. Unfortunately, the performance of the device cannot be evaluated since the operational characteristics of their ZnO-based TFT were not included in their report.

Table 2-1: Selected previous work on solution processed ZnO semiconductors based on the number of citations. (SC: spin-coating, SP: spray pyrolysis, CBD: chemical bath deposition, Zn(OAc)₂: zinc acetate, ATO: Al₂O₃/TiO₂, superlattice, LAO: lanthanum aluminate, AlTiO: Aluminum titanate, ITO: tin doped indium oxide, T_{dep}: deposition temperature, t_{ox}: gate dielectric thickness, SD: source drain, I_{on}/I_{off}: current modulation, μ_{FE}: field effect mobility).

Method	Precursor	T _{dep} (°C)	Insulator	Gate/SD	I _{on} /I _{off}	μ _{FE} (cm ² /Vs)	year	Ref
SC	Zn(NO ₃) ₂ ·6H ₂ O	700	ATO	ITO/ITO	10 ⁷	0.2	2003	[5]
SC	Zn(OAc) ₂	230	SiO ₂	Si/(Cr/Au)	10 ⁵	0.61	2005	[6]
SC	Zn(OAc) ₂	500	ATO	ITO/Zn	10 ⁵	5.25	2007	[7]
SC	Zn(OAc) ₂	270	SiO ₂	Si/Al	10 ⁶	1.2	2007	[8]
CBD	ZnCl ₂	600	SiO ₂	Si/Al	10 ⁵	3.5	2007	[9]
SC	Zn(NO ₃) ₂ ·6H ₂ O	300	SiO ₂	Si/(Cr/Au)	10 ⁶	3	2008	[10]
SP	Zn(OAc) ₂ ·2H ₂ O	400	SiO ₂	Si/Al	10 ⁶	15	2009	[11]
SP	Zn(OAc) ₂ ·2H ₂ O	400	SiO ₂	Si/(Al, Au, Ca)	10 ⁶	20	2009	[12]
SC	Zn(OAc) ₂ ·2H ₂ O	500	ATO	ITO/Zn	10 ⁵	5.26	2009	[13]
SP	Zn(OAc) ₂	400	SiO ₂	Si/Al	10 ⁷	54	2010	[14]
SC	Zn(OAc) ₂	400	Ion gel	Cu/Al	10 ⁵	14.8	2010	[15]
SC	Zn(OAc) ₂ ·2H ₂ O	600	SiO ₂	Si/Al	10 ⁵	9.4	2010	[16]
SC	Zn(OH) ₂	140	SiO ₂	Si/Al	10 ⁷	107	2011	[17]
SP	Zn(OAc) ₂	500	SiO ₂	Si/Al	10 ⁶	25	2011	[18]
SC	ZnO·xH ₂ O	125	SiO ₂	Si/Al	10 ⁶	0.25	2011	[19]
SC	ZnO	300	SiO ₂	Si/Al	10 ⁷	7.34	2012	[20]
SC	ZnO·xH ₂ O	180	SiO ₂	Si/Al	10 ⁷	11	2013	[21]
Ink-jet	Zn(OAc) ₂ ·2H ₂ O	150	SiO ₂	Si/(Cr/Au)	10 ⁶	3.03	2014	[22]
SP	Zn(OAc) ₂ ·2H ₂ O	400	LAO	ITO/Al	10 ⁶	12	2015	[23]
SP	Zn(OAc) ₂ ·2H ₂ O	400	AlTiO	ITO/Al	10 ⁶	10	2015	[24]

In 2003, Norris et al., developed spin-coated zinc oxide based thin film transistors (TFTs) [5]. They used a glycine-deionised water-based solution of zinc nitrate hexahydrate ($\text{Zn}(\text{NO}_3)_2 \cdot 6\text{H}_2\text{O}$). The TFTs were prepared by depositing the zinc-nitrate based solution on the top of a glass/ITO/ATO substrate by spin-coating. Tin doped indium oxide (ITO) served as the gate electrode while, the superlattice of Al_2O_3 and TiO_2 served as the gate dielectric. The stack was annealed at 600 °C for 10 mins in air following by a post-annealing treatment of rapid thermal annealing (RTA) in oxygen at 700 °C. Finally, ITO source and drain electrodes were deposited via ion-beam sputtering. The solution processed ZnO-based TFT showed encouraging operational characteristics, such as an electron channel mobility as high as $0.2 \text{ cm}^2/\text{Vs}$ and a current modulation ratio of about 10^7 .

Norris et al., report on solution processed ZnO-based TFTs gave rise to several studies on optimisation methods and techniques to enhance the performance of solution-processed oxide-based TFTs. In Table 2-1 selected reports on solution processed ZnO-based TFTs are presented.

From Table 2-1, among the various solution based thin film deposition techniques, spray pyrolysis seems to provide high performance ZnO-based TFTs. Indeed, in 2009 and 2011 Adamopoulos et al., reported on the electronic properties of the ZnO-based field-effect transistor fabricated by the spray pyrolysis [12], [18]. The transistors were fabricated by methanol-based zinc acetate dihydrate solutions that was sprayed on top of a heavily doped silicon (Si^{++}) acting as common gate electrode and employing a 200-400 nm SiO_2 gate dielectric at a moderate temperature of 400 °C. Finally, metal source-drain electrodes were deposited via thermal evaporation under high vacuum through shadow masks. Their devices showed excellent operational characteristics such as high electron mobilities in excess of $20 \text{ cm}^2/\text{Vs}$ and high current on/off ratios in the range of 10^6 - 10^8 .

Recently high-performance spray deposited ZnO-based TFTs employing gate dielectrics that they are at the same time of wide band gap and high- k , have been reported. Afouxenidis et al., fabricated ZnO-based TFTs employing aluminum titanate as gate dielectric by spray pyrolysis at ambient air [24]. The devices exhibit excellent

electron transport characteristics with low operating voltages (~ 10 V), negligible hysteresis, high on/ off current modulation ratio of $\sim 10^6$, subthreshold swing (SS) of ~ 550 mV/dec and electron mobility of ~ 10 cm²/Vs. In the same content, Esro et al., report on ZnO-based (TFTs) employing lanthanum aluminate gate dielectrics deposited by spray pyrolysis in ambient air [23]. The devices exhibit operational characteristics with low operation voltages (~ 10 V), high on/off ratio in excess of 10^6 , subthreshold swing of 650 mV/dec, and electron mobility of about 12 cm²/Vs.

2.1.1.2 Indium Oxide (In_2O_3)

Indium oxide (In_2O_3) is an n-type transparent conductive oxide (TCO). It is a metallic sesquioxide (M_2O_3) that crystallizes in the cubic structure (bixbyite). Bixbyite structure is in close relation to fluorite (CaF_2) structure but, with one quarter of the anions removed [25]. It exhibits a $Ia\bar{3}$ space group symmetry with a lattice constant of 10.117 Å. In Figure 2-3 the crystal structure of cubic (bixbyite) structure of In_2O_3 is illustrated.

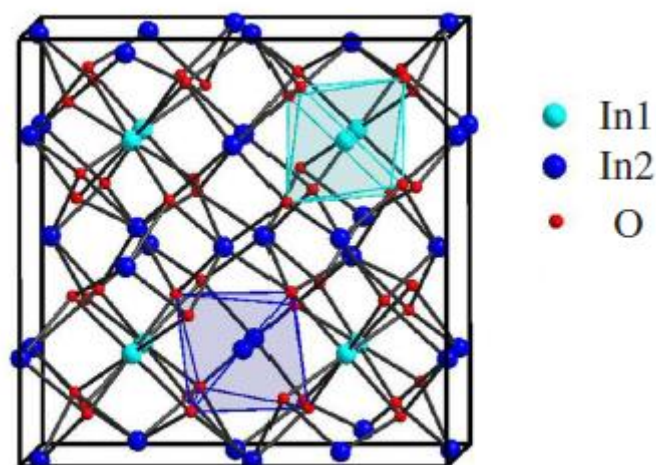


Figure 2-3: Crystal structure of cubic (bixbyite) In_2O_3 , after [26].

The unit cell of bixbyite type- In_2O_3 contains 8 formula units. Also, it consists of two types of indium and one type of oxygen atoms. The distribution of the indium's types is based on the different co-ordinations with the oxygen atoms. An indium atom

could be surrounded by oxygen forming either octahedra or trigonal prisms. The average In-O interatomic distances has been estimated to be 2.18 Å [27].

The electronic band structure of In_2O_3 has attracted scientific interest due to the optoelectronic applications of In_2O_3 thin films. Weiher and Ley investigated the fundamental optical absorption edge of In_2O_3 [28]. They observed direct-allowed transitions with an energy gap of 3.75 eV. In their study, they also observed indirect-forbidden transitions with an energy gap of 2.619 eV and an assisting phonon of 69 meV. Several theoretical and experimental studies were conducted to elucidate the band structure of In_2O_3 . Most of the studies were based on the structure of the valence band and whether the valence band maximum is located at the Γ -point or not [26], [29]–[31]. In Figure 2-4 the energy band structure of In_2O_3 is presented.

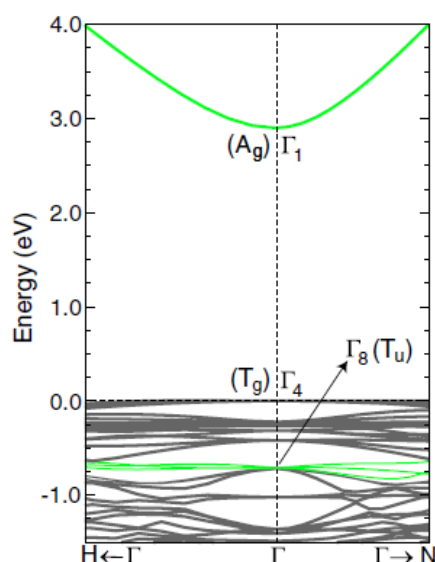


Figure 2-4: Band structure of In_2O_3 , after [31].

As shown in Figure 2-4, even if the separation of VBM-CBM ($\Gamma_4 \rightarrow \Gamma_1$ transition) has been estimated to be of 2.89 eV, the onset of optical absorption is observed at 3.7 eV [31]. The $\Gamma_8 \rightarrow \Gamma_1$ transitions are responsible for the experimentally calculated band gap of 3.7 eV fact that demonstrates that the valence band, that are states located within 0.8 eV of the VBM, have no significant impact to low energy photon absorption.

Besides the various applications of In_2O_3 thin films, the implementation of In_2O_3 as the active channel material in TFTs is of particular interest. The high inherent free carrier concentration of In_2O_3 was controlled by changing of the film's thickness and the oxygen partial pressure, the latter in vacuum-based deposition techniques. In_2O_3 -based TFTs have been developed by a number of deposition techniques including RF sputtering [32], [33], ion beam assisted evaporation [34], [35], radio-frequency plasma enhanced reactive thermal evaporation [36], ink-jet [37], spin coating [38], [39], spray pyrolysis [40], [41].

In Table 2-2 selected works on solution-processed In_2O_3 -based TFTs are shown. Most of the reported solution processed TFTs were prepared by indium nitrate hydrate ($\text{In}(\text{NO}_3)_3 \cdot x\text{H}_2\text{O}$) precursor. It has been reported that solution-processed TFTs developed by using metal nitrate ($\text{M}(\text{NO}_3)_x$) precursors, could be deposited at lower processing temperatures because of the lower decomposition temperature of the $\text{M}(\text{NO}_3)_x$ [42].

Although the majority of the solution-processed In_2O_3 -based TFTs were developed by using $\text{In}(\text{NO}_3)_3 \cdot x\text{H}_2\text{O}$ precursors, the first reported solution processed In_2O_3 -based TFT was prepared by using indium chloride (InCl_3) [39]. Kim et al., reported on In_2O_3 TFTs fabricated on SiO_2 and self-assembled nanodielectrics (SANDs) by spin-coating. The In_2O_3 film precursor solutions were prepared by dissolving InCl_3 in a mixture of ethanalamine (EAA) methoxyethanol (MEA). Their optimised TFTs with EEA/ In^{3+} =10 molar ratio having a device structure of n^+ -Si/SAND/ In_2O_3 /Au were exhibited high field-effect mobilities ($\sim 44 \text{ cm}^2/\text{Vs}$) and high current modulation ($\sim 10^6$) at low operating voltages ($< 5 \text{ V}$).

Table 2-2: Selected previous work on solution processed In_2O_3 semiconductors based on the number of citations. (SC: spin-coating, USP: ultrasonic spray pyrolysis, ITO: tin doped indium oxide, T_{dep} : deposition temperature, SD: source drain, $I_{\text{on}}/I_{\text{off}}$: current modulation, μ_{FE} : field effect mobility, iXsenic: precursor solution developed by Evonik, FUV: far ultraviolet, FLA: flash lamp annealing, VisLzr: visible laser, UV- O_3 : Ultraviolet-ozone), SAND: self-assembled nanodielectric.

Method	Precursor	T_{dep} (°C)	Insulator	Gate/SD	$I_{\text{on}}/I_{\text{off}}$	μ_{FE} (cm^2/Vs)	Year	Ref
SC	InCl_3	400	SAND	Si/Au	10^6	43.7	2008	[39]
SC	InCl_3	500	SiO_2	Si/Al	10^7	55.26	2011	[38]
SC	InCl_3	250	AlO_x (250)	Si/Al	10^6	127	2013	[43]
SC	$\text{In}(\text{NO}_3)_3 \cdot x\text{H}_2\text{O}$	250	$\text{ZrO}_2:\text{B}$	Si/Al	10^7	39.3	2013	[44]
SC	$\text{In}(\text{NO}_3)_3 \cdot x\text{H}_2\text{O}$	200	SiO_2	Si/Al	10^6	8.6	2013	[45]
SC	$\text{In}(\text{NO}_3)_3 \cdot x\text{H}_2\text{O}$	250	ZrO_x	Si/Al	10^7	23.6	2014	[46]
SC	$\text{In}(\text{NO}_3)_3 \cdot x\text{H}_2\text{O}$	200+FUV	SiO_2	Si/Al	10^6	7.5	2014	[47]
USP	$\text{In}(\text{NO}_3)_3 \cdot x\text{H}_2\text{O}$	250	SiO_2	Si/Al	10^6	16	2015	[41]
SC	$\text{In}(\text{NO}_3)_3 \cdot x\text{H}_2\text{O}$	300	SiO_2	Mo/Al	10^7	7.5	2015	[48]
SC	$\text{In}(\text{NO}_3)_3 \cdot x\text{H}_2\text{O}$	300	SiO_2	Si/Al	10^8	3.08	2015	[49]
SC	iXsenic S	350	SiO_2	Si/(ITO/Au)	10^8	28	2015	[50]
SC	$\text{In}(\text{NO}_3)_3 \cdot x\text{H}_2\text{O}$	250	SiO_2	Si/Al	10^6	1.21	2016	[51]
SC	InCl_3	350+UV	SiO_2	Si/Al	10^7	3.53	2016	[52]
SC	$\text{In}(\text{NO}_3)_3 \cdot x\text{H}_2\text{O}$	200	SiO_2	Si/Al	10^7	0.94	2016	[53]
SC	$\text{In}(\text{NO}_3)_3 \cdot x\text{H}_2\text{O}$	120+FLA	SiO_2	Si/Al	10^4	38.9	2016	[54]
SC	$\text{In}(\text{NO}_3)_3 \cdot x\text{H}_2\text{O}$	120+(UV- O_3)	SiO_2	Si/Al	10^7	1.25	2016	[55]
SC	$\text{In}(\text{NO}_3)_3 \cdot x\text{H}_2\text{O}$	320	MgO (500)	Si/Al	10^7	5.48	2016	[56]
SC	$\text{In}(\text{NO}_3)_3 \cdot x\text{H}_2\text{O}$	310	SrO_x (600)	Si/Al	10^7	5.61	2017	[57]
USP	$\text{In}(\text{NO}_3)_3 \cdot x\text{H}_2\text{O}$	250	SiO_2	Si/Al	10^7	38.5	2017	[58]
SC	$\text{In}(\text{NO}_3)_3 \cdot x\text{H}_2\text{O}$	100+VisLzr	ZrO_2 (400)	Si/W	10^6	2.76	2017	[59]

Han et al., reported on solution-processed In_2O_3 TFTs fabricated by a spin-coating process using InCl_3 dissolved in a mixture of acetonitrile (AN) and ethylene glycol (EG) [38]. The TFTs were annealed at 500 °C under air and exhibited high field-effect mobilities ($55.26 \text{ cm}^2/\text{Vs}$) and high current modulation (10^7). To explore the role of annealing atmosphere they characterise In_2O_3 TFTs annealed under an O_2/O_3 atmosphere at temperatures from 200 to 300 °C. The O_2/O_3 annealed TFTs were exhibited excellent performance with field-effect mobilities in the range of $0.85\text{-}22.14 \text{ cm}^2/\text{Vs}$ and current modulation ratio in the range of $10^5\text{-}10^6$.

Faber et al., exploited the use of ultrasonic spray pyrolysis for the growth of In_2O_3 -based TFTs by using an aqueous $\text{In}(\text{NO}_3)_3$ precursor solution [41]. The TFTs fabricated at ~ 250 °C exhibited optimum performance with field-effect mobility in the range of $15\text{-}20 \text{ cm}^2/\text{Vs}$ and current modulation ratio in excess of 10^6 .

The highest performing solution-processed In_2O_3 -based TFT ever reported was by Nayak et al., [43]. They reported on In_2O_3 -based TFTs developed by spin-coating using an InCl_3 dissolved in a mixture of acetonitrile (AN) and ethylene glycol (EG) on chemically derived aluminum oxide (AlO_x) thin-film dielectrics. The resulting TFTs exhibited extremely high field-effect mobility of $127 \text{ cm}^2/\text{Vs}$ and a current modulation ratio of 10^6 .

2.1.2 Multicomponent Oxides

Besides the high-performance binary metal-oxide (M_xO_y) based-TFTs, where basically the metal-oxide semiconductor is crystalline, amorphous-oxide-semiconductor (AOS) based TFTs are of high scientific and industrial interest. AOSs, in contrast to their crystalline counterparts, benefit from the fact that they show high mobilities, high uniformity, room temperature processing and low fabrication cost [60]–[64]. AOSs are usually ternary or quaternary metal-oxide systems. Such multicomponent metal-oxide systems are generally based on the In_2O_3 , ZnO and SnO_2 [65]–[69].

Since Nomura's pioneering work [60] back in 2004, a lot of work has been conducted to elucidate the role of each metal in the multicomponent oxide system. In general, the vacant $5s$ orbitals of In or Sn are responsible for the high conductivity of the indium or tin based thin films.

One of the most studied multi-component metal oxide systems, is indium-zinc-oxide (IZO). Depending on the In/Zn ratio and the deposition conditions, IZO could be either crystalline (c-IZO) or amorphous (a-IZO). As can be seen from Figure 2-5, for compositions close to single metal oxides (ZnO and In_2O_3), films are crystalline and exhibit low mobilities in contrast to the intermediate compounds where the films are amorphous and the mobility exhibit the highest value for a In/Zn ratio of 7/3 [70].

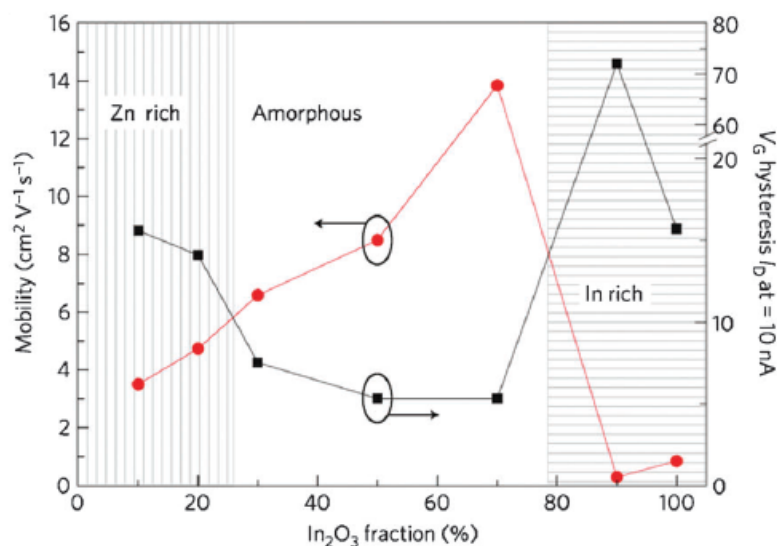


Figure 2-5: The mobility and hysteresis of solution deposited IZO TFTs annealed at 550 °C by Banger et al. [70]

Besides indium-based TFTs, tin (Sn) based ones offer some serious advantages. Tin is a non-toxic material and definitely of lower cost compared to indium. The tin's electronic configuration is identical to indium's, except for the $5p$ orbitals, so it is of similar electrical properties. Because of that, amorphous zinc-tin oxide (a-ZTO) became subject of extensive scientific research as an alternative to IZO [71]–[80].

As a-IZO exhibits high carrier concentration ($N_c > 10^{17}$), Nomura et al., used Ga^{3+} to reduce the carrier concentration and therefore to control the conductivity of

IZO thin films. Since then the ternary amorphous system indium-gallium-zinc oxide (a-IGZO) triggered much scientific interest.

In 2012, Sharp was first to start production of LCD panels incorporating IGZO-TFT. Sharp uses IGZO-TFT for smartphones, tablets, and 32" LCDs. There was an improvement in the aperture ratio of the LCD along with an improvement in power consumption due to the high mobility and low off current of IGZO-TFT. Sharp has started to release high pixel-density panels for notebook applications. IGZO-TFT is also employed in the 14" 3,200 x 1,800 LCD of an ultrabook PC supplied by Fujitsu, also used in the Razer Blade 14" (Touchscreen Variant) Gaming Laptop and a 55" OLED TV supplied by LG Electronics.²

Besides the large number of scientific reports based on gallium doped a-IZO TFTs, alternative metal cations have been considered as carrier suppressors in the a-IZO system. Metal cations such as Hf, Y, W, Zr, Mg, La, Ba, Ti, Sc, Al, Li, Na, K and Si have been implemented in the a-IZO matrix as carrier suppressors. In the roadmap of a more effective carrier suppressor rather than Ga it has been reported that the candidate metal cations should, in principal, satisfy three criteria; low standard electrode potential (SEP), large band gap and low electronegativity [66]. These three criteria, along with a metal cation of a suitable ionic radius, which should be small to avoid any lattice expansion, limit the metal cation candidates as carrier suppressors.

In 2007, Lee et al., fabricated a-IZO based TFTs using ink-jet printing [81]. They dissolved $ZnCl_2$ and $InCl_3$ powder in acetonitrile (AN) to prepare their precursor solutions. To print the active layer, they used a modified thermal ink-jet printer and commercially available spreadsheet software. They printed the active layer on top of a $(p^+)_{Si}/SiO_2$ (100 nm) substrate with the $(p^+)_{Si}$ serving as the gate electrode while the SiO_2 (100 nm) was the gate dielectric. The devices were annealed at 600 °C in ambient atmosphere for 1 hr. Finally, aluminum contacts were deposited by thermal evaporation. The device exhibited a high field-effect mobility of ($\mu_{FE}=7.4 \text{ cm}^2/Vs$), and a reasonable current on-off current ratio of ($I_{on}/I_{off}=10^4$).

² https://en.wikipedia.org/wiki/Indium_gallium_zinc_oxide

Choi et al., in 2008 fabricated a-IZO based transparent thin-film transistors (TTFTs) by spin coating technique [82]. They dissolved zinc acetate dihydrate ($\text{Zn(OAc)}_2 \cdot 2\text{H}_2\text{O}$) and indium acetate (In(OAc)_3) in a mixture of 2-methoxyethanol, diethanolamine and acetylacetone with a 1:4:4 molar ratio. The solution was spun onto a (p^+) $_{\text{Si}}$ / SiO_2 (100 nm) substrate and was annealed at 500 °C for 1h in air. Finally, aluminum contacts were evaporated on top of the a-IZO layer through a shadow mask. The spin-coated IZO TTFTs exhibited a high field-effect mobility ($\mu_{\text{FE}}=7.3 \text{ cm}^2/\text{Vs}$), a threshold voltage of 2.5 V, an on-to-off current ratio $>10^7$, and a subthreshold swing of $SS=1.47 \text{ V/dec}$.

Solution processed a-IGZO based TFTs were reported for first time by Kim et al., in 2009 [83]. The ever first reported solution processed a-IGZO based TFTs were prepared by the spin-coating method. Zinc acetate dihydrate ($\text{Zn(OAc)}_2 \cdot 2\text{H}_2\text{O}$), gallium nitrate hydrate ($\text{Ga(NO}_3)_3 \cdot x\text{H}_2\text{O}$), and indium nitrate hydrate ($\text{In(NO}_3)_3 \cdot x\text{H}_2\text{O}$) were dissolved in a mixture of 2-methoxyethanol and monoethanolamine. The solution was spun onto a glass/MoW/ SiN_x (200 nm) substrate and the film was annealed at 450 °C for 1h. Finally, $\text{In}_2\text{O}_3:\text{Zn}(10\%)$, source and drain electrodes deposited by RF sputtering. The TFTs exhibited an on-to-off ratio of about 10^6 , field effect mobility of $0.96 \text{ cm}^2/\text{Vs}$, and subthreshold swing voltage of 1.39 V/dec .

In 2010, Shin et al., reported on yttrium–indium–zinc-oxide (YIZO) based solution processed TFTs [84]. The TFT devices were developed on a glass/ SiO_2 /Mo (200 nm)/ SiN_x (200 nm) substrate. The YIZO thin films were formed as an active layer by spin-coating of a precursor solution containing zinc acetate dihydrate ($\text{Zn(OAc)}_2 \cdot 2\text{H}_2\text{O}$), yttrium nitrate hexahydrate ($\text{Y(NO}_3)_3 \cdot 6\text{H}_2\text{O}$), and indium nitrate hydrate ($\text{In(NO}_3)_3 \cdot x\text{H}_2\text{O}$) in a blend of 2-methoxyethanol and monoethanolamine, and the resulting films annealed at various temperatures. Tantalum source and drain (S/D) electrodes, deposited through a shadow mask by sputtering. The best performing TFTs was the one with 15% of Y (annealed at 550 °C) exhibited an on-to-off current ratio of 4.61×10^5 , a field-effect mobility of $1.12 \text{ cm}^2/\text{Vs}$, a threshold voltage of 0.54 V and a subthreshold swing of 1.03 V/dec .

In the same year, 2010, Kim et al., reported on the carrier suppressing efficiency of La^{3+} for solution processed a-IZO based TFTs [85]. They deposited lanthanum-indium-zinc oxide (LIZO) films onto glass/MoW/ SiN_x substrate by spin-coating of a solution containing zinc acetate dihydrate ($\text{Zn}(\text{OAc})_2 \cdot 2\text{H}_2\text{O}$), lanthanum nitrate hydrate ($\text{La}(\text{NO}_3)_3 \cdot x\text{H}_2\text{O}$), and indium nitrate hydrate ($\text{In}(\text{NO}_3)_3 \cdot x\text{H}_2\text{O}$) in 2-methoxyethanol and monoethanolamine. The device was annealed at 550 °C for 1 h in ambient atmosphere. The optimised LIZO-based TFTs with 5% La content, exhibited high on-to-off current ratio of 10^6 , field-effect mobility of 2.64 cm^2/Vs , threshold voltage of 7.86 V and subthreshold swing of 0.6 V/dec.

In 2010, Kim et al. reported on solution processed amorphous zinc-indium-tin oxide (a-ZITO) based TFTs [86]. They deposited a-ZITO thin films by spin-coating from solutions of zinc acetate dihydrate ($\text{Zn}(\text{OAc})_2 \cdot 2\text{H}_2\text{O}$), tin chloride pentahydrate ($\text{SnCl}_2 \cdot 5\text{H}_2\text{O}$), and indium chloride (InCl_3) in 2-methoxyethanol and ethanolamine. The solutions were spun onto $(n^+)_{\text{Si}}/\text{SiO}_2$ (300 nm) and $(n^+)_{\text{Si}}/\text{SAND}$ substrates, annealed at 250-400 °C for 1 h, while the TFT fabrication finalised by deposition of gold (Au) contacts on top of the $(n^+)_{\text{Si}}/\text{SiO}_2$ (300 nm)/ZITO and $(n^+)_{\text{Si}}/\text{SAND}/\text{ZITO}$ structures by thermal evaporation through shadow masks. It was found that TFTs of the best performance were those with composition of $\text{ZnIn}_4\text{Sn}_4\text{O}_{13}$. The optimised a-ZITO TFTs implementing SiO_2 as gate dielectric exhibited on-off current ratio in the range of 10^4 - 10^5 , field-effect mobility of 11.4 cm^2/Vs , threshold voltage of 41.3 V and subthreshold swing of 9.5 V/dec. Moreover, TFTs implementing organic self-assembled nanodielectric (SAND) exhibited on-off current ratio in the range of 10^5 - 10^6 , field-effect mobility of 100 cm^2/Vs , threshold voltage of 1 V and subthreshold swing of 0.23 V/dec. In their study they showed that Zn^{2+} acts as carrier suppressor in the In-Sn system resulting to low off-currents while the mobility was not significantly affected.

An investigation on the effects of Mg incorporation into IZO for high-stability solution-processed thin film transistors was carried out by Kim et al., [87]. The magnesium-indium-zinc oxide (MIZO) TFTs were fabricated by spin coating of the MIZO precursor of zinc acetate dihydrate ($\text{Zn}(\text{OAc})_2 \cdot 2\text{H}_2\text{O}$), magnesium nitrate hydrate ($\text{Mg}(\text{NO}_3)_2 \cdot x\text{H}_2\text{O}$), and indium nitrate hydrate ($\text{In}(\text{NO}_3)_3 \cdot x\text{H}_2\text{O}$) in 2-

methoxyethanol, on glass/Mo/SiN_x stack, followed by a Mo deposition as S/D electrodes. The optimised TFTs ([Mg]/([In]+[Zn])=0.2, 450 °C, 3 h) exhibited on-off current ratio of $\sim 5 \times 10^8$, field-effect mobility of 2.7 cm²/Vs, turn-on voltage of -3 V and subthreshold slope of 0.2 V/dec. They reported that the inclusion of Mg atoms in the IZO resulted in the control of the optical band gap, carrier concentration, and the grain size of the film.

The carrier suppressor ability of Sr in the solution processed IZO system was investigated by Yoon et al., [88]. They implemented solution processed strontium-indium-zinc-oxide (SIZO) as the active layer in TFT devices of a glass/Mo (200 nm)/SiN_x (200 nm)/SIZO/Al architecture. They prepared the SIZO solution by dissolving strontium nitrate (Sr(NO₃)₂), indium nitrate hydrate (In(NO₃)₃.xH₂O), and zinc acetate dihydrate (Zn(OAc)₂.2H₂O) in 2-methoxyethanol and monoethanolamine. The optimized amorphous SIZO based TFTs (Sr=20 at.%, 500 °C) exhibited on-off current ratio of 4.54×10^6 , field-effect mobility of 0.34 cm²/Vs, threshold voltage of 3.25 V and subthreshold slope of 0.61 V/dec. The role of Sr in the SIZO system was investigated by TFT measurements. The decrease of the on (I_{on}) and off-current (I_{off}) as well as the positive shift of the threshold voltage (V_{th}) as the content of Sr²⁺ increased, suggested suppressed carrier generation.

Park et al., reported on the impact of indium content on the solution-processed silicon-indium-zinc oxide (SiIZO) based TFTs [89]. SiIZO thin films were deposited onto (p⁺)₂Si/SiO₂ (200 nm) substrates by spin coating. The SiIZO precursor solution was prepared from dissolving zinc acetate dihydrate (Zn(OAc)₂.2H₂O), indium nitrate hydrate (In(NO₃)₃.xH₂O), and silicon tetraacetate (Si(OAc)₂) in 2-methoxyethanol and monoethanolamine. The optimised TFT devices ((p⁺)₂Si/SiO₂ (200 nm)/SiIZO/(Au/Ti), [Si]:[In]:[Zn]=0.05:5:1, 250 °C, 2 h) exhibited on-off current ratio of 1.14×10^7 , field-effect mobility of 4.59 cm²/Vs, threshold voltage of -0.75 V and subthreshold swing of 0.8 V/dec. It was reported that as indium content was increasing there was a negative shift of threshold voltage and an increase of on-current and field effect mobility because of an increase in carrier concentration. In the same framework, Choi et al., reported on the role of silicon doping on the electrical properties of low temperature solution processed SiInZnO TFTs [90]. They prepared all-chloride precursor solutions

of silicon tetrachloride (SiCl_4), indium chloride (InCl_3) and zinc chloride (ZnCl_2) in acetonitrile (AN) and ethylene glycol (EG). The electrical properties of the TFTs ($(\text{p}^+)_\text{Si}/\text{SiO}_2/\text{SiIZO}/(\text{Au}/\text{Ti})$, 250 °C) were found to depend on the Si content of the films. The threshold voltage was positively shifted as the Si concentration was increased. Also, the on-off current ratio and the field-effect mobility were decreased by increasing the Si content. Based on their results, it was concluded that due to silicon's low standard electrode potential (SEP), Si can efficiently suppress the formation of oxygen vacancies, resulting in devices with enhanced performance and stability.

Hennek et al., studied, the IXZO series, where $X = \text{Ga}^{3+}$ vs the progression $X = \text{Sc}^{3+} \rightarrow \text{Y}^{3+} \rightarrow \text{La}^{3+}$, of similar chemical characteristics but increasing ionic radii [91]. They concluded that besides the enhanced amorphous character of the IXZO films employing Sc^{3+} , Y^{3+} , La^{3+} , such metal cations cannot act as strong oxygen binders. Instead they suggested that apart from the metal ion electronegativity, the metal oxide lattice enthalpy (ΔH_L) could be used as a more accurate index of oxygen getter efficiency in IXZO systems.

In Table 2-3 selected solution processed multicomponent metal oxide based TFTs are presented. The deposition techniques, precursors, deposition conditions, gate dielectric material, materials acting as gate and source/drain electrodes, current modulation ($I_{\text{on}}/I_{\text{off}}$) and field effect mobility are also included.

Table 2-3: Selected previous work on solution processed multicomponent metal oxide-based semiconductors. (IJP: ink-jet printing, SC: spin-coating, ITO: indium-tin oxide, T_{dep} : deposition temperature, SD: source drain, I_{on}/I_{off} : current modulation, μ_{FE} : field effect mobility, IZO: indium-zinc oxide, ZTO: zinc-tin oxide, IGZO: indium-gallium-zinc oxide, YIZO: yttrium-indium-zinc oxide, LIZO: lanthanum-indium-zinc oxide, ZITO: zinc-indium-tin oxide, MIZO: magnesium-indium-zinc oxide, SrIZO: strontium-indium-zinc oxide, SiIZO: silicon-indium-zinc oxide, ZIZO: zirconium-indium-zinc oxide, GSIZO: gallium-silicon-indium-zinc oxide, LZTO: lanthanum-zinc-tin oxide, L-YIZO: lithium-yttrium-indium-zinc oxide, AIZO: aluminum-indium-zinc oxide, HIZO: hafnium-indium-zinc oxide, GeIZO: germanium-indium-zinc oxide, WIZO: tungsten-indium-zinc oxide, BIZO: borium-indium-zinc oxide)

Method	Semiconductor	Precursor	T_{dep} (°C)	Insulator	Gate/SD	I_{on}/I_{off}	μ_{FE} (cm^2/Vs)	year	REF
IJP	IZO	ZnCl ₂ - InCl ₃	600	SiO ₂	Si/Al	10 ⁴	7,4	2007	[81]
SC	IZO	Zn(OAc) ₂ ·2H ₂ O - In(OAc) ₃	500	SiO ₂	Si/Al	10 ⁷	7,3	2008	[82]
SC	ZTO	Zn(OAc) ₂ ·2H ₂ O - SnCl ₂	500	SiO ₂	ITO/Al	10 ⁵	2,1	2008	[92]
SC	IGZO	Zn(OAc) ₂ ·2H ₂ O - Ga(NO ₃) ₃ ·xH ₂ O - In(NO ₃) ₃ ·xH ₂ O	450	SiN _x	MoW/IZO	10 ⁶	0,96	2009	[83]
DC	ZTO	ZnCl ₂ - SnCl ₂	600	SBA	ITO/Al	10 ⁴	28	2009	[93]
DC	IGZO	Zn(OAc) ₂ ·2H ₂ O - Ga(NO ₃) ₃ ·xH ₂ O - In(NO ₃) ₃ ·xH ₂ O	300	SiO ₂	Si/Ag	10 ⁶	0,1	2009	[94]
SC	IZO	ZnCl ₂ - InCl ₃	500	SiO ₂	Si/Cr	10 ³	2,13	2009	[95]
SC	IGZO	ZnCl ₂ - InCl ₃ - GaCl ₃	600	SiO ₂	Si/Al	10 ⁷	1,1	2010	[96]

Method	Semiconductor	Precursor	T _{dep} (°C)	Insulator	Gate/SD	I _{on} /I _{off}	μ _{FE} (cm ² /Vs)	year	REF
SC	YIZO	Zn(OAc) ₂ ·2H ₂ O - Y(NO ₃) ₃ ·6H ₂ O - In(NO ₃) ₃ ·xH ₂ O	535	SiN _x	Mo/Ta	10 ⁵	1,12	2010	[84]
SC	IGZO	Zn(OAc) ₂ ·2H ₂ O - Ga(NO ₃) ₃ ·xH ₂ O - In(NO ₃) ₃ ·xH ₂ O	400	SiO ₂	Si/Al	10 ⁷	1,54	2010	[97]
SC	IZO	Zn(OAc) ₂ ·2H ₂ O - In(NO ₃) ₃ ·xH ₂ O	300	SiO ₂	Si/Al	10 ⁷	0,54	2010	[98]
SC	IZO	Zn(OAc) ₂ ·2H ₂ O - In(NO ₃) ₃ ·xH ₂ O	450	SiN _x	Mo/Mo	10 ⁹	6,57	2010	[99]
SC	IGZO	Zn(NO ₃) ₂ ·6H ₂ O - Ga(NO ₃) ₃ ·xH ₂ O - In(NO ₃) ₃ ·xH ₂ O	95	SiO ₂	Cr/Au	10 ⁶	2,3	2010	[100]
SC	IGZO	Zn(NO ₃) ₂ ·6H ₂ O - Ga(NO ₃) ₃ ·xH ₂ O - In(NO ₃) ₃ ·xH ₂ O	500	SiO ₂	Si/Al	10 ⁷	1,13	2010	[101]
SC	LIZO	Zn(OAc) ₂ ·2H ₂ O - La(NO ₃) ₃ ·xH ₂ O - In(NO ₃) ₃ ·xH ₂ O	550	SiN _x	MoW/Ta	10 ⁶	2,64	2010	[85]
SC	IGZO	Zn(OAc) ₂ ·2H ₂ O - Ga(NO ₃) ₃ ·xH ₂ O - In(NO ₃) ₃ ·xH ₂ O	550	YHZO	Si/Al	10 ⁵	0,29	2010	[102]
SC	ZITO	Zn(OAc) ₂ ·2H ₂ O InCl ₃ SnCl ₂ ·5H ₂ O	400	SiO ₂	Si/Al	10 ⁵	11	2010	[86]

Method	Semiconductor	Precursor	T _{dep} (°C)	Insulator	Gate/SD	I _{on} /I _{off}	μ _{FE} (cm ² /Vs)	year	REF
GP	IGZO	Zn(OAc) ₂ ·2H ₂ O Ga(NO ₃) ₃ ·xH ₂ O In(NO ₃) ₃ ·xH ₂ O	550	SiN _x	MoW/Ta	10 ⁶	0,81	2010	[103]
SC	IZO	Zn(OAc) ₂ ·2H ₂ O In(OAc) ₃	230	PVP	Al/Al	10 ⁶	6,9	2010	[104]
SC	ZITO:N	ZnCl ₂ - InCl ₃ - SnCl ₂ - NH ₄ OH	600	SiN _x	Si/Al	10 ⁷	5,33	2010	[105]
SC	IGZO	Zn(OAc) ₂ ·2H ₂ O - In(OAc) ₃ - Ga(NO ₃) ₃ ·xH ₂ O	400	ATO	ITO/Al	10 ⁷	5,8	2010	[106]
SC	ZTO	ZnCl ₂ - SnCl ₂	500	SiO ₂	Si/IZO	10 ⁶	0,14	2010	[107]
SC	ZITO:N	ZnCl ₂ - InCl ₃ - SnCl ₂ - NH ₄ OH	600	SiN _x	Si/Al	10 ⁶	1,2	2010	[108]
SC	IZO	ZnCl ₂ - InCl ₃	500	SiO ₂	Si/Al	10 ⁷	6,06	2010	[109]
SC	MIZO	Zn(OAc) ₂ ·2H ₂ O - Mg(NO ₃) ₂ ·xH ₂ O - In(NO ₃) ₃ ·xH ₂ O	450	SiN _x	Mo/Mo	10 ⁸	2,7	2010	[87]
SC	ZITO	ZnCl ₂ InCl ₃ SnCl ₂	600	SiN _x	Si/Al	10 ⁵	4,36	2011	[110]

Method	Semiconductor	Precursor	T _{dep} (°C)	Insulator	Gate/SD	I _{on} /I _{off}	μ _{FE} (cm ² /Vs)	year	REF
SC	IGZO	Zn(OAc) ₂ ·2H ₂ O - Ga(NO ₃) ₃ ·xH ₂ O - In(NO ₃) ₃ ·xH ₂ O	300	TEOS	MoW/Al	10 ⁷	1,02	2011	[111]
SC	SrIZO	Zn(OAc) ₂ ·2H ₂ O - Sr(NO ₃) ₂ - In(NO ₃) ₃ ·xH ₂ O	500	SiN _x	Mo/Al	10 ⁶	0,34	2011	[88]
SC	IZO	Zn(OAc) ₂ ·2H ₂ O - In(NO ₃) ₃ ·xH ₂ O	150MW	SiO ₂	Si/Al	10 ⁶	0,1	2011	[112]
SC	IZO	ZnCl ₂ - InCl ₃	300+O2/O3	SiO ₂	Si/Al	10 ⁶	0,94	2011	[113]
SC	SiIZO	Zn(OAc) ₂ ·2H ₂ O - In(NO ₃) ₃ ·xH ₂ O - Si(OAc) ₄	250	SiO ₂	Si/(Au-Ti)	10 ⁷	4,59	2011	[89]
IJP	IGZO	Zn(OAc) ₂ ·2H ₂ O - Ga(NO ₃) ₃ ·xH ₂ O - In(NO ₃) ₃ ·xH ₂ O	400	SiO ₂	Si/ITO	10 ⁷	7,6	2011	[114]
SC	ZIZO	Zn(OAc) ₂ ·2H ₂ O - In(NO ₃) ₃ ·xH ₂ O - ZrCl ₄	500	SiN _x	MoW/Ta	10 ⁶	0,77	2011	[115]
SC	IGZO	Zn(NO ₃) ₂ ·6H ₂ O - Ga(NO ₃) ₃ ·xH ₂ O - In(NO ₃) ₃ ·xH ₂ O	350	AlPO	(Mo-AlNd)/Mo	10 ⁹	4,5	2011	[116]
IJP – SC	ZTO	ZnCl ₂ SnCl ₂	300	AlO _x	Mo/IZO	10 ⁸ (SC) 10 ⁷ (IJP)	33 (SC) 36(IJP)	2011	[117]

Method	Semiconductor	Precursor	T _{dep} (°C)	Insulator	Gate/SD	I _{on} /I _{off}	μ _{FE} (cm ² /Vs)	year	REF
SC	IZO	Zn(NO ₃) ₂ ·6H ₂ O - In(NO ₃) ₃ ·xH ₂ O	300	SiO ₂	MoW/Al	10 ⁶	1,92	2012	[42]
SC	GSIZO	Zn(OAc) ₂ ·2H ₂ O - In(NO ₃) ₃ ·xH ₂ O - Si(OAc) ₄ - Ga(NO ₃) ₃ ·xH ₂ O	200	SiO ₂	Si/(Au-Ti)	10 ⁵	0,022	2012	[118]
DC	LZTO	Zn(OAc) ₂ ·2H ₂ O - SnCl ₂ - La(NO ₃) ₃ ·xH ₂ O	500	PMMA	Al/Al	10 ⁴	3,07	2012	[119]
IJP	IGZO	Zn(OAc) ₂ ·2H ₂ O - Ga(NO ₃) ₃ ·xH ₂ O - In(NO ₃) ₃ ·xH ₂ O	400	SiO ₂	Si/ITO	10 ⁶	2,45	2012	[120]
SC	L-YIZO	Zn(OAc) ₂ ·2H ₂ O - In(OAc) ₃ - Y(OAc) ₃ ·xH ₂ O - Li(OAc) ₂ ·2H ₂ O	350	SiO ₂	Si/Al	10 ⁸	3,51	2012	[121]
SC	IGZO	ZnCl ₂ - InCl ₃ - Ga(NO ₃) ₃ ·xH ₂ O	400+O ₂ /O ₃	ATO	ITO/Al	10 ⁷	11,2	2012	[122]
SC	ZIZO	Zn(OAc) ₂ ·2H ₂ O - In(NO ₃) ₃ ·xH ₂ O - ZrOCl ₂ ·8H ₂ O	500	SiO ₂	Si/Al	10 ⁷	3,8	2012	[123]
SC	IZO	Zn(NO ₃) ₂ ·6H ₂ O - In(NO ₃) ₃ ·xH ₂ O	350	ZrO ₂	Si/Al	10 ⁷	7,21	2013	[124]
SC	IZO	Zn(OAc) ₂ ·2H ₂ O - In(NO ₃) ₃ ·xH ₂ O	500	SiN _x	ITO/ITO	10 ⁶	0,13	2013	[125]

Method	Semiconductor	Precursor	T _{dep} (°C)	Insulator	Gate/SD	I _{on} /I _{off}	μ _{FE} (cm ² /Vs)	year	REF
SC	IZO	Zn(NO ₃) ₂ ·6H ₂ O - In(NO ₃) ₃ ·xH ₂ O	350	SiO ₂	Si/Al	10 ⁷	12,65	2013	[126]
SC	IGZO	Zn(OAc) ₂ ·2H ₂ O - Ga(NO ₃) ₃ ·xH ₂ O - In(NO ₃) ₃ ·xH ₂ O	300	SiO ₂	ITO/ITO	10 ⁵	0,04	2013	[127]
SC	IZO:F	ZnF ₂ - InF ₃ ·3H ₂ O	200	Al ₂ O ₃	ITO/ITO	10 ⁸	4,1	2013	[128]
SC	ZITO	Zn(NO ₃) ₂ ·6H ₂ O - InCl ₃ - SnCl ₂	250	SiO ₂	Mo/ITO	10 ⁷	2,04	2013	[129]
SC	IGZO	Zn(OAc) ₂ ·2H ₂ O - Ga(NO ₃) ₃ ·xH ₂ O - In(NO ₃) ₃ ·xH ₂ O	300	PVP	Al/Al	10 ⁶	2,04	2013	[130]
SC	ZITO	ZnCl ₂ - In(NO ₃) ₃ ·xH ₂ O - SnCl ₂	350	Al ₂ O ₃	Si/IZO	10 ⁸	2,2	2013	[131]
SC	ZITO	Zn(OAc) ₂ ·2H ₂ O - SnCl ₂ - In(NO ₃) ₃ ·xH ₂ O	700	ZrO ₂	Si/Al	10 ³	9,8	2013	[132]
DC	AIZO	Zn(OAc) ₂ ·2H ₂ O - AlCl ₃ - In(NO ₃) ₃ ·xH ₂ O	500	PMMA	Al/Al	10 ⁴	26,8	2013	[133]
SC	IZO	Zn(OAc) ₂ ·2H ₂ O ZnCl ₂ In(NO ₃) ₃ ·xH ₂ O	450	SiO ₂	Si/IZO	10 ⁵	1,45	2013	[134]

Method	Semiconductor	Precursor	T _{dep} (°C)	Insulator	Gate/SD	I _{on} /I _{off}	μ _{FE} (cm ² /Vs)	year	REF
SC	IZO	Zn(OAc) ₂ ·2H ₂ O - In(NO ₃) ₃ ·xH ₂ O	250	SiO ₂	Si/Al	10 ⁵	2,81	2013	[135]
IJP	IGZO	Zn(NO ₃) ₂ ·6H ₂ O - Ga(NO ₃) ₃ ·xH ₂ O - In(NO ₃) ₃ ·xH ₂ O	300	Hf-SAND	Si/Al	10 ⁷	20,6	2013	[136]
SC	HIZO	Zn(OAc) ₂ ·2H ₂ O - HfCl ₄ - In(NO ₃) ₃ ·xH ₂ O	400	AZO	ITO/ITO	10 ⁷	18,1	2013	[137]
SC	IZO	Zn(OAc) ₂ ·2H ₂ O - In(NO ₃) ₃ ·xH ₂ O	450	MTO	Al/Al	10 ⁶	3,41	2014	[138]
SC	IGZO	Zn(OAc) ₂ ·2H ₂ O - Ga(NO ₃) ₃ ·xH ₂ O - In(NO ₃) ₃ ·xH ₂ O	200	SiO ₂	Si/Al	10 ⁶	0.0572	2014	[139]
IJP	IZO	Zn(OAc) ₂ ·2H ₂ O - In(NO ₃) ₃ ·xH ₂ O	200	SiO ₂	Si/Al	10 ⁵	0.45	2014	[140]
SC	IGZO	Zn(OAc) ₂ ·2H ₂ O - Ga(NO ₃) ₃ ·xH ₂ O - In(NO ₃) ₃ ·xH ₂ O	300	SiO ₂	Si/(Ti-Al)	10 ⁷	1.24	2014	[141]
SC	ZIZO	Zn(OAc) ₂ ·2H ₂ O - In(NO ₃) ₃ ·xH ₂ O - Zr(OCH ₂ CH ₂ CH ₃) ₄	400	SiO ₂	Si/Al	10 ⁶	7	2014	[142]

Method	Semiconductor	Precursor	T _{dep} (°C)	Insulator	Gate/SD	I _{on} /I _{off}	μ _{FE} (cm ² /Vs)	year	REF
SC	IMZO (M=Sr, Ba)	Zn(OCH ₂ CH ₂ OCH ₃) ₂ In ₅ O(OCH(CH ₃) ₂) ₁₃ Ba(OCH(CH ₃) ₂) ₂ Sr(OCH(CH ₃) ₂) ₂	450	SiO ₂	Si/Al	10 ⁸ (Ba) 10 ⁹ (Sr)	8.63 (Ba) 8.57 (Sr)	2014	[143]
SP	IZO	Zn(NO ₃) ₂ ·6H ₂ O In(NO ₃) ₃ ·xH ₂ O	300	SiO ₂	Si/Al	10 ⁶	14.1	2014	[144]
SC	IGZO	Zn(OAc) ₂ ·2H ₂ O Ga(NO ₃) ₃ ·xH ₂ O In(NO ₃) ₃ ·xH ₂ O	400	SiO ₂	Si/Al	10 ⁷	0.97	2014	[145]
SC	IZO	Zn(NO ₃) ₂ ·6H ₂ O In(NO ₃) ₃ ·xH ₂ O	250+DUV	SiO ₂	Si/Al	10 ⁶	1.2	2014	[146]
SC	IXZO (X = Ga, Sb, Sn, Mg, Be, Ag, Y, Ca, Al, Ni, Cu, Mn, Mo, Pd)	Zn(OAc) ₂ ·2H ₂ O In(NO ₃) ₃ ·xH ₂ O X(OAc) _m	450	SiO ₂	Si/(Au-Ti)	10 ⁷ (Ga)	8.5 (Ga)	2014	[147]
SC	IZO	Zn(OAc) ₂ ·2H ₂ O In(NO ₃) ₃ ·xH ₂ O	350	SiO ₂	Si/Al	10 ⁸	13,8	2014	[148]
IJP	ZITO	ZnCl ₂ - InCl ₃ - SnCl ₂	300	AlO _x	Mo/IZO	10 ⁶	114	2014	[149]
SC	IZO	Zn(OAc) ₂ ·2H ₂ O - In(NO ₃) ₃ ·xH ₂ O	350	ZrO _x /AlO _x	Al/Al	10 ⁶	7,8	2015	[150]
SC	ZITO	ZnCl ₂ InCl ₃ SnCl ₂	300	ZrO _x	Mo/IZO	10 ⁸	2,6	2015	[151]

Method	Semiconductor	Precursor	T _{dep} (°C)	Insulator	Gate/SD	I _{on} /I _{off}	μ _{FE} (cm ² /Vs)	year	REF
SC	SilZO	Zn(OAc) ₂ ·2H ₂ O - In(NO ₃) ₃ ·xH ₂ O - SiCl ₄	300	SiO ₂	Si/(Au-Ti)	10 ⁵	1,37	2015	[152]
SC	ZITO	Zn(OAc) ₂ ·2H ₂ O - InCl ₃ - SnCl ₂	500	HAO	ITO/ITO	~10 ⁷	13,5	2015	[153]
SC	HIZO	Zn(OAc) ₂ ·2H ₂ O - In(NO ₃) ₃ ·xH ₂ O - HfCl ₄	300	SiO ₂	ITO/ITO	10 ⁶	0,27	2015	[154]
SC	ZTO	Zn(NO ₃) ₂ ·6H ₂ O - SnCl ₂	350	AlO _x	Si/Al	10 ⁴	2,6	2015	[155]
SCS	IGZO	Zn(NO ₃) ₂ ·6H ₂ O - Ga(NO ₃) ₃ ·xH ₂ O - In(NO ₃) ₃ ·xH ₂ O	300	SiO ₂	Si/Al	10 ⁷	6,34	2015	[156]
SC	SilZO	ZnCl ₂ - InCl ₃ - SiCl ₄	250	SiO ₂	Si/(Ti-Au)	10 ⁷	2,96	2015	[90]
SC	IZO	Zn(NO ₃) ₂ ·6H ₂ O - In(NO ₃) ₃ ·xH ₂ O	230	YO _x	Si/Al	10 ⁷	25,9	2015	[157]
SC	IGZO	Zn(OAc) ₂ ·2H ₂ O - Ga(NO ₃) ₃ ·xH ₂ O - In(NO ₃) ₃ ·xH ₂ O	VUV + MW	SiO ₂	Si/Al	10 ⁸	0,3	2015	[158]
SC	IZO - IGZO	Zn(NO ₃) ₂ ·6H ₂ O - Ga(NO ₃) ₃ ·xH ₂ O - In(NO ₃) ₃ ·xH ₂ O	WVA 400	SiO ₂	Si/Al	10 ⁴ (IZO) 10 ⁵ (IGZO)	19.2 (IZO) 17.4 (IGZO)	2015	[159]

Method	Semiconductor	Precursor	T _{dep} (°C)	Insulator	Gate/SD	I _{on} /I _{off}	μ _{FE} (cm ² /Vs)	year	REF
SC	AIZO	Zn(NO ₃) ₂ ·6H ₂ O - AlCl ₃ - In(NO ₃) ₃ ·xH ₂ O	500	AZO	ITO/ITO	10 ⁶	20,8	2015	[160]
SC	GeIZO	Zn(NO ₃) ₂ ·6H ₂ O - GeCl ₄ - In(NO ₃) ₃ ·xH ₂ O	280	SiO ₂	Si/Al	10 ⁷	0,25	2015	[161]
wire-bar printing	IGZO	Zn(OAc) ₂ ·2H ₂ O - Ga(NO ₃) ₃ ·xH ₂ O - In(NO ₃) ₃ ·xH ₂ O	350	AlO _x	Si/Al	10 ⁵	5,25	2015	[162]
SC	ZITO	Zn(OAc) ₂ ·2H ₂ O - In(NO ₃) ₃ ·xH ₂ O - SnCl ₂	350 + O ₂ - plasma	SiO ₂	Si/Al	10 ⁶	20,06	2015	[163]
SC	ZIZO	In(acac) ₃ - ZnCl ₂ - Zr(OC ₄ H ₉) ₄	550	LZO	Ru ₂ O/(Ru ₂ O- ITO)	10 ⁵	2,68	2015	[164]
SC	ZITO/GNS	Zn(OAc) ₂ ·2H ₂ O - InCl ₃ - SnCl ₄ ·5H ₂ O	500	HfO _x	ITO/ITO	10 ⁷	45,9	2015	[165]
SC	LiIZO	Zn(OAc) ₂ ·2H ₂ O - In(NO ₃) ₃ ·xH ₂ O - LiOH		SiO ₂	Si/Al	10 ⁷	34,5	2015	[166]
SC	IGZO	Zn(OAc) ₂ ·2H ₂ O - Ga(NO ₃) ₃ ·xH ₂ O - In(NO ₃) ₃ ·xH ₂ O	DUV	ZAO	(Cr-Au)/IZO	10 ⁸	6,21	2016	[167]
SC	IZO	Zn(NO ₃) ₂ ·6H ₂ O - In(NO ₃) ₃ ·xH ₂ O	DUV+150	SiO ₂	Si/ITO	10 ⁵	16,2	2016	[168]

Method	Semiconductor	Precursor	T _{dep} (°C)	Insulator	Gate/SD	I _{on} /I _{off}	μ _{FE} (cm ² /Vs)	year	REF
SC	ZITO	ZnCl ₂ - InCl ₃ - SnCl ₂	400	SiO ₂	Si/Al	10 ⁶	8,62	2016	[169]
SC	ZITO	ZnCl ₂ - InCl ₃ - SnCl ₂	UV/O ₃ +300	ZrO _x	Mo/IZO	10 ⁸	2,65	2016	[151]
SC	ZITO	ZnCl ₂ - InCl ₃ - SnCl ₂	350	ZrO _x	Mo/IZO	10 ⁹	4,75	2016	[170]
SC	IGZO	Zn(OAc) ₂ ·2H ₂ O - Ga(NO ₃) ₃ ·xH ₂ O - In(NO ₃) ₃ ·xH ₂ O	DWD	AlO _x	Si/IZO	10 ⁹	6,94	2016	[171]
IJP	IGZO	Zn(NO ₃) ₂ ·6H ₂ O - Ga(NO ₃) ₃ ·xH ₂ O - In(NO ₃) ₃ ·xH ₂ O	300	SiO ₂	Si/Graphene	>10 ⁵	>6	2016	[172]
SC	IGZO	Zn(NO ₃) ₂ ·6H ₂ O - Ga(NO ₃) ₃ ·xH ₂ O - In(NO ₃) ₃ ·xH ₂ O	350	SAO	Si/Al	10 ⁵	1,74	2017	[173]
SC	LiIZO	Zn(C ₅ H ₇ O ₂)·xH ₂ O - In(NO ₃) ₃ ·xH ₂ O - LiNO ₃	300	ZrO _x	Si/W	10 ⁶	12	2017	[174]
DC	AIZO	Zn(OAc) ₂ ·2H ₂ O - In(NO ₃) ₃ ·xH ₂ O - AlCl ₃	500	PMMA	Al/Al	10 ⁵	14,6	2017	[175]

Method	Semiconductor	Precursor	T _{dep} (°C)	Insulator	Gate/SD	I _{on} /I _{off}	μ _{FE} (cm ² /Vs)	year	REF
SC	WIZO	Zn(OAc) ₂ ·2H ₂ O - In(NO ₃) ₃ ·xH ₂ O - WCl ₆		SiO ₂	Si/(Cr-Au)	10 ⁷	30,5	2018	[176]
SC	BIZO	Zn(OAc) ₂ ·2H ₂ O - In(NO ₃) ₃ ·xH ₂ O - B(OH) ₃	500	SiO ₂	Si/Al	10 ⁸	10,15	2018	[177]
SC	IGZO	Zn(OAc) ₂ ·2H ₂ O - Ga(NO ₃) ₃ ·xH ₂ O - In(NO ₃) ₃ ·xH ₂ O	DUV	Al ₂ O ₃ /ZrO ₂	Cr/IZO	10 ⁸	13,5	2018	[178]

2.2 Solution Processed Metal Oxide Dielectrics

Dielectric materials are insulators in which the electrical conductivity is limited by their large band gap. Dielectric materials, especially in the form of thin films, play an important role in electronics industry. For the metal-oxide-semiconductor field effect transistor (MOSFET) technology in integrated circuits (ICs), the dielectric thin films have the same technological impact as the semiconductors. The working principle of MOSFETs is based on the carrier flow modulation in the channel by an externally applied voltage across.

2.2.1 Low-*k* Dielectrics

In semiconductor manufacturing, the term low-*k* dielectric refers to a material with smaller dielectric constant compared to silicon dioxide ones. Generally, low-*k* dielectrics are used as interlayer dielectrics (ILDs) in microelectronics industry regarding multilevel interconnect structures in ultra-large-scale integrated (ULSI) circuits. An excellent review paper on low-*k* dielectric materials, their classification, the characterization techniques, the properties, and characteristic process interactions published by Maex et al. [179]. Hatton et al. summarise the chemical and physical property requirements for (ILD) materials to fit into current industrial processes [180].

Since a detailed report based on low-*k* dielectric materials, processing techniques and their properties is out of the scope of this report, further details on low-*k* dielectrics should be sought in the literature [179]–[192].

2.2.2 High-*k* Dielectrics

The term high-*k* dielectric refers to a material with a higher dielectric constant (*k*) than silicon dioxide (SiO₂). The replacement of SiO₂ gate dielectrics with metal oxides of higher dielectric constant led to the investigation of a wide range of materials with superior properties compared with SiO₂.

Semiconductor industry demands miniaturization of complementary metal-oxide semiconductor (CMOS) transistors. In the new generation of transistors with channel dimensions below 45 nm the thickness of the SiO_2 layer, used as gate insulator, must be lower than 1 nm. Below this thickness, the gate leakage current dramatically increases due quantum mechanical tunnelling effect. This is a limiting factor that cannot be easily surpassed without looking for new device structures or dielectric materials [193]. One of the most promising alternatives for overcoming this, involves the use of high- k dielectrics. Implementation of physically thicker high- k dielectrics, while maintaining the same capacitance per unit area, enables better device performance in terms of high current when in on-state (ON-current) and, simultaneously, low operation voltages (Turn-On voltage), enabling low power consumption devices.

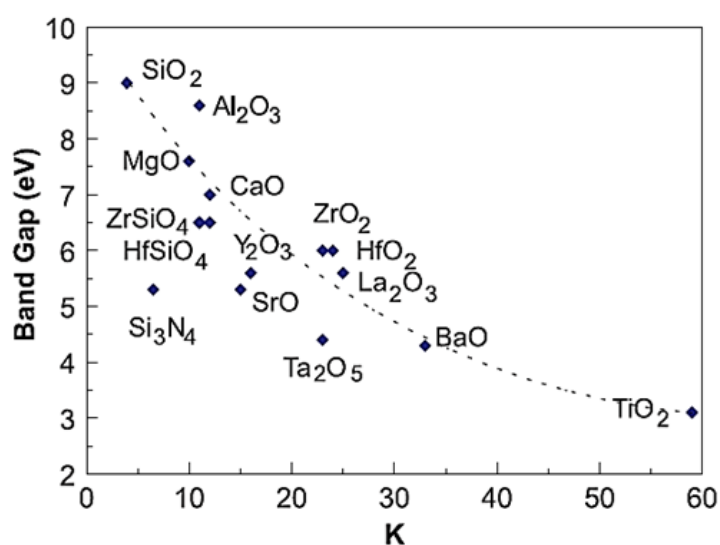


Figure 2-6: Variation of band gap and dielectric constant for various oxides, reproduced from [194].

Robertson summarised the criteria which a gate oxide candidate should fulfil [194]. The requirements for CMOS and memory applications (as opposed to TFTs) of a new oxide are six-fold.

1. The dielectric constant (k) must be high enough to be used for a reasonable number of years of scaling. For gate dielectric applications, the appropriate dielectric constant of the metal oxide should be over 10, preferably 25-30. However, there is a trade-off between the k -value and the band offset [195].

Generally, the k -value of the candidate dielectrics tends to vary inversely with the bandgap. This trend is shown in Figure 2-6.

- The oxide is in direct contact with the channel material, so it must be thermodynamically stable with it. Since the interface reactivity with the channel material dominates the over electrical properties of electronic devices, there should be no reaction of the high- k with the channel material to prevent any parasitic interfacial layers.
- It must be kinetically stable and be compatible with processing temperature range. Sometimes devices should be treated with a post-deposition annealing process. The high- k dielectric should remain stable, without a structural alternation.
- It must act as an insulator, by having band offsets with the semiconductor of over 1 eV to minimise carrier injection into its bands. Figure 2-7 shows the calculated band offset of some dielectrics with the values normalised to the VBM of ZnO [196].

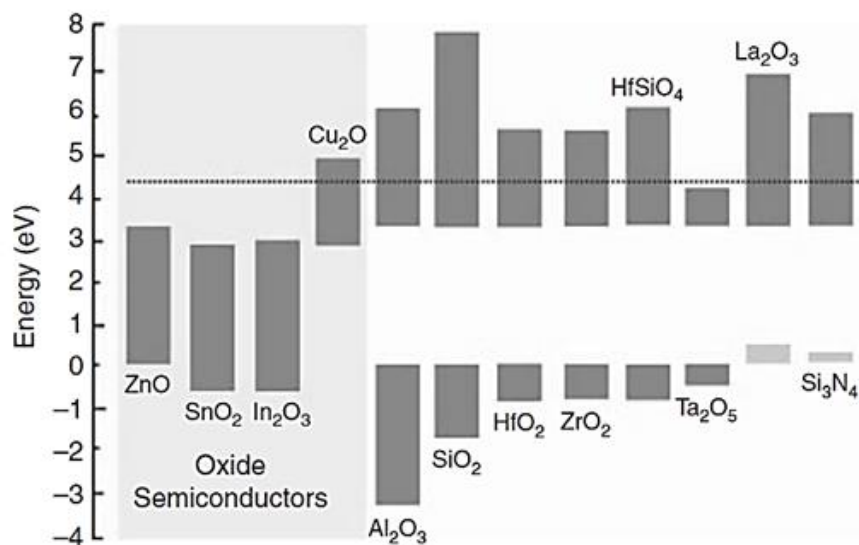


Figure 2-7: Calculated band offset of some dielectrics. The values are normalised to the VBM of ZnO. The thinner line indicates the minimum of 1 eV for CBO. Reproduced from [196]

- It must form a good electrical interface with the channel material so that the structure should be of low interfacial trap density [193], [195], [197]–[201].
- It must have few bulk electrically active defects. Usually, high- k materials because of their processing temperatures have high oxide trap densities related with off

stoichiometric defects such as O vacancies. This limits the mobility of a FET due to Coulomb scattering by this charged defects and increases the leakage currents.

In Table 2-4 the dielectric constant (k) and band gap (E_g) values of some gate oxides are presented [202].

Table 2-4 Dielectric constant (k) and band gap (E_g) values of some gate oxides, reproduced from [202]

Oxide	k -value	E_G (eV)	Oxide	k -value	E_G (eV)
Al ₂ O ₃	9	8.8	Sm ₂ O ₃	10–43	5.0
Ta ₂ O ₅	22	4.4	Eu ₂ O ₃	15	4.3
HfO ₂	25	5.8	Gd ₂ O ₃	14–23	5.4
ZrO ₂	25	5.8	Tb ₂ O ₃	12	3.8
TiO ₂	80	3.5	Dy ₂ O ₃	14	4.9
Y ₂ O ₃	15	6	Ho ₂ O ₃	12	5.3
La ₂ O ₃	8–23	5.5	Er ₂ O ₃	7–14	5.3
CeO ₂	52	3.78	Tm ₂ O ₃	7–22	5.4
Pr ₂ O ₃	30	3.8	Yb ₂ O ₃	13	4.9
Nd ₂ O ₃	27	4.6	Lu ₂ O ₃	14	5.5

Among the various high- k metal oxides Al₂O₃, is one of the most widely studied alternatives of SiO₂ as gate dielectric. It has a high band gap (~ 8.8 eV) and a dielectric constant of ~ 9 . To overcome such barrier, a ternary, aluminum oxide based, metal oxide in form of M_{1-x}Al_xO_y has been proposed [23], [24], [203]–[209].

In this study, aluminum oxide (Al₂O₃) was the main gate dielectric used. To engineer its physical properties (band gap, dielectric constant) ternary metal oxides based on the systems of aluminum-titanium oxide and aluminum-niobium oxide were studied. Both are of very high dielectric constant ($k > 30$) while their value depends on the material's processing. These two metal oxides exhibit relatively narrow band gaps ($E_g < 4.5$ eV), a fact that limits their implementation in the field of T-TFTs because they do not meet the band offset criterion.

2.2.2.1 Binary Dielectric Oxides

2.2.2.1.1 Aluminum Oxide (Al_2O_3)

Aluminum oxide (Al_2O_3) is one of the most widely studied metal oxides as gate dielectric in TFT technology. Its main advantages include the wide band gap ($E_g \sim 9\text{eV}$) and the fact that, at low and moderate deposition temperatures ($<550\text{ }^\circ\text{C}$) is of an amorphous structure. The only drawback of Al_2O_3 is its low k value ($k \sim 9$).

Table 2-5 summarises the works on solution processed aluminum oxide and their implementation on solution processed metal oxide based TFTs. Spin coating (SC) and spray pyrolysis (SP), are the two most extensively used solution processed techniques, to deposited high quality aluminum oxide (Al_2O_3) thin films. Also, aluminum nitrate nonahydrate ($Al(NO_3)_3 \cdot 9H_2O$) is the precursor of choice for the solution processed Al_2O_3 dielectrics, especially for those that was deposited by spin-coating. This is due to its low decomposition temperature, high solubility and availability at reasonable cost. For the spray deposited Al_2O_3 , aluminum chloride ($AlCl_3$) and aluminum acetylacetonate ($Al(C_5H_7O_2)_3$) were the precursors of choice. Among the various precursors, $AlCl_3$ is the one with the higher content of aluminum, is highly soluble to organic solvents such as methanol, ethanol, etc. In particular, it has been found that methanol (CH_3OH) is one of the solvents that produce very dense and smooth thin films when it is used in the spray pyrolysis technique [23], [24], [210].

Table 2-5: Literature review of solution processed aluminum oxide gate dielectrics used in various TFTs. (SC: Spin coating, SP: spray pyrolysis, 2-ME: 2-methoxyethanol, AN: acetonitrile, EG: ethyleneglycol, MeOH: methanol, EtOH: ethanol, acac: acetylacetone, DIW: deionised water, DMF: N,N-dimethylformamide, GPTMS: (3-glycidioxy-propyl)trimethoxysilane, ZGO: zinc-gallium oxide, ZTO: zinc-tin oxide, GZTO: gallium-zinc-tin oxide, IGZO: indium-gallium-zinc oxide, ITZO: indium-tin-zinc oxide, IWO: indium-tungsten oxide, IZO: indium-zinc oxide, T_{dep} : maximum deposition temperature, k : dielectric constant, J_{leak} : leakage current density, μ_{FE} : field-effect mobility, SS: subthreshold slope, V_{TH} : threshold voltage, I_{on}/I_{off} : on-off current ratio).

Deposition Technique	Precursor	Solvent	T_{dep} (°C)	k	J_{leak} (A/cm ²)	Semiconductor	μ_{FE} (cm ² /Vs)	SS (mV/dec)	V_{th} (V)	I_{on}/I_{off}	Ref.
SC	Al(NO ₃) ₃ ·9H ₂ O	2-ME	600	10.25	-	ZGO	4.7	240	0.2	10 ³	[211]
SC	AlCl ₃	AN-EG	300	6.3	63 u @1MV/cm	ZTO	33	96	1.2	10 ⁸	[117]
SP	Al(acac)	MeOH	400	9.2	0.1 u	ZnO	7	-	-	10 ⁵	[210]
SC	Al(NO ₃) ₃ ·9H ₂ O	2-ME/water+ Urea	350	7.1	0.76 u	GZTO	1.3	300	0.8	10 ⁵	[212]
SC	Al(NO ₃) ₃ ·9H ₂ O	2-ME GPTMS	250	8.7	3.29 n @2MV	ZnO	24.7	-	6.35	10 ⁵	[213]
SC	Al(NO ₃) ₃ ·9H ₂ O	EtOH	300	10.4	4.2 u @2MV	InO	21.6	160	-0.9	10 ⁴	[214]
SC	Al(NO ₃) ₃ ·9H ₂ O	2-ME	350	7.85	-	IGZO	84.4	-	-	10 ⁵	[215]
SC	Al(NO ₃) ₃ ·9H ₂ O	2-ME EG	250	6.25	-	InO	136	280	-	10 ⁵	[216]
SC	Al(NO ₃) ₃ ·9H ₂ O	DIW	350	7	< 1 n @1MV	InO	14.1	80	0.5	10 ⁷	[217]
SP	AlCl ₃	MeOH Acac	420	9	0.8 m @ 3MV	ZnO	10	990	-	10 ⁵	[24]
SC	AlCl ₃	AN-EG	550	12.42	2.7 n @1MV	ITZO	23.7	220	1.5	10 ⁶	[218]
SC	Al(NO ₃) ₃ ·9H ₂ O	EtOH	300	11.4	0.7 u @1MV	IZO	10.1	170	2.07	10 ⁵	[219]
SP	Al(acac)	MeOH DMF	440	7.5	~20 n @1MV	ZnO	10	1000	-	10 ⁵	[23]
SC	Al(NO ₃) ₃ ·9H ₂ O	DIW	250	-	10 n @ 2MV	NiO	4.4	250	-1.3	10 ⁵	[220]
SC	Al(NO ₃) ₃ ·9H ₂ O	DIW	350	7	0.4 n @ 1MV	IWO	15.3	68	0.37	10 ⁷	[221]

Deposition Technique	Precursor	Solvent	Tdep (°C)	k	J _{leak} (A/cm ²)	Semiconductor	μ _{FE} (cm ² /Vs)	SS (mV/dec)	V _{th} (V)	I _{on} /I _{off}	Ref.
SP	Al(NO ₃) ₃ ·9H ₂ O	2-ME acac NH ₄ OH	350	7.07	94 n @1MV	IGZO	3.5	-	-0.8	10 ⁵	[222]
SC	Al(NO ₃) ₃ ·9H ₂ O	DIW	250	8.6	0.3 u @1MV	IZO	2.73	240	0	10 ⁵	[223]

In all the cases the deposited film exhibited very low leakage currents and high dielectric strength. On top of that, when aluminum oxide was implemented as gate dielectric in a TFT with various oxide semiconductors serving as the active material, low voltage and high-performance oxide based TFTs were demonstrated.

Avis and Jang reported on the low temperature (<300 °C) fabrication of solution processed Al₂O₃ dielectric for all-solution-processed zinc-tin-oxide (ZTO) TFTs [117]. Solutions of aluminum chloride (AlCl₃) in acetonitrile (AN) and ethyleneglycole (EG) were spin coated onto glass/Mo substrates followed by deposition of indium-zinc oxide (IZO). The Al₂O₃-based MIM devices exhibited high dielectric strength (~4 MV/cm) and low leakage current density of 63 μA/cm² at an electric field of 1 MV/cm. Zinc-tin oxide (ZTO) based TFTs employing the solution processed Al₂O₃ gate dielectric showed high performance ($I_{on}/I_{off}=10^8$, $\mu_{FE}=33$ cm²/Vs, $V_{th}=1.2$ V and $SS=96$ mV/dec) at low operational voltages ($V_{GS}=5$ V, $V_{DS}=2$ V).

Adamopoulos et al., reported on low-voltage ZnO thin-film transistors based on Al₂O₃ high-*k* dielectrics deposited by spray pyrolysis in air [210]. They deposited amorphous Al₂O₃ thin film on a glass/ITO substrate with ITO serving as a bottom electrode by spray pyrolysis, from methanol-based solutions of aluminum acetylacetonate (Al(acac)₃) at 400 °C. Aluminum oxide-based metal-insulator-metal (MIM) capacitors (glass/ITO/Al₂O₃/Al) exhibited high dielectric strength (>1.8 MV/cm) and low leakage current (<0.1 μA/cm²). The ZnO based TFTs employing spray deposited Al₂O₃ gate dielectrics showed low voltage operation, high on-off current ratio ($I_{on}/I_{off}=10^5$) and high electron mobility of 7 cm²/Vs.

Besides the high performance of Al₂O₃ as gate dielectric, the relatively low dielectric constant ($k\sim 9$) ranks it as a short term industrial solution [193]. On the other hand, metal oxides with higher dielectric constant are of lower band gap, in contrast to the band offset criterion [198]. To overcome such issue, metal oxides with high dielectric constant and wide band gaps were suggested, using multicomponent metal oxides or even stacked multilayers.

2.2.2.2 Metal Aluminate Based Dielectric

There is not any thermodynamically stable single metal oxide (M_xO_y) that exhibits at the same time high dielectric constant ($k > \sim 30$) and wide band gap ($E_g > \sim 8$ eV). Yim et al., using ab-initio calculations for band gap and permittivity reported that c-BeO exhibits an unusual combination of high permittivity ($k \sim 275$) and large band gap ($E_g \sim 10.1$ eV) [224]. Despite this unique property, c-BeO is thermodynamically unstable. The thermodynamically stable w-BeO, besides its high band gap, it exhibits a relatively low dielectric constant ($k \sim 7$), fact that limits its consideration as candidate dielectric for microelectronic devices. Yim et al., suggested that c-BeO could be stabilised by doping and it is expected the stabilised c-BeO to exhibit similar physical properties with the calculated ones [224].

Table 2-4 summarises single metal oxides that have been considered as candidates for gate dielectrics. Among them, aluminum oxide (Al_2O_3) has the widest band gap ($E_g \sim 8.8$ eV), while titanium dioxide (TiO_2) exhibits the largest permittivity ($k \sim 80-110$) that depended on its crystal structure. Aluminum titanate ($Ti_{1-x}Al_xO_y$ -TAO) films and multi-layered stacks of Al_2O_3/TiO_2 have been considered as potential dielectrics for microelectronic applications. Auciello et al., reported on hybrid titanium–aluminum oxide layer as alternative high- k gate dielectric for MOSFETs [225]. The sputtered AlTi (25/75 at.%) film deposited on Si substrates, was oxidised to TAO via post-deposition thermal annealing. The TAO thin film was amorphous with a permittivity of 30, and a band gap of ~ 4 eV. The leakage current was reduced by 4-5 orders of magnitude compared to that of SiO_2 film of the same equivalent oxide thickness (EOT).

Besides Ti^{4+} , other metal cations have been incorporated into the AlO_x . Hafnium aluminate ($HfAlO_x$), zirconium aluminate ($ZrAlO_x$) and lanthanum aluminate ($LaAlO_x$) are composite metal oxides that besides titanium aluminate ($TiAlO_x$) have been studied as potential gate dielectrics for TFTs. Such binary metal aluminates have been deposited using vacuum and solution processed techniques.

In Table 2-6, selected solution processed metal aluminates and their electrical properties are listed. Most of the metal aluminates, were deposited by spin coating.

Only titanium aluminate (TAO) and lanthanum aluminate (LAO) thin films were deposited by spray pyrolysis.

Zhu et al., developed a solution processed high- k hafnium-aluminium oxide (HAO) dielectric films [226]. They used solutions of hafnium dichloride oxide octahydrate ($\text{HfCl}_2\text{O}\cdot 8\text{H}_2\text{O}$) and aluminum-tri-sec-butoxide ($\text{Al}(\text{OC}_4\text{H}_9)_3$) in 2-methoxyethanol. The precursor solutions were spin coated onto commercially available glass/ITO substrates. Finally, the thin films underwent post-deposition annealing at 500 °C for 2 h in ambient atmosphere. The HAO films were amorphous exhibiting excellent dielectric properties. In particular, HAO films ([Hf:[Al]=2:1) were of high dielectric constant ($k=12.1$) and low leakage current density ($J_{\text{leak}}=1.69\times 10^7$ A/cm²) at a high electric field (2 MV/cm), while the dielectric strength was higher than 4 MV/cm.

Yang et al., reported on solution-deposited Zr-doped AlO_x (ZAO) gate dielectrics for high-performance TFTs [227]. They used solutions of AlCl_3 and ZrCl_4 in of acetonitrile (AN) and ethylene glycol (EG). Diverse substrates of p^+Si , glass/ITO, and flexible polyimide/ITO were spin coated with the precursor solutions and annealed under different temperatures. Amorphous ZAO films annealed at 250 °C exhibited low leakage current density ($<10^{-6}$ A/cm² at 2 MV/cm). The dielectric constant (k) was in the range of 8.4-11.8 depending on the annealing temperature. The performance of ZAO thin films as gate dielectric was investigated in TFTs employing IZO or ZnO semiconducting channels. For the IZO based TFTs the on-off ratio was in the order of 10^6 , field effect mobility of 53 cm²/Vs, threshold voltage of 1.07 V and subthreshold voltage swing of 0.12 V/dec.

The simplicity of the accurate adjustment of the atomic ratio of multi-metal oxide system by simple physical blending of the metal's precursor solutions, demonstrates the ability to control the resulting film's stoichiometry using solution processed techniques. Equally, the high yield of solution processing techniques over large area, indicates the potential for the rapid development of electronic devices at low manufacturing cost.

Table 2-6: Literature review of solution processed metal aluminate gate dielectrics. (SC: Spin coating, SP: spray pyrolysis, 2-ME: 2-methoxyethanol, AN: acetonitrile, EG: ethyleneglycol, MeOH: methanol, acac: acetylacetone, n-buto: n-butoxide, DIW: deionised water, DMF: N,N-dimethylformamide, IGZO: indium-gallium-zinc oxide, ITZO: indium-tin-zinc oxide, IZO: indium-zinc oxide, T_{dep} : maximum deposition temperature, k: dielectric constant, J_{leak} : leakage current density, E_b : dielectric strength, μ_{FE} : field-effect mobility, SS: subthreshold slope, V_{TH} : threshold voltage, I_{on}/I_{off} : on-off current ratio, HAO: hafnium aluminate, ZAO: zirconium aluminate, TAO: titanium aluminate, LAO: lanthanum aluminate, *: no available data).

Deposition Technique	Dielectric	Precursor	Solvent	T_{dep} (°C)	k	J_{leak} (A/cm ²)	E_b (MV/cm)	Semiconductor	μ_{FE} (cm ² /Vs)	SS (mV/dec)	I_{on}/I_{off}	Ref.
SC	HAO	HfCl ₂ O·8H ₂ O Al(OC ₄ H ₉) ₃	2-ME	500	12,1	1.7x10 ⁻⁷ @2MV/cm	4,5	*	*	*	*	[226]
SC	HAO	HfCl ₂ O·8H ₂ O Al(OC ₄ H ₉) ₃	2-ME	600	11,3	*	>2.5	ITZO	13,5	87	10 ⁷	[153]
SC	ZAO	AlCl ₃ - ZrCl ₄	AN EG	350	11,8	*	>8	IZO	53	120	10 ⁶	[227]
SC	ZAO	Al(NO ₃) ₃ ·9H ₂ O Zr(acac) ₄	2-ME	DUV	7,35	10 ⁻⁹ @2MV/cm	>7	IGZO	7,71	153	10 ⁹	[228]
SP	TAO	AlCl ₃ Ti(n-buto) ₄	MeOH acac	420	~13	<5x10 ⁻⁹ @3MV/cm	>3	ZnO	10	549	10 ⁶	[24]
SC	LAO	Al(NO ₃) ₃ ·9H ₂ O La ₂ O ₃	DIW HNO ₃	600	11,5	*	>3,5	IGZO	4,5	*	10 ⁶	[203]
SP	LAO	Al(acac) ₃ La(acac) ₃	MeOH DMF	440	16	<6x10 ⁻⁹ @3MV/cm	>5	ZnO	12	650	10 ⁶	[23]
SC	ZAO	Al(NO ₃) ₃ ·9H ₂ O ZrO(NO ₃) ₂ ·xH ₂ O	DIW	500	~10	10 ⁻⁸ @1MV/cm	~3	*	*	*	*	[229]

2.3 References

- [1] H. Morkoc and U. Ozgur, 'General Properties of ZnO', Weinheim, Germany: Wiley-VCH Verlag GmbH & Co. KGaA, 2009, pp. 1–76.
- [2] M. Samadi, M. Zirak, A. Naseri, E. Khorashadizade, and A. Z. Moshfegh, 'Recent progress on doped ZnO nanostructures for visible-light photocatalysis', *Thin Solid Films*, vol. 605, pp. 2–19, Apr. 2016.
- [3] D. Vogel, P. Krüger, and J. Pollmann, 'Self-interaction and relaxation-corrected pseudopotentials for II-VI semiconductors', *Phys. Rev. B*, vol. 54, no. 8, pp. 5495–5511, Aug. 1996.
- [4] Y. Ohya, T. Niwa, T. Ban, and Y. Takahashi, 'Thin Film Transistor of ZnO Fabricated by Chemical Solution Deposition', *Jpn. J. Appl. Phys.*, vol. 40, no. Part 1, No. 1, pp. 297–298, Jan. 2001.
- [5] B. J. Norris, J. Anderson, J. F. Wager, and D. A. Keszler, 'Spin-coated zinc oxide transparent transistors', *J. Phys. D. Appl. Phys.*, vol. 36, no. 20, pp. L105–L107, Oct. 2003.
- [6] B. Sun and H. Siringhaus, 'Solution-Processed Zinc Oxide Field-Effect Transistors Based on Self-Assembly of Colloidal Nanorods', *Nano Lett.*, vol. 5, no. 12, pp. 2408–2413, Dec. 2005.
- [7] B. S. Ong, C. Li, Y. Li, Y. Wu, and R. Loutfy, 'Stable, Solution-Processed, High-Mobility ZnO Thin-Film Transistors', *J. Am. Chem. Soc.*, vol. 129, no. 10, pp. 2750–2751, Mar. 2007.
- [8] B. Sun, R. L. Peterson, H. Siringhaus, and K. Mori, 'Low-Temperature Sintering of In-Plane Self-Assembled ZnO Nanorods for Solution-Processed High-Performance Thin Film Transistors', *J. Phys. Chem. C*, vol. 111, no. 51, pp. 18831–18835, Dec. 2007.
- [9] D. Redinger and V. Subramanian, 'High-Performance Chemical-Bath-Deposited Zinc Oxide Thin-Film Transistors', *IEEE Trans. Electron Devices*, vol. 54, no. 6, pp. 1301–1307, Jun. 2007.
- [10] S. T. Meyers, J. T. Anderson, C. M. Hung, J. Thompson, J. F. Wager, and D. A. Keszler, 'Aqueous Inorganic Inks for Low-Temperature Fabrication of ZnO TFTs', *J. Am. Chem. Soc.*, vol. 130, no. 51, pp. 17603–17609, Dec. 2008.
- [11] A. Bashir, P. H. Wöbkenberg, J. Smith, J. M. Ball, G. Adamopoulos, D. D. C. Bradley, and T. D. Anthopoulos, 'High-performance zinc oxide transistors and circuits fabricated by spray pyrolysis in ambient atmosphere', *Adv. Mater.*, vol. 21, pp. 2226–2231, 2009.
- [12] G. Adamopoulos, A. Bashir, P. H. Wöbkenberg, D. D. C. Bradley, and T. D. Anthopoulos, 'Electronic properties of ZnO field-effect transistors fabricated by spray pyrolysis in ambient air', *Appl. Phys. Lett.*, vol. 95, no. 13, p. 133507, Sep. 2009.

- [13] C. Li, Y. Li, Y. Wu, B.-S. Ong, and R.-O. Loutfy, 'Fabrication conditions for solution-processed high-mobility ZnO thin-film transistors', *J. Mater. Chem.*, vol. 19, no. 11, p. 1626, Jun. 2009.
- [14] G. Adamopoulos, A. Bashir, S. Thomas, W. P. Gillin, S. Georgakopoulos, M. Shkunov, M. a. Baklar, N. Stingelin, R. C. Maher, L. F. Cohen, D. D. C. Bradley, and T. D. Anthopoulos, 'Spray-Deposited Li-Doped ZnO Transistors with Electron Mobility Exceeding 50 cm²/Vs', *Adv. Mater.*, vol. 22, no. 42, pp. 4764–4769, Nov. 2010.
- [15] H. Bong, W. H. Lee, D. Y. Lee, B. J. Kim, J. H. Cho, and K. Cho, 'High-mobility low-temperature ZnO transistors with low-voltage operation', *Appl. Phys. Lett.*, vol. 96, no. 19, p. 192115, May 2010.
- [16] Y. H. Hwang, S.-J. Seo, and B.-S. Bae, 'Fabrication and characterization of sol-gel-derived zinc oxide thin-film transistor', *J. Mater. Res.*, vol. 25, no. 04, pp. 695–700, Apr. 2010.
- [17] T. Jun, K. Song, Y. Jeong, K. Woo, D. Kim, C. Bae, and J. Moon, 'High-performance low-temperature solution-processable ZnO thin film transistors by microwave-assisted annealing', *J. Mater. Chem.*, vol. 21, no. 4, pp. 1102–1108, 2011.
- [18] G. Adamopoulos, A. Bashir, W. P. Gillin, S. Georgakopoulos, M. Shkunov, M. A. Baklar, N. Stingelin, D. D. C. Bradley, and T. D. Anthopoulos, 'Structural and Electrical Characterization of ZnO Films Grown by Spray Pyrolysis and Their Application in Thin-Film Transistors', *Adv. Funct. Mater.*, vol. 21, no. 3, pp. 525–531, Feb. 2011.
- [19] R. Theissmann, S. Bubel, M. Sanlialp, C. Busch, G. Schierning, and R. Schmechel, 'High performance low temperature solution-processed zinc oxide thin film transistor', *Thin Solid Films*, vol. 519, no. 16, pp. 5623–5628, Jun. 2011.
- [20] S. Y. Park, B. J. Kim, K. Kim, M. S. Kang, K.-H. Lim, T. Il Lee, J. M. Myoung, H. K. Baik, J. H. Cho, and Y. S. Kim, 'Low-Temperature, Solution-Processed and Alkali Metal Doped ZnO for High-Performance Thin-Film Transistors', *Adv. Mater.*, vol. 24, no. 6, pp. 834–838, Feb. 2012.
- [21] Y.-H. Lin, H. Faber, K. Zhao, Q. Wang, A. Amassian, M. McLachlan, and T. D. Anthopoulos, 'High-Performance ZnO Transistors Processed Via an Aqueous Carbon-Free Metal Oxide Precursor Route at Temperatures Between 80-180 °C', *Adv. Mater.*, vol. 25, no. 31, pp. 4340–4346, Aug. 2013.
- [22] S. C. Lim, J. B. Koo, C. W. Park, S. Jung, B. S. Na, S. S. Lee, and H. Y. Chu, 'Device characteristics of inkjet-printed ZnO TFTs by solution process', *Jpn. J. Appl. Phys.*, vol. 53, no. 5S3, p. 05HB10, May 2014.
- [23] M. Esro, R. Mazzocco, G. Vourlias, O. Kolosov, A. Krier, W. I. Milne, and G. Adamopoulos, 'Solution processed lanthanum aluminate gate dielectrics for use in metal oxide-based thin film transistors', *Appl. Phys. Lett.*, vol. 106, no. 20, p. 203507, May 2015.

- [24] D. Afouxenidis, R. Mazzocco, G. Vourlias, P. J. Livesley, A. Krier, W. I. Milne, O. Kolosov, and G. Adamopoulos, 'ZnO-based Thin Film Transistors Employing Aluminum Titanate Gate Dielectrics Deposited by Spray Pyrolysis at Ambient Air', *ACS Appl. Mater. Interfaces*, vol. 7, no. 13, pp. 7334–7341, Apr. 2015.
- [25] Y. Shigesato, 'In Based TCOs', in *Handbook of Transparent Conductors*, vol. 30, no. 7 R, Boston, MA: Springer US, 2011, pp. 149–169.
- [26] S. Z. Karazhanov, P. Ravindran, P. Vajeeston, A. Ulyashin, T. G. Finstad, and H. Fjellvåg, 'Phase stability, electronic structure, and optical properties of indium oxide polytypes', *Phys. Rev. B*, vol. 76, no. 7, p. 075129, Aug. 2007.
- [27] M. Marezio, 'Refinement of the crystal structure of In_2O_3 at two wavelengths', *Acta Crystallogr.*, vol. 20, no. 6, pp. 723–728, Nov. 1966.
- [28] R. L. Weiher and R. P. Ley, 'Optical Properties of Indium Oxide', *J. Appl. Phys.*, vol. 37, no. 1, pp. 299–302, Jan. 1966.
- [29] P. D. C. King, T. D. Veal, F. Fuchs, C. Y. Wang, D. J. Payne, A. Bourlange, H. Zhang, G. R. Bell, V. Cimalla, O. Ambacher, R. G. Egdell, F. Bechstedt, and C. F. McConville, 'Band gap, electronic structure, and surface electron accumulation of cubic and rhombohedral In_2O_3 ', *Phys. Rev. B - Condens. Matter Mater. Phys.*, vol. 79, no. 20, p. 205211, May 2009.
- [30] P. Erhart, A. Klein, R. G. Egdell, and K. Albe, 'Band structure of indium oxide: Indirect versus direct band gap', *Phys. Rev. B*, vol. 75, no. 15, p. 153205, Apr. 2007.
- [31] A. Walsh, J. L. F. Da Silva, S. H. Wei, C. Körber, A. Klein, L. F. J. Piper, A. Demasi, K. E. Smith, G. Panaccione, P. Torelli, D. J. Payne, A. Bourlange, and R. G. Egdell, 'Nature of the band gap of In_2O_3 revealed by first-principles calculations and X-ray spectroscopy', *Phys. Rev. Lett.*, vol. 100, no. 16, p. 167402, Apr. 2008.
- [32] Joo Hyon Noh, Seung Yoon Ryu, Sung Jin Jo, Chang Su Kim, Sung-Woo Sohn, P. D. Rack, Dong-Joo Kim, and Hong Koo Baik, 'Indium Oxide Thin-Film Transistors Fabricated by RF Sputtering at Room Temperature', *IEEE Electron Device Lett.*, vol. 31, no. 6, pp. 567–569, Jun. 2010.
- [33] H. Z. Zhang, H. T. Cao, A. H. Chen, L. Y. Liang, Z. M. Liu, and Q. Wan, 'Enhancement of electrical performance in In_2O_3 thin-film transistors by improving the densification and surface morphology of channel layers', *Solid. State. Electron.*, vol. 54, no. 4, pp. 479–483, Apr. 2010.
- [34] Y. Vygranenko, K. Wang, R. Chaji, M. Vieira, J. Robertson, and A. Nathan, 'Stability of indium-oxide thin-film transistors by reactive ion beam assisted deposition', *Thin Solid Films*, vol. 517, no. 23, pp. 6341–6344, 2009.
- [35] Y. Vygranenko, K. Wang, and A. Nathan, 'Stable indium oxide thin-film transistors with fast threshold voltage recovery', *Appl. Phys. Lett.*, vol. 91, no. 26, p. 263508, Dec. 2007.

- [36] G. Lavareda, C. Nunes de Carvalho, E. Fortunato, a. R. Ramos, E. Alves, O. Conde, and a. Amaral, 'Transparent thin film transistors based on indium oxide semiconductor', *J. Non. Cryst. Solids*, vol. 352, no. 23–25, pp. 2311–2314, 2006.
- [37] J. S. Lee, Y. J. Kwack, and W. S. Choi, 'Inkjet-printed In_2O_3 thin-film transistor below 200°C ', *ACS Appl. Mater. Interfaces*, vol. 5, no. 22, pp. 11578–11583, Nov. 2013.
- [38] S.-Y. Y. Han, G. S. Herman, and C. H. Chang, 'Low-Temperature, High-Performance, Solution-Processed Indium Oxide Thin-Film Transistors', *J. Am. Chem. Soc.*, vol. 133, no. 14, pp. 5166–5169, Apr. 2011.
- [39] H. S. Kim, P. D. Byrne, A. Facchetti, and T. J. Marks, 'High Performance Solution-Processed Indium Oxide Thin-Film Transistors', *J. Am. Chem. Soc.*, vol. 130, no. 38, pp. 12580–12581, Sep. 2008.
- [40] L. Petti, H. Faber, N. Münzenrieder, G. Cantarella, P. A. Patsalas, G. Tröster, and T. D. Anthopoulos, 'Low-temperature spray-deposited indium oxide for flexible thin-film transistors and integrated circuits', *Appl. Phys. Lett.*, vol. 106, no. 9, p. 092105, Mar. 2015.
- [41] H. Faber, Y.-H. Lin, S. R. Thomas, K. Zhao, N. Pliatsikas, M. a. McLachlan, A. Amassian, P. a. Patsalas, and T. D. Anthopoulos, 'Indium Oxide Thin-Film Transistors Processed at Low Temperature via Ultrasonic Spray Pyrolysis', *ACS Appl. Mater. Interfaces*, vol. 7, no. 1, pp. 782–790, Jan. 2015.
- [42] W. H. Jeong, J. H. Bae, and H. J. Kim, 'High-performance oxide thin-film transistors using a volatile nitrate precursor for low-temperature solution process', *IEEE Electron Device Lett.*, vol. 33, no. 1, pp. 68–70, 2012.
- [43] P. K. Nayak, M. N. Hedhili, D. Cha, and H. N. Alshareef, 'High performance In_2O_3 thin film transistors using chemically derived aluminum oxide dielectric', *Appl. Phys. Lett.*, vol. 103, no. 3, p. 033518, Jul. 2013.
- [44] J. H. Park, Y. B. Yoo, K. H. Lee, W. S. Jang, J. Y. Oh, S. S. Chae, H. W. Lee, S. W. Han, and H. K. Baik, 'Boron-Doped Peroxo-Zirconium Oxide Dielectric for High-Performance, Low-Temperature, Solution-Processed Indium Oxide Thin-Film Transistor', *ACS Appl. Mater. Interfaces*, vol. 5, no. 16, pp. 8067–8075, Aug. 2013.
- [45] K. Choi, M. Kim, S. Chang, T.-Y. Oh, S. W. Jeong, H. J. Ha, and B.-K. Ju, 'High-Performance Amorphous Indium Oxide Thin-Film Transistors Fabricated by an Aqueous Solution Process at Low Temperature', *Jpn. J. Appl. Phys.*, vol. 52, no. 6R, p. 060204, Jun. 2013.
- [46] A. Liu, G. X. Liu, H. H. Zhu, F. Xu, E. Fortunato, R. Martins, and F. K. Shan, 'Fully Solution-Processed Low-Voltage Aqueous In_2O_3 Thin-Film Transistors Using an Ultrathin ZrO_x Dielectric', *ACS Appl. Mater. Interfaces*, vol. 6, no. 20, pp. 17364–17369, Oct. 2014.

- [47] J. Leppäniemi, K. Ojanperä, T. Kololuoma, O.-H. Huttunen, J. Dahl, M. Tuominen, P. Laukkanen, H. Majumdar, and A. Alastalo, 'Rapid low-temperature processing of metal-oxide thin film transistors with combined far ultraviolet and thermal annealing', *Appl. Phys. Lett.*, vol. 105, no. 11, p. 113514, Sep. 2014.
- [48] C.-H. Choi, S.-Y. Han, Y.-W. Su, Z. Fang, L.-Y. Lin, C.-C. Cheng, and C. Chang, 'Fabrication of high-performance, low-temperature solution processed amorphous indium oxide thin-film transistors using a volatile nitrate precursor', *J. Mater. Chem. C*, vol. 3, no. 4, pp. 854–860, 2015.
- [49] Y. Meng, G. Liu, A. Liu, H. Song, Y. Hou, B. Shin, and F. Shan, 'Low-temperature fabrication of high performance indium oxide thin film transistors', *RSC Adv.*, vol. 5, no. 47, pp. 37807–37813, 2015.
- [50] F. Jaehnike, D. V. Pham, R. Anselmann, C. Bock, and U. Kunze, 'High-Quality Solution-Processed Silicon Oxide Gate Dielectric Applied on Indium Oxide Based Thin-Film Transistors', *ACS Appl. Mater. Interfaces*, vol. 7, no. 25, pp. 14011–14017, Jul. 2015.
- [51] R. A. John, N. A. Chien, S. Shukla, N. Tiwari, C. Shi, N. G. Ing, and N. Mathews, 'Low-Temperature Chemical Transformations for High-Performance Solution-Processed Oxide Transistors', *Chem. Mater.*, vol. 28, no. 22, pp. 8305–8313, Nov. 2016.
- [52] B. S. Kim and H. J. Kim, 'Influence of Annealing on Solution-Processed Indium Oxide Thin-Film Transistors Under Ambient Air and Wet Conditions', *IEEE Trans. Electron Devices*, vol. 63, no. 9, pp. 3558–3561, Sep. 2016.
- [53] C.-M. Kang, J. H. Ryu, H. Kim, Y.-W. O. K.-H. Baek, and L.-M. Do, 'Improved Thin-Film Transistor Performance of Low-Temperature, Solution-Processed Indium Oxide by Controlling Solution Temperature', *J. Nanosci. Nanotechnol.*, vol. 16, no. 8, pp. 8473–8477, Aug. 2016.
- [54] C. Kang, H. Kim, Y.-W. Oh, K.-H. Baek, and L.-M. Do, 'High-Performance, Solution-Processed Indium-Oxide TFTs Using Rapid Flash Lamp Annealing', *IEEE Electron Device Lett.*, vol. 37, no. 5, pp. 595–598, May 2016.
- [55] H. Kim, C. Kang, Y.-W. Oh, J. H. Ryu, K.-H. Baek, and L.-M. Do, 'Low-temperature, solution-processed indium-oxide thin-film transistors fabricated by using an ultraviolet-ozone treatment', *J. Korean Phys. Soc.*, vol. 68, no. 8, pp. 971–974, Apr. 2016.
- [56] G. Jiang, A. Liu, G. Liu, C. Zhu, Y. Meng, B. Shin, E. Fortunato, R. Martins, and F. Shan, 'Solution-processed high-k magnesium oxide dielectrics for low-voltage oxide thin-film transistors', *Appl. Phys. Lett.*, vol. 109, no. 18, p. 183508, Oct. 2016.
- [57] C. Fan, A. Liu, Y. Meng, Z. Guo, G. Liu, and F. Shan, 'Solution-Processed SrO_x - Gated Oxide Thin-Film Transistors and Inverters', *IEEE Trans. Electron Devices*, vol. 64, no. 10, pp. 4137–4143, Oct. 2017.

- [58] I. Isakov, H. Faber, M. Grell, G. Wyatt-Moon, N. Pliatsikas, T. Kehagias, G. P. Dimitrakopoulos, P. P. Patsalas, R. Li, and T. D. Anthopoulos, 'Exploring the Leidenfrost Effect for the Deposition of High-Quality In_2O_3 Layers via Spray Pyrolysis at Low Temperatures and Their Application in High Electron Mobility Transistors', *Adv. Funct. Mater.*, vol. 27, no. 22, p. 1606407, Jun. 2017.
- [59] J.-W. Choi, S. Han, M.-C. Nguyen, A. H. Nguyen, J. Y. Kim, S. Choi, J. Cheon, H. Ji, and R. Choi, 'Low-Temperature Solution-Based In_2O_3 Channel Formation for Thin-Film Transistors Using a Visible Laser-Assisted Combustion Process', *IEEE Electron Device Lett.*, vol. 38, no. 9, pp. 1259–1262, Sep. 2017.
- [60] K. Nomura, H. Ohta, A. Takagi, T. Kamiya, M. Hirano, and H. Hosono, 'Room-temperature fabrication of transparent flexible thin-film transistors using amorphous oxide semiconductors.', *Nature*, vol. 432, no. November, pp. 488–492, Nov. 2004.
- [61] T. Kamiya and H. Hosono, 'Material characteristics and applications of transparent amorphous oxide semiconductors', *NPG Asia Mater.*, vol. 2, no. 1, pp. 15–22, Jan. 2010.
- [62] H. Yabuta, M. Sano, K. Abe, T. Aiba, T. Den, H. Kumomi, K. Nomura, T. Kamiya, and H. Hosono, 'High-mobility thin-film transistor with amorphous InGaZnO_4 channel fabricated by room temperature rf-magnetron sputtering', *Appl. Phys. Lett.*, vol. 89, no. 11, p. 112123, Sep. 2006.
- [63] H. Hosono, 'Ionic amorphous oxide semiconductors: Material design, carrier transport, and device application', *J. Non. Cryst. Solids*, vol. 352, no. 9–20, pp. 851–858, Jun. 2006.
- [64] H. Hosono, 'Recent progress in transparent oxide semiconductors: Materials and device application', *Thin Solid Films*, vol. 515, no. 15 SPEC. ISS., pp. 6000–6014, 2007.
- [65] J. S. Park, W.-J. Maeng, H.-S. Kim, and J.-S. Park, 'Review of recent developments in amorphous oxide semiconductor thin-film transistor devices', *Thin Solid Films*, vol. 520, no. 6, pp. 1679–1693, Jan. 2012.
- [66] S. J. Kim, S. Yoon, and H. J. Kim, 'Review of solution-processed oxide thin-film transistors', *Jpn. J. Appl. Phys.*, vol. 53, no. 2S, p. 02BA02, Feb. 2014.
- [67] B. Du Ahn, H.-J. Jeon, J. Sheng, J. Park, and J.-S. Park, 'A review on the recent developments of solution processes for oxide thin film transistors', *Semicond. Sci. Technol.*, vol. 30, no. 6, p. 064001, Jun. 2015.
- [68] J.-Y. Kwon, D.-J. Lee, and K.-B. Kim, 'Review paper: Transparent amorphous oxide semiconductor thin film transistor', *Electron. Mater. Lett.*, vol. 7, no. 1, pp. 1–11, 2011.
- [69] E. Fortunato, P. Barquinha, and R. Martins, 'Oxide Semiconductor Thin-Film Transistors: A Review of Recent Advances', *Adv. Mater.*, vol. 24, no. 22, pp. 2945–2986, Jun. 2012.

- [70] K. K. Banger, Y. Yamashita, K. Mori, R. L. Peterson, T. Leedham, J. Rickard, and H. Sirringhaus, 'Low-temperature, high-performance solution-processed metal oxide thin-film transistors formed by a "sol-gel on chip" process', *Nat. Mater.*, vol. 10, no. 1, pp. 45–50, Jan. 2011.
- [71] H. Q. Chiang, J. F. Wager, R. L. Hoffman, J. Jeong, and D. A. Keszler, 'High mobility transparent thin-film transistors with amorphous zinc tin oxide channel layer', *Appl. Phys. Lett.*, vol. 86, no. 1, pp. 22–24, Jan. 2005.
- [72] S. Jeong, Y. Jeong, and J. Moon, 'Solution-processed zinc tin oxide semiconductor for thin-film transistors', *J. Phys. Chem. C*, vol. 112, no. 30, pp. 11082–11085, 2008.
- [73] Y.-J. Chang, D.-H. Lee, G. S. Herman, and C.-H. Chang, 'High-Performance, Spin-Coated Zinc Tin Oxide Thin-Film Transistors', *Electrochem. Solid-State Lett.*, vol. 10, no. 5, p. H135, 2007.
- [74] D. Kim, Y. Jeong, K. Song, S.-K. Park, G. Cao, and J. Moon, 'Inkjet-Printed Zinc Tin Oxide Thin-Film Transistor', *Langmuir*, vol. 25, no. 18, pp. 11149–11154, Sep. 2009.
- [75] W. B. Jackson, G. S. Herman, R. L. Hoffman, C. Taussig, S. Braymen, F. Jeffery, and J. Hauschildt, 'Zinc tin oxide transistors on flexible substrates', *J. Non. Cryst. Solids*, vol. 352, no. 9–20 SPEC. ISS., pp. 1753–1755, Jun. 2006.
- [76] S.-J. Seo, C. G. Choi, Y. H. Hwang, and B.-S. Bae, 'High performance solution-processed amorphous zinc tin oxide thin film transistor', *J. Phys. D: Appl. Phys.*, vol. 42, no. 3, p. 035106, Feb. 2008.
- [77] P. Görrn, P. Hölzer, T. Riedl, W. Kowalsky, J. Wang, T. Weimann, P. Hinze, and S. Kipp, 'Stability of transparent zinc tin oxide transistors under bias stress', *Appl. Phys. Lett.*, vol. 90, no. 6, p. 063502, Feb. 2007.
- [78] Y. H. Kim, J. I. Han, and S. K. Park, 'Effect of Zinc/Tin composition ratio on the operational stability of solution-processed Zinc-Tin-Oxide Thin-Film transistors', *IEEE Electron Device Lett.*, vol. 33, no. 1, pp. 50–52, 2012.
- [79] J. Heo, S. B. Kim, and R. G. Gordon, 'Atomic layer deposited zinc tin oxide channel for amorphous oxide thin film transistors', *Appl. Phys. Lett.*, vol. 101, no. 11, 2012.
- [80] C.-G. Lee and A. Dodabalapur, 'Solution-processed zinc-tin oxide thin-film transistors with low interfacial trap density and improved performance', *Appl. Phys. Lett.*, vol. 96, no. 24, p. 243501, Jun. 2010.
- [81] D.-H. Lee, Y.-J. Chang, G. S. Herman, and C.-H. Chang, 'A General Route to Printable High-Mobility Transparent Amorphous Oxide Semiconductors', *Adv. Mater.*, vol. 19, no. 6, pp. 843–847, Mar. 2007.
- [82] C. G. Choi, S.-J. Seo, and B.-S. Bae, 'Solution-Processed Indium-Zinc Oxide Transparent Thin-Film Transistors', *Electrochem. Solid-State Lett.*, vol. 11, no. 1, p. H7, 2008.

- [83] G. H. Kim, H. S. Shin, B. Du Ahn, K. H. Kim, W. J. Park, and H. J. Kim, 'Formation Mechanism of Solution-Processed Nanocrystalline InGaZnO Thin Film as Active Channel Layer in Thin-Film Transistor', *J. Electrochem. Soc.*, vol. 156, no. 1, p. H7, 2009.
- [84] H. S. Shin, G. H. Kim, W. H. Jeong, B. Du Ahn, and H. J. Kim, 'Electrical Properties of Yttrium-Indium-Zinc-Oxide Thin Film Transistors Fabricated Using the Sol-Gel Process and Various Yttrium Compositions', *Jpn. J. Appl. Phys.*, vol. 49, no. 3, p. 03CB01, Mar. 2010.
- [85] D. N. Kim, D. L. Kim, G. H. Kim, S. J. Kim, and H. J. Kim, 'P-23: Solution-processed Amorphous Lanthanum Indium Zinc Oxide Thin-film Transistors', *SID Symp. Dig. Tech. Pap.*, vol. 41, no. 1, p. 1308, 2010.
- [86] M.-G. Kim, H. S. Kim, Y.-G. Ha, J. He, M. G. Kanatzidis, A. Facchetti, and T. J. Marks, 'High-Performance Solution-Processed Amorphous Zinc-Indium-Tin Oxide Thin-Film Transistors', *J. Am. Chem. Soc.*, vol. 132, no. 30, pp. 10352–10364, Aug. 2010.
- [87] G. H. Kim, W. H. Jeong, B. Du Ahn, H. S. Shin, H. J. Kim, H. J. Kim, M.-K. Ryu, K.-B. Park, J.-B. Seon, and S.-Y. Lee, 'Investigation of the effects of Mg incorporation into InZnO for high-performance and high-stability solution-processed thin film transistors', *Appl. Phys. Lett.*, vol. 96, no. 16, p. 163506, Apr. 2010.
- [88] D. H. Yoon, S. J. Kim, W. H. Jeong, D. L. Kim, Y. S. Rim, and H. J. Kim, 'Investigation of solution-processed amorphous SrInZnO thin film transistors', *J. Cryst. Growth*, vol. 326, no. 1, pp. 171–174, Jul. 2011.
- [89] K.-H. Park, E. Chong, B.-K. Ju, and S. Y. Lee, 'Effect of Indium Contents on the Solution-Processed SiInZnO Thin Film Transistors Annealed at Low Temperature', *Electrochem. Solid-State Lett.*, vol. 14, no. 12, p. H491, 2011.
- [90] J. Y. Choi, S. S. Kim, and S. Y. Lee, 'Investigation of addition of silicon on the electrical properties of low temperature solution processed SiInZnO thin film transistor', *J. Sol-Gel Sci. Technol.*, vol. 74, no. 2, pp. 482–487, 2015.
- [91] J. W. Hennek, J. Smith, A. Yan, M. Kim, W. Zhao, V. P. Dravid, A. Facchetti, and T. J. Marks, 'Oxygen "Getter" Effects on Microstructure and Carrier Transport in Low Temperature Combustion-Processed a-InXZnO (X = Ga, Sc, Y, La) Transistors', *J. Am. Chem. Soc.*, vol. 135, no. 29, pp. 10729–10741, Jul. 2013.
- [92] S.-J. Seo, C. G. Choi, Y. H. Hwang, and B.-S. Bae, 'P-23: Transparent Amorphous Oxide Thin Film Transistors Fabricated by Solution Coating Process', *SID Symp. Dig. Tech. Pap.*, vol. 39, no. 1, p. 1254, 2008.
- [93] B. N. Pal, B. M. Dhar, K. C. See, and H. E. Katz, 'Solution-deposited sodium beta-alumina gate dielectrics for low-voltage and transparent field-effect transistors', *Nat. Mater.*, vol. 8, no. 11, pp. 898–903, Nov. 2009.
- [94] S. K. Park, Y.-H. Kim, and J.-I. Han, 'All solution-processed high-resolution bottom-contact transparent metal-oxide thin film transistors', *J. Phys. D: Appl. Phys.*, vol. 42, no. 12, 2009.

- [95] C.-K. Chen, H.-H. Hsieh, J.-J. Shyue, and C.-C. Wu, 'The Influence of Channel Compositions on the Electrical Properties of Solution-Processed Indium-Zinc Oxide Thin-Film Transistors', *J. Disp. Technol.*, vol. 5, no. 12, pp. 509–514, Dec. 2009.
- [96] M. S. Park, D. H. Lee, E. J. Bae, D.-H. Kim, J. G. Kang, D.-H. Son, and S. O. Ryu, 'Fabrication of Indium Gallium Zinc Oxide (IGZO) TFTs Using a Solution-Based Process', *Mol. Cryst. Liq. Cryst.*, vol. 529, no. 1, pp. 137–146, Oct. 2010.
- [97] S. Jeong, Y.-G. Ha, J. Moon, A. Facchetti, and T. J. Marks, 'Role of Gallium Doping in Dramatically Lowering Amorphous-Oxide Processing Temperatures for Solution-Derived Indium Zinc Oxide Thin-Film Transistors', *Adv. Mater.*, vol. 22, no. 12, pp. 1346–1350, Mar. 2010.
- [98] C. Y. Koo, K. Song, T. Jun, D. Kim, Y. Jeong, S.-H. Kim, J. Ha, and J. Moon, 'Low Temperature Solution-Processed InZnO Thin-Film Transistors', *J. Electrochem. Soc.*, vol. 157, no. 4, p. J1111, 2010.
- [99] Kyung-Bae Park, Jong-Baek Seon, Gun Hee Kim, Mino Yang, Bonwon Koo, Hyun Jae Kim, Myung-Kwan Ryu, and Sang-Yoon Lee, 'High Electrical Performance of Wet-Processed Indium Zinc Oxide Thin-Film Transistors', *IEEE Electron Device Lett.*, vol. 31, no. 4, pp. 311–313, Apr. 2010.
- [100] Ya-Hui Yang, S. S. Yang, Chen-Yen Kao, and Kan-San Chou, 'Chemical and Electrical Properties of Low-Temperature Solution-Processed In-Ga-Zn-O Thin-Film Transistors', *IEEE Electron Device Lett.*, vol. 31, no. 4, pp. 329–331, Apr. 2010.
- [101] Y.-H. Kim, M.-K. Han, J.-I. Han, and S. K. Park, 'Effect of Metallic Composition on Electrical Properties of Solution-Processed Indium-Gallium-Zinc-Oxide Thin-Film Transistors', *IEEE Trans. Electron Devices*, vol. 57, no. 5, pp. 1009–1014, May 2010.
- [102] S. J. Kim, G. H. Kim, D. L. Kim, D. N. Kim, and H. J. Kim, 'InGaZnO thin-film transistors with YHfZnO gate insulator by solution process', *Phys. status solidi*, vol. 207, no. 7, pp. 1668–1671, May 2010.
- [103] Y. Choi, G. H. Kim, W. H. Jeong, H. J. Kim, B. D. Chin, and J.-W. Yu, 'Characteristics of gravure printed InGaZnO thin films as an active channel layer in thin film transistors', *Thin Solid Films*, vol. 518, no. 22, pp. 6249–6252, Sep. 2010.
- [104] H.-C. Cheng and C.-Y. Tsay, 'Flexible a-IZO thin film transistors fabricated by solution processes', *J. Alloys Compd.*, vol. 507, no. 1, pp. L1–L3, Sep. 2010.
- [105] B.-J. Kim, H.-J. Kim, T.-S. Yoon, Y.-S. Kim, and H. H. Lee, 'Effects on Annealing Temperature for Solution-Processed IZTO TFTs by Nitrogen Incorporation', *Electrochem. Solid-State Lett.*, vol. 13, no. 12, p. H419, 2010.
- [106] P. K. Nayak, T. Busani, E. Elamurugu, P. Barquinha, R. Martins, Y. Hong, and E. Fortunato, 'Zinc concentration dependence study of solution processed amorphous indium gallium zinc oxide thin film transistors using high-k dielectric', *Appl. Phys. Lett.*, vol. 97, no. 18, p. 183504, Nov. 2010.

- [107] Y.-J. Kim, J.-S. Lee, Y.-U. Lee, S.-H. Cho, Y.-H. Kim, and M.-K. Han, 'Solution-Processed Oxide Thin-Film Transistor with Spin-Coated Zinc Tin Oxide Active Layer and Indium Zinc Oxide Source/Drain Electrodes', in *ECS Transactions*, 2010, vol. 33, no. May 2012, pp. 289–294.
- [108] B.-J. Kim, H.-J. Kim, S. M. Jung, T.-S. Yoon, Y.-S. Kim, and H. H. Lee, 'Solution-Processed Oxide Thin Film Transistors with Indium Zinc Tin Oxide Semiconductor: Nitrogen Effect', 2010, vol. 33, no. 5, pp. 295–299.
- [109] S. Han, G. Herman, and C. Chang, 'Low Temperature, High-Performance, Solution-Processed Indium Oxide Based Thin Film Transistors', in *ECS Transactions*, 2010, vol. 33, no. 5, pp. 275–281.
- [110] B.-J. Kim, H.-J. Kim, T.-S. Yoon, Y.-S. Kim, D.-H. Lee, Y. Choi, B.-H. Ryu, and H. H. Lee, 'Solution processed IZTO thin film transistor on silicon nitride dielectric layer', *J. Ind. Eng. Chem.*, vol. 17, no. 1, pp. 96–99, Jan. 2011.
- [111] Y. S. Rim, D. L. Kim, W. H. Jeong, H. S. Shin, and H. J. Kim, 'P-14: High Performance Solution-Processed IGZO TFTs Formed by Using a High-Pressure Annealing Method', *SID Symp. Dig. Tech. Pap.*, vol. 42, no. 1, pp. 1148–1150, Jun. 2011.
- [112] K. Song, C. Young Koo, T. Jun, D. Lee, Y. Jeong, and J. Moon, 'Low-temperature soluble InZnO thin film transistors by microwave annealing', *J. Cryst. Growth*, vol. 326, no. 1, pp. 23–27, Jul. 2011.
- [113] S.-Y. Han and C. Chang, 'Effects of Ozone Annealing on Solution-Processed Indium Zinc Oxide (IZO) Thin Film Transistors', *Electrochem. Solid-State Lett.*, vol. 14, no. 11, p. H442, 2011.
- [114] S. Jeong, J.-Y. Lee, S. S. Lee, S.-W. Oh, H. H. Lee, Y.-H. Seo, B.-H. Ryu, and Y. Choi, 'Chemically improved high performance printed indium gallium zinc oxide thin-film transistors', *J. Mater. Chem.*, vol. 21, no. 43, p. 17066, 2011.
- [115] T. H. Jeong, S. J. Kim, D. H. Yoon, W. H. Jeong, D. L. Kim, H. S. Lim, and H. J. Kim, 'Study on the Effects of Zr-Incorporated InZnO Thin-Film Transistors Using a Solution Process', *Jpn. J. Appl. Phys.*, vol. 50, no. 7, p. 070202, Jul. 2011.
- [116] K. M. Kim, C. W. Kim, J.-S. Heo, H. Na, J. E. Lee, C. B. Park, J.-U. Bae, C.-D. Kim, M. Jun, Y. K. Hwang, S. T. Meyers, A. Grenville, and D. A. Keszler, 'Competitive device performance of low-temperature and all-solution-processed metal-oxide thin-film transistors', *Appl. Phys. Lett.*, vol. 99, no. 24, p. 242109, Dec. 2011.
- [117] C. Avis and J. Jang, 'High-performance solution processed oxide TFT with aluminum oxide gate dielectric fabricated by a sol-gel method', *J. Mater. Chem.*, vol. 21, no. 29, p. 10649, 2011.
- [118] J. Y. Choi, S. Kim, and S. Y. Lee, 'Threshold voltage shift by controlling Ga in solution processed Si-In-Zn-O thin film transistors', *Thin Solid Films*, vol. 520, no. 10, pp. 3774–3777, Mar. 2012.
- [119] L. Yue, H. Pu, S. Pang, H. Li, and Q. Zhang, 'Top-gate LZTO thin-film transistors with PMMA gate insulator by solution process', *EPL (Europhysics Lett.)*, vol. 97, no. 6, p. 67006, Mar. 2012.

- [120] J. W. Hennek, Y. Xia, K. Everaerts, M. C. Hersam, A. Facchetti, and T. J. Marks, 'Reduced Contact Resistance in Inkjet Printed High-Performance Amorphous Indium Gallium Zinc Oxide Transistors', *ACS Appl. Mater. Interfaces*, vol. 4, no. 3, pp. 1614–1619, Mar. 2012.
- [121] C. Y. Koo, K. Song, Y. Jung, W. Yang, S.-H. Kim, S. Jeong, and J. Moon, 'Enhanced Performance of Solution-Processed Amorphous LiYInZnO Thin-Film Transistors', *ACS Appl. Mater. Interfaces*, vol. 4, no. 3, pp. 1456–1461, Mar. 2012.
- [122] P. K. Nayak, M. N. Hedhili, D. Cha, and H. N. Alshareef, 'High performance solution-deposited amorphous indium gallium zinc oxide thin film transistors by oxygen plasma treatment', *Appl. Phys. Lett.*, vol. 100, no. 20, p. 202106, May 2012.
- [123] Y.-W. Chung, F.-C. Chen, Y.-P. Chen, Y.-Z. Chen, and Y.-L. Chueh, 'High-performance solution-processed amorphous ZrInZnO thin-film transistors', *Phys. status solidi - Rapid Res. Lett.*, vol. 6, no. 9–10, pp. 400–402, Oct. 2012.
- [124] J. H. Park, Y. B. Yoo, K. H. Lee, W. S. Jang, J. Y. Oh, S. S. Chae, and H. K. Baik, 'Low-Temperature, High-Performance Solution-Processed Thin-Film Transistors with Peroxo-Zirconium Oxide Dielectric', *ACS Appl. Mater. Interfaces*, vol. 5, no. 2, pp. 410–417, Jan. 2013.
- [125] X. Li, Q. Li, E. Xin, and J. Zhang, 'Sol-gel processed indium zinc oxide thin film and transparent thin-film transistors', *J. Sol-Gel Sci. Technol.*, vol. 65, no. 2, pp. 130–134, Feb. 2013.
- [126] K. H. Lee, J. H. Park, Y. B. Yoo, W. S. Jang, J. Y. Oh, S. S. Chae, K. J. Moon, J. M. Myoung, and H. K. Baik, 'Effects of Solution Temperature on Solution-Processed High-Performance Metal Oxide Thin-Film Transistors', *ACS Appl. Mater. Interfaces*, vol. 5, no. 7, pp. 2585–2592, Apr. 2013.
- [127] X. Li, Q. Li, and J. Zhang, 'Transparent amorphous Indium-Gallium-Zinc-Oxygen thin film transistors using solution technology at low temperature', *J. Sol-Gel Sci. Technol.*, vol. 66, no. 3, pp. 497–503, Jun. 2013.
- [128] J.-S. Seo, J.-H. Jeon, Y. H. Hwang, H. Park, M. Ryu, S.-H. K. Park, and B.-S. Bae, 'Solution-Processed Flexible Fluorine-doped Indium Zinc Oxide Thin-Film Transistors Fabricated on Plastic Film at Low Temperature', *Sci. Rep.*, vol. 3, no. 1, p. 2085, Dec. 2013.
- [129] B. S. Kim, Y. Taek Jeong, D. Lee, T. Choi, S.-H. Jung, J. Whan Choi, C. Yang, K. Jo, B. Lee, E. Park, D. Na Kim, Y. Kim, and S. Shin, 'Solution-processed zinc-indium-tin oxide thin-film transistors for flat-panel displays', *Appl. Phys. Lett.*, vol. 103, no. 7, p. 072110, Aug. 2013.
- [130] H. Pu, Q. Zhou, L. Yue, and Q. Zhang, 'Solution-processed indium gallium zinc oxide thin-film transistors with infrared irradiation annealing', *Semicond. Sci. Technol.*, vol. 28, no. 10, p. 105002, Oct. 2013.

- [131] Y.-H. Kim, K.-H. Kim, and S. K. Park, 'Effects of Annealing Conditions on the Dielectric Properties of Solution-Processed Al₂O₃ Layers for Indium-Zinc-Tin-Oxide Thin-Film Transistors', *J. Nanosci. Nanotechnol.*, vol. 13, no. 11, pp. 7779–7782, Nov. 2013.
- [132] S. M. Hwang, S. M. Lee, J. H. Choi, J. H. Lim, and J. Joo, 'Fabrication of Solution-Processed InSnZnO/ZrO₂ Thin Film Transistors', *J. Nanosci. Nanotechnol.*, vol. 13, no. 11, pp. 7774–7778, Nov. 2013.
- [133] L. Yue, H. Pu, H. Li, S. Pang, and Q. Zhang, 'Dip-coated Al-In-Zn-O thin-film transistor with poly-methylmethacrylate gate dielectric', *J. Phys. D. Appl. Phys.*, vol. 46, no. 44, p. 445106, Nov. 2013.
- [134] D. H. Lee, S. M. Park, J. Il Yang, D. K. Cho, S. H. Woo, Y. S. Lim, D. K. Kim, and M. Yi, 'Effect of Chloride Precursors on the Stability of Solution-Processed Indium Zinc Oxide Thin-Film Transistors', *Jpn. J. Appl. Phys.*, vol. 52, no. 10S, p. 10MA02, Oct. 2013.
- [135] B.-Y. Su, S.-Y. Chu, Y.-D. Juang, and H. Lee, 'Improved Negative Bias Stress Stability of IZO Thin Film Transistors via Post-Vacuum Annealing of Solution Method', *ECS J. Solid State Sci. Technol.*, vol. 2, no. 7, pp. Q99–Q103, May 2013.
- [136] K. Everaerts, L. Zeng, J. W. Hennek, D. I. Camacho, D. Jariwala, M. J. Bedzyk, M. C. Hersam, and T. J. Marks, 'Printed indium gallium zinc oxide transistors. Self-assembled nanodielectric effects on low-temperature combustion growth and carrier mobility', *ACS Appl. Mater. Interfaces*, vol. 5, no. 22, pp. 11884–11893, 2013.
- [137] Y. Gao, X. Li, L. Chen, J. Shi, X. W. Sun, and J. Zhang, 'High mobility solution-processed hafnium indium zinc oxide TFT with an Al-Doped ZrO₂ gate dielectric', *IEEE Electron Device Lett.*, vol. 35, no. 5, pp. 554–556, May 2014.
- [138] Z. Yang, H. Pu, C. Cui, L. Zhang, C. Dong, and Q. Zhang, 'Solution-processed indium-zinc-oxide thin film transistors with high-*k* Magnesium titanium oxide dielectric', *IEEE Electron Device Lett.*, vol. 35, no. 5, pp. 557–559, May 2014.
- [139] H. J. Cheong, N. Fukuda, H. Sakai, S. Ogura, K. Takeuchi, R. Nagahata, and S. Uemura, 'Characterization of an oxide semiconductor prepared by microwave sintering', *Jpn. J. Appl. Phys.*, vol. 53, no. 5S3, p. 05HA12, May 2014.
- [140] J. S. Lee and W.-S. Choi, 'Low-temperature processing of inkjet-printed IZO thin-film transistors', *J. Korean Phys. Soc.*, vol. 64, no. 5, pp. 701–705, Mar. 2014.
- [141] K.-S. Kim, Y.-H. Hwang, I. Hwang, and W.-J. Cho, 'Improved performance of solution-processed a-InGaZnO thin-film transistors due to Ar/O₂ mixed-plasma treatment', *J. Korean Phys. Soc.*, vol. 65, no. 3, pp. 399–403, Aug. 2014.
- [142] W. S. Choi, H. Jo, M. S. Kwon, and B. J. Jung, 'Control of electrical properties and gate bias stress stability in solution-processed a-IZO TFTs by Zr doping', *Curr. Appl. Phys.*, vol. 14, no. 12, pp. 1831–1836, Dec. 2014.

- [143] K. K. Banger, R. L. Peterson, K. Mori, Y. Yamashita, T. Leedham, and H. Sirringhaus, 'High Performance, Low Temperature Solution-Processed Barium and Strontium Doped Oxide Thin Film Transistors', *Chem. Mater.*, vol. 26, no. 2, pp. 1195–1203, Jan. 2014.
- [144] S. Oertel, M. P. M. M. Jank, E. Teuber, A. J. Bauer, and L. Frey, 'High-mobility metal-oxide thin-film transistors by spray deposition of environmentally friendly precursors', in *Thin Solid Films*, 2014, vol. 553, pp. 114–117.
- [145] J. M. Kwon, J. Jung, Y. S. Rim, D. L. Kim, and H. J. Kim, 'Improvement in Negative Bias Stress Stability of Solution-Processed Amorphous In-Ga-Zn-O Thin-Film Transistors Using Hydrogen Peroxide', *ACS Appl. Mater. Interfaces*, vol. 6, no. 5, pp. 3371–3377, Mar. 2014.
- [146] J. H. Park, S. S. Chae, Y. B. Yoo, J. H. Lee, T. Il Lee, and H. K. Baik, 'Fabrication of solution-processed amorphous indium zinc oxide thin-film transistors at low temperatures using deep-UV irradiation under wet conditions', *Chem. Phys. Lett.*, vol. 597, pp. 121–125, Mar. 2014.
- [147] M. Benwadih, J. A. Chroboczek, G. Ghibaudo, R. Coppard, and D. Vuillaume, 'Impact of dopant species on the interfacial trap density and mobility in amorphous In-X-Zn-O solution-processed thin-film transistors', *J. Appl. Phys.*, vol. 115, no. 21, p. 214501, Jun. 2014.
- [148] Y. H. Kang, S. Jeong, J. M. Ko, J.-Y. Lee, Y. Choi, C. Lee, and S. Y. Cho, 'Two-component solution processing of oxide semiconductors for thin-film transistors via self-combustion reaction', *J. Mater. Chem. C*, vol. 2, no. 21, pp. 4247–4256, 2014.
- [149] C. Avis, H. R. Hwang, and J. Jang, 'Effect Of Channel Layer Thickness On The Performance Of Indium-Zinc-Tin Oxide Thin Film Transistors Manufactured By Inkjet Printing', *ACS Appl. Mater. Interfaces*, vol. 6, no. 14, pp. 10941–10945, Jul. 2014.
- [150] Y. Li, L. Lan, P. Xiao, Z. Lin, S. Sun, W. Song, E. Song, P. Gao, D. Wang, H. Ning, and J. Peng, 'Solution-processed indium-zinc-oxide thin-film transistors based on anodized aluminum oxide gate insulator modified with zirconium oxide', *RSC Adv.*, vol. 5, no. 63, pp. 51440–51445, 2015.
- [151] B. R. Naik, C. Avis, D. H. Chowdhury, T. Kim, T. Lin, and J. Jang, 'Improvement in performance of solution-processed indium-zinc-tin oxide thin-film transistors by UV/O₃ treatment on zirconium oxide gate insulator', *Am-Fpd*, vol. 02, no. V, pp. 0–6, 2015.
- [152] S. Y. Lee, T. Kang, S. M. Han, Y. S. Lee, and J. Y. Choi, 'Temperature Dependence of SiInZnO Thin Film Transistor Fabricated by Solution Process', *Trans. Electr. Electron. Mater.*, vol. 16, no. 1, pp. 46–48, Feb. 2015.
- [153] X. Li, L. Zhu, Y. Gao, and J. Zhang, 'Solution-processed low-operating-voltage thin-film transistors with bottom-gate top-contact structure', *IEEE Trans. Electron Devices*, vol. 62, no. 3, pp. 875–881, Mar. 2015.

- [154] X. Li, E. Xin, and J. Zhang, 'Effects of Hf incorporation on indium zinc oxide thin-film transistors using solution process', *Electron. Mater. Lett.*, vol. 11, no. 1, pp. 143–148, Jan. 2015.
- [155] R. Branquinho, D. Salgueiro, A. Santa, A. Kiazadeh, P. Barquinha, L. Pereira, R. Martins, and E. Fortunato, 'Towards environmental friendly solution-based ZTO/ AlO_x TFTs', *Semicond. Sci. Technol.*, vol. 30, no. 2, p. 024007, Feb. 2015.
- [156] X. Yu, J. Smith, N. Zhou, L. Zeng, P. Guo, Y. Xia, A. Alvarez, S. Aghion, H. Lin, J. Yu, R. P. H. Chang, M. J. Bedzyk, R. Ferragut, T. J. Marks, and A. Facchetti, 'Spray-combustion synthesis: Efficient solution route to high-performance oxide transistors', *Proc. Natl. Acad. Sci.*, vol. 112, no. 11, pp. 3217–3222, Mar. 2015.
- [157] G. Liu, A. Liu, H. Zhu, B. Shin, E. Fortunato, R. Martins, Y. Wang, and F. Shan, 'Low-Temperature, Nontoxic Water-Induced Metal-Oxide Thin Films and Their Application in Thin-Film Transistors', *Adv. Funct. Mater.*, vol. 25, no. 17, pp. 2564–2572, May 2015.
- [158] H. Cheong, S. Ogura, H. Ushijima, M. Yoshida, N. Fukuda, and S. Uemura, 'Rapid preparation of solution-processed InGaZnO thin films by microwave annealing and photoirradiation', *AIP Adv.*, vol. 5, no. 6, p. 067127, Jun. 2015.
- [159] W. T. Park, I. Son, H. W. Park, K. B. Chung, Y. Xu, T. Lee, and Y. Y. Noh, 'Facile Routes To Improve Performance of Solution-Processed Amorphous Metal Oxide Thin Film Transistors by Water Vapor Annealing', *ACS Appl. Mater. Interfaces*, vol. 7, no. 24, pp. 13289–13294, 2015.
- [160] Y. Gao, J. Lu, J. Zhang, and X. Li, 'Influence of annealing temperatures on solution-processed AlInZnO thin film transistors', *J. Alloys Compd.*, vol. 646, no. 3, pp. 675–679, Oct. 2015.
- [161] T. S. Jung, S. J. Kim, C. H. Kim, J. Jung, J. Na, M. M. Sabri, and H. J. Kim, 'Replacement and Rearrangement of an Oxide Lattice by Germanium Doping in Solution-Processed Indium-Zinc-Oxide Thin-Film Transistors', *IEEE Trans. Electron Devices*, vol. 62, no. 9, pp. 2888–2893, Sep. 2015.
- [162] W.-J. Lee, W.-T. Park, S. Park, S. Sung, Y.-Y. Noh, and M.-H. Yoon, 'Large-Scale Precise Printing of Ultrathin Sol-Gel Oxide Dielectrics for Directly Patterned Solution-Processed Metal Oxide Transistor Arrays', *Adv. Mater.*, vol. 27, no. 34, pp. 5043–5048, Sep. 2015.
- [163] S. W. Ko, S. K. Kim, J. M. Kim, J. H. Cho, H. S. Park, and B. D. Choi, 'Electrical Properties and Reliability Analysis of Solution-Processed Indium Tin Zinc Oxide Thin Film Transistors with O_2 -Plasma Treatment', *J. Nanosci. Nanotechnol.*, vol. 15, no. 10, pp. 7476–7481, Oct. 2015.
- [164] S. Inoue, T. T. Phan, T. Hori, H. Koyama, and T. Shimoda, 'Electrophoretic displays driven by all-oxide thin-film transistor backplanes fabricated using a solution process', *Phys. status solidi*, vol. 212, no. 10, pp. 2133–2140, Oct. 2015.

- [165] J. Zhang, P. Dong, Y. Gao, C. Sheng, and X. Li, 'Performance Enhancement of ZITO Thin-Film Transistors via Graphene Bridge Layer by Sol-Gel Combustion Process', *ACS Appl. Mater. Interfaces*, vol. 7, no. 43, pp. 24103–24109, Nov. 2015.
- [166] D. Wan, X. Liu, L. Xu, C. Liu, X. Xiao, S. Guo, and L. Liao, 'The Study for Solution-Processed Alkali Metal-Doped Indium-Zinc Oxide Thin-Film Transistors', *IEEE Electron Device Lett.*, vol. 37, no. 1, pp. 50–52, Jan. 2016.
- [167] J.-W. Jo, J. S. Heo, K.-T. Kim, J. Kim, M.-G. Kim, and S. K. Park, '(Invited) Low-Temperature Sol-Gel Derived Ultra-Flexible Metal-Oxide Thin-Film-Transistors and Their Applications', *ECS Trans.*, vol. 75, no. 10, pp. 123–126, Sep. 2016.
- [168] H. J. Seul, H.-G. Kim, M.-Y. Park, and J. K. Jeong, 'A solution-processed silicon oxide gate dielectric prepared at a low temperature via ultraviolet irradiation for metal oxide transistors', *J. Mater. Chem. C*, vol. 4, no. 44, pp. 10486–10493, 2016.
- [169] R. A. John, A. C. Nguyen, Y. Chen, S. Shukla, S. Chen, and N. Mathews, 'Modulating Cationic Ratios for High-Performance Transparent Solution-Processed Electronics', *ACS Appl. Mater. Interfaces*, vol. 8, no. 2, pp. 1139–1146, 2016.
- [170] R. N. Bukke, C. Avis, and J. Jang, 'Solution-Processed Amorphous In-Zn-Sn Oxide Thin-Film Transistor Performance Improvement by Solution-Processed Y_2O_3 Passivation', *IEEE Electron Device Lett.*, vol. 37, no. 4, pp. 433–436, Apr. 2016.
- [171] J. S. Heo, J.-W. Jo, J. Kang, C.-Y. Jeong, H. Y. Jeong, S. K. Kim, K. Kim, H.-I. Kwon, J. Kim, Y.-H. Kim, M.-G. Kim, and S. K. Park, 'Water-Mediated Photochemical Treatments for Low-Temperature Passivation of Metal-Oxide Thin-Film Transistors', *ACS Appl. Mater. Interfaces*, vol. 8, no. 16, pp. 10403–10412, Apr. 2016.
- [172] E. B. Secor, J. Smith, T. J. Marks, and M. C. Hersam, 'High-Performance Inkjet-Printed Indium-Gallium-Zinc-Oxide Transistors Enabled by Embedded, Chemically Stable Graphene Electrodes', *ACS Appl. Mater. Interfaces*, vol. 8, no. 27, pp. 17428–17434, Jul. 2016.
- [173] J. Kim, S. Choi, M. Kim, T. J. Ha, and Y. H. Kim, 'Strontium doping effects on the characteristics of solution-processed aluminum oxide dielectric layer and its application to low-voltage-operated indium-gallium-zinc-oxide thin-film transistors', *Ceram. Int.*, vol. 43, no. 16, pp. 13576–13580, 2017.
- [174] S.-Y. Han, M.-C. Nguyen, A. H. T. Nguyen, J.-W. Choi, J.-Y. Kim, and R. Choi, 'Effect of Li-doping on low temperature solution-processed indium-zinc oxide thin film transistors', *Thin Solid Films*, vol. 641, pp. 19–23, Nov. 2017.
- [175] L. Yue, F. Meng, and J. Chen, 'Effect of active-layer composition and structure on device performance of coplanar top-gate amorphous oxide thin-film transistors', *Semicond. Sci. Technol.*, vol. 33, no. 1, p. 015012, Jan. 2018.

- [176] D. Wan, X. Liu, A. Abliz, C. Liu, Y. Yang, W. Wu, G. Li, J. Li, H. Chen, T. Guo, and L. Liao, 'Design of Highly Stable Tungsten-Doped IZO Thin-Film Transistors With Enhanced Performance', *IEEE Trans. Electron Devices*, vol. 65, no. 3, pp. 1018–1022, Mar. 2018.
- [177] D.-Y. Zhong, J. Li, C.-Y. Zhao, C.-X. Huang, J.-H. Zhang, X.-F. Li, X.-Y. Jiang, and Z.-L. Zhang, 'Enhanced Electrical Performance and Negative Bias Illumination Stability of Solution-Processed InZnO Thin-Film Transistor by Boron Addition', *IEEE Trans. Electron Devices*, vol. 65, no. 2, pp. 520–525, Feb. 2018.
- [178] J.-W. Jo, K.-H. Kim, J. Kim, S. G. Ban, Y.-H. Kim, and S. K. Park, 'High-Mobility and Hysteresis-Free Flexible Oxide Thin-Film Transistors and Circuits by Using Bilayer Sol-Gel Gate Dielectrics', *ACS Appl. Mater. Interfaces*, vol. 10, no. 3, pp. 2679–2687, Jan. 2018.
- [179] K. Maex, M. R. Baklanov, D. Shamiryman, F. Iacopi, S. H. Brongersma, and Z. S. Yanovitskaya, 'Low dielectric constant materials for microelectronics', *J. Appl. Phys.*, vol. 93, no. 11, pp. 8793–8841, 2003.
- [180] B. D. Hatton, K. Landskron, W. J. Hunks, M. R. Bennett, D. Shukaris, D. D. Perovic, and G. a. Ozin, 'Materials chemistry for low-k materials', *Mater. Today*, vol. 9, no. 3, pp. 22–31, 2006.
- [181] J. Bennett, M. Quevedo-Lopez, and S. Satyanarayana, 'Characterizing high-k and low-k dielectric materials for semiconductors: Progress and challenges', *Appl. Surf. Sci.*, vol. 252, no. 19, pp. 7167–7171, 2006.
- [182] H. Treichel, G. Ruhl, P. Ansmann, R. Würfl, C. Müller, and M. Dietlmeier, 'Low dielectric constant materials for interlayer dielectric', *Microelectron. Eng.*, vol. 40, no. 1, pp. 1–19, 1998.
- [183] M. R. Baklanov, J.-F. de Marneffe, D. Shamiryman, A. M. Urbanowicz, H. Shi, T. V. Rakhimova, H. Huang, and P. S. Ho, 'Plasma processing of low-k dielectrics', *J. Appl. Phys.*, vol. 113, no. 4, p. 041101, Jan. 2013.
- [184] A. Grill, S. M. Gates, T. E. Ryan, S. V. Nguyen, and D. Priyadarshini, 'Progress in the development and understanding of advanced low k and ultralow k dielectrics for very large-scale integrated interconnects-State of the art', *Appl. Phys. Rev.*, vol. 1, no. 1, p. 011306, Mar. 2014.
- [185] A. Delan, M. Rennau, S. . Schulz, and T. Gessner, 'Thermal conductivity of ultra low-k dielectrics', *Microelectron. Eng.*, vol. 70, no. 2–4, pp. 280–284, Nov. 2003.
- [186] E. T. Ryan, A. J. McKerrow, J. Leu, and P. S. Ho, 'Materials issues and characterization of low-k dielectric materials', *MRS Bull.*, vol. 22, no. 10, pp. 49–54, Oct. 1997.
- [187] A. Grill, 'Novel Low k Dielectrics Based on Diamondlike Carbon Materials', *J. Electrochem. Soc.*, vol. 145, no. 5, p. 1649, May 1998.

- [188] R. J. O. M. Hoofman, G. J. A. M. Verheijden, J. Michelon, F. Iacopi, Y. Travaly, M. R. Baklanov, Z. Tökei, and G. P. Beyer, 'Challenges in the implementation of low-k dielectrics in the back-end of line', *Microelectron. Eng.*, vol. 80, pp. 337–344, Jun. 2005.
- [189] D. Shamiryanyan, T. Abell, F. Iacopi, and K. Maex, 'Low-k dielectric materials', *Mater. Today*, vol. 7, no. 1, pp. 34–39, Jan. 2004.
- [190] R. D. Miller, 'DEVICE PHYSICS: In Search of Low-k Dielectrics', *Science (80)*, vol. 286, no. 5439, pp. 421–423, Oct. 1999.
- [191] J. Veres, S. D. Ogier, S. W. Leeming, D. C. Cupertino, and S. Mohialdin Khaffaf, 'Low-k Insulators as the Choice of Dielectrics in Organic Field-Effect Transistors', *Adv. Funct. Mater.*, vol. 13, no. 3, pp. 199–204, Mar. 2003.
- [192] P. S. Raja and R. J. Daniel, 'Low-K Dielectrics for Nanoscale MOSFETS', *Procedia Eng.*, vol. 38, pp. 2048–2052, 2012.
- [193] G. D. Wilk, R. M. Wallace, and J. M. Anthony, 'High- κ gate dielectrics: Current status and materials properties considerations', *J. Appl. Phys.*, vol. 89, no. 10, pp. 5243–5275, May 2001.
- [194] J. Robertson, 'High dielectric constant gate oxides for metal oxide Si transistors', *Reports Prog. Phys.*, vol. 69, no. 2, pp. 327–396, Feb. 2006.
- [195] J. Robertson, 'High dielectric constant oxides', *Eur. Phys. J. Appl. Phys.*, vol. 28, no. 3, pp. 265–291, Dec. 2004.
- [196] P. Barquinha, R. Martins, L. Pereira, E. Fortunato, and L. P. and E. F. Pedro Barquinha, Rodrigo Martins, *Transparent Oxide Electronics*. Chichester, UK: John Wiley & Sons, Ltd, 2012.
- [197] H. Wong and H. Iwai, 'On the scaling issues and high- κ replacement of ultrathin gate dielectrics for nanoscale MOS transistors', *Microelectron. Eng.*, vol. 83, no. 10, pp. 1867–1904, Oct. 2006.
- [198] J. Robertson, 'Band offsets of wide-band-gap oxides and implications for future electronic devices', *J. Vac. Sci. Technol. B Microelectron. Nanom. Struct.*, vol. 18, no. 3, p. 1785, May 2000.
- [199] P. W. Peacock and J. Robertson, 'Band offsets and Schottky barrier heights of high dielectric constant oxides', *J. Appl. Phys.*, vol. 92, no. 8, pp. 4712–4721, 2002.
- [200] J. Robertson, 'High k Dielectrics for Future CMOS Devices', in *ECS Transactions*, 2009, vol. 19, no. 2, pp. 579–591.
- [201] J. Robertson, 'Electronic Structure and Band Offsets of High-Dielectric-Constant Gate Oxides', *MRS Bull.*, vol. 27, no. 03, pp. 217–221, Mar. 2002.
- [202] G. He and Z. Sun, Eds., *High-k Gate Dielectrics for CMOS Technology*. Weinheim, Germany: Wiley-VCH Verlag GmbH & Co. KGaA, 2012.

- [203] P. N. Plassmeyer, K. Archila, J. F. Wager, and C. J. Page, 'Lanthanum Aluminum Oxide Thin-Film Dielectrics from Aqueous Solution', *ACS Appl. Mater. Interfaces*, vol. 7, no. 3, pp. 1678–1684, Jan. 2015.
- [204] M. Sobhani, H. R. Rezaie, and R. Naghizadeh, 'Sol-gel synthesis of aluminum titanate (Al_2TiO_5) nano-particles', *J. Mater. Process. Technol.*, vol. 206, no. 1–3, pp. 282–285, Sep. 2008.
- [205] L. Shi, Y. D. Xia, B. Xu, J. Yin, and Z. G. Liu, 'Thermal stability and electrical properties of titanium-aluminum oxide ultrathin films as high-k gate dielectric materials', *J. Appl. Phys.*, vol. 101, no. 3, p. 034102, Feb. 2007.
- [206] P. De Rouffignac and R. G. Gordon, 'Atomic layer deposition of praseodymium aluminum oxide for electrical applications', *Chem. Vap. Depos.*, vol. 12, no. 2–3, pp. 152–157, 2006.
- [207] A. N. Meza-Rocha, E. Zaleta-Alejandre, R. Balderas, Z. Rivera, M. L. Perez-Arrieta, and C. Falcony, 'Structural, Optical and Electrical Properties of Thin Films of Lanthanum Aluminum Oxide Synthesized by Spray Pyrolysis', in *ECS Transactions*, 2011, vol. 41, no. 3, pp. 183–191.
- [208] O. Rico-Fuentes, J. C. Alonso, G. Santana, and A. Ortiz, 'Ultrasonic Spray Pyrolysis Deposition and Characterization of Tantalum-Aluminum Oxide Thin Films', *J. Electrochem. Soc.*, vol. 154, no. 12, p. G277, 2007.
- [209] S. T. Meyers, J. T. Anderson, D. Hong, C. M. Hung, J. F. Wager, and D. A. Keszler, 'Solution-Processed Aluminum Oxide Phosphate Thin-Film Dielectrics', *Chem. Mater.*, vol. 19, no. 16, pp. 4023–4029, Aug. 2007.
- [210] G. Adamopoulos, S. Thomas, D. D. C. Bradley, M. a. McLachlan, and T. D. Anthopoulos, 'Low-voltage ZnO thin-film transistors based on Y_2O_3 and Al_2O_3 high-k dielectrics deposited by spray pyrolysis in air', *Appl. Phys. Lett.*, vol. 123503, no. 12, pp. 1–4, Mar. 2011.
- [211] D. X. Xia and J. B. Xu, 'High mobility and low operating voltage ZnGaO and ZnGaLiO transistors with spin-coated Al_2O_3 as gate dielectric', *J. Phys. D. Appl. Phys.*, vol. 43, no. 44, p. 442001, Nov. 2010.
- [212] R. Branquinho, D. Sagueiro, L. Santos, P. Barquinha, L. Pereira, R. Martins, and E. Fortunato, 'Aqueous Combustion Synthesis of Aluminum Oxide Thin Films and Application as Gate Dielectric in GZTO Solution-Based TFTs', *ACS Appl. Mater. Interfaces*, vol. 6, no. 22, pp. 19592–19599, Nov. 2014.
- [213] E. J. Bae, Y. H. Kang, M. Han, C. Lee, and S. Y. Cho, 'Soluble oxide gate dielectrics prepared using the self-combustion reaction for high-performance thin-film transistors', *J. Mater. Chem. C*, vol. 2, no. 28, p. 5695, Jun. 2014.
- [214] W. Xu, H. Wang, L. Ye, and J. Xu, 'The role of solution-processed high-k gate dielectrics in electrical performance of oxide thin-film transistors', *J. Mater. Chem. C*, vol. 2, no. 27, p. 5389, 2014.

- [215] Y. S. Rim, H. Chen, Y. Liu, S.-H. Bae, H. J. Kim, and Y. Yang, 'Direct Light Pattern Integration of Low-Temperature Solution-Processed All-Oxide Flexible Electronics', *ACS Nano*, vol. 8, no. 9, pp. 9680–9686, Sep. 2014.
- [216] H. Park, Y. Nam, J. Jin, and B.-S. Bae, 'Space charge-induced unusually-high mobility of a solution-processed indium oxide thin film transistor with an ethylene glycol incorporated aluminum oxide gate dielectric', *RSC Adv.*, vol. 5, no. 124, pp. 102362–102366, 2015.
- [217] A. Liu, G. Liu, H. Zhu, B. Shin, E. Fortunato, R. Martins, and F. Shan, 'Eco-friendly water-induced aluminum oxide dielectrics and their application in a hybrid metal oxide/polymer TFT', *RSC Adv.*, vol. 5, no. 105, pp. 86606–86613, 2015.
- [218] H. Tan, G. Liu, A. Liu, B. Shin, and F. Shan, 'The annealing effects on the properties of solution-processed alumina thin film and its application in TFTs', *Ceram. Int.*, vol. 41, no. S1, pp. S349–S355, Jul. 2015.
- [219] W. Xu, H. Wang, F. Xie, J. Chen, H. Cao, and J.-B. Xu, 'Facile and Environmentally Friendly Solution-Processed Aluminum Oxide Dielectric for Low-Temperature, High-Performance Oxide Thin-Film Transistors', *ACS Appl. Mater. Interfaces*, vol. 7, no. 10, pp. 5803–5810, Mar. 2015.
- [220] A. Liu, G. Liu, H. Zhu, B. Shin, E. Fortunato, R. Martins, and F. Shan, 'Hole mobility modulation of solution-processed nickel oxide thin-film transistor based on high-*k* dielectric', *Appl. Phys. Lett.*, vol. 108, no. 23, p. 233506, Jun. 2016.
- [221] A. Liu, G. Liu, H. Zhu, B. Shin, E. Fortunato, R. Martins, and F. Shan, 'Eco-friendly, solution-processed In-W-O thin films and their applications in low-voltage, high-performance transistors', *J. Mater. Chem. C*, vol. 4, no. 20, pp. 4478–4484, 2016.
- [222] B. Wang, X. Yu, P. Guo, W. Huang, L. Zeng, N. Zhou, L. Chi, M. J. Bedzyk, R. P. H. Chang, T. J. Marks, and A. Facchetti, 'Solution-Processed All-Oxide Transparent High-Performance Transistors Fabricated by Spray-Combustion Synthesis', *Adv. Electron. Mater.*, vol. 2, no. 4, p. 1500427, Apr. 2016.
- [223] W. Xu, M. Long, T. Zhang, L. Liang, H. Cao, D. Zhu, and J. Bin Xu, 'Fully solution-processed metal oxide thin-film transistors via a low-temperature aqueous route', *Ceram. Int.*, vol. 43, no. 8, pp. 6130–6137, Jun. 2017.
- [224] K. Yim, Y. Yong, J. Lee, K. Lee, H.-H. Nahm, J. Yoo, C. Lee, C. Seong Hwang, and S. Han, 'Novel high-*k* dielectrics for next-generation electronic devices screened by automated ab initio calculations', *NPG Asia Mater.*, vol. 7, no. 6, pp. e190–e190, Jun. 2015.
- [225] O. Auciello, W. Fan, B. Kabius, S. Saha, J. A. Carlisle, R. P. H. Chang, C. Lopez, E. A. Irene, and R. A. Baragiola, 'Hybrid titanium-aluminum oxide layer as alternative high-*k* gate dielectric for the next generation of complementary metal-oxide-semiconductor devices', *Appl. Phys. Lett.*, vol. 86, no. 4, p. 042904, Jan. 2005.

- [226] L. Zhu, Y. Gao, X. Li, X. W. Sun, and J. Zhang, 'Development of high- k hafnium-aluminum oxide dielectric films using sol-gel process', *J. Mater. Res.*, vol. 29, no. 15, pp. 1620–1625, Aug. 2014.
- [227] W. Yang, K. Song, Y. Jung, S. Jeong, and J. Moon, 'Solution-deposited Zr-doped AlO_x gate dielectrics enabling high-performance flexible transparent thin film transistors', *J. Mater. Chem. C*, vol. 1, no. 27, p. 4275, 2013.
- [228] J.-W. Jo, J. Kim, K.-T. Kim, J.-G. Kang, M.-G. Kim, K.-H. Kim, H. Ko, Y.-H. Kim, and S. K. Park, 'Highly Stable and Imperceptible Electronics Utilizing Photoactivated Heterogeneous Sol-Gel Metal-Oxide Dielectrics and Semiconductors', *Adv. Mater.*, vol. 27, no. 7, pp. 1182–1188, Feb. 2015.
- [229] K. N. Woods, E. C. Waddington, C. A. Crump, E. A. Bryan, T. S. Gleckler, M. R. Nellist, B. A. Duell, D. P. Nguyen, S. W. Boettcher, and C. J. Page, 'Tunable high- k $\text{Zr}_x\text{Al}_{1-x}\text{O}_y$ thin film dielectrics from all-inorganic aqueous precursor solutions', *RSC Adv.*, vol. 7, no. 62, pp. 39147–39152, 2017.

3. Theory and Operational Characteristics

3.1 Introduction

Electronic devices are an integral part of our everyday life. Most of the electronic devices that are in use nowadays are based on metal-insulator-metal (MIM) structures [1]. MIM structures can be found in the core of each electronic device including a whole suite of components such as capacitors, diodes, transistors (BJTs and FETs) [2]–[10]. The investigation of such structures, for applications in memories as NAND flash and Dynamic Random Access Memories (DRAMs), is of particular interest [11]–[13]. A simple metal-insulator-metal (MIM) device consists of an insulator placed between two metals acting as electrodes.

In devices like DRAMs (MIM devices), high capacitance and low leakage currents are key requirements. The capacitance of a MIM device is proportional to the dielectric constant of the insulator and inversely proportional to the thickness of the materials so, the capacitance of the MIM device is strongly affected by the physical thickness of the insulating material. On the other hand, there is a lower limit of the insulating thickness. For example, in the case of SiO_2 , for a thickness below 2nm the current passing through the insulator (leakage current), because of tunnelling effects, is becoming extremely high. To overcome such issues alternative materials with higher dielectric constants are implemented as insulators.

The insulator could be organic or inorganic. Organic materials that have been used in electronic industry as insulators (i.e. CYTOP, PMMA) are out of the scope of this thesis but can be found in literature [14], [15].

Inorganic materials that have been used in the electronic industry as insulators are mainly metal oxides and nitrides. The most widely used inorganic insulator in electronic industry for decades is silicon dioxide (SiO_2). Silicon dioxide has a wide band gap ($E_g \sim 9$ eV) and low dielectric constant ($k \sim 3.9$). SiO_2 is the native oxide of silicon (Si), the widely used semiconductor in electronics.

Silicon is one of the most abundant elements in Earth's crust. It is an intrinsic semiconductor, with a narrow band gap ($E_g \sim 1.1$ eV). The diverse dopability of silicon, that tunes its electrical properties, is one of the reasons why it is the material of choice

till nowadays in electronics industry. Depending on the dopant either from group 13 or group 15, silicon can be either p-type or n-type semiconductor.

Silicon and its native oxide, silicon dioxide or silica (SiO_2), are the basis of nowadays' electronics. The metal oxide semiconductor (MOS) structure is similar to the metal-insulator-metal (MIM) capacitor, where the insulator is a dielectric oxide and one of the metal electrodes has been replaced by a semiconductor. MOS capacitor is not an electronic device itself but is the basis of the MOS based transistor the metal-oxide-semiconductor-field-effect-transistor (MOSFET).

In this chapter, the MIM, as well as MOS and MOSFET device architectures and their operational characteristics will be briefly described.

3.2 MIM Devices

MIM structures have been extensively used to investigate the dielectric properties of thin films. In Figure 3-1, the basic metal-insulator-metal (MIM) structure is presented.

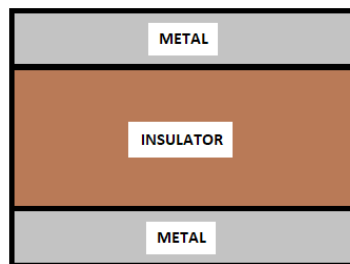


Figure 3-1: Metal-insulator-metal (MIM) structure used to assess the properties of the insulator.

A basic MIM device structure is a parallel plate capacitor. A parallel plate capacitor consists of two metal plates separated by an insulator. A capacitor is characterized by its capacitance which is the ability to store an electric charge. For a parallel plate capacitor consisting of two parallel metal plates of area A separated by a distance d (thickness of dielectric material) the capacitance C in Farads is:

$$C = k\epsilon_0 \frac{A}{d} \quad (3-1)$$

where, k the dielectric constant of the insulator and ϵ_0 the vacuum permittivity (8.85×10^{12} F/m). The dielectric constant of a material is directly related to its electric susceptibility (χ_e), which is a measure of polarizability of the dielectric in response to an external electric field.

$$\chi_e = k - 1 \quad (3-2)$$

Susceptibility is a frequency-dependent electrical parameter. Because of the frequency dependency of the susceptibility, the dielectric constant is frequency-dependent as well.

The typical equivalent circuit that is used to analyse MIM capacitor characteristics and its frequency response, is presented in Figure 3-2.

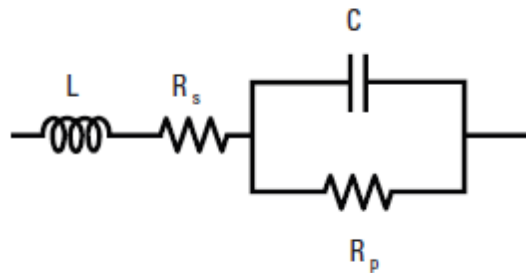


Figure 3-2: Equivalent circuit of a MIM capacitor.

In Figure 3-2, R_s and L represent the resistance and the inductance because of the wires and the metal electrodes, while R_p represents the dielectric loss of the dielectric material.

The most important parameter of a MIM capacitor is the dielectric constant of the material sandwiched between the metal plates.

3.2.1 Impedance Characteristics

One of the most important parameters used to investigate the properties of a dielectric is its impedance (\mathbf{Z}). It is defined as the total opposition to the flow of an alternating current (AC) at a given frequency and is represented by a complex quantity which is graphically shown on a vector plane, as shown in Figure 3-3.

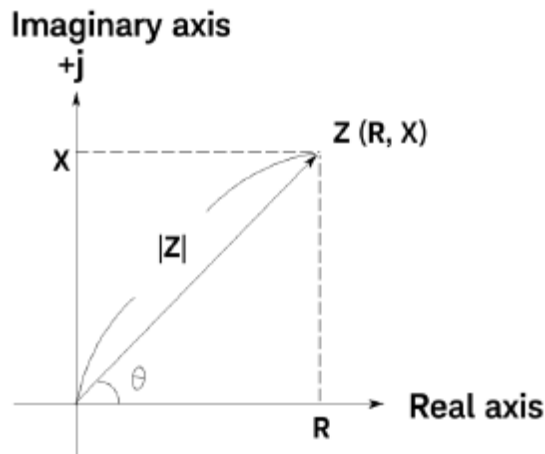


Figure 3-3: Impedance vector plane representation³.

An impedance vector consists of a real part (resistance, \mathbf{R}) and an imaginary part (reactance, \mathbf{X}). Impedance can be expressed (in polar coordinates) as:

$$Z = R + jX \quad (3-3)$$

where j is the imaginary unit. Resistance and reactance can be expressed as:

$$\begin{cases} R = |Z| \cos \theta \\ X = |Z| \sin \theta \end{cases} \quad (3-4)$$

where

$$|Z| = \sqrt{R^2 + X^2} \text{ and } \theta = \tan^{-1} \left(\frac{X}{R} \right) \quad (3-5)$$

³ Keysight Handbook

where (θ) is the phase angle. Reactance (\mathbf{X}) could be either inductive (\mathbf{X}_L) or capacitive (\mathbf{X}_C). For an electrical circuit where a resistor (\mathbf{R}), a capacitor (\mathbf{C}) and an inductor (\mathbf{L}) are connected in series, the total impedance is:

$$Z = R + jX \xleftrightarrow{X=X_L-X_C} Z = R + j(X_L - X_C) \Leftrightarrow Z = R + j\left(2\pi fL - \frac{1}{2\pi fC}\right) \Leftrightarrow \boxed{Z = R + j\left(\omega L - \frac{1}{\omega C}\right)} \quad (3-6)$$

where f is the frequency and ω the angular frequency. Equally, the admittance which is the reciprocal of impedance is:

$$Y = \frac{1}{Z} \Leftrightarrow Y = \frac{1}{R + jX} \Leftrightarrow Y = \frac{RX^2}{R^2 + X^2} + j\frac{R^2X}{R^2 + X^2} \Leftrightarrow \boxed{Y = G + jB} \quad (3-7)$$

where \mathbf{Y} is the admittance, \mathbf{G} the conductance and \mathbf{B} the susceptance.

For a parallel plate capacitor, the total impedance solely consists of the X_C component. The total impedance of an ideal MIM device can be written as:

$$Z = X_C \Leftrightarrow \boxed{Z_{MIMideal} = -\frac{1}{\omega C}} \quad (3-8)$$

A metric of the capacitor's quality is the quality factor (\mathbf{Q}), which is defined as the ratio of the energy stored in a component to the energy dissipated by the component. Quality factor (\mathbf{Q}) is dimensionless and is given by:

$$Q = \frac{Z_{Im}}{Z_{Real}} = \frac{X}{R} \quad (3-9)$$

Usually, dissipation factor (\mathbf{D}) is used instead. Dissipation factor (\mathbf{D}) is the reciprocal of the quality factor (\mathbf{Q}), $D = 1/Q$.

A typical capacitor frequency response, in terms of the impedance (\mathbf{Z}) and impedance's phase angle (θ) is shown in Figure 3-4. At the low frequencies the system is mostly resistive. The phase angle (θ) of impedance is $\sim 0^\circ$, which is characteristic for pure resistive systems. At such low frequencies, the capacitor acts as an open part of the circuit, so the current pass across the resistance (\mathbf{R}_p). The value of the parallel resistance (\mathbf{R}_p) can be estimated from the intercept of the graph with the axis of impedance magnitude. For the frequency range where the phase angle (θ) of impedance is $\sim -90^\circ$, the impedance of the system is capacitive. For this frequency range, from the slope of the impedance magnitude graph, the capacitance (\mathbf{C}) of the capacitor can be estimated by using the expression:

$$\text{slope} = \frac{1}{\omega C} \quad (3-10)$$

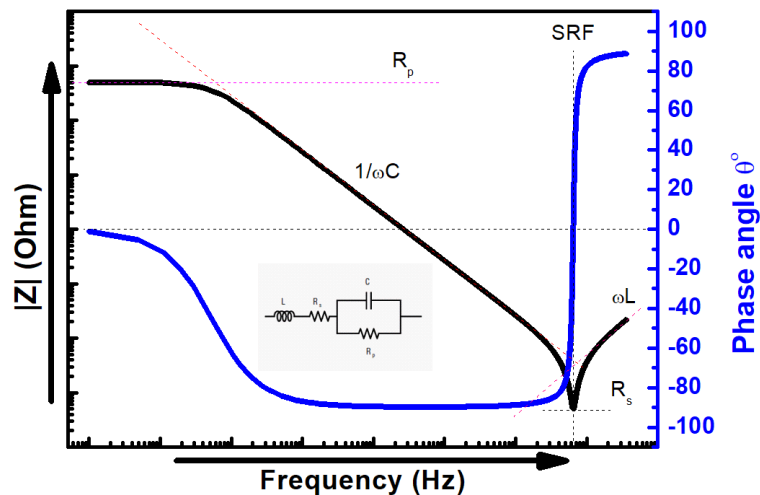


Figure 3-4: Frequency response of the equivalent circuit (inset) used to describe impedance characteristics of a MIM device.

In Figure 3-5 the frequency dependence of the real and imaginary part of the complex dielectric constant are shown. The complex dielectric constant can be written as:

$$\epsilon_r = \epsilon_r' + j\epsilon_r'' \quad (3-11)$$

where, ϵ_r' is the real part and ϵ_r'' is the imaginary part. Both parts are frequency dependent. The real part represents the relative permittivity while the imaginary part represents energy loss in the dielectric. The dissipation factor (D) or loss tangent is defined using the magnitudes of real and imaginary parts of dielectric constant as:

$$\tan \delta = \frac{\epsilon_r''}{\epsilon_r'} \quad (3-12)$$

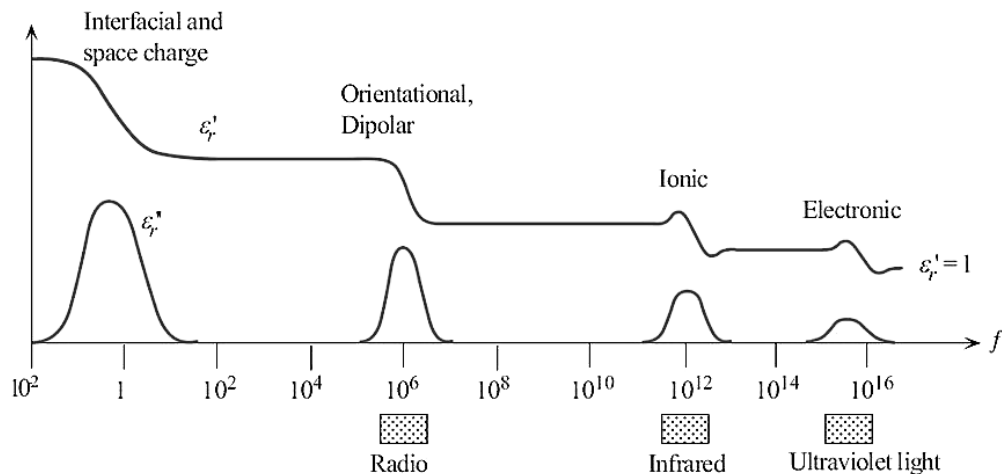


Figure 3-5: Frequency dependence of the real and imaginary parts of the dielectric constant, reproduced from⁴.

Since a dielectric is a material that it could be polarised under the stimulus of an external electric field, the dielectric behaviour is specified with respect to the time of frequency domain. As can be seen from Figure 3-5, at low frequencies (<100 Hz), the dielectric relaxation (peak in ϵ_r'') is due to charges at interfaces or space charges that may become oriented as result of the stimulus of an external field, contributing to the polarisation. At higher frequencies (10^4 - 10^8 Hz), orientation polarisation due to natural dipoles of a dielectric, is taking place. At even higher frequencies ($>10^{10}$ Hz), ionic and electronic polarisation occurs. For ionic crystals mutual displacement of positive and negative sub-lattice happens. Further increase in frequency leads to displacement of electron shell against positive nucleus.

⁴ Principles of Electronic Materials and Devices, p. 608

3.2.2 Leakage Current and Conduction Mechanisms

One of the key features of insulating materials is their electrical properties i.e. the conduction mechanisms (leakage current mechanisms) and dielectric strength. Leakage current is of crucial concern in memory devices such as DRAMs. Since oxide dielectrics are of particular interest in electronic industry, the conduction mechanism of such films is particularly important in order for the conduction current via such insulating films be minimized.

In thin films there are two kinds of conduction mechanisms; i) the electrode-limited conduction (*ELCM*) which depends on the electrical properties of the electrode-dielectric interface and ii) bulk-limited conduction mechanism (*BLCM*) which depends on the electrical properties of the oxide itself [16]. Figure 3-6 summarizes the conduction mechanisms in thin films.

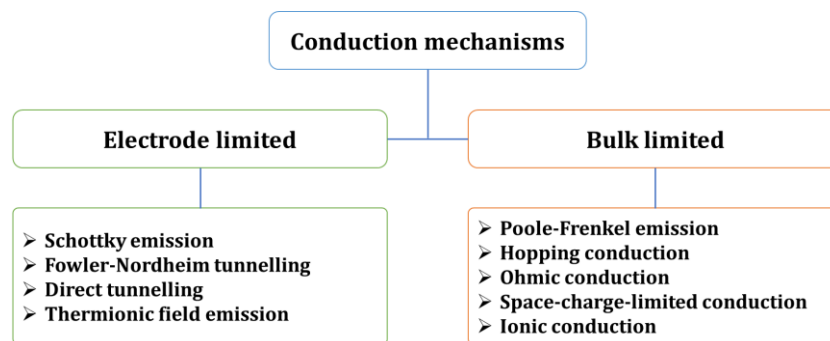


Figure 3-6: Classification of conduction mechanisms in dielectric films reproduced from [16]

From the analysis of the plots that describe each conduction mechanism, important information such as the barrier height at the electrode-dielectric interface, the effective mass of the charge carriers in dielectric films, the trap level, the trap spacing, the trap density, the carrier drift mobility and the dielectric relaxation time could be obtained [16].

Electrode-limited conduction depends on the electrical properties of the electrode-dielectric interface. Based on this type of conduction mechanism, the physical properties of the barrier height of the electrode-dielectric interface and the effective mass of the conduction carriers in dielectric films can be extracted.

Electrode-limited conduction mechanisms include (1) Schottky or thermionic emission [17]–[19], (2) Fowler-Nordheim tunneling [20], [21], (3) direct tunneling [22], and (4) thermionic-field emission [23], [24].

The bulk-limited conduction mechanism depends on the electrical properties of the dielectric itself. According to the analyses of bulk-limited conduction mechanisms, several important physical parameters of the dielectric films can be obtained, including the trap energy level, the trap spacing, the trap density, the carrier drift mobility, the dielectric relaxation time, and the density of states in the conduction band.

The bulk-limited conduction mechanisms include (1) Poole-Frenkel emission [25], [26], (2) hopping conduction [27], (3) ohmic conduction, and (4) space charge-limited conduction.

Among the various conduction mechanisms that describe conduction in insulating materials, Poole-Frenkel emission (PF) and Fowler-Nordheim tunneling (FN) along with Schottky or thermionic emission (SE) are the dominant ones of a thin insulating film, while for an ultrathin film (<3nm) direct tunneling dominates [28]. For highly defective films trap-assisted conduction, hopping, and space charge limited conduction have been reported.

3.2.2.1 Schottky emission (SE)

Schottky or thermionic emission is due to the thermal activation of electrons. The energy-band diagram of an ideal MIM structure is shown in Figure 3-7.

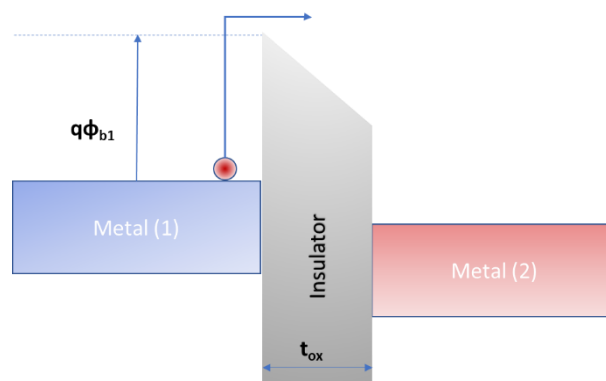


Figure 3-7: Schematic energy-band diagram of Schottky emission in a MIM structure.

In Figure 3-7, the quantity $(q\cdot\phi_{b1})$ is the so called Schottky energy barrier height. For Schottky conduction, charges have sufficient thermal energy to overcome the potential energy barrier at the metal-dielectric interface and be diffused to the dielectric. Schottky emission has been considered the predominant conduction mechanism in dielectric films at relatively high temperatures [16], [18], [29]–[33]. The expression of standard Schottky emission is:

$$J_{SE} = A^*T^2 \exp \left[\frac{-q \left(\phi_b - \sqrt{\frac{qE}{4\pi\epsilon_r\epsilon_0}} \right)}{k_B T} \right] \quad (3-13)$$

where,

$$A^* = \frac{4\pi q k_B^2 m_{in}^*}{h^3} = 120 \frac{m_{in}^*}{m_0}$$

(J_{SE}) is the current density, (A^*) is the effective Richardson constant, (T) the temperature, (q) is the electronic charge, $(q\phi_b)$ is the Schottky barrier height, (E) is the applied electric field, (ϵ_r) is the dielectric constant of the material, (ϵ_0) is the permittivity of the free space, (k_B) is Boltzmann's constant, (h) is Planck's constant, (m_0) is the free electron mass and (m_{in}^*) is the electron effective mass in the insulator/dielectric.

The thickness of the insulator is crucial for the Schottky emission. Simmons modified the standard Schottky emission expression considering the dielectric thickness [34]. When the electronic mean free-path is less than the dielectric thickness the standard Schottky emission expression should be rewritten as:

$$J_{modSE} = aT^{3/2} E \mu \left(\frac{m_{in}^*}{m_0} \right)^{3/2} \exp \left[\frac{-q \left(\phi_b - \sqrt{\frac{qE}{4\pi\epsilon_r\epsilon_0}} \right)}{k_B T} \right] \quad (3-14)$$

where $\alpha=3\times 10^{-4} \text{ A}\cdot\text{s}\cdot\text{cm}^{-3}\cdot\text{K}^{-3/2}$ and (μ) is the electronic mobility in the insulator. The other notations have the above defined meanings.

3.2.2.2 Fowler-Nordheim tunneling (FN)

Besides the thermal-induced current due to thermionic emission, cold-electron current has been observed [20], [21], [29], [35], [36]. This conduction mechanism is due to the penetration of the potential barrier by the electron wave function. This potential barrier penetration is due to the tunnelling effect and is called Fowler-Nordheim tunnelling (FN). Figure 3-8 shows the principle of the FN tunnelling.

FN tunnelling is the predominant electrode limited conduction mechanism when the temperature of the system is very low, the applied electrical field is high, and dielectric film is relatively thick ($t_{\text{ox}}>4\text{nm}$). Taking into account the above considerations, an electron could penetrate the triangular potential barrier and be free to move in the conduction band of the dielectric.

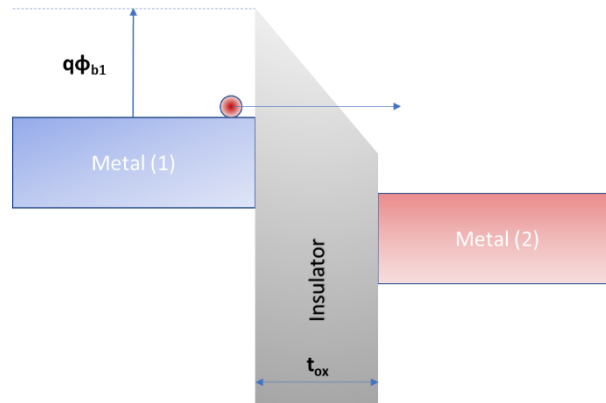


Figure 3-8: Schematic energy-band diagram of Fowler-Nordheim tunnelling in a MIM structure.

The equation of the Fowler-Nordheim tunneling is:

$$J_{FN} = \frac{q^3 E^2}{8\pi h q \phi_{b1}} \exp \left[\frac{-8\pi \sqrt{2q m_T^*}}{3hE} \phi_{b1}^{3/2} \right] \quad (3-15)$$

where, m_T^* is the tunnelling effective mass in the dielectric while the other symbols have their usual meanings.

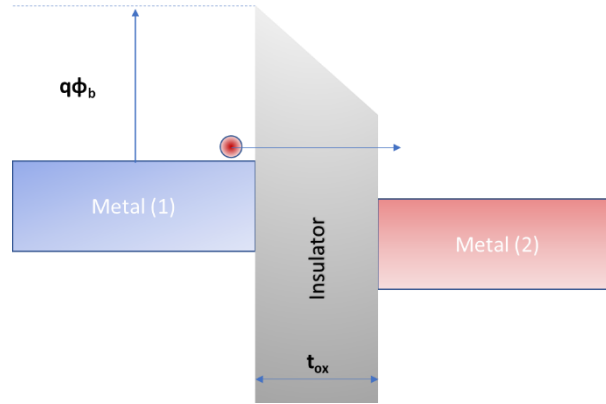


Figure 3-9: Schematic energy-band diagram of direct tunnelling in MIM structure.

For very thin insulators ($t_{ox} < 4\text{nm}$) the electrons could penetrate a trapezoidal potential barrier. In this case (Figure 3-9) the conduction is due to direct tunnelling (DT) of the electrons through the trapezoidal potential barrier. An approximate equation describing the current density due to the direct tunnelling (DT) of the electrons is [37]:

$$\begin{aligned}
 J_{DT} &\sim \exp \left[-\frac{8\pi(q\phi_b)^{3/2} \sqrt{2m_T^*} [3|V|]}{3hq|E| [2\phi_b]} \right] \\
 &\sim \exp \left[-\frac{8\pi\sqrt{2q}}{3h} (m_T^* \phi_b)^{1/2} \cdot k \cdot t_{ox,eq} \right] \quad (3-16)
 \end{aligned}$$

According to Yeo et al. tunnelling leakage current depends on the dielectric constant (k) of the material, the tunnelling barrier height (ϕ_b) and the tunnelling effective mass (m_T^*) [37].

3.2.2.3 Poole-Frenkel emission (PF)

Poole-Frenkel emission is a bulk limited conduction mechanism. Sometimes, it is called internal Schottky emission due to the thermal activation character of the

process. In Figure 3-10, the principle of the Poole-Frenkel (PF) conduction mechanism is shown. Trapped electrons could be released to conduction band of the dielectric, by applying an electric field. The applied electric field reduces the potential barrier height energy, so if the electron obtains enough thermal energy it will be released out of the trap to the dielectric's conduction band.

The current density due to the Poole-Frenkel (PF) emission conduction mechanism is given by:

$$J_{PF} = q\mu N_c \cdot E \cdot \exp \left[\frac{-q \left(\phi_b - \sqrt{\frac{qE}{\pi\epsilon_r\epsilon_0}} \right)}{k_B T} \right] \quad (3-17)$$

where, (μ) is the electronic drift mobility, (N_c) is the density of the states in the conduction band, ($q\phi_b$) the trap energy barrier level.

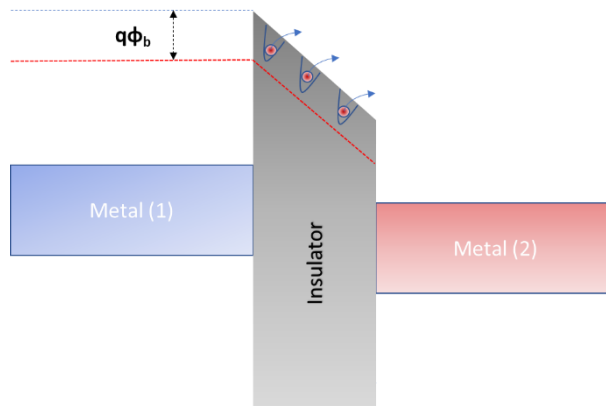


Figure 3-10: Schematic energy-band diagram of Poole-Frenkel (PF) emission in MIM structure.

To that point, it should be highlighted that the conduction in thin dielectric films is strongly related to the structural characteristics of the MIM device. The structural characteristics include, among others, the composition of the dielectric material, the thickness of the dielectric, the traps, the energy level of the traps, the materials that are used as electrodes and their work function.

Finally, it has been shown that for a given gate dielectric one or two conduction mechanisms are governing the current transport [28], [29], [32], [38]. In fact, the

different conduction mechanisms are appearing for different conditions. In general, Schottky emission (SE) and Poole-Frenkel (PF) conduction are two mechanisms that are mainly temperature-dependent, and they take place at relatively low electric fields. On the other hand, Fowler-Norheim (FN) tunnelling takes place at low temperatures and high electric fields.

3.3 Metal Oxide Semiconductor (MOS)

Metal oxide semiconductor (MOS) capacitor is one of the key parts of complementary metal-oxide-semiconductor (CMOS) technology which is the base of nowadays' electronics. The performance of the most widely used semiconductor device, metal-oxide-semiconductor field effect transistor (MOSFET), strongly depends on the performance of the MOS capacitor which is the core element of the MOSFET. A MOSFET is a MOS capacitor with two metal-semiconductor junctions at two ends. In Figure 3-11, a typical MOSFET structure is presented along with its core component, the MOS capacitor.

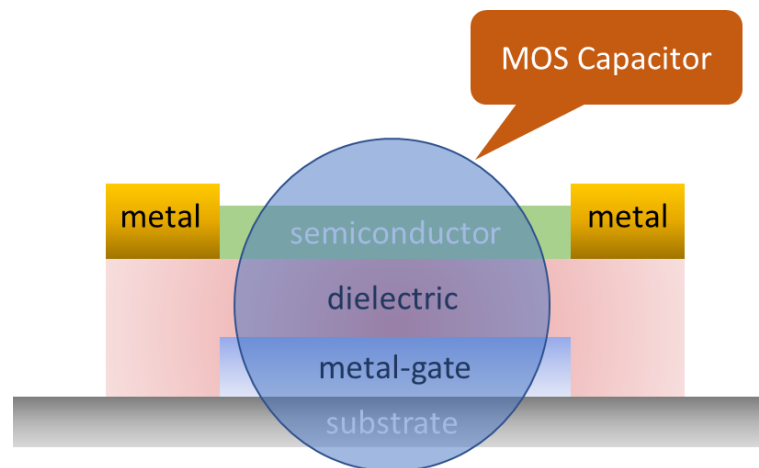


Figure 3-11: Typical metal-oxide-semiconductor field effect transistor (MOSFET) structure.

The operation characteristics of a MOS capacitor are studied by using the energy-band diagrams. The energy-band diagram of an ideal MOS capacitor is shown in Figure 3-12. A MOS capacitor is defined as ideal under the following considerations:

- Charges can exist only in the semiconductor layer and there are no interface traps nor any kind of oxide charge
- There is no conduction through the insulator under any biasing conditions.
- The quantity $\phi_{ms} = \phi_m - (\chi + \phi_n) = 0$ under no applied voltage. (Flat-band condition at $V_{app}=0$)

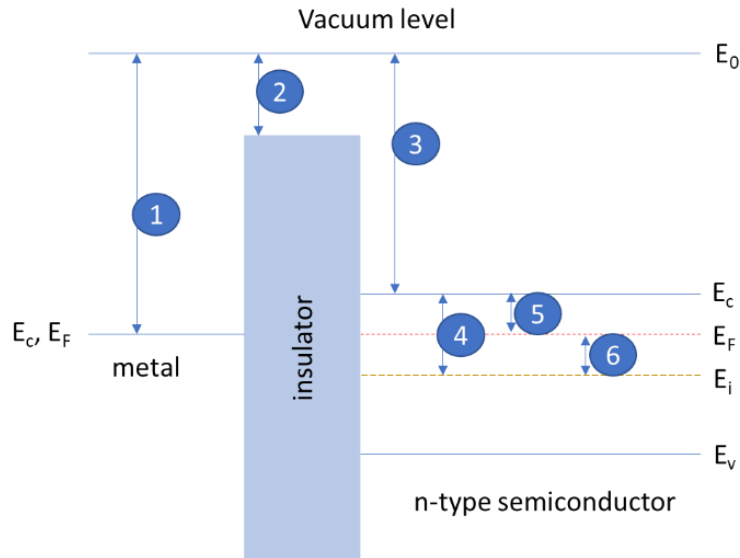


Figure 3-12: Energy band diagram for ideal MOS capacitor employing n-type semiconductor at equilibrium ($V_{app}=0$). (1) $q\phi_m$: ϕ_m is the metal work function, (2) $q\chi_i$: χ_i is the electron affinity of the insulator, (3) $q\chi$: χ is the electron affinity of the semiconductor, (4) $E_g/2$: E_g is the band gap of the semiconductor, (5) $q\phi_n$: ϕ_n is the Fermi potential with respect to conduction band edge, (6) $q\psi_{Bn}$: ψ_{Bn} is the Fermi potential with respect to midgap edge.

Considering the ideal MOS capacitor described in Figure 3-12, by applying positive or negative voltages, there are basically three conditions that can exist at the semiconductor-insulator interface, the accumulation, the depletion and the inversion conditions.

3.3.1 Accumulation

When a positive voltage ($V_{app}=V_g>0$) is applied to the metal contact of the MOS capacitor, the semiconductor's conduction-band edge (E_{cs}) bends downward near the semiconductor-insulator interface and is closer to the Fermi level (E_F). Because E_{cs} is now close to E_F at the interface, the interfacial electron concentration is larger than

the bulk electron concentration. So, there is an accumulation layer of electrons, giving a rise to an accumulation charge (Q_{acc}) at the semiconductor-insulator interface (surface accumulation).

In Figure 3-13, the schematic energy-band diagram for the surface accumulation condition of a MOS capacitor employing n-type semiconductor is shown.

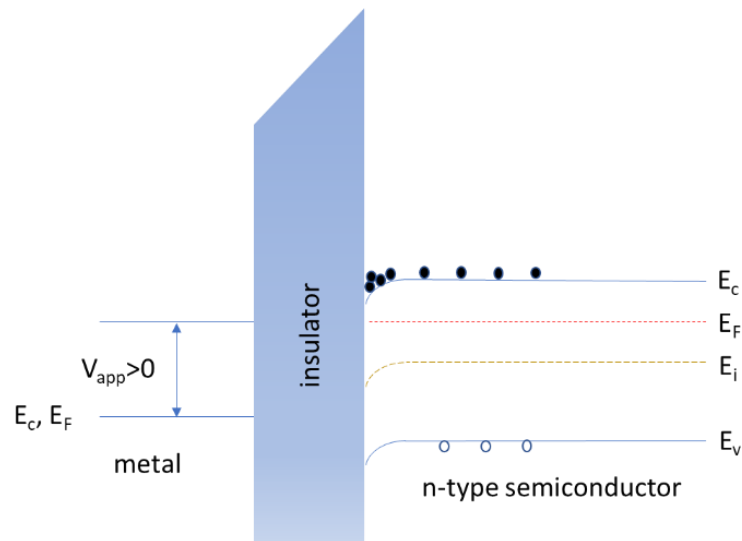


Figure 3-13: Schematic energy-band diagram MOS capacitor employing n-type semiconductor under positive voltage bias ($V_{app} > 0$).

3.3.2 Depletion

When a small negative voltage ($V_{app} = V_g < 0$) is applied to the metal contact of the MOS capacitor, the semiconductor's bands bend upward near the semiconductor-insulator interface. In this case the interfacial concentration of electrons is reduced because of the depletion of the electrons (surface depletion).

In Figure 3-14, the schematic energy-band diagram for the surface accumulation condition of a MOS capacitor employing n-type semiconductor is illustrated.

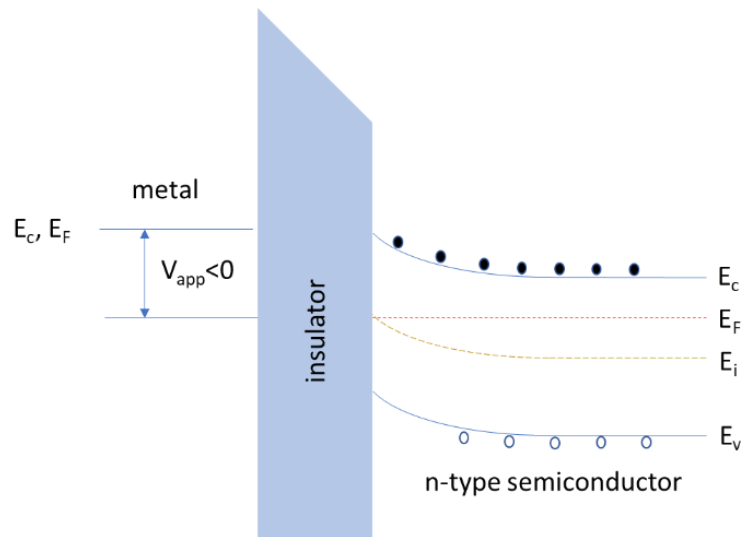


Figure 3-14: Schematic energy-band diagram MOS capacitor employing n-type semiconductor under small negative voltage bias ($V_{app} < 0$).

3.3.3 Inversion

When a higher negative voltage ($V_{app} = V_g \ll 0$) is applied to the contact of the MOS capacitor, the semiconductor's bands bend even more upward near the semiconductor-insulator interface. When the intrinsic level ($E_i = E_g/2$) at the interface crosses over the Fermi level (E_F), the concentration of the minority carriers (holes) is larger than that of electrons. In this case, the interfacial concentration of carriers is inverted from majority to minority. This condition is called inversion.

The characteristic applied voltage at which,

$$(E_F - E_V)_{interface} = (E_C - E_F)_{bulk} \quad (3-18)$$

is called **threshold voltage (V_t)**.

In Figure 3-15, the schematic of the energy-band diagram for the surface accumulation condition of a MOS capacitor employing n-type semiconductor is presented.

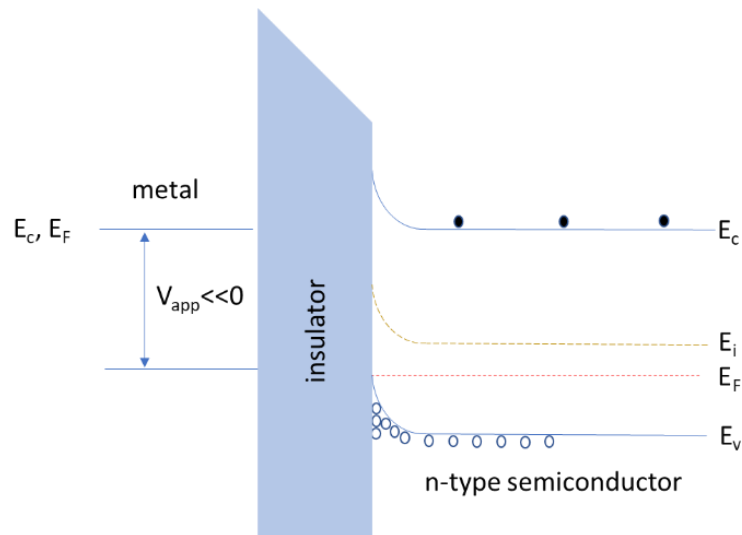


Figure 3-15: Schematic energy-band diagram MOS capacitor employing n-type semiconductor under high negative voltage bias ($V_g=V_{app}\ll 0$).

3.4 Metal Oxide Semiconductor Field Effect Transistors (MOSFETs)

One of the most interesting physical mechanisms of a great importance to semiconductor devices is the field effect. The field effect is the modulation of the conductivity of an underlying semiconductor layer by the application of an electric field to a gate electrode on the surface [39].

The metal-oxide-semiconductor field-effect transistors (MOSFETs) became the most-important device for forefront high-density integrated circuits (ICs) of microprocessors and semiconductor memories. MOSFET is the main member of the family of field-effect transistors. A family tree of field-effect transistors is shown in Figure 3-16. The three first-level main members are IGFET (insulated-gate FET), JFET (junction FET), and MESFET (metal-semiconductor FET). They are distinguished by the way the gate capacitor is formed. In an IGFET, the gate capacitor is an insulator. In a JFET or a MESFET, the capacitor is formed by the depletion layer of a p-n junction or a Schottky barrier, respectively. In the branch of IGFET, we further divide it into MOSFET/MISFET (metal-insulator-semiconductor FET) and HFET (hetero-junction FET). In the MOSFET, specifically, the insulator is a grown oxide layer, whereas in the MISFET the insulator is a deposited dielectric.

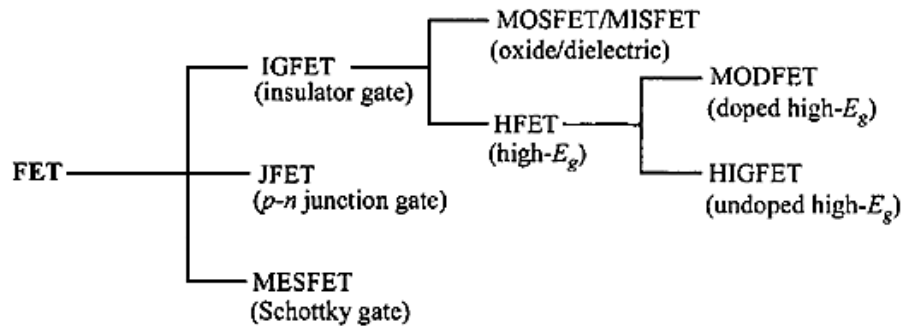


Figure 3-16: Family tree of Field-Effect Transistors (FETs). Reproduced from [10]

Thin-film transistors (TFTs) such as MOSFETs, in their most simplistic form, are constructed by three components, namely: (1) the dielectric, (2) the semiconductor layer, and (3) the source, drain and gate electrodes. The source and drain contacts are directly in contact with the semiconductor, whilst the gate contact is separated from the semiconductor layer by the dielectric layer. They can be fabricated using several different structural layouts. Figure 3-17 illustrates the four most commonly used device architectures.

The geometry of a TFT requires the definition of two geometric parameters governing its performance, namely transistor's channel length and width. The channel length (L) of a transistor is defined as the distance between the source and drain contact, whereas the channel width (W) is defined as the distance over which the source and drain contacts run parallel to each other.

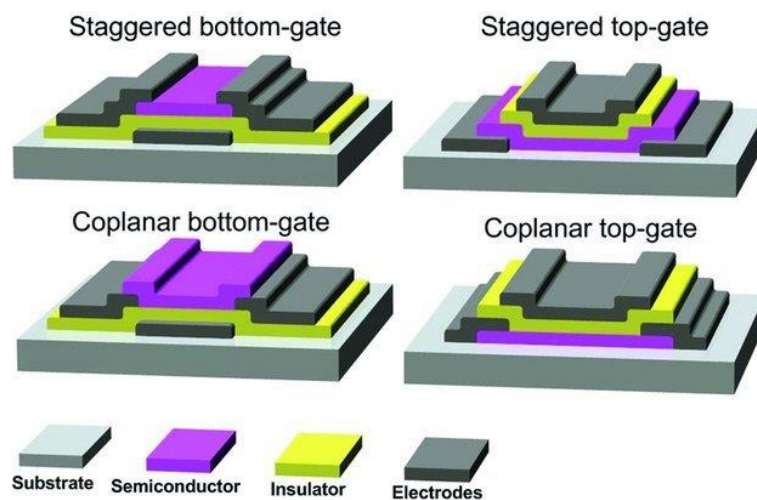


Figure 3-17: Schematics showing some of the most conventional TFT structures, according to the position of the gate electrode and the distribution of the electrodes relative to the semiconductor, reproduced from [40].

3.4.1 TFT Operating Characteristics

There are two major operating modes of the field effect transistors (TFTs). A MOSFET is called an **enhancement type** TFT if it is normally OFF. Normally OFF means that there is no current flow for zero gate-source voltage. For the case of a normally ON TFT, **depletion type** TFT, at zero gate-source voltage there is current flowing from source to drain.

Considering the structure shown in Figure 3-18 and assuming an n-type enhancement mode TFT, by grounding the source terminal ($V_S = 0$ V) and applying a positive voltage to the gate (V_G), charge carriers (electrons in this case) will start accumulating at the semiconductor/dielectric interface.

For small values of drain voltage (V_D), a channel current (I_D) through the device is observed. As V_D is increased, I_D will continue to be increased until the channel current saturates. Under these operating conditions, where the applied V_D is significantly smaller than V_G there is a linear I-V relationship and the device is operating in the linear regime (ohmic region). When the field strength parallel to the device channel, V_D , is comparable to that imposed by V_G , there is insufficient field strength across the dielectric to maintain charge accumulation at the drain end of the device, therefore the area around the drain contact is depleted of charge and the channel is said to be 'pinched off'. Under these conditions the device is operating in the saturation regime and I_D becomes V_D independent.

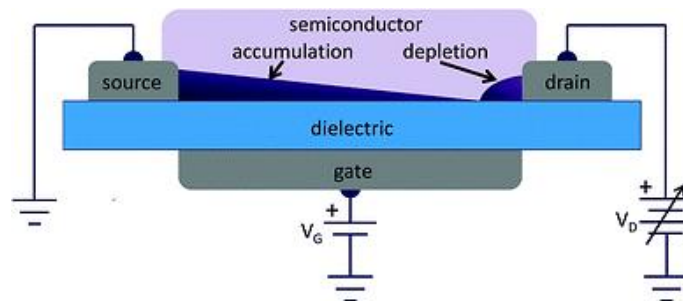


Figure 3-18: Schematic of a thin-film transistor showing the source, drain and gate contacts, dielectric layer and semiconductor with a graphic representation of the charge accumulation and depletion regions. The device is shown in the saturation regime where $V_D > V_G - V_T$, reproduced from [41]

According to gradual channel approximation [42], the current-voltage relationship at the linear region is:

$$I_D = \mu C_{ox} \frac{W}{L} (V_G - V_T) V_D \quad (3-19)$$

where W and L are the channel width and length, respectively, C_{ox} is the gate dielectric geometric capacitance, μ the charge carrier (hole or electron) mobility, V_G the external applied to gate voltage and V_T the threshold voltage. The current-voltage relationship at the saturation region is:

$$I_D = \mu C_{ox} \frac{W}{L} (V_G - V_T)^2 \quad (3-20)$$

The MOSFET characteristics that can be extracted from the output and transfer characteristics shown in Figure 3-19, are the mobility (μ), current modulation ratio or on/off ratio (I_D^{On}/I_D^{Off}), turn-on voltage (V_{On}) and subthreshold swing (SS) respectively.

3.4.1.1 Current modulation or on/off ratio

This is defined as the ratio of the maximum to the minimum drain current (I_D). The minimum I_D is due to the noise level of the measurement equipment or due to the gate leakage current (I_G), while the maximum I_D depends on the semiconductor material itself and on the effectiveness of capacitive injection by the field effect. A large current modulation ratio value (I_D^{On}/I_D^{Off}), typically above 10^6 , in TFTs, is required for their successful implementation in devices.

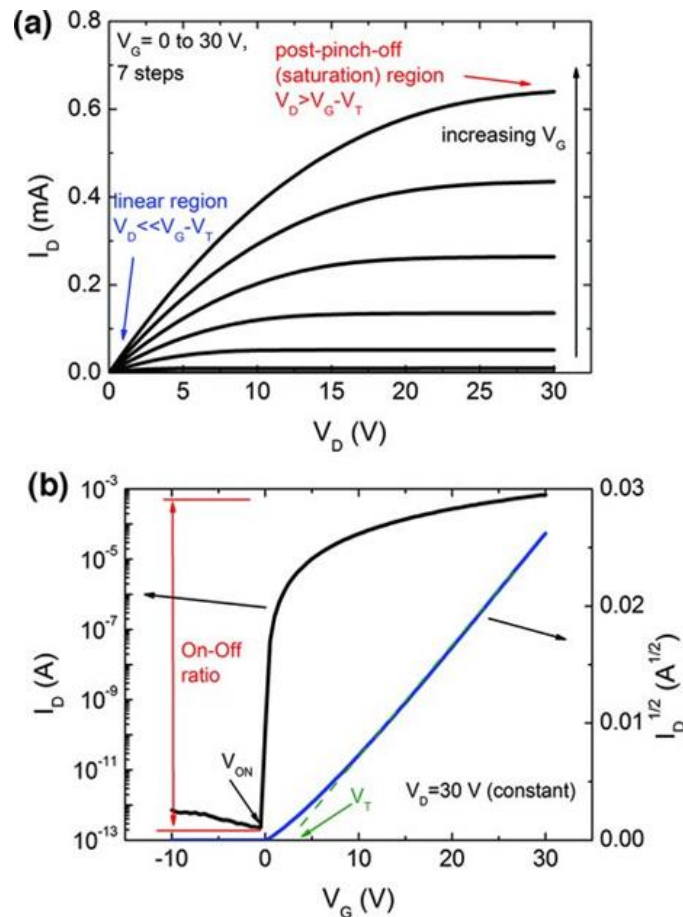


Figure 3-19: Typical a) output and b) transfer characteristics of a n-type oxide TFT, reproduced from[40]

3.4.1.2 Threshold/Turn on Voltage (V_T/V_{on})

The threshold voltage (V_T) corresponds to the applied gate voltage (V_G) for which an accumulation layer or conductive channel is formed close to the dielectric/semiconductor interface, between the source and drain electrodes (i.e. channel region) [40]. For an n-type MOSFET, depending upon whether V_T is positive or negative, the devices are designated as enhancement or depletion mode, respectively. Both types are useful for circuit fabrication, but generally, enhancement mode is preferable because no V_G is required to turn off the transistor, simplifying the circuit design and minimising power dissipation. Ortiz et al. reviewed and scrutinised existing methods based on the I_D - V_G plot for extracting V_T in single-crystal MOSFETs, biased at linear and saturation regions [43].

V_T can be determined using different methodologies, such as linear extrapolation of the I_D - V_G plot (for low V_D) or of the $I_D^{1/2}$ - V_G plot (for high V_D). The

concept of the turn-on voltage (V_{on}) is largely used in literature, corresponding to the V_G at which I_D starts to increase as seen in a $\log(I_D) - V_G$ plot, or in other words, to the V_G necessary to fully turn-off the transistor [44].

3.4.1.3 Subthreshold swing (SS)

Subthreshold swing (SS) is defined as the inverse of the maximum slope of the transfer characteristic. It indicates the necessary V_G to increase I_D by one decade and is given by [45], [46]:

$$SS = \left(\frac{d \log(I_D)}{dV_G} \Big|_{max} \right)^{-1} \quad (3-21)$$

Typically, $SS \ll 1$, (i.e., 0.10–0.30 V/dec), and small values result in higher speeds and lower power consumption. From the SS value, the trap density per unit energy at the semiconductor/dielectric interface could be calculated as:

$$N_{SS}^{max} = C_{ox} \cdot \left(\frac{SS}{2.3ek_B T} - \frac{1}{e^2} \right) \quad (3-22)$$

where C_{ox} is the geometric capacitance of the dielectric, e is the elementary charge, k_B is Boltzmann constant, and T is the temperature [47].

3.4.1.4 Mobility (μ)

Mobility (μ) is related to the efficiency of carrier transport in a material, affecting directly the maximum I_D and operating frequency of devices. In a given material, the I_D is affected by several scattering mechanisms, such as lattice vibrations, ionised impurities, grain boundaries and other structural defects. On a MOSFET, since the motion of carriers is constrained to a narrow region close to the dielectric/semiconductor interface, additional sources of scattering should be considered, such as Coulomb scattering from dielectric charges and from interface states or surface roughness scattering [48]. The mobility of a MOSFET is modulated by

V_G , so scattering mechanisms become less relevant for bias conditions. The mobility of a MOSFET can be extracted using different methodologies [40]. The widely used expression for mobility extraction from the experimentally acquired transfer characteristics (i.e. I_D - V_G plot) is given by [49]:

$$\mu_{lin} = \frac{L}{WC_{ox}} \cdot \frac{1}{V_D} \cdot \frac{\partial I_D}{\partial V_G} \quad (3-23)$$

for the linear region and

$$\mu_{sat} = \frac{L}{WC_{ox}} \cdot \frac{\partial^2 I_D}{\partial V_G^2} \quad (3-24)$$

for the saturation region.

3.5 References

- [1] R. M. Wallace and G. D. Wilk, 'High- k Dielectric Materials for Microelectronics', *Crit. Rev. Solid State Mater. Sci.*, vol. 28, no. 4, pp. 231–285, Oct. 2003.
- [2] C. H. Ng, C.-S. Ho, S.-F. S. Chu, and S.-C. Sun, 'MIM Capacitor Integration for Mixed-Signal/RF Applications', *IEEE Trans. Electron Devices*, vol. 52, no. 7, pp. 1399–1409, Jul. 2005.
- [3] Hang Hu, Chunxiang Zhu, Y. F. Lu, M. F. Li, Byung Jin Cho, and W. K. Choi, 'A high performance MIM capacitor using HfO_2 dielectrics', *IEEE Electron Device Lett.*, vol. 23, no. 9, pp. 514–516, Sep. 2002.
- [4] S.-S. Song, S.-W. Lee, J. Gil, and H. Shin, 'Simple Wide-Band Metal-Insulator-Metal (MIM) Capacitor Model for RF Applications and Effect of Substrate Grounded Shields', *Jpn. J. Appl. Phys.*, vol. 43, no. 4B, pp. 1746–1751, Apr. 2004.
- [5] P. Periasamy, H. L. Guthrey, A. I. Abdulagatov, P. F. Ndione, J. J. Berry, D. S. Ginley, S. M. George, P. A. Parilla, and R. P. O'Hayre, 'Metal-Insulator-Metal Diodes: Role of the Insulator Layer on the Rectification Performance', *Adv. Mater.*, vol. 25, no. 9, pp. 1301–1308, Mar. 2013.
- [6] J.-C. Woo, Y.-S. Chun, Y.-H. Joo, and C.-I. Kim, 'Low leakage current in metal-insulator-metal capacitors of structural $\text{Al}_2\text{O}_3/\text{TiO}_2/\text{Al}_2\text{O}_3$ dielectrics', *Appl. Phys. Lett.*, vol. 100, no. 8, p. 081101, Feb. 2012.

- [7] Xiongfei Yu, Chunxiang Zhu, Hang Hu, A. Chin, M. F. Li, Byung Jin Cho, Dim-Lee Kwong, P. D. Foo, and Ming Bin Yu, 'A high-density MIM capacitor (13 fF/ μm^2) using ALD HfO₂ dielectrics', *IEEE Electron Device Lett.*, vol. 24, no. 2, pp. 63–65, Feb. 2003.
- [8] S. Chen, C. Lai, A. Chin, J. Hsieh, and J. Liu, 'High-density MIM capacitors using Al₂O₃ and AlTiOx dielectrics', *IEEE Electron Device Lett.*, vol. 23, no. 4, pp. 185–187, Apr. 2002.
- [9] S. M. Sze and M.-K. Lee, 'Semiconductor Devices: Physics and Technology', *Technology*, 2013.
- [10] S. M. Sze and K. K. Ng, *Physics of Semiconductor Devices*. Hoboken, NJ, USA: John Wiley & Sons, Inc., 2006.
- [11] J. A. A. Kittl, K. Opsomer, M. Popovici, N. Menou, B. Kaczer, X. P. P. Wang, C. Adelman, M. A. A. Pawlak, K. Tomida, A. Rothschild, B. Govoreanu, R. Degraeve, M. Schaekers, M. Zahid, A. Delabie, J. Meersschaut, W. Polspoel, S. Clima, G. Pourtois, W. Knaepen, C. Detavernier, V. V. Afanas'ev, T. Blomberg, D. Pierreux, J. Swerts, P. Fischer, J. W. W. Maes, D. Manger, W. Vandervorst, T. Conard, A. Franquet, P. Favia, H. Bender, B. Brijs, S. Van Elshocht, M. Jurczak, J. Van Houdt, D. J. J. Wouters, V. V. Afanas'ev, T. Blomberg, D. Pierreux, J. Swerts, P. Fischer, J. W. W. Maes, D. Manger, W. Vandervorst, T. Conard, A. Franquet, P. Favia, H. Bender, B. Brijs, S. Van Elshocht, M. Jurczak, J. Van Houdt, and D. J. J. Wouters, 'High-*k* dielectrics for future generation memory devices (Invited Paper)', *Microelectron. Eng.*, vol. 86, no. 7–9, pp. 1789–1795, Jul. 2009.
- [12] J. F. Scott, 'High-Dielectric constant thin films for dynamic random access memories (DRAM)', *Annu. Rev. Mater. Sci.*, vol. 28, no. 1, pp. 79–100, Aug. 1998.
- [13] G. D. Wilk, R. M. Wallace, and J. M. Anthony, 'High-*k* gate dielectrics: Current status and materials properties considerations', *J. Appl. Phys.*, vol. 89, no. 10, pp. 5243–5275, May 2001.
- [14] A. Facchetti, M.-H. Yoon, and T. J. Marks, 'Gate Dielectrics for Organic Field-Effect Transistors: New Opportunities for Organic Electronics', *Adv. Mater.*, vol. 17, no. 14, pp. 1705–1725, Jul. 2005.
- [15] J. Veres, S. Ogier, G. Lloyd, and D. de Leeuw, 'Gate Insulators in Organic Field-Effect Transistors', *Chem. Mater.*, vol. 16, no. 23, pp. 4543–4555, Nov. 2004.
- [16] F.-C. Chiu, 'A Review on Conduction Mechanisms in Dielectric Films', *Adv. Mater. Sci. Eng.*, vol. 2014, pp. 1–18, 2014.
- [17] C. R. Crowell, 'Richardson constant and tunneling effective mass for thermionic and thermionic-field emission in Schottky barrier diodes', *Solid. State. Electron.*, vol. 12, no. 1, pp. 55–59, Jan. 1969.
- [18] J. G. Simmons, 'Poole-Frenkel Effect and Schottky Effect in Metal-Insulator-Metal Systems', *Phys. Rev.*, vol. 155, no. 3, pp. 657–660, Mar. 1967.

-
- [19] J. G. Simmons, 'Transition from Electrode-Limited to Bulk-Limited Conduction Processes in Metal-Insulator-Metal Systems', *Phys. Rev.*, vol. 166, no. 3, pp. 912–920, Feb. 1968.
- [20] M. Lenzlinger and E. H. Snow, 'Fowler-Nordheim Tunneling into Thermally Grown SiO₂', *J. Appl. Phys.*, vol. 40, no. 1, pp. 278–283, Jan. 1969.
- [21] E. H. Snow, 'Fowler-Nordheim tunneling in SiO₂ films', *Solid State Commun.*, vol. 5, no. 10, pp. 813–815, Oct. 1967.
- [22] W. C. Lee, C. Hu, Wen-Chin Lee, and Chenming Hu, 'Modeling CMOS tunneling currents through ultrathin gate oxide due to conduction- and valence-band electron and hole tunneling', *IEEE Trans. Electron Devices*, vol. 48, no. 7, pp. 1366–1373, Jul. 2001.
- [23] E. L. Murphy and R. H. Good, 'Thermionic Emission, Field Emission, and the Transition Region', *Phys. Rev.*, vol. 102, no. 6, pp. 1464–1473, Jun. 1956.
- [24] F. A. Padovani and R. Stratton, 'Field and thermionic-field emission in Schottky barriers', *Solid. State. Electron.*, vol. 9, no. 7, pp. 695–707, Jul. 1966.
- [25] C. A. Mead, 'Electron Transport Mechanisms in Thin Insulating Films', *Phys. Rev.*, vol. 128, no. 5, pp. 2088–2093, Dec. 1962.
- [26] F.-C. Chiu, C.-Y. Lee, and T.-M. Pan, 'Current conduction mechanisms in Pr₂O₃/oxynitride laminated gate dielectrics', *J. Appl. Phys.*, vol. 105, no. 7, p. 074103, Apr. 2009.
- [27] F.-C. Chiu, W.-C. Shih, and J.-J. Feng, 'Conduction mechanism of resistive switching films in MgO memory devices', *J. Appl. Phys.*, vol. 111, no. 9, p. 094104, May 2012.
- [28] H. Wong, 'The Current Conduction Issues in High-*k* Gate Dielectrics', in *2007 IEEE Conference on Electron Devices and Solid-State Circuits*, 2007, no. CityU 121707, pp. 31–36.
- [29] J. G. Simmons, 'Conduction in thin dielectric films', *J. Phys. D. Appl. Phys.*, vol. 4, no. 5, p. 202, May 1971.
- [30] F.-C. Chiu, P.-W. Li, and W.-Y. Chang, 'Reliability characteristics and conduction mechanisms in resistive switching memory devices using ZnO thin films', *Nanoscale Res. Lett.*, vol. 7, no. 1, p. 178, 2012.
- [31] J. F. Wager, 'Transparent electronics: Schottky barrier and heterojunction considerations', *Thin Solid Films*, vol. 516, no. 8, pp. 1755–1764, Feb. 2008.
- [32] F. C. Chiu, 'Interface characterization and carrier transportation in metal/HfO₂/silicon structure', *J. Appl. Phys.*, vol. 100, no. 11, p. 114102, Dec. 2006.
- [33] P. W. Peacock and J. Robertson, 'Band offsets and Schottky barrier heights of high dielectric constant oxides', *J. Appl. Phys.*, vol. 92, no. 8, pp. 4712–4721, 2002.

-
- [34] J. G. Simmons, 'Richardson-Schottky Effect in Solids', *Phys. Rev. Lett.*, vol. 15, no. 25, pp. 967–968, Dec. 1965.
- [35] Z. A. Weinberg, 'On tunneling in metal-oxide-silicon structures', *J. Appl. Phys.*, vol. 53, no. 7, pp. 5052–5056, Jul. 1982.
- [36] N. M. Ravindra and J. Zhao, 'Fowler-Nordheim tunneling in thin SiO₂ films', *Smart Mater. Struct.*, vol. 1, no. 3, pp. 197–201, Sep. 1992.
- [37] Y.-C. Yeo, T.-J. King, and C. Hu, 'Direct tunneling leakage current and scalability of alternative gate dielectrics', *Appl. Phys. Lett.*, vol. 81, no. 11, pp. 2091–2093, Sep. 2002.
- [38] B. L. Yang, P. T. Lai, and H. Wong, 'Conduction mechanisms in MOS gate dielectric films', *Microelectron. Reliab.*, vol. 44, no. 5, pp. 709–718, May 2004.
- [39] K. F. Brennan, *The physics of semiconductors: with applications to optoelectronic devices*. Cambridge University Press, 1999.
- [40] E. Fortunato, P. Barquinha, and R. Martins, 'Oxide Semiconductor Thin-Film Transistors: A Review of Recent Advances', *Adv. Mater.*, vol. 24, no. 22, pp. 2945–2986, Jun. 2012.
- [41] S. R. Thomas, P. Pattanasattayavong, and T. D. Anthopoulos, 'Solution-processable metal oxide semiconductors for thin-film transistor applications', *Chem. Soc. Rev.*, vol. 42, no. 16, p. 6910, 2013.
- [42] W. Shockley, 'A Unipolar "Field-Effect" Transistor', *Proc. IRE*, vol. 40, no. 11, pp. 1365–1376, Nov. 1952.
- [43] A. Ortiz-Conde, F. J. García Sánchez, J. J. Liou, A. Cerdeira, M. Estrada, and Y. Yue, 'A review of recent MOSFET threshold voltage extraction methods', *Microelectron. Reliab.*, vol. 42, no. 4–5, pp. 583–596, Apr. 2002.
- [44] R. L. Hoffman, 'ZnO-channel thin-film transistors: Channel mobility', *J. Appl. Phys.*, vol. 95, no. 10, pp. 5813–5819, May 2004.
- [45] W. J. Park, H. S. Shin, B. Du Ahn, G. H. Kim, S. M. Lee, K. H. Kim, and H. J. Kim, 'Investigation on doping dependency of solution-processed Ga-doped ZnO thin film transistor', *Appl. Phys. Lett.*, vol. 93, no. 8, p. 083508, Aug. 2008.
- [46] R. Martins, P. Barquinha, I. Ferreira, L. Pereira, G. Gonçalves, and E. Fortunato, 'Role of order and disorder on the electronic performances of oxide semiconductor thin film transistors', *J. Appl. Phys.*, vol. 101, no. 4, p. 044505, Feb. 2007.
- [47] P. Pattanasattayavong, S. Thomas, G. Adamopoulos, M. a. McLachlan, and T. D. Anthopoulos, 'P-channel thin-film transistors based on spray-coated Cu₂O films', *Appl. Phys. Lett.*, vol. 102, no. 2013, pp. 0–4, 2013.
- [48] D. K. Schroder, *Semiconductor Material and Device Characterization: Third Edition*. 2005.

- [49] D. Hong, G. Yerubandi, H. Q. Chiang, M. C. Spiegelberg, and J. F. Wager, 'Electrical Modeling of Thin-Film Transistors', *Crit. Rev. Solid State Mater. Sci.*, vol. 33, no. 2, pp. 101–132, May 2008.

4. Experimental Methods

4.1 Introduction

Metal oxides were deposited by a solution processed technique, the so-called spray pyrolysis. The metal contacts of the devices were deposited by thermal evaporation.

Several characterisation techniques were used throughout this study to characterise the spray deposited metal oxides. Simultaneous thermal analysis (STA) measurements to assess the thermal profile of the precursor materials, ultraviolet-visible (UV-Vis) and Fourier-transform infrared (FTIR) spectroscopy were used for optical characterisation, x-ray diffraction (XRD) and atomic force microscopy (AFM) for structural and surface characterisation, impedance spectroscopy (IS) to evaluate the dielectric properties of the dielectric oxides and I-V measurements to assess the electrical performance of the deposited materials and devices.

4.2 Deposition Techniques

There are two groups into which the deposition techniques employed for thin oxide film deposition can be divided; i) the physical deposition techniques include physical vapour deposition (PVD), laser ablation, molecular beam epitaxy, and sputtering and ii) the chemical deposition techniques comprised of gas phase deposition methods as well as solution techniques. The gas phase methods are chemical vapour deposition (CVD) and atomic layer deposition (ALD), while spray pyrolysis, sol-gel, spin- and dip-coating methods employ precursor solutions.

In this study, the so-called spray pyrolysis or more precisely, thermochemical spray coating, was used for the deposition of metal oxide thin films while the metal contacts of the devices were deposited by the means of thermal evaporation (PVD).

4.2.1 Thermo-Chemical Spray Coating

Among the various processes for film deposition, the thermochemical spray coating (TCSC) process (often mistakenly called 'spray pyrolysis (SP)') represents a very

simple and relatively cost-effective processing method. TCSC is a process in which a thin film is deposited by spraying aerosols of a precursor or several precursors onto a heated substrate, where thermolysis, combustion and solvent vaporisation occur. The chemical reactants are selected so that the products other than the desired compound, to be volatile at the deposition temperature [1].

The TCSC process does not require any sophisticated equipment such as high vacuum pumps, electron guns, high current sources, RF generators etc. There are many studies on the process since the pioneering work of Chamberlein and Skarman in 1966 on CdS films for solar cells [2]–[5]. Figure 4-1 presents a characteristic schematic diagram of the TCSC equipment configuration.

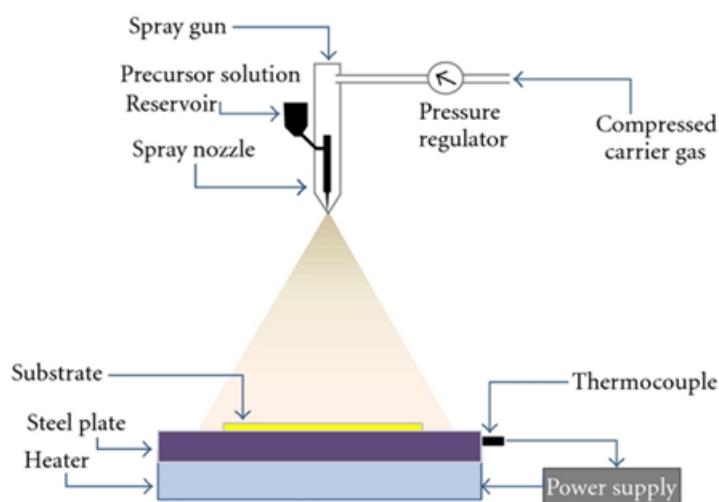


Figure 4-1: Schematic diagram of spray pyrolysis equipment configuration, reproduced from [6].

TCSC equipment consists of an atomiser, a substrate heater such as a hotplate and a temperature controller. The only restriction is that the whole procedure should take place in a well-ventilated place in order for the by-products to be extracted.

Throughout this study, the metal oxide thin films were spray deposited onto the substrates using non-automated methods. A very simple pneumatic airbrush was used to atomize the precursor's solution and to deposit it onto the heated substrates. The carrier gas that was used was nitrogen (N_2) regulated at a pressure of 3 bar.

There are three basic factors affecting the quality of thin films: the deposition temperature, the precursor's chemistry and the spray rate. Each one plays an

important role on the deposition process. Vigue and Spitz proposed a model on the processes which occur with increasing the substrate temperature[7]. Since TCSC is a solution-based process, the properties of the precursor solution plays a very important role [4], [5]. Such properties include solubility of the precursor in a given solvent [8]–[15], precursors themselves [16], [17], molarity of the solution [18]–[26], pH [27]–[29] and additives [30]–[36].

There are many metal-oxides and chalcogenides, ranging from dielectrics to superconductors, which have been deposited by the TCSC technique. Patil demonstrated the chemical versatility of TCSC or SP along with a literature review on spray deposited transition metal oxides, metallic spinel type oxides, binary, ternary and quaternary chalcogenides and superconducting thin films [5]. In this review paper, a survey on TCSC revealed that despite the simplicity of the technique, it is an attractive method to prepare a wide range of thin film materials for several industrial applications.

At this point it could be said that despite its simplicity, TCSC technique is an advantageous technique as i) it offers an easy but efficient way to deposit doped films by adding any soluble dopant to the precursor's solution; ii) unlike the other vapor deposition techniques it does not require high-quality targets nor does it require vacuum at any stage; iii) film thickness and growth rate can be easily controlled by altering the parameters.

4.2.2 Thermal Evaporation

Evaporation includes a variety of techniques from simple resistive heating of a wire in a moderate vacuum to “molecular beam epitaxy” or MBE, where precisely controlled molecular beams are generated in an ultrahigh vacuum environment (less than $\sim 10^{-9}$ Pa or 10^{-14} atmospheres of residual gas pressure).

A schematic of an evaporator is shown in Figure 4-2. Every thermal evaporator system consists of a vacuum vessel (i.e. vacuum chamber), where the whole process occurs, a heating system, a substrate holder and a system of vacuum pumps.

During this process, a material is heated up until its vapour pressure is high enough to produce a flux of several Angstroms per second by using an electrically resistive heater. The process takes place under high vacuum so that the evaporated particles travel directly to the substrate without colliding with the residual gas molecules. For instance, if aluminium is going to be deposited as a metallic contact, the presence of remaining oxygen in the vacuum chamber, could lead to the formation of aluminium oxide.

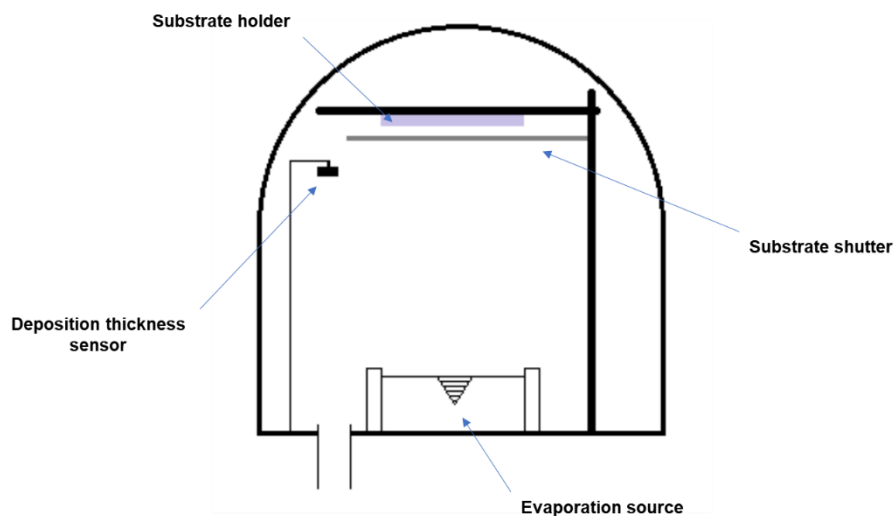


Figure 4-2: Schematic of evaporation system used to deposit metallic contacts.

In this study, the metallic contacts used as the top electrode for metal-insulator-metal capacitors or as the source-drain (S-D) electrodes in the TFT devices were deposited by thermal evaporation. Aluminum or gold contacts were deposited through shadow masks, under high vacuum (10^{-6} mbar).

4.3 Characterisation techniques

A number of characterisation techniques were used to investigate the structural, optical and electrical characteristics of the thin films as well as the performance of the devices.

Initially, prior to deposition the thermal properties of the precursors were investigated by simultaneous thermal analysis (STA). The structural and surface

properties of the films were investigated by XRD and AFM and the optical properties by UV-Vis and FT-IR spectroscopy. To investigate the dielectric properties, impedance spectroscopy was used. The films' thickness was estimated by single wavelength ellipsometry. Finally, the electrical performance was assessed by I-V measurements in 2-terminal devices or TFTs.

4.3.1 Simultaneous thermal analysis (STA)

There are several analytical methods for the thermal analysis of the materials. Such methods include the thermogravimetric analysis (TGA) and the differential scanning calorimetry (DSC).

TGA of the precursors provides information about the required temperatures for the complete decomposition of the precursors during the deposition process. In this technique, the monitoring of the mass change of the material under investigation, as a function of increasing temperature, provides information about the materials' decomposition process.

DSC is used to measure the amount of heat that is absorbed or released by a sample as a function of temperature, for example during phase transitions. DSC measures the difference, between the heat required to increase the temperature of a sample and reference material.

For the results shown in this work, the measurements were carried out using a simultaneous thermal analyser NETZSCH STA 449 F3 Jupiter[®] system, with aluminium crucibles. All the measurements were carried out in the range of 50-550 °C with a heating rate of 10 K/min under a nitrogen atmosphere.

4.3.2 X-Ray Diffraction (XRD)

The structural properties of the spray deposited metal oxide thin films were assessed by x-ray diffraction (XRD) measurements.

The working principle of the technique is based on the diffraction effects produced by the interaction of the x-rays with the periodic lattice of the materials. When an incident beam of a very short wavelength ($\sim 1 \text{ \AA}$) interacts with periodic lattice planes of a crystal acting as a diffraction grating, the beam is diffracted.

An X-ray source typically Cu, emits high energy K- α radiation whose wavelength is on the order of the atomic spacing of crystalline materials. The sample is placed in the beam across a range of angles on the material under investigation. In Figure 4-3, a schematic diagram of x-ray diffraction from a periodic atom structure is depicted.

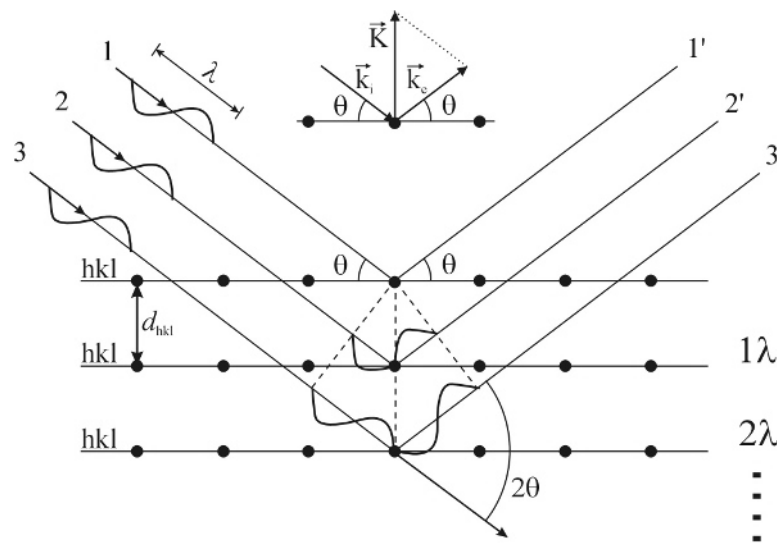


Figure 4-3: Schematic design of x-ray diffraction from a periodic atom structure.

The general relationship between the wavelength of the incident X-rays, angle of incidence and spacing between the crystal lattice planes of atoms is known as Bragg's Law, expressed as:

$$n \cdot \lambda = 2d_{hkl} \cdot \sin\theta \quad (4-1)$$

where, n is the diffraction order, λ is the wavelength of the incident X-rays, d_{hkl} is the interplanar spacing of the crystal and θ is the angle of incidence.

A diffraction pattern is a graph of intensity of light (diffraction peak) as a function of the 2θ angle. Since normally a degree of disorder is expected in solids and thin films, there is a broadening of the diffraction peaks in XRD spectrum. The disorder is due to distribution of lattice spacings, crystal domain size and orientation. The widening of the diffraction peaks is related to the average size of the crystallite domains $\langle d \rangle$:

$$\langle d \rangle = \frac{K \cdot \lambda}{\beta_w \cdot \cos\theta} \quad (4-2)$$

where, K is the so-called Scherrer constant and is typically taken as 0.9, λ is the wavelength of the x-rays, β_w is the full width at the half maximum of the peak's intensity and θ is the Bragg angle. The Scherrer approach is only a rough estimation which enables to evaluate a trend between different samples in a relative way.

The grazing incidence x-ray diffraction (GIXRD) measurements were performed using a Rigaku Ultima⁺ diffractometer, with CuK α radiation operating at 40 kV and 30 mA.

4.3.3 Atomic Force Microscopy (AFM)

The surface morphology of the spray deposited thin films was studied by AFM. AFM is used to investigate the surface properties of materials. Information about the surface roughness and morphology at nanoscale level can be obtained by AFM.

An atomic force microscope consists of a sharp tip, which is mounted at the end of a cantilever arm that is usually coated by a highly reflecting film, a laser, a quadrant photodiode and a piezoelectric scanner, which the sample is mounted on. In AFM, the tip motion is controlled by a feedback loop and a piezoelectric scanner. The topographic profiles of the surfaces are acquired by detecting the deflection of the cantilever, by measuring the reflected laser beam with the photodiode. In Figure 4-4, a schematic diagram of an atomic force microscope is presented.

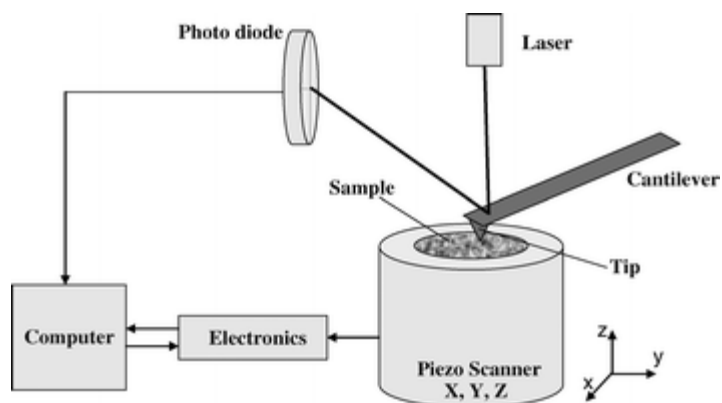


Figure 4-4: Schematic representation of an atomic force microscope setup.

There are two major scanning modes of AFM operation depending on the nature of the contact between the tip and the sample, namely contact and tapping modes. In the contact mode the tip is always in contact with the surface of the sample, while in tapping mode the tip oscillates in very close proximity to the surface of the sample. A drawback of the contact mode AFM arises when the lateral force exerted on the sample is high. This could damage the surface of a sample or in some cases results to the movement of relatively loosely attached objects. In such cases tapping mode imaging is preferred.

In this work, AFM images were taken in contact mode under ambient conditions using a MultiMode scanning probe microscope (MM-SPM) fitted to a Nanoscope IIIa controller unit employing a silicon tip of a radius <math><10\text{ nm}</math>.

4.3.4 Ultraviolet-Visible-near IR absorption spectroscopy (UV-Vis-NIR)

The optical properties such as optical transmittance, absorption spectra, optical band gap and Urbach tail energy of the spray deposited thin films were obtained by ultraviolet-visible to near IR (UV-Vis-NIR) absorption spectroscopy.

The relative intensity of the light transmitted through the films on fused silica substrates was collected. Fused silica substrates were used due to their high transparency in the wavelength region of 190-1000 nm.

The absorption coefficient (a) was calculated from the relative transmittance spectra by:

$$a = \frac{2 - \log(T(\%))}{t} \quad (4-3)$$

where, $T(\%)$ is the relative transmittance and t is the thickness of the film.

The optical band gap of the spray deposited thin films was extracted from the Tauc plot of $(a \cdot hv)^n$ versus hv where a is the absorption coefficient, h is the Planck constant and ν is the frequency of the wavelength. The exponent index n for the case of indirect band gap is $n = 2$ while for the case of a direct band gap is $n = 1/2$. In Figure 4-5 a typical Tauc plot is shown.

The Urbach tail energy was calculated from the plots of $\ln a$ versus hv . The linear part of the resulting curve was fitted and the Urbach tail energy was calculated by the inverse slope of the fitting curve.

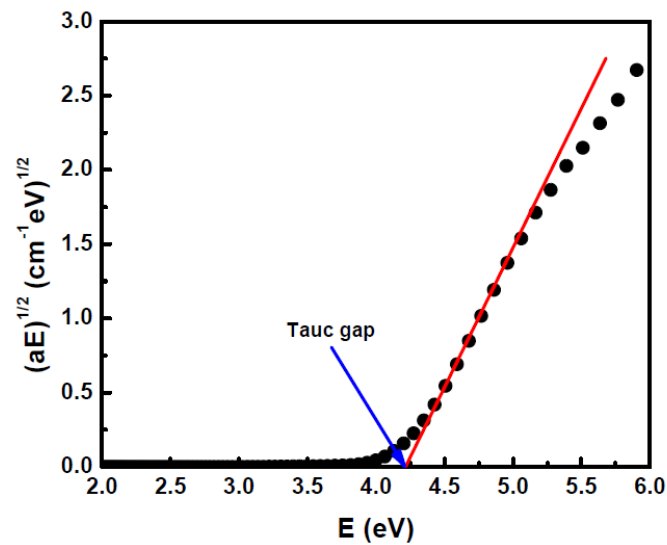


Figure 4-5: Tauc plot and linear fit for analysis of the Tauc-gap.

In this study, a Perkin Elmer Lambda 35 spectrophotometer was used to extract the optical properties of the resulting spray deposited thin films.

In Figure 4-6, a schematic of the operational principles of UV-Vis spectrophotometry is illustrated.

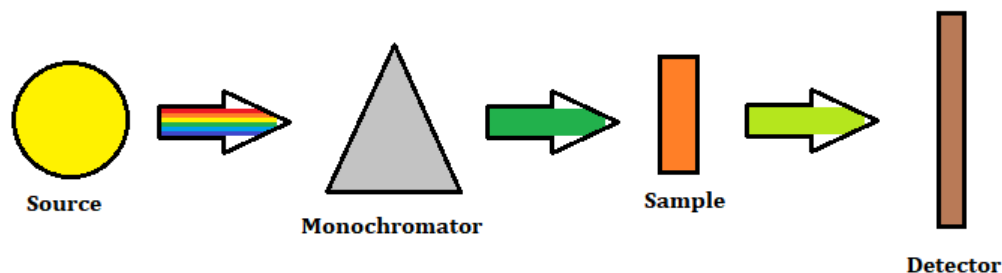


Figure 4-6: Schematic of the operational principles of a UV-Vis spectrophotometer.

4.3.5 Fourier Transformed Infrared Spectroscopy (FT-IR)

Fourier transformed infrared spectroscopy (FT-IR) is a spectroscopic technique based on the absorption of electromagnetic radiation in the infrared region from the solids. This technique is suitable for identification of the chemical bonds in the solids, by studying the absorbed electromagnetic radiation by vibrating atoms in molecules or solids in the infrared region.

When light interacts with matter, the vibrational mode of the chemical bonds in the molecules changes if the vibrating dipole is in phase with the electric vector of the incident radiation. Each chemical bond in a molecule vibrates at a frequency which is characteristic of that bond and the characteristic frequencies correspond to the frequencies of infrared light.

The characteristic frequency depends on the mass of the atom and the length and strength of the bonds. For each molecule, a variety of characteristic vibrations are possible, and each corresponds to a different frequency.

FT-IR differs from the traditional IR spectroscopy which records the absorption of the IR radiation from a sample of one IR wavelength at a time. FT-IR is based on the optical interferometry, in which by using a beamsplitter, a beam coming from a light source is split into two arms. Each of those light beams is reflected back, by a set of optical mirrors toward the beamsplitter, which then combines their amplitudes using the superposition principle. The resulting interference beam is directed to the sample under test and the absorption of the beam's intensity because of the sample is

recorded by a detector. The resulting interferogram is finally turned into an actual spectrum by using a mathematical Fourier transformation.

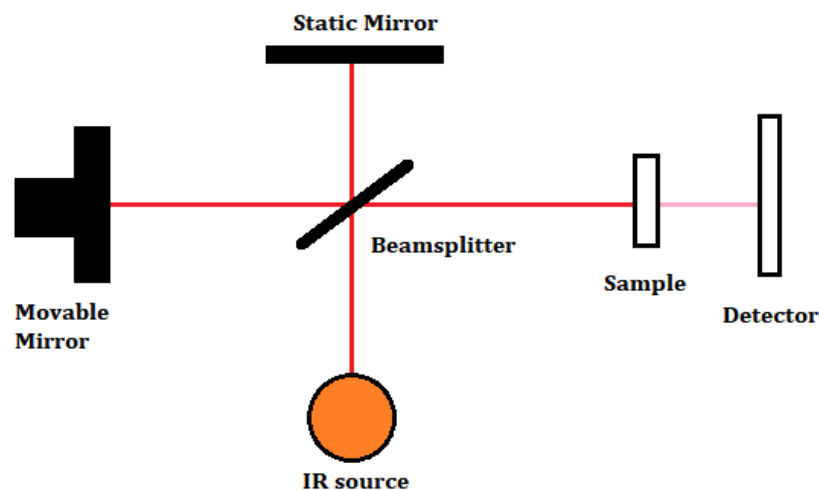


Figure 4-7: Schematic of an FT-IR experimental setup.

In Figure 4-7, a schematic of the FT-IR principle is presented. In this study a Perkin Elmer spectrum 2000 FT-IR spectrometer was used. The measurements were conducted in ambient atmosphere in the wavenumber region of $400\text{-}4000\text{ cm}^{-1}$ by using a KBr beamsplitter with a resolution of 4 cm^{-1} and 150 scans per sample.

4.3.6 Ellispometry

In general, ellispometry is an analytical technique which measures the change in polarisation between an incident light beam and the reflected beam from a surface. In Figure 4-8 a single wavelength ellispometry setup is depicted. It consists of a light source that produces a non-linear polarized light beam, and a linear polarizer that is used to linearly polarize the light from the source. The light passes via a compensator which polarizes elliptically the linear polarized light beam and hits the surface of the sample. The reflected light from the sample, which is linear polarized, is detected from the analyser while the photodetector detects the light for data processing.

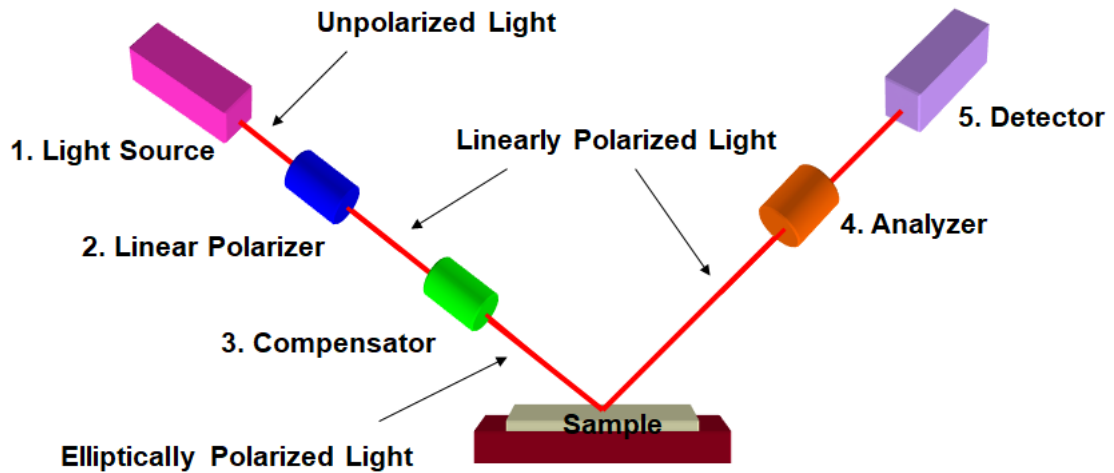


Figure 4-8: Single wavelength ellipsometer setup.

The mathematical expression that describes the change of polarisation is given by:

$$P = \frac{R_p}{R_s} = \tan(\Psi) e^{i\Delta} \quad (4-4)$$

where, (P) the change in polarisation, (R_p) the component oscillating in the plane of incident, (R_s) the oscillating component perpendicular to the plane of incidence, ($\tan(\Psi)$) the amplitude ratio of reflection and (Δ) the phase shift.

In this study a single wavelength ellipsometer (Rudolph AutoEL II) was used to estimate the thickness and the optical constant of the deposited metal oxide thin films. Rudolph AutoEL II uses an HeNe laser (632.8 nm) as a light source.

4.3.7 Impedance spectroscopy

The impedance and dielectric properties such as resistance (R), reactance (X) and dielectric constant (k) of the spray deposited films were investigated by impedance spectroscopy.

Metal-insulator-metal (MIM) 2-terminal devices, consisting of indium-tin oxide (ITO) as bottom electrode, the spray deposited metal oxide and aluminum contacts were used to assess the dielectric properties of the metal oxide thin films. The

dispersions of resistance (R) and reactance (X) of the films over a frequency range from 1 kHz to 50 MHz, with a peak-to-peak voltage of 100 mV, was recorded by using a Wayne Kerr 6500B impedance analyser.

The geometric capacitance (C_{ox}) was calculated from the reactance as:

$$C_{ox} = -\frac{1}{2\pi f \cdot X} \cdot A^{-1} \quad (4-5)$$

where, f is the frequency, X the reactance and A the area of the top electrode in cm^2 . The dielectric constant (k) of the spray deposited thin film was calculated from the capacitance and the thickness (t) of the film as:

$$k = \frac{C_{ox} \cdot t}{\varepsilon_0} \quad (4-6)$$

where, $\varepsilon_0 = 8.85 \times 10^{-12} \text{ F} \cdot \text{m}^{-1}$ the vacuum permittivity.

4.3.8 Current Voltage Measurements

The leakage current properties, of the resulting spray deposited films, were investigated by current-voltage ($I - V$) measurements. MIM device architecture was used to evaluate the dielectric strength, the leakage current density and identify the conduction mechanism of the metal oxide gate dielectrics.

The conduction mechanisms of an insulating film can be identified by I-V measurements. In general, conduction mechanisms such as Schottky emission, Fowler-Nordheim tunnelling and Poole-Frenkel tunnelling, are some conduction mechanisms. In Table 4-1, the equations describing each one of the conduction mechanisms are summarised and presented.

Table 4-1: Summary of the conduction mechanisms used to assess the conductivity of thin insulating films.

Conduction Mechanism	Expression
Schottky Emission	$J = A \cdot T^2 \cdot \exp \left[-\frac{q \left(\varphi_b - \sqrt{\frac{qE}{4\pi\epsilon_r\epsilon_0}} \right)}{k_B T} \right]$
Fowler-Nordheim tunnelling	$J = B \cdot E^2 \cdot \exp \left[\frac{-8\pi\sqrt{2qm_T^*}}{3hE} \varphi_b^{3/2} \right]$
Poole-Frenkel tunnelling	$J = C \cdot E \cdot \exp \left[-\frac{q \left(\varphi_b - \sqrt{\frac{qE}{4\pi\epsilon_r\epsilon_0}} \right)}{k_B T} \right]$

* $A = 120 m_{ox}^*/m_0 Acm^{-1}K^{-2}$ the effective Richardson constant, J is the current density, T is the absolute temperature, q is the electronic charge, $q\varphi_b$ is the Schottky barrier height, E is the electric field, k_B is Boltzmann's constant, ϵ_r is the dynamic dielectric constant, ϵ_0 is the vacuum permittivity, B is a constant, m_T^* is the tunnelling effective mass, h is Planck's constant and C is a proportionally constant which is function of the density of trap centres.

From the intercept of the Schottky plot ($\ln(J/T^2)$ versus \sqrt{E}) and the slope of the Fowler-Norheim plot ($\ln(J/E^2)$ versus $1/E$) the electron effective mass in the metal oxide and the barrier height at the metal-contact/metal-oxide interface can be determined, assuming that $m_{ox}^* = m_T^*$ [37]. The intercept from Schottky plots is given by:

$$Intercept = \ln \left(120 \frac{m_{ox}^*}{m_0} \right) - \frac{q\varphi_b}{k_B T} \quad (4-7)$$

while, the slope of the Fowler-Norheim plot can be expressed as:

$$slope = -6.83 \times 10^7 \sqrt{\frac{m_T^*}{m_0}} \varphi_b^3 \quad (4-8)$$

For the current voltage measurements an Agilent B1500A semiconductor device analyser running the EasyEXPERT group+ software was used. All the current

voltage measurements were conducted by using a Lakeshore TTPX probe station, under vacuum ($\sim 10^{-4}$ mbar) and dark conditions at room temperature.

4.4 References

- [1] A. J. C. Fiddes, K. Durose, A. W. Brinkman, J. Woods, P. D. Coates, and A. J. Banister, 'Preparation of ZnO films by spray pyrolysis', *J. Cryst. Growth*, vol. 159, no. 1–4, pp. 210–213, Feb. 1996.
- [2] L. Filipovic, S. Selberherr, G. C. Mutinati, E. Brunet, S. Steinhauer, K. Anton, J. Teva, J. Kraft, and F. Schrank, 'Modeling Spray Pyrolysis Deposition', *Proc. World Congr. Eng.*, vol. II, pp. 6–11, 2013.
- [3] R. R. Chamberlin and J. S. Skarman, 'Chemical Spray Deposition Process for Inorganic Films', *J. Electrochem. Soc.*, vol. 113, no. 1, p. 86, Jan. 1966.
- [4] D. Perednis and L. J. Gauckler, 'Thin film deposition using spray pyrolysis', *J. Electroceramics*, vol. 14, pp. 103–111, 2005.
- [5] P. S. Patil, 'Versatility of chemical spray pyrolysis technique', *Mater. Chem. Phys.*, vol. 59, no. 3, pp. 185–198, Jun. 1999.
- [6] A. Bashir, P. H. Wöbkenberg, J. Smith, J. M. Ball, G. Adamopoulos, D. D. C. Bradley, and T. D. Anthopoulos, 'High-performance zinc oxide transistors and circuits fabricated by spray pyrolysis in ambient atmosphere', *Adv. Mater.*, vol. 21, pp. 2226–2231, 2009.
- [7] J. C. Viguié, J. C. Vigui, and J. Spitz, 'Chemical Vapor Deposition at Low Temperatures', *J. Electrochem. Soc.*, vol. 122, no. 4, p. 585, Apr. 1975.
- [8] S. Oertel, M. P. M. M. Jank, E. Teuber, A. J. Bauer, and L. Frey, 'High-mobility metal-oxide thin-film transistors by spray deposition of environmentally friendly precursors', in *Thin Solid Films*, 2014, vol. 553, pp. 114–117.
- [9] M. Dudita, L. Isac, and A. Duta, 'Influence of solvents on properties of solar selective coatings obtained by spray pyrolysis', *Bull. Mater. Sci.*, vol. 35, no. 6, pp. 997–1002, 2012.
- [10] A. Hernandez-Valdes, R. A. Zarate, A. I. Martinez, M. I. Pech-Canul, M. A. Garcia-Lobato, and R. Villaroel, 'The role of solvents on the physical properties of sprayed iron oxide films', *Vacuum*, vol. 105, pp. 26–32, Jul. 2014.
- [11] S. Benramache, A. Rahal, and B. Benhaoua, 'The effects of solvent nature on spray-deposited ZnO thin film prepared from $\text{Zn}(\text{CH}_3\text{COO})_2 \cdot 2\text{H}_2\text{O}$ ', *Opt. - Int. J. Light Electron Opt.*, vol. 125, no. 2, pp. 663–666, Jan. 2014.

- [12] J. C. Ugucioni and M. Mulato, 'Influence of deposition temperature, solvent, and solute concentration on the deposition mechanisms and final structure of mercury iodide fabricated using the spray pyrolysis technique', *J. Appl. Phys.*, vol. 100, no. 4, 2006.
- [13] I. Lj. Validžić, V. Jakanović, D. P. Uskoković, and J. M. Nedeljković, 'Influence of solvent on the structural and morphological properties of AgI particles prepared using ultrasonic spray pyrolysis', *Mater. Chem. Phys.*, vol. 107, no. 1, pp. 28–32, Jan. 2008.
- [14] M. Tomakin, 'Structural and optical properties of ZnO and Al-doped ZnO microrods obtained by spray pyrolysis method using different solvents', *Superlattices Microstruct.*, vol. 51, no. 3, pp. 372–380, Mar. 2012.
- [15] C. Jiang, W. L. Koh, M. Y. Leung, W. Hong, Y. Li, and J. Zhang, 'Influences of alcoholic solvents on spray pyrolysis deposition of TiO₂ blocking layer films for solid-state dye-sensitized solar cells', *J. Solid State Chem.*, vol. 198, pp. 197–202, Feb. 2013.
- [16] G. Kenanakis, N. Katsarakis, and E. Koudoumas, 'Influence of precursor type, deposition time and doping concentration on the morphological, electrical and optical properties of ZnO and ZnO:Al thin films grown by ultrasonic spray pyrolysis', *Thin Solid Films*, vol. 555, pp. 62–67, Mar. 2014.
- [17] L. Cattin, B. A. Reguig, A. Khelil, M. Morsli, K. Benchouk, and J. C. Bernède, 'Properties of NiO thin films deposited by chemical spray pyrolysis using different precursor solutions', *Appl. Surf. Sci.*, vol. 254, no. 18, pp. 5814–5821, Jul. 2008.
- [18] N. Koteeswara Reddy and K. T. Ramakrishna Reddy, 'Preparation and characterisation of sprayed tin sulphide films grown at different precursor concentrations', *Mater. Chem. Phys.*, vol. 102, no. 1, pp. 13–18, Mar. 2007.
- [19] F. Zahedi, R. S. Dariani, and S. M. Rozati, 'Structural, Optical and Electrical Properties of ZnO Thin Films Prepared by Spray Pyrolysis: Effect of Precursor Concentration', *Bull. Mater. Sci.*, vol. 37, no. 3, pp. 433–439, Jun. 2014.
- [20] D. Chen, E. H. Jordan, and M. Gell, 'Effect of solution concentration on splat formation and coating microstructure using the solution precursor plasma spray process', *Surf. Coatings Technol.*, vol. 202, no. 10, pp. 2132–2138, Feb. 2008.
- [21] S. Manolache, A. Duta, L. Isac, M. Nanu, A. Goossens, and J. Schoonman, 'The influence of the precursor concentration on CuSbS₂ thin films deposited from aqueous solutions', *Thin Solid Films*, vol. 515, no. 15, pp. 5957–5960, May 2007.
- [22] B. A. Reguig, M. Regragui, M. Morsli, A. Khelil, M. Addou, and J. C. Bernède, 'Effect of the precursor solution concentration on the NiO thin film properties deposited by spray pyrolysis', *Sol. Energy Mater. Sol. Cells*, vol. 90, no. 10, pp. 1381–1392, Jun. 2006.

- [23] F. Zahedi and R. S. Dariani, 'Effect of precursor concentration on structural and optical properties of ZnO microrods by spray pyrolysis', *Thin Solid Films*, vol. 520, no. 6, pp. 2132–2135, Jan. 2012.
- [24] M. Baneto, A. Enesca, Y. Lare, K. Jondo, K. Napo, and A. Duta, 'Effect of precursor concentration on structural, morphological and opto-electric properties of ZnO thin films prepared by spray pyrolysis', *Ceram. Int.*, vol. 40, no. 6, pp. 8397–8404, 2014.
- [25] S. B. Weber, H. L. Lein, T. Grande, and M.-A. Einarsrud, 'Influence of the precursor solution chemistry on the deposition of thick coatings by spray pyrolysis', *Surf. Coatings Technol.*, vol. 221, pp. 53–58, Apr. 2013.
- [26] D. Sivalingam, J. B. Gopalakrishnan, and J. B. Balaguru Rayappan, 'Influence of precursor concentration on structural, morphological and electrical properties of spray deposited ZnO thin films', *Cryst. Res. Technol.*, vol. 46, no. 7, pp. 685–690, Jul. 2011.
- [27] F. Caillaud, A. Smith, and J.-F. Baumard, 'Effect of pH of the Solution on the Deposition of Zinc Oxide Films by Spray Pyrolysis', *J. Am. Ceram. Soc.*, vol. 76, no. 4, pp. 998–1002, Apr. 1993.
- [28] A. Maldonado, R. Asomoza, J. Cañetas-Ortega, E. Zironi, R. Hernández, R. Patiño, and O. Solorza-Feria, 'Effect of the pH on the physical properties of ZnO:In thin films deposited by spray pyrolysis', *Sol. Energy Mater. Sol. Cells*, vol. 57, no. 4, pp. 331–344, Apr. 1999.
- [29] Y. B. K. Kumar, G. S. Babu, P. U. Bhaskar, and V. S. Raja, 'Effect of starting-solution pH on the growth of Cu₂ZnSnS₄ thin films deposited by spray pyrolysis', *Phys. Status Solidi Appl. Mater. Sci.*, vol. 206, no. 7, pp. 1525–1530, 2009.
- [30] P. K. Nayak, T. Busani, E. Elamurugu, P. Barquinha, R. Martins, Y. Hong, and E. Fortunato, 'Zinc concentration dependence study of solution processed amorphous indium gallium zinc oxide thin film transistors using high-*k* dielectric', *Appl. Phys. Lett.*, vol. 97, no. 18, p. 183504, Nov. 2010.
- [31] C. H. Chen, E. M. Kelder, and J. Schoonman, 'Electrostatic sol-spray deposition (ESSD) and characterisation of nanostructured TiO₂ thin films', *Thin Solid Films*, vol. 342, no. 1–2, pp. 35–41, Mar. 1999.
- [32] L. Castañeda, A. Maldonado, J. Rodríguez-Baez, J. C. Cheang-Wong, M. López-Fuentes, and M. de la L. Olvera, 'Chemical spray pyrolysis deposited fluorine-doped zinc oxide thin films: Effect of acetic acid content in the starting solution on the physical properties', *Mater. Sci. Semicond. Process.*, vol. 15, no. 3, pp. 232–239, Jun. 2012.

- [33] M. Okuya, S. Kaneko, K. Hiroshima, I. Yagi, and K. Murakami, 'Low temperature deposition of SnO₂ thin films as transparent electrodes by spray pyrolysis of tetra-n-butyltin(IV)', *J. Eur. Ceram. Soc.*, vol. 21, no. 10–11, pp. 2099–2102, Jan. 2001.
- [34] M.-G. Kim, M. G. Kanatzidis, A. Facchetti, and T. J. Marks, 'Low-temperature fabrication of high-performance metal oxide thin-film electronics via combustion processing', *Nat. Mater.*, vol. 10, no. 5, pp. 382–388, May 2011.
- [35] T. Kosugi and S. Kaneko, 'Novel Spray-Pyrolysis Deposition of Cuprous Oxide Thin Films', *J. Am. Ceram. Soc.*, vol. 81, no. 12, pp. 3117–3124, Dec. 1998.
- [36] P. Pattanasattayavong, S. Thomas, G. Adamopoulos, M. A. McLachlan, and T. D. Anthopoulos, 'P-channel thin-film transistors based on spray-coated Cu₂O films', *Appl. Phys. Lett.*, vol. 102, no. 2013, pp. 0–4, 2013.
- [37] F. C. Chiu, 'Interface characterization and carrier transportation in metal/HfO₂/silicon structure', *J. Appl. Phys.*, vol. 100, no. 11, p. 114102, Dec. 2006.

5. Aluminum Titanate $\text{Ti}_{1-x}\text{Al}_{2x}\text{O}_y$ Thin Films

5.1 Introduction

Thin-film transistors (TFTs) based on oxide semiconductors constitute a promising technology for a host of large-volume electronic applications [1], [2]. The majority of TFTs based on oxide semiconductors reported to date have employed In-based oxide compounds as the active layer (IZO, IGZO, HIZO). They employ conventional dielectrics (e.g., SiO_2) that are relatively thick, which usually results in high voltage operation and hence, increased power consumption [1]. On the other hand, the scaling of complementary metal oxide semiconductor transistors (CMOS) has led to the silicon dioxide dielectric being so thin (1.4 nm) that its leakage current is unacceptably large. Hence, the decrease of device dimensions led to the need for oxides with a high dielectric constant (k) to replace silicon dioxide in CMOS. An alternative route would be the use of thicker layers of high- k dielectrics, with comparable equivalent silicon dioxide capacitance [3].

Among the various known high- k materials, aluminum oxide (Al_2O_3) [4]–[6] and titanium oxide (TiO_2) [7]–[10] are two well-characterised compounds that exhibit higher relative permittivity than SiO_2 .

Al_2O_3 is a wide band gap ($E_g \sim 9$ eV) material with a relatively low dielectric constant ($k \sim 9$), compared to other metal oxides, however, it has been considered as an attractive gate dielectric [1], [11]–[13].

On the other hand, TiO_2 has a relatively small band gap (3–3.5 eV) but its dielectric constant can vary from 40 to 173 depending on its crystal structure [7]. TiO_2 exhibits three polymorphs i.e. anatase, rutile and brookite, depending on the growth conditions [15]–[19]. Anatase and brookite are metastable phases and can be transformed to rutile at high (> 600 °C) temperatures [20]. Among these three crystal structures, rutile is the thermally stable one and the one with the higher (~ 114) dielectric constant [21], [22].

Besides the high dielectric constant of TiO_2 , its relatively narrow band gap disadvantages its use as gate dielectric in TFTs implementing wide band gap semiconductors, such as ZnO. This is because of the band offset criterion [14], [23],

which imposes that the gate dielectric should have band offset with the active channel material of over 1 eV to minimise carrier injection in its bands.

It should be noted that a small number of metal oxides (A_xO_y) that exhibit a relatively high permittivity and wide band gap at the same time [23]–[27]. There is an empirical relationship that describes the trade-off between the band gap and the permittivity of a dielectric [28]:

$$E_g \approx 20 \left[\frac{3}{2 + k} \right]^2 \quad (5-1)$$

A possible methodology to overcome this limitation is the use of a composite and/or multilayer dielectric material. There are few reports in the literature that discuss the potential implementation of a TiO_2 incorporated Al_2O_3 (TAO) film as potential high- k gate dielectric [29]–[31]. Aucellio et al. [29], deposited TAO layer on Si via atomic oxygen exposure of room temperature sputtered metallic alloy films. The deposited TAO films (Ti:Al=75:25at. %) were amorphous with a band gap of ~ 4 eV, high permittivity of ~ 30 and for an applied voltage of 1 V across the TAO layer, the leakage current density was on the order of ~ 5 A/cm². Considering that the estimated equivalent oxide thickness (EOT), for the TAO films, was in the range of 0.42-0.48 nm, the leakage current was 4-5 decades lower than that of SiO_2 with a similar EOT.

Shi et al. [30], reported on the thermal stability and electrical properties of titanium-aluminum oxide [$(TiO_2)_{0.28}(Al_2O_3)_{0.72}$, (TAO)] ultra-thin films, of 1.2 nm EOT, deposited by pulsed laser deposition (PLD). The films were amorphous for temperatures up to 900 °C, exhibiting a dielectric constant of ~ 30 , while the leakage current density of the film was 6.02×10^{-4} A/cm² at a gate bias voltage of 1 V.

Kuo and Tzeng [31] reported on the growth and properties of Al_2O_3 - TiO_2 films deposited by r.f. magnetron sputtering. The atomic composition [Al/(Al+Ti)] of the film was of 0.47. The Al_2O_3 - TiO_2 films were amorphous. In their study, the dielectric constant of the Al_2O_3 - TiO_2 films, was found to be in the range of 11-15.

Baek et al. [32], reported on the implementation of Al_2O_3/TiO_2 nanolaminates as gate dielectrics in organic field effect transistors (OFETs). In their report, the Al_2O_3/TiO_2 nanolaminate gate dielectric films were deposited on heavily doped Si

substrates via plasma-enhanced atomic layer deposition (PEALD). The Al_2O_3/TiO_2 films exhibited a dielectric constant of 17.8 measured at 1 kHz. The measured leakage current density for an applied electric field of 2 MV/cm was found to be of 8.6×10^{-9} A/cm².

Al_2O_3 , TiO_2 and $Al_2O_3-TiO_2$ films have been successfully deposited on a number of substrates by several deposition techniques, including magnetron sputtering [31], [33], [34], atomic layer deposition (ALD) [32], [35], [36], spin coating [12], [37] and spray coating [1], [38]. Although vacuum-based deposition techniques, such as sputtering and ALD, offer the advantage of a more controlled deposition process, they suffer from the high operational costs. On the other hand, solution-processed techniques such as spin coating and spray coating are employed in air, are large area compatible and of significantly lower operational costs.

In this chapter, the optical, structural and dielectric properties of $Ti_{1-x}Al_{2x}O_y$ thin films and their implementation as gate dielectrics in TFTs employing ZnO semiconducting channels are being reported.

5.2 Experimental

5.2.1 Precursor Solution Chemistry

The precursors that were used in this study were $AlCl_3$ (Alfa Aesar, 99%), titanium butoxide $[Ti(OCH_2CH_2CH_2CH_3)_4]$ (Alfa Aesar, 99+%) and $Zn(O_2C_2H_3)_2 \cdot 2H_2O$ (Alfa Aesar, ACS, 98-101%). All the precursor materials were used as they received without any further purification. In this study, methanol (CH_3OH , VWR, ACS, $\geq 99.8\%$) was used as solvent. However, methanol has low boiling point ($\sim 65^\circ C$) and evaporates rapidly. To slow down solvent evaporation, and thereby to hinder particle formation, methanol was mixed with acetylacetone ($CH_3COCH_2COCH_3$, Alfa Aesar, 99%) which has higher boiling point ($\sim 140^\circ C$).

$AlCl_3$ and $Ti(OCH_2CH_2CH_2CH_3)_4$ were selected due to their high solubility in methanol, the solvent of choice throughout the study along with their desired thermal

decomposition temperatures. Other precursors, such as $Al(NO_3)_3 \cdot 9H_2O$, $Al(C_5H_7O_2)_3$, $TiCl_3$, were investigated as well; however the resultant aluminum-titanate films were of poor quality both optically and electrically.

For the preparation of the aluminum-titanate precursor solutions, two methanol-based solutions of $AlCl_3$ and $(Ti(OCH_2CH_2CH_2CH_3)_4)$ at a concentration of 50 mg/mL were prepared. Acetylacetone (AcAc) was added to both the precursor solutions at $CH_3OH:AcAc$ molar ratio of 5:1. The solutions were left under continuous stirring for at least 1 h prior to deposition, ensuring complete dissolution. The stoichiometry of titanium to aluminium atomic ratio was controlled by simple blending of the appropriate amount of the precursors solutions.

The zinc oxide precursor solution was prepared by dissolving $Zn(O_2C_2H_3)_2 \cdot 2H_2O$ in methanol at a concentration of 25 mg/mL [39].

5.2.2 Device Fabrication

Metal-insulator-metal (MIM) 2-terminal devices (Figure 5-1.a) were fabricated by spray coating commercially available indium tin oxide (ITO) coated glass (sheet resistivity $R_s \sim 15 \Omega/sq$) with the aluminum-titanate's precursor solution, followed by deposition of thermally evaporated aluminum contacts (~ 100 nm) through shadow mask. Aerosols of the aluminum-titanate's precursor solution were sprayed onto the glass/ITO substrates at $420^\circ C$ employing a pneumatic airbrush, held at a vertical distance of about 30 cm. Aerosols of the precursors and blends were spray-coated for 30 s while the spray coating process was interrupted for 20 s to allow the vapours to settle. The cycle was repeated until films of typical thicknesses in the range between 100 and 200 nm were obtained.

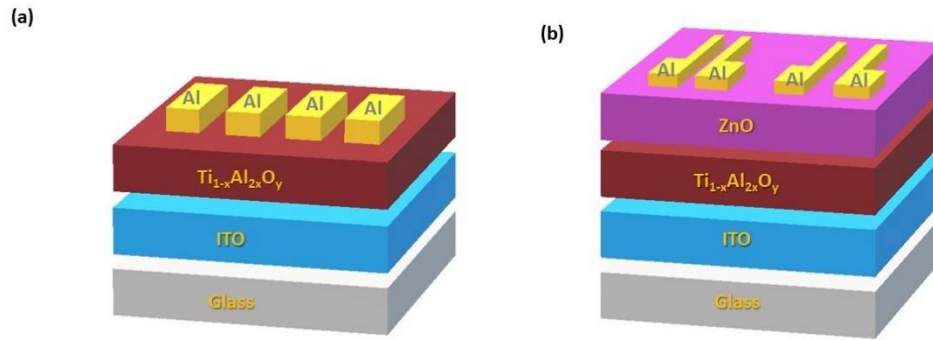


Figure 5-1:(a) MIM capacitor and (b) Bottom gate-top contact (BG-TC) ZnO-based TFT structures used in this study, implementing $Ti_{1-x}Al_{2x}O_y$ thin film dielectric.

Bottom gate-top contact (BG-TC) transistors (Figure 5-1.b) were fabricated by spray coating the glass/ITO/ $Ti_{1-x}Al_{2x}O_y$ stack with the ZnO precursor solution, followed by deposition of thermally evaporated aluminum source and drain (S/D) electrodes (~ 60 nm) through a shadow mask. The ZnO precursor solution were sprayed onto the glass/ITO substrates at 400 °C, employing the same experimental conditions as previously, until a film of typical thickness of ~ 30 nm was obtained.

5.2.3 Thin Film & Device Characterisation Techniques

The thermal properties of the precursors were investigated by the means of thermal gravimetric analysis (TGA) and differential scanning calorimetry (DSC). All the measurements were conducted using a simultaneous thermal analyser NETZSCH STA 449 F3 Jupiter®. The thermal analysis measurements were performed in the temperature range of 40 - 550 °C at a constant heating rate of 10 K/min under inert atmosphere.

The microstructure of the spray deposited $Ti_{1-x}Al_{2x}O_y$ thin films were characterised by X-ray diffraction. The optical properties of the $Ti_{1-x}Al_{2x}O_y$ films were investigated by spectroscopic ellipsometry (SE) and UV-Vis absorption spectroscopy measurements. The dielectric properties of the $Ti_{1-x}Al_{2x}O_y$ films were assessed by impedance spectroscopy and current-voltage (I-V) measurements. Finally, the performance of $Ti_{1-x}Al_{2x}O_y$ as gate dielectric was investigated utilising a bottom-gate,

top-contact (BG–TC) TFT architecture (Figure 6-1.b) employing spray coated ZnO as the channel semiconductor. The electron mobility was extracted from the transfer characteristics in both the linear and saturation regime using the gradual channel approximation [40].

The devices were thermally annealed at 100°C in air for 30 min prior to their characterization. The latter constitutes a routine process for solution-processed ZnO-based transistors employing aluminum contacts. Although the underlying mechanism is not clear yet, such post-annealing in air at 100°C improved the transistors characteristics by significantly reducing the negative threshold voltage, subthreshold swing and hysteresis. We postulate that devices annealing in air repairs the damaged ZnO lattice by eliminating the uncontrollable oxygen vacancies in the surface of the subjacent ZnO layer.

5.3 Results and Discussion

5.3.1 Precursor thermal properties

Figure 5-2 illustrates the TGA and DSC data of aluminum (III) chloride. There is a pronounced mass loss in the temperature range of 150-200 °C, with an endothermic peak in DSC at about 180 °C. That mass loss is attributed to chloride part decomposition [41]. It has been reported that in the temperature range of 200-550 °C there is an amorphous Al_2O_3 which contains Cl^- and OH^- .

In Figure 5-3, the TGA and DSC data of titanium (IV) butoxide are presented. As shown there is a large mass loss (> 80 %) in the temperature range between 200 and 260 °C which is attributed to the release of CO_x as result of the burning process of the organic species originated from the butoxy group [42]. In the temperature range between 260 and 340 °C, Madarász et al. reported that the mass loss is due to the degradation of the remaining poly-butoxy group to a tarred carbonaceous chain which finally turned into TiO_2 at a temperature above 350 °C.

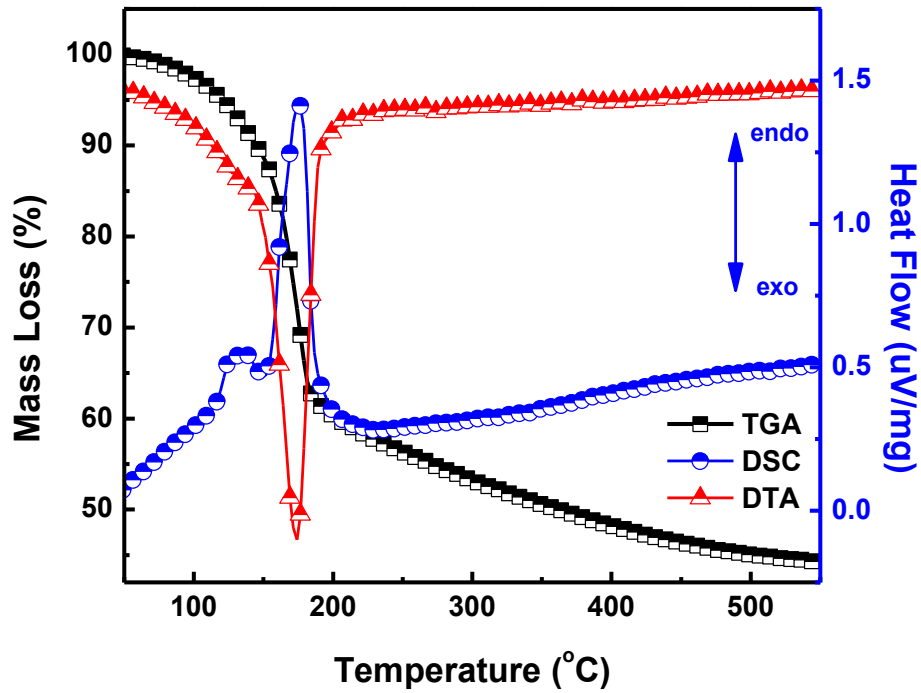


Figure 5-2: TGA and DSC data of aluminium (III) chloride powder. TGA and DSC measurements conducted under nitrogen at a heating rate of 10 K/min.

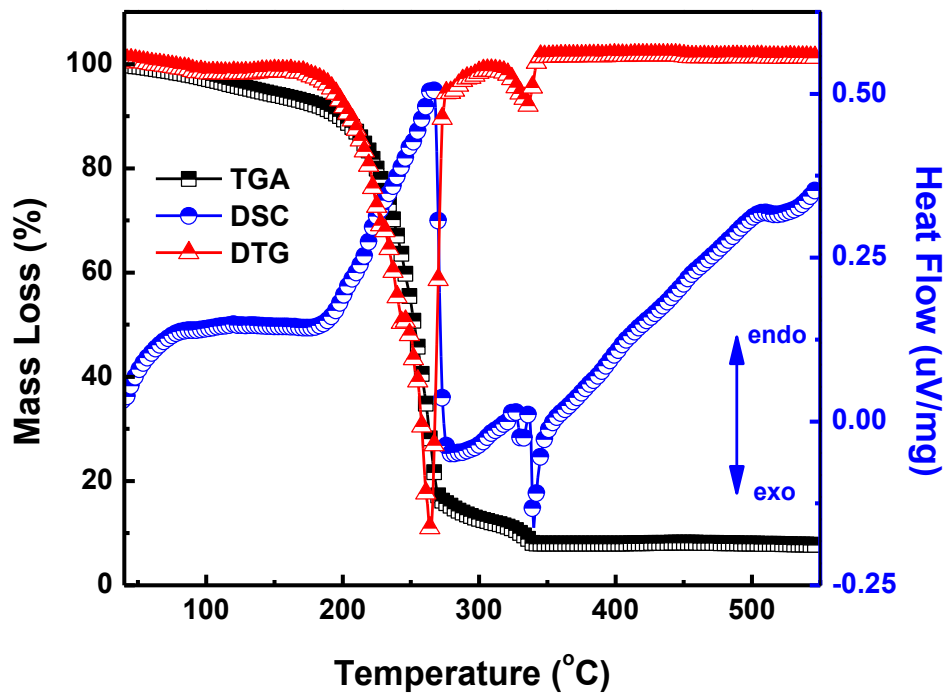


Figure 5-3: TGA and DSC data of titanium (IV) butoxide. TGA and DSC measurements conducted under nitrogen at a scan rate of 10K/min.

5.3.2 X-Ray Diffraction (XRD)

To investigate the microstructure of $Ti_{1-x}Al_{2x}O_y$ films, grazing incidence XRD (GIXRD) experiments were performed. Figure 5-4 presents the GIXRD patterns of selected $Ti_{1-x}Al_{2x}O_y$ films. Basal spacings is calculated using the Bragg equations while the average crystallite size is obtained using the Debye-Scherrer formula [43].

As can be seen from Figure 5-4, there are no diffraction peaks for the $Ti_{1-x}Al_{2x}O_y$ films other than the spray deposited TiO_2 . The absence of diffraction peaks in XRD pattern indicates amorphous $Ti_{1-x}Al_{2x}O_y$ films. It is already mentioned that amorphous structures are preferable for device applications. Besides the better environmental stability of amorphous oxides, such oxide structures exhibit high electrical quality interfaces with the active channel material [25]. The latter is of particular interest regarding the implementation of metal oxides as gate dielectrics in TFTs.

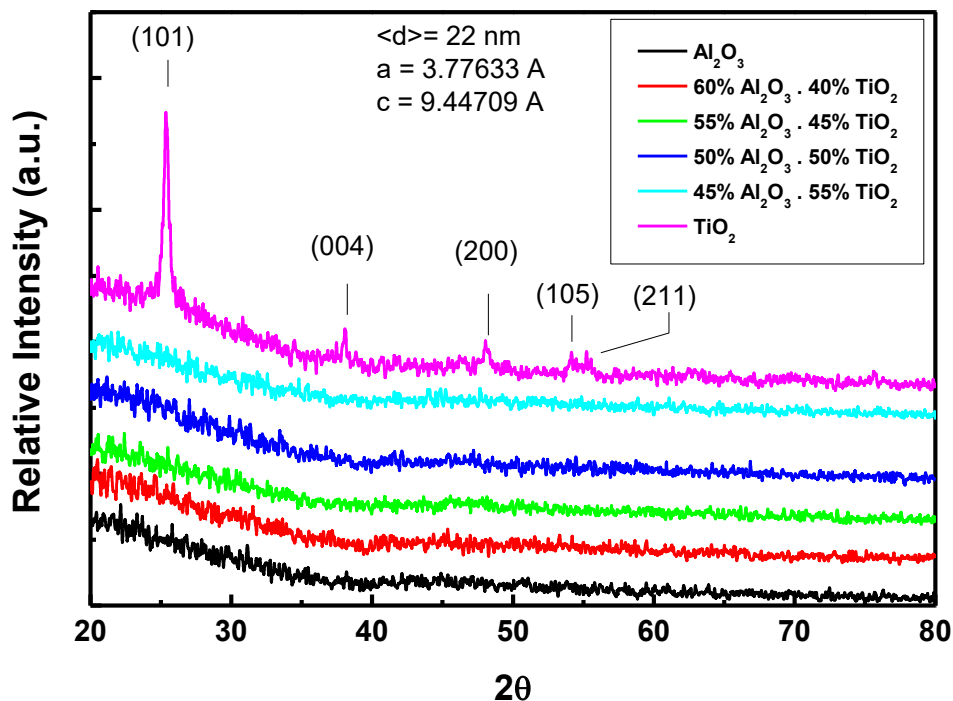


Figure 5-4: GIXRD patterns of selected $Ti_{1-x}Al_{2x}O_y$ films deposited by spray pyrolysis on c-Si substrates.

Analysis of the TiO_2 pattern (101) diffraction peak ($\sim 25.3^\circ$) using Debye-Scherrer formula yields an average crystal size of 22 nm. It should be noted that the indexing is based on the tetragonal anatase phase (ICDD 21-1272). Based on the crystallographic data the lattice parameters were in turn calculated and found to be $a=3.7763 \text{ \AA}$ and $c=9.4471 \text{ \AA}$ that are in excellent agreement with previous reported values [20].

5.3.3 Atomic Force Microscopy (AFM)

The surface morphologies of the spray deposited $Ti_{1-x}Al_{2x}O_y$ films were investigated by atomic force microscopy (AFM). Representative images of Al_2O_3 , TiO_2 and stoichiometric Al_2TiO_y films on silicon substrates are illustrated in Figure 5-5. The topography images of the spray deposited $Ti_{1-x}Al_{2x}O_y$ films reveal films of low roughness. Such smooth films are desired for the implementation of $Ti_{1-x}Al_{2x}O_y$ films as gate dielectric.

As it has been reported, a gate dielectric exhibiting a smooth surface is a low trap density at the interface between the gate dielectric and the semiconductor layer. It is well known that the surface roughness of the gate dielectric directly affects the quality of the interface between the insulator and the semiconductor in bottom gate (BG) structure TFTs. High quality interfaces between dielectric and semiconductor layer reduces the impact of scattering of the charge carriers on the mobility of a semiconductor.

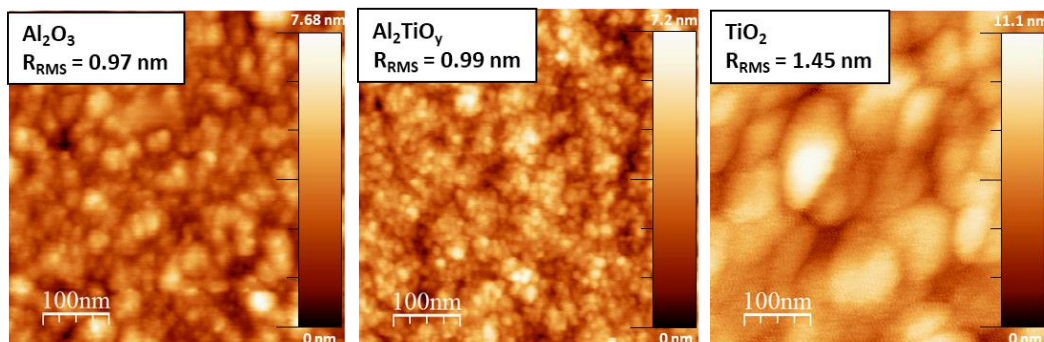


Figure 5-5: AFM topography images (RMS roughness inset) of spray deposited Al_2O_3 , stoichiometric Al_2TiO_y , and (c) TiO_2 films on silicon substrate.

5.3.4 UV-Vis-NIR Spectroscopy

The UV-Vis-NIR transmission spectra of $Ti_{1-x}Al_{2x}O_y$ films, deposited on fused silica substrates with varying $[Ti^{4+}]$ to $[Al^{3+}]$ atomic ratio, were recorded in transmission mode in the range of 190-1000 nm. The Tauc plots [44] of selected $Ti_{1-x}Al_{2x}O_y$ thin films are illustrated in Figure 5-6. The optical band gap as a function of the $[Ti^{4+}]/([Ti^{4+}]+2\cdot[Al^{3+}])$ ratio is shown in Figure 5-7.

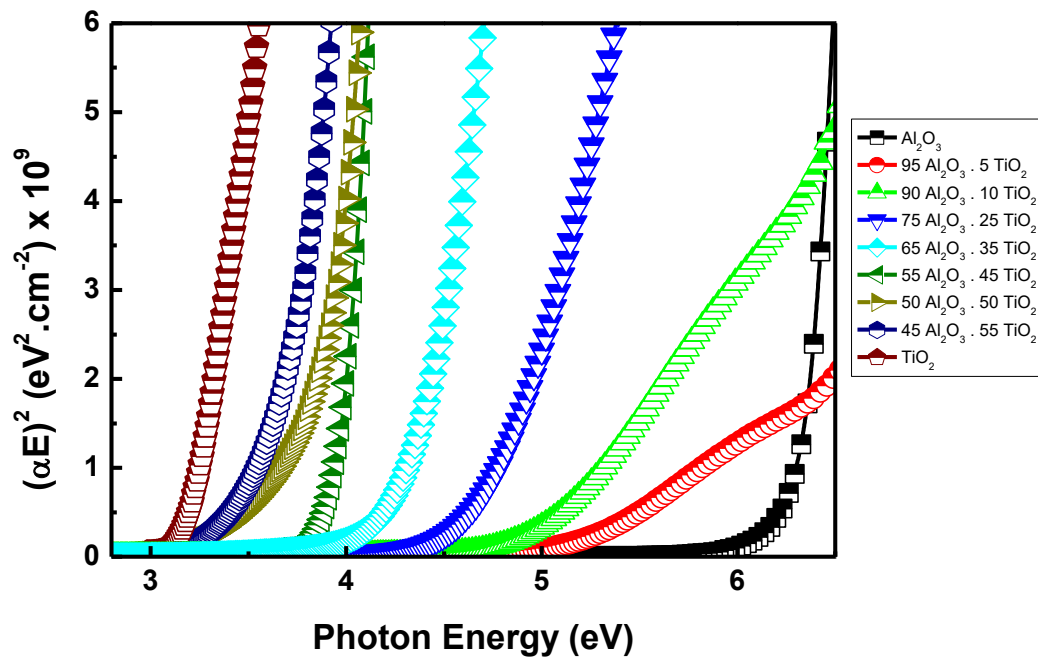


Figure 5-6: Tauc plots of selected $Ti_{1-x}Al_{2x}O_y$ films as function of the $[Ti^{4+}]/([Ti^{4+}]+2[Al^{3+}])$ ratio.

The optical band gap shows a monotonic decrease with increase in the $[Ti^{4+}]/([Ti^{4+}]+2\cdot[Al^{3+}])$ atomic ratio and varies between the 3.7 eV for TiO_2 and 6.5 eV for Al_2O_3 , respectively. Such trend has also been reported for other binary metal oxides [45].

The Urbach tail energy (E_u) is another optical parameter of interest that can be evaluated from UV-Vis-NIR measurements. Initially, E_u had been associated with band-to-band electronic transitions in alkali and silver halides. Over the last few decades, it has been proven to be a widespread tool for the study of disordered systems in general [46], [47]. E_u is often interpreted as the width of the tail of localised

states in the band gap. This exponential tail is a characteristic feature of disordered or low crystalline materials. In disordered and low crystalline materials, the degree of distortion is associated with the existence of localised states extended in the band gap. The presence of a high concentration of localised states in the band gap is related to the narrowing of the band gap in the case of disordered systems. In crystalline materials the disorder can be both static and dynamic. Dynamic disorder is due to exciton-phonon coupling, while the static atomic structural disorder is related to the presence of structural defects like atom vacancies and interstitials.

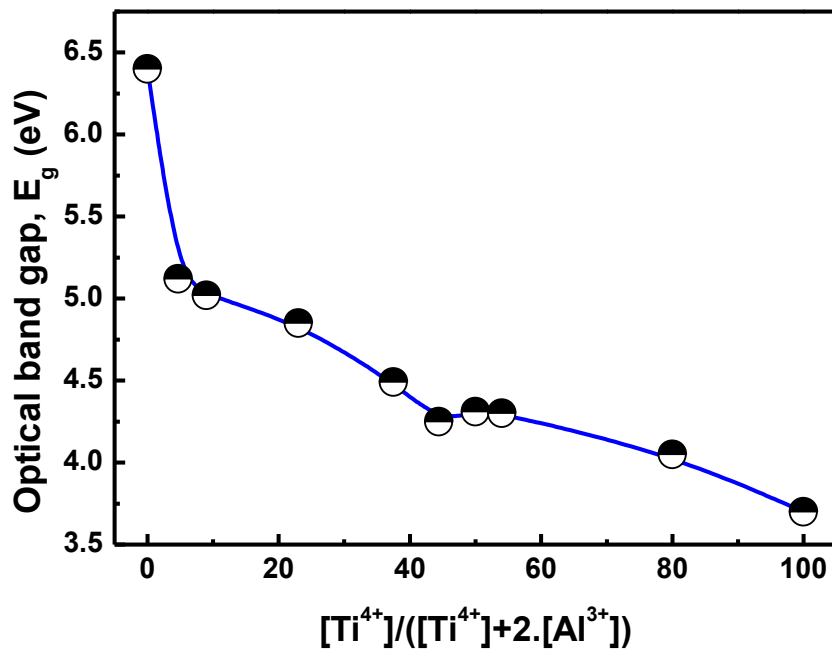


Figure 5-7: Optical band gap of $Ti_{1-x}Al_{2x}O_y$ thin films as a function of the $[Ti^{4+}]/([Ti^{4+}]+2[Al^{3+}])$ ratio. The solid line is a guide to the eye.

As shown in Figure 5-8, the E_u of $Ti_{1-x}Al_{2x}O_y$ films decrease monotonically with the increase of the $[Ti^{4+}]/([Ti^{4+}]+2[Al^{3+}])$ ratio, with a discontinuity at $[Ti^{4+}]/([Ti^{4+}]+2[Al^{3+}]) \sim 45\%$. This finding could be explained considering the thermal (dynamic) (E_v) as well as the static (E_s) components of E_u as described by [48]. A decrease of the dynamic disorder, E_v with the increase of titanium fraction in the films is expected to decrease the Urbach tail energy, which is considered as a qualitative measurement of disordering.

The sharp decrease of the $Ti_{1-x}Al_{2x}O_y$ composite at $[Ti^{4+}]/([Ti^{4+}]+2\cdot[Al^{3+}])\sim 45\%$ (in the solution), could be attributed to a further decrease of the so called static disorder [49]. At this ratio, the deposition of stoichiometric $Ti_{1-x}Al_{2x}O_y$, ($Al_2O_3\cdot Ti_2O$) is occurred. It should be pointed that the divergence from the 50 % is attributed to the hygroscopic nature of precursors i.e. the contribution of the H_2O molecules to the overall precursors' mass.

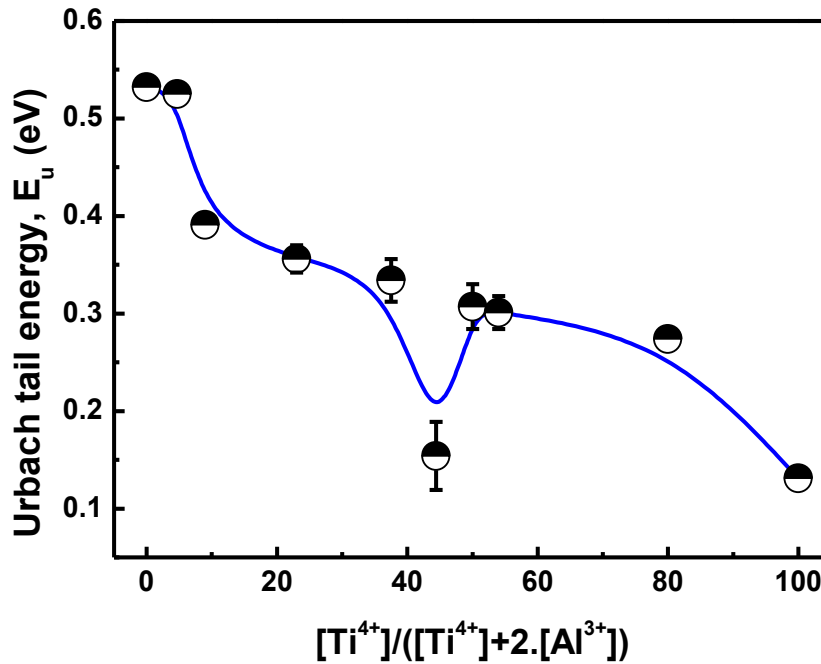


Figure 5-8: Urbach tail energy (E_u) as a function of the $[Ti^{4+}]/([Ti^{4+}]+2[Al^{3+}])$ ratio. The solid line guides the eye.

5.3.5 Spectroscopic Ellipsometry

Of particular importance is knowledge of the Schottky barrier heights between the dielectrics and contacts, in order to minimise carrier transport through the dielectric which leads to high leakage currents.

For a metal-semiconductor contact the Schottky barrier height is given by [23]:

$$\phi_n = S(\Phi_M - \Phi_S) + (\Phi_S - \chi_S) \quad (5-2)$$

where, (Φ_M) is the metal work function, (Φ_S) is the charge neutrality level of the semiconductor, (χ_S) is the electron affinity of the semiconductor and (S) is a dimensionless pinning factor which is empirically related to the electronic part of dielectric constant ϵ_∞ ,

$$S = \frac{1}{1 + 0.1(\epsilon_\infty - 1)^2} \quad (5-3)$$

The dimensionless parameter (S) describes the pinning degree of Schottky barriers. Its value is in the range $0 \leq S \leq 1$, where $S = 1$ for unpinned Schottky barriers and $S = 0$ for totally pinned barrier heights because of a large density of interfacial states.

Similarly, the electron barrier ϕ_n or conduction band offset of a high- k dielectric and a semiconductor is given by:

$$\phi_n = (\chi_a - \Phi_{S,a}) - (\chi_b - \Phi_{S,b}) + S(\Phi_{S,a} - \Phi_{S,b}) \quad (5-4)$$

and S depends on the ϵ_∞ of the wider gap material, the high- k oxide.

The high energy dielectric constant can be experimentally estimated by ellipsometry.

$$\epsilon_\infty = n^2 \quad (5-5)$$

where, (n) is the refractive index of the high- k oxide. In Figure 5-9 the Schottky barrier pinning factor S of the spray deposited Al_2O_3 , TiO_2 , and stoichiometric in the solution TAO dielectrics as well as a wide range of dielectrics grown by vacuum-based deposition techniques as well as solutions is presented.

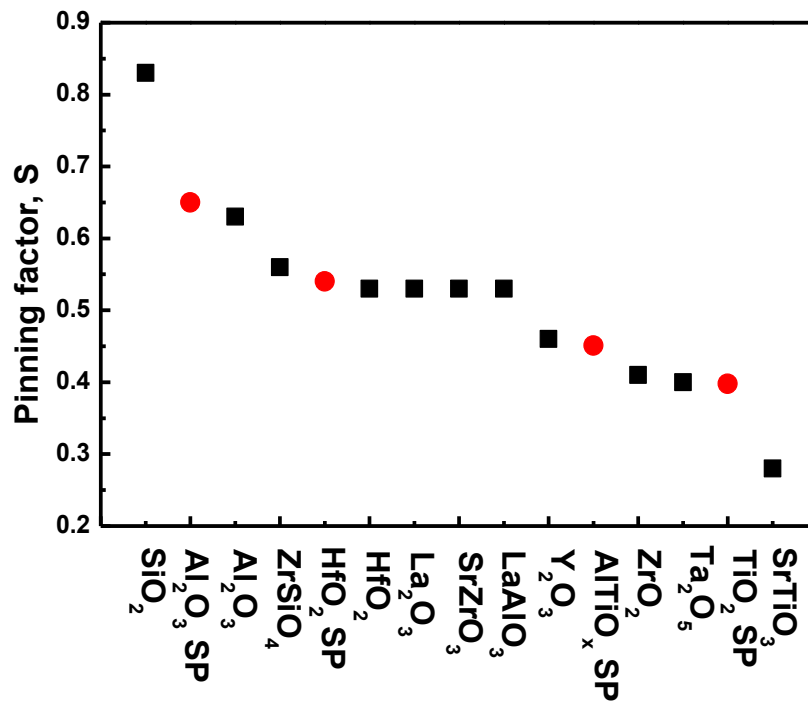


Figure 5-9: Schottky barrier pinning factor S of solution processed (SP) Al_2O_3 , TiO_2 , and stoichiometric in the solution dielectrics as well as a wide range of dielectrics grown by vacuum-based deposition techniques as well as solutions.

5.3.6 Impedance Spectroscopy

The frequency dispersions of the static dielectric constant of selected $Ti_{1-x}Al_{2x}O_y$ films, are illustrated in Figure 5-10. A distinct feature that is observed in Figure 5-10 is the shift of the dielectric loss toward higher frequencies of the film deposited from solutions having a stoichiometry of $[Ti^{4+}]/([Ti^{4+}]+2 \cdot [Al^{3+}]) \sim 50\%$. Considering the fact that a low frequencies dielectric loss denotes deteriorated dielectrics, it is obvious that films with such stoichiometry should be of improved insulating properties [18].

Another interesting feature is related to the dielectric constant dispersion of TiO_2 . As can be seen from Figure 5-10, a frequency dependence of the k value at low frequencies (<100 kHz) is observed in TiO_2 films. A k value of 63.5 was obtained at 100 Hz, but this value was reduced to a k value of 40.7 at 100 kHz. This frequency dependence of the dielectric constant is a very well-known issue in high- k dielectrics, especially in polycrystalline materials and it is related to grain size [50].

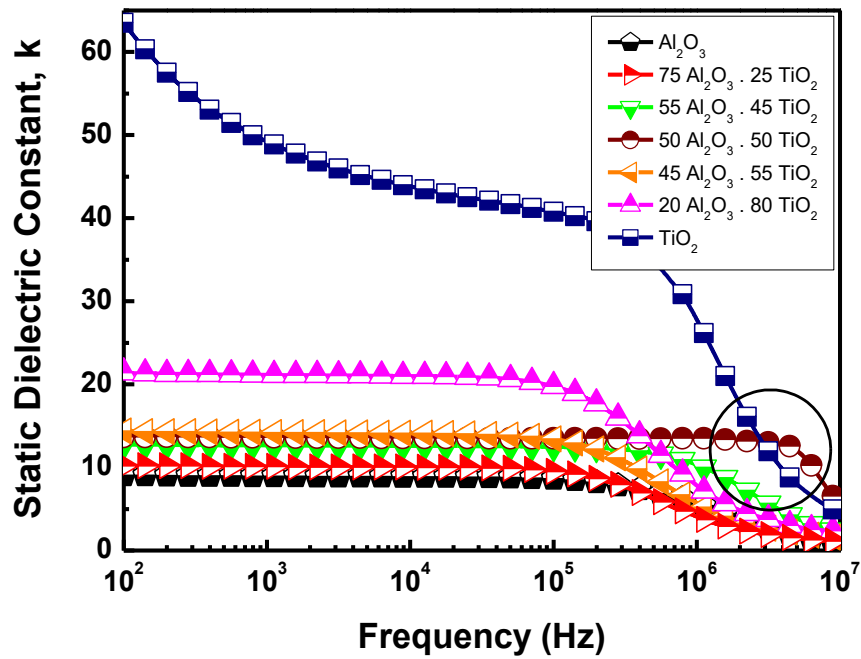


Figure 5-10: Static dielectric constant (k) dispersions of selected $Ti_{1-x}Al_{2x}O_y$ films deposited by spray pyrolysis.

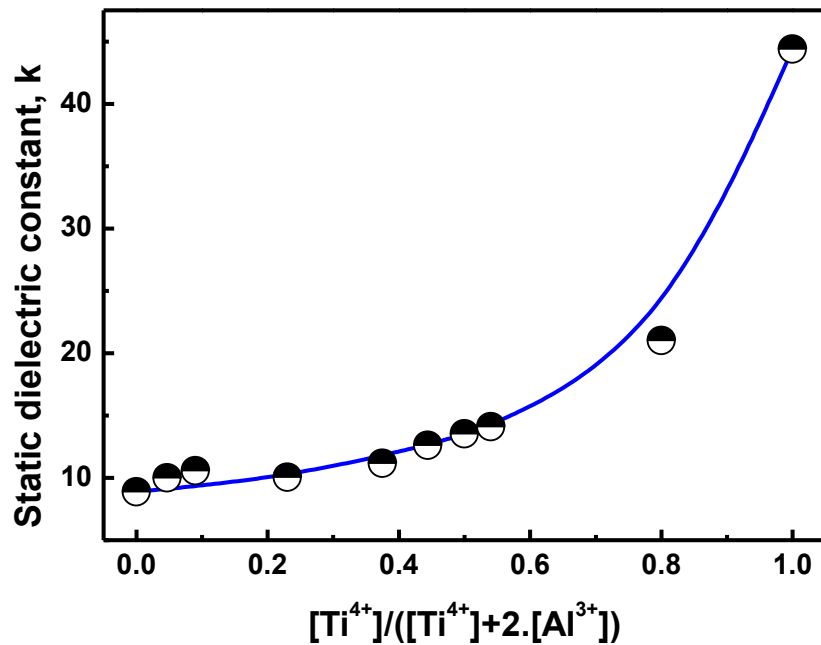


Figure 5-11: Dielectric constant (estimated at 10 kHz) of $Ti_{1-x}Al_{2x}O_y$ films as a function of the $[Ti^{4+}]/([Ti^{4+}]+2[Al^{3+}])$ ratio. The solid line guides the eye.

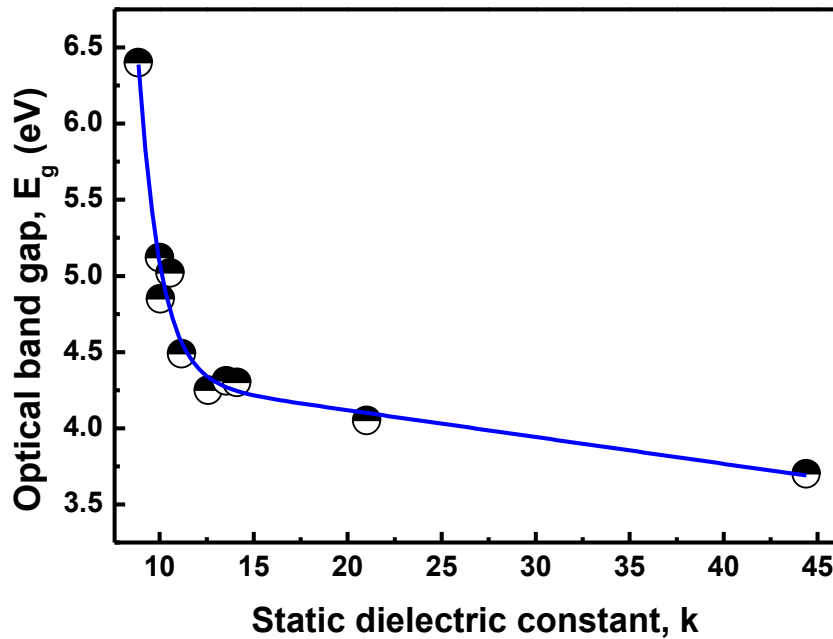


Figure 5-12: Static dielectric constant versus band gap of $Ti_{1-x}Al_{2x}O_y$ gate dielectrics deposited by spray pyrolysis. The solid line is a guide to the eye.

In Figure 5-11 the static dielectric constant (calculated at 10 kHz) of $Ti_{1-x}Al_{2x}O_y$ films as a function of the $[Ti^{4+}]/([Ti^{4+}]+2\cdot[Al^{3+}])$ ratio, is illustrated. As can be seen, there is a monotonic increase of the static dielectric constant with increasing the titanium content. Such trend has been reported and for other binary metal oxides where a low- k oxide is combined with a high- k one [45], [51].

It has been reported that the static dielectric constant varies inversely with the band gap [28]. This trend is also confirmed as shown in Figure 5-12.

5.3.7 I-V characteristics and leakage currents

To further investigate the dielectric properties of the spray deposited $Ti_{1-x}Al_{2x}O_y$ films, the current-voltage characteristics were measured. In Figure 5-13 the leakage current density versus electric field (J-E) of selected $Ti_{1-x}Al_{2x}O_y$ films for different $[Ti^{4+}]/([Ti^{4+}]+2\cdot[Al^{3+}])$ ratios are presented. Interestingly, even for a very high applied electric field of 3 MVcm^{-1} , no dielectric breakdown was observed.

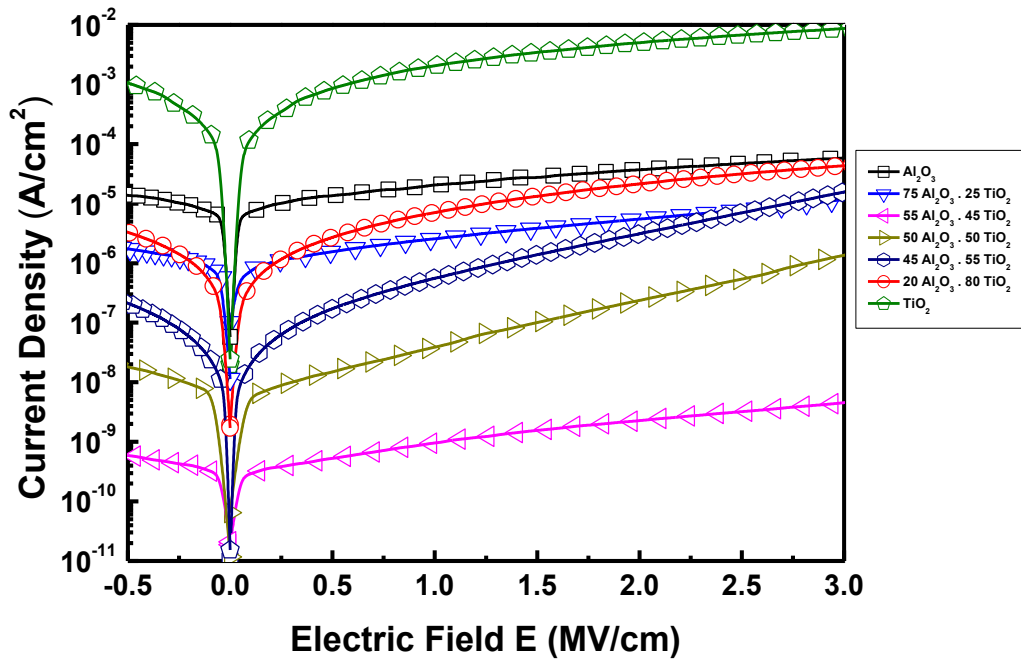


Figure 5-13: Current-Voltage characteristics of selected $Ti_{1-x}Al_{2x}O_y$ spray deposited dielectrics with different $[Ti^{4+}]/([Ti^{4+}]+2[Al^{3+}])$ ratio.

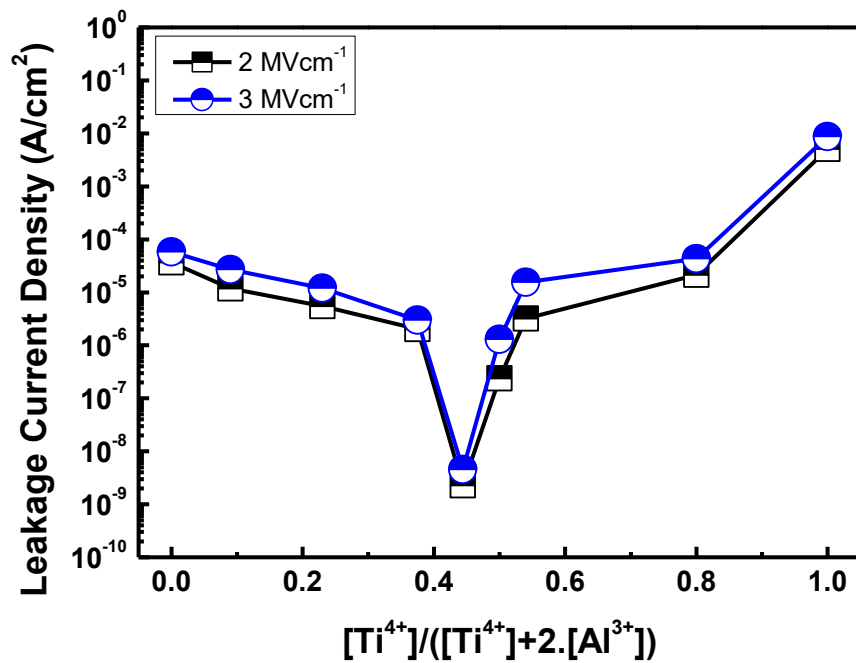


Figure 5-14: Leakage current density of solution processed $Ti_{1-x}Al_{2x}O_y$ gate dielectrics at 2 and 3 MV/cm as a function of the $[Ti^{4+}]/([Ti^{4+}]+2[Al^{3+}])$ ratio. The solid lines guide the eye.

The leakage current density of the solution processed $Ti_{1-x}Al_{2x}O_y$ gate dielectrics at 2 and 3 MV cm^{-1} as a function of the $[Ti^{4+}]/([Ti^{4+}]+2\cdot[Al^{3+}])$ ratio is presented in Figure 5-14. The stoichiometric $Ti_{1-x}Al_{2x}O_y$ exhibits the lowest leakage current. For the stoichiometric $Ti_{1-x}Al_{2x}O_y$ when an electric field of 2 MV/cm was applied, the leakage current density was of about ~ 2.3 nA/cm², while for an applied electrical field of 3 MV/cm the leakage current density was ~ 5 nA/cm².

It should be highlighted that the lowest Urbach tail energy appears at the same stoichiometry where the minimum leakage current is also observed. This is of particular interest, as it could be assumed that, at this stoichiometry, $[Ti^{4+}]/([Ti^{4+}]+2\cdot[Al^{3+}])\sim 45\%$ (where the formation of stoichiometric $Al_2O_3\cdot TiO_2$ is anticipated) the minimised disorder, as it is described by Urbach energy, gives rise to the reduced leakage current density. As mentioned before, the Urbach tail energy is associated with the width of localised states within the band gap of the materials. The existence of localised states in the band gap has been attributed to structural point defects, such as oxygen vacancies and metal interstitial, acting as electron and hole traps. So, the minimum of leakage current density for the case of the stoichiometric $Ti_{1-x}Al_{2x}O_y$, could be fairly attributed to the reduced localised states in the band gap for this ratio, which is associated with the minimum Urbach energy (E_u).

5.3.8 I-V Characteristics of TFTs

Finally, the performance of $Ti_{1-x}Al_{2x}O_y$ films as gate dielectrics was investigated. Bottom-gate, top-contact (BG-TC) TFT architectures (inset, Figure 5-15, Figure 5-16) employing spray coated ZnO as the channel material were used.

Initially, the $Ti_{1-x}Al_{2x}O_y$ films were deposited onto glass/ITO substrates followed by the sequential deposition of ZnO under ambient conditions. Thermally evaporated aluminium (Al) source and drain (S/D) contacts were then deposited, through a shadow mask, under high vacuum (10^{-6} mbar).

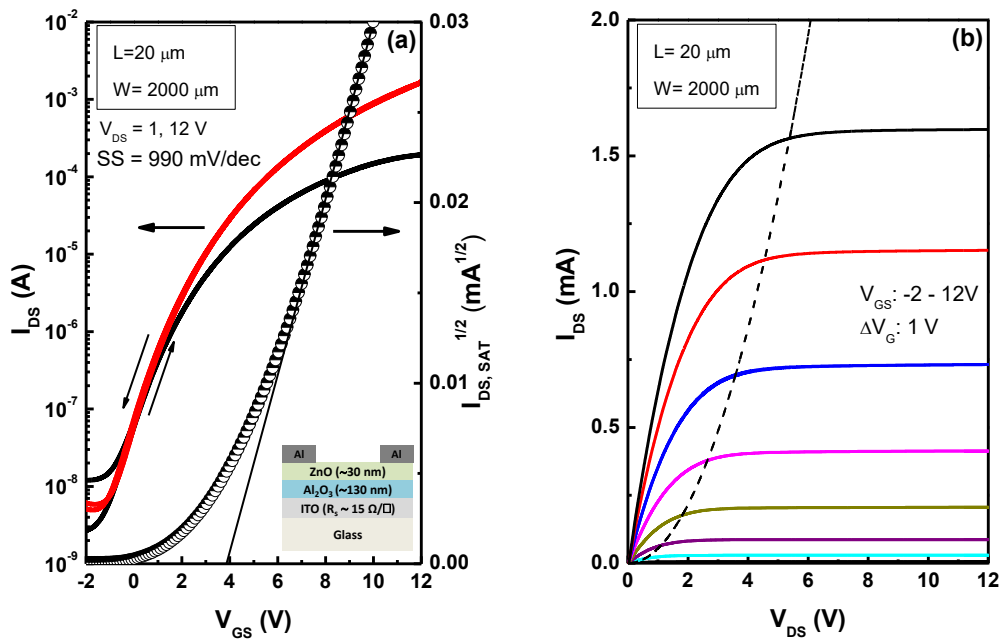


Figure 5-15: a) Transfer and b) output characteristics of ZnO-based TFTs employing spray coated Al_2O_3 gate dielectric.

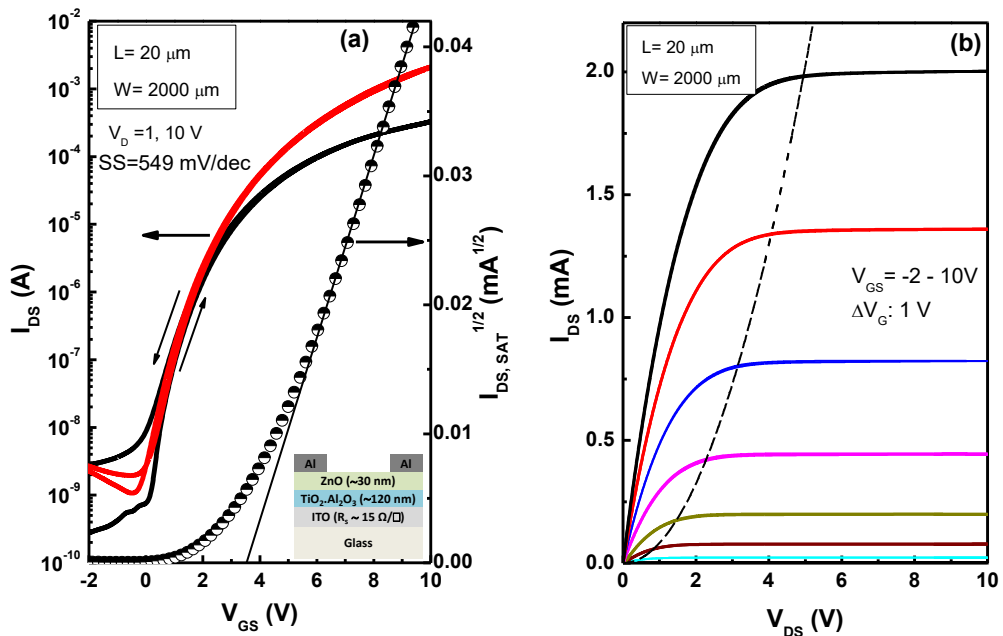


Figure 5-16: a) Transfer and b) output characteristics of ZnO-based TFTs employing $Ti_{1-x}Al_{2x}O_y$ gate dielectric ($[Ti^{4+}]/([Ti^{4+}] + 2[Al^{3+}]) \sim 45\%$).

Figure 5-15 and Figure 5-16 show a set of transfer and output characteristics obtained from a ZnO-based TFT ($L = 20 \mu\text{m}$, $W = 1000 \mu\text{m}$) consisted of a $\sim 120 \text{ nm}$ thick Al_2O_3 and 130 nm thick $Ti_{1-x}Al_{2x}O_y$ at $[Ti^{4+}]/([Ti^{4+}] + 2 \cdot [Al^{3+}]) \sim 45\%$.

The TFTs show excellent operating characteristics such as negligible hysteresis, high on/off current modulation ratio and electron mobility of about $10 \text{ cm}^2/\text{Vs}$. The implementation of stoichiometric $Ti_{1-x}Al_{2x}O_y$ (rather than Al_2O_3) as a gate dielectric had no significant impact on the electron mobility. However stoichiometric $Ti_{1-x}Al_{2x}O_y$ improved the on/off current modulation ratio by one order of magnitude (10^5 for Al_2O_3 and 10^6 for stoichiometric $Ti_{1-x}Al_{2x}O_y$). Also, the subthreshold swing (SS) decreased from 990 mV/dec for Al_2O_3 to 549 mV/dec for devices employing stoichiometric $Ti_{1-x}Al_{2x}O_y$. Interestingly, there were no working devices implementing TiO_2 gate dielectrics. This fact could be attributed to negative band offsets between TiO_2 and ZnO.

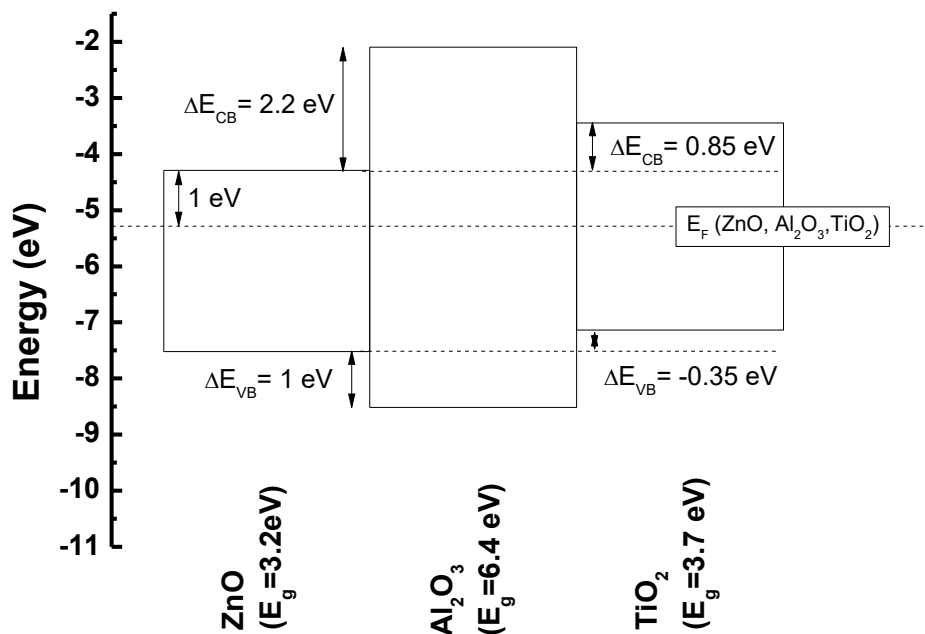


Figure 5-17: Band diagrams of ZnO, Al_2O_3 and TiO_2 and estimated conduction and valence band offsets on ZnO.

In Figure 5-17, a representation of the assumed band alignment diagram of Al_2O_3 and TiO_2 on ZnO is illustrated. It should be mentioned that the conduction band

minimum (E_{CB}) of ZnO is taken as the electron affinity (χ_e) of ZnO (4.2 eV) [52] and the work function, i.e., the position the fermi level (EF) for zinc oxide has been previously estimated to be 5.2 eV [53], [54]. In Figure 5-17 the conduction band minimum (E_{CB}) and valence band maximum (E_{VB}) of both Al_2O_3 and TiO_2 were estimated taking into account the calculated band gap values, 6.4 eV and 3.7 eV respectively, and assuming that the fermi level, in both the oxides, is located in the middle of their band gap and it is aligned with the fermi level of ZnO. As can be seen from Figure 5-17, the calculated conduction band offsets (ΔE_{CB}) of Al_2O_3 and TiO_2 on ZnO are of 2.2 eV and 0.85 eV respectively. From these findings, it becomes evident that TiO_2 does not meet the band offset criterion.

5.4 Conclusions

In this chapter the properties of the solution processed $Ti_{1-x}Al_{2x}O_y$ dielectrics as a function of the $[Ti^{4+}]/([Ti^{4+}]+2\cdot[Al^{3+}])$ atomic ratio (in the solution) were investigated. The films were deposited by spray coating in air at moderate substrate temperatures (420 °C) and were implemented as gate dielectrics in TFTs employing spray coated ZnO semiconducting channels.

All the $Ti_{1-x}Al_{2x}O_y$ films found to be amorphous and only TiO_2 was found to be crystalline. Further analysis shown (tetragonal) anatase phase of TiO_2 . Films exhibit very smooth surfaces, high dielectric constants, wide band gaps and low leakage currents. The stoichiometric $Ti_{1-x}Al_{2x}O_y$ showed high dielectric constant (~ 13), wide band gap (4.5 eV), and very low leakage currents ($\sim 5 \text{ nA/cm}^2$) at a high applied electric field of 3 MV/cm. There was not dielectric breakdown up to 3 MV/cm indicating the high dielectric strength of the spray deposited $Ti_{1-x}Al_{2x}O_y$ thin films.

Finally, the performance of the spray deposited $Ti_{1-x}Al_{2x}O_y$ films as gate dielectrics was investigated. The ZnO-based TFTs employing stoichiometric $Ti_{1-x}Al_{2x}O_y$ dielectrics, showed excellent characteristics, i.e., low operation voltage, hysteresis-free operation, high electron mobilities ($\sim 10 \text{ cm}^2/\text{Vs}$) high on/off current modulation ratio ($>10^5$) and low subthreshold swing (549 mV/dec).

5.5 References

- [1] G. Adamopoulos, S. Thomas, D. D. C. Bradley, M. a. McLachlan, and T. D. Anthopoulos, 'Low-voltage ZnO thin-film transistors based on Y_2O_3 and Al_2O_3 high- k dielectrics deposited by spray pyrolysis in air', *Appl. Phys. Lett.*, vol. 123503, no. 12, pp. 1–4, Mar. 2011.
- [2] A. Facchetti and T. J. Marks, *Transparent Electronics: From Synthesis to Applications*. Chichester, UK: John Wiley & Sons, Ltd, 2010.
- [3] J. Robertson, 'High dielectric constant gate oxides for metal oxide Si transistors', *Reports Prog. Phys.*, vol. 69, no. 2, pp. 327–396, Feb. 2006.
- [4] M. Ishida, K. Sawada, S. Yamaguchi, T. Nakamura, and T. Suzuki, 'Heteroepitaxial Si/ Al_2O_3 /Si structures', *Appl. Phys. Lett.*, vol. 55, no. 6, pp. 556–558, Aug. 1989.
- [5] H. Joon Kim, S. Yong No, D. Eom, and C. Seong Hwang, 'Property Improvement of Aluminum-Oxide Thin Films Deposited under Photon Radiation by Using Atomic Layer Deposition', *J. Korean Phys. Soc.*, vol. 49, no. 3, pp. 1271–1275, 2006.
- [6] M. S. Park, D. H. Lee, E. J. Bae, D.-H. Kim, J. G. Kang, D.-H. Son, and S. O. Ryu, 'Fabrication of Indium Gallium Zinc Oxide (IGZO) TFTs Using a Solution-Based Process', *Mol. Cryst. Liq. Cryst.*, vol. 529, no. 1, pp. 137–146, Oct. 2010.
- [7] S. a. Campbell, H.-S. Kim, D. C. Gilmer, B. He, T. Ma, and W. L. Gladfelter, 'Titanium dioxide (TiO_2)-based gate insulators', *IBM J. Res. Dev.*, vol. 43, no. 3, pp. 383–392, May 1999.
- [8] T. Fuyuki and H. Matsunami, 'Electronic Properties of the Interface between Si and TiO_2 Deposited at Very Low Temperatures', *Jpn. J. Appl. Phys.*, vol. 25, no. Part 1, No. 9, pp. 1288–1291, Sep. 1986.
- [9] N. Rausch, 'Thin TiO_2 Films Prepared by Low Pressure Chemical Vapor Deposition', *J. Electrochem. Soc.*, vol. 140, no. 1, p. 145, 1993.
- [10] H.-S. Kim, S. Cambell, and D. Gilmer, 'Charge trapping and degradation in high-permittivity TiO_2 dielectric films', *IEEE Electron Device Lett.*, vol. 18, no. 10, pp. 465–467, 1997.
- [11] J. B. Kim, C. Fuentes-Hernandez, W. J. Potscavage, X.-H. Zhang, and B. Kippelen, 'Low-voltage InGaZnO thin-film transistors with Al_2O_3 gate insulator grown by atomic layer deposition', *Appl. Phys. Lett.*, vol. 94, no. 14, p. 142107, Apr. 2009.
- [12] R. Branquinho, D. Salgueiro, L. Santos, P. Barquinha, L. Pereira, R. Martins, and E. Fortunato, 'Aqueous Combustion Synthesis of Aluminum Oxide Thin Films and Application as Gate Dielectric in GZTO Solution-Based TFTs', *ACS Appl. Mater. Interfaces*, vol. 6, no. 22, pp. 19592–19599, Nov. 2014.

- [13] Y. Li, Y. L. Pei, R. Q. Hu, Z. M. Chen, Y. Zhao, Z. Shen, B. F. Fan, J. Liang, and G. Wang, 'Effect of channel thickness on electrical performance of amorphous IGZO thin-film transistor with atomic layer deposited alumina oxide dielectric', *Curr. Appl. Phys.*, vol. 14, no. 7, pp. 941–945, Jul. 2014.
- [14] G. D. Wilk, R. M. Wallace, and J. M. Anthony, 'High- k gate dielectrics: Current status and materials properties considerations', *J. Appl. Phys.*, vol. 89, no. 10, pp. 5243–5275, May 2001.
- [15] I. Oja, A. Mere, M. Krunk, R. Nisumaa, C. H. Solterbeck, and M. Es-Souni, 'Structural and electrical characterization of TiO_2 films grown by spray pyrolysis', *Thin Solid Films*, vol. 515, no. 2 SPEC. ISS., pp. 674–677, 2006.
- [16] I. Oja, A. Mere, M. Krunk, C.-H. Solterbeck, and M. Es-Souni, 'Properties of TiO_2 Films Prepared by the Spray Pyrolysis Method', *Solid State Phenom.*, vol. 99–100, pp. 259–264, 2004.
- [17] P. S. Shinde, P. S. Patil, P. N. Bhosale, and C. H. Bhosale, 'Structural, optical, and photoelectrochemical properties of sprayed TiO_2 thin films: Effect of precursor concentration', *J. Am. Ceram. Soc.*, vol. 91, no. 4, pp. 1266–1272, 2008.
- [18] H. Tang, K. Prasad, R. Sanjinès, P. E. Schmid, and F. Lévy, 'Electrical and optical properties of TiO_2 anatase thin films', *J. Appl. Phys.*, vol. 75, no. 4, p. 2042, Feb. 1994.
- [19] A. Nakaruk, D. Ragazzon, and C. C. Sorrell, 'Anatase-rutile transformation through high-temperature annealing of titania films produced by ultrasonic spray pyrolysis', *Thin Solid Films*, vol. 518, no. 14, pp. 3735–3742, 2010.
- [20] D. A. H. Hanaor and C. C. Sorrell, 'Review of the anatase to rutile phase transformation', *J. Mater. Sci.*, vol. 46, no. 4, pp. 855–874, Feb. 2011.
- [21] A. Thilagam, D. J. Simpson, and R. Gerson, 'A first-principles study of the dielectric properties of TiO_2 polymorphs', *J. Phys. Condens. Matter*, vol. 23, no. 2, p. 025901, Jan. 2011.
- [22] L. J. Berberich and M. E. Bell, 'The Dielectric Properties of the Rutile Form of TiO_2 ', *J. Appl. Phys.*, vol. 11, no. 10, pp. 681–692, Oct. 1940.
- [23] J. Robertson, 'Band offsets of wide-band-gap oxides and implications for future electronic devices', *J. Vac. Sci. Technol. B Microelectron. Nanom. Struct.*, vol. 18, no. 3, p. 1785, May 2000.
- [24] J. Robertson, 'Electronic Structure and Band Offsets of High-Dielectric-Constant Gate Oxides', *MRS Bull.*, vol. 27, no. 03, pp. 217–221, Mar. 2002.
- [25] J. Robertson, 'High dielectric constant oxides', *Eur. Phys. J. Appl. Phys.*, vol. 28, no. 3, pp. 265–291, Dec. 2004.

- [26] J. Robertson, K. Xiong, and S. J. Clark, 'Band gaps and defect levels in functional oxides', *Thin Solid Films*, vol. 496, pp. 1–7, 2006.
- [27] J. Robertson and R. M. Wallace, 'High- k materials and metal gates for CMOS applications', *Mater. Sci. Eng. R Reports*, vol. 88, pp. 1–41, Feb. 2015.
- [28] S. A. Campbell, D. C. Gilmer, Xiao-Chuan Wang, Ming-Ta Hsieh, Hyeon-Seag Kim, W. L. Gladfelter, and Jinhua Yan, 'MOSFET transistors fabricated with high permittivity TiO_2 dielectrics', *IEEE Trans. Electron Devices*, vol. 44, no. 1, pp. 104–109, 1997.
- [29] O. Auciello, W. Fan, B. Kabius, S. Saha, J. A. Carlisle, R. P. H. Chang, C. Lopez, E. A. Irene, and R. A. Baragiola, 'Hybrid titanium-aluminum oxide layer as alternative high- k gate dielectric for the next generation of complementary metal-oxide-semiconductor devices', *Appl. Phys. Lett.*, vol. 86, no. 4, p. 042904, Jan. 2005.
- [30] L. Shi, Y. D. Xia, B. Xu, J. Yin, and Z. G. Liu, 'Thermal stability and electrical properties of titanium-aluminum oxide ultrathin films as high- k gate dielectric materials', *J. Appl. Phys.*, vol. 101, no. 3, p. 034102, Feb. 2007.
- [31] D. . Kuo and K. . Tzeng, 'Growth and properties of titania and aluminum titanate thin films obtained by r.f. magnetron sputtering', *Thin Solid Films*, vol. 420–421, no. 1, pp. 497–502, Dec. 2002.
- [32] Y. Baek, S. Lim, L. H. Kim, S. Park, S. W. Lee, T. H. Oh, S. H. Kim, and C. E. Park, ' Al_2O_3/TiO_2 nanolaminate gate dielectric films with enhanced electrical performances for organic field-effect transistors', *Org. Electron.*, vol. 28, pp. 139–146, Jan. 2016.
- [33] D. A. D. C. Weerakkody, 'Engineered High- k Oxides', University of Liverpool, 2016.
- [34] P. K. Nayak, J. A. Caraveo-Frescas, Z. Wang, M. N. Hedhili, Q. X. Wang, and H. N. Alshareef, 'Thin film complementary metal oxide semiconductor (CMOS) device using a single-step deposition of the channel layer.', *Sci. Rep.*, vol. 4, p. 4672, Apr. 2014.
- [35] M. S. Oh, K. Lee, J. H. Song, B. H. Lee, M. M. Sung, D. K. Hwang, and S. Im, 'Improving the Gate Stability of ZnO Thin-Film Transistors with Aluminum Oxide Dielectric Layers', *J. Electrochem. Soc.*, vol. 155, no. 12, p. H1009, 2008.
- [36] P. D. Ye, B. Yang, K. K. Ng, J. Bude, G. D. Wilk, S. Halder, and J. C. M. Hwang, 'GaN metal-oxide-semiconductor high-electron-mobility-transistor with atomic layer deposited Al_2O_3 as gate dielectric', *Appl. Phys. Lett.*, vol. 86, no. 6, p. 063501, Feb. 2005.

- [37] G. Huang, L. Duan, G. Dong, D. Zhang, and Y. Qiu, 'High-Mobility Solution-Processed Tin Oxide Thin-Film Transistors with High- k Alumina Dielectric Working in Enhancement Mode', *ACS Appl. Mater. Interfaces*, vol. 6, no. 23, pp. 20786–20794, Dec. 2014.
- [38] B. P. Dhonge, T. Mathews, S. T. Sundari, C. Thinaharan, M. Kamruddin, S. Dash, and A. K. Tyagi, 'Spray pyrolytic deposition of transparent aluminum oxide (Al_2O_3) films', *Appl. Surf. Sci.*, vol. 258, no. 3, pp. 1091–1096, Nov. 2011.
- [39] G. Adamopoulos, A. Bashir, W. P. Gillin, S. Georgakopoulos, M. Shkunov, M. A. Baklar, N. Stingelin, D. D. C. Bradley, and T. D. Anthopoulos, 'Structural and Electrical Characterization of ZnO Films Grown by Spray Pyrolysis and Their Application in Thin-Film Transistors', *Adv. Funct. Mater.*, vol. 21, no. 3, pp. 525–531, Feb. 2011.
- [40] D. Hong, G. Yerubandi, H. Q. Chiang, M. C. Spiegelberg, and J. F. Wager, 'Electrical Modeling of Thin-Film Transistors', *Crit. Rev. Solid State Mater. Sci.*, vol. 33, no. 2, pp. 101–132, May 2008.
- [41] M. Hartman, O. Trnka, and O. Šolcová, 'Thermal Decomposition of Aluminum Chloride Hexahydrate', *Ind. Eng. Chem. Res.*, vol. 44, no. 17, pp. 6591–6598, Aug. 2005.
- [42] J. Madarász, A. Brăileanu, M. Crișan, and G. Pokol, 'Comprehensive evolved gas analysis (EGA) of amorphous precursors for S-doped titania by in situ TG–FTIR and TG/DTA–MS in air: Part 2. Precursor from thiourea and titanium(IV)-*n*-butoxide', *J. Anal. Appl. Pyrolysis*, vol. 85, no. 1–2, pp. 549–556, May 2009.
- [43] A. L. Patterson, 'The Scherrer Formula for X-Ray Particle Size Determination', *Phys. Rev.*, vol. 56, no. 10, pp. 978–982, Nov. 1939.
- [44] J. Tauc, 'Optical properties and electronic structure of amorphous Ge and Si', *Mater. Res. Bull.*, vol. 3, no. 1, pp. 37–46, Jan. 1968.
- [45] M. Esro, R. Mazzocco, G. Vourlias, O. Kolosov, A. Krier, W. I. Milne, and G. Adamopoulos, 'Solution processed lanthanum aluminate gate dielectrics for use in metal oxide-based thin film transistors', *Appl. Phys. Lett.*, vol. 106, no. 20, p. 203507, May 2015.
- [46] F. Urbach, 'The Long-Wavelength Edge of Photographic Sensitivity and of the Electronic Absorption of Solids', *Phys. Rev.*, vol. 92, no. 5, pp. 1324–1324, Dec. 1953.
- [47] D. J. Dunstan, 'Evidence for a common origin of the Urbach tails in amorphous and crystalline semiconductors', *J. Phys. C Solid State Phys.*, vol. 15, no. 13, p. 008, May 1982.

-
- [48] G. D. Cody, T. Tiedje, B. Abeles, B. Brooks, and Y. Goldstein, 'Disorder and the Optical-Absorption Edge of Hydrogenated Amorphous Silicon', *Phys. Rev. Lett.*, vol. 47, no. 20, pp. 1480–1483, Nov. 1981.
- [49] K. Tanaka, 'Minimal Urbach energy in non-crystalline materials', *J. Non. Cryst. Solids*, vol. 389, pp. 35–37, Apr. 2014.
- [50] C. C. C. Z. Zhao, C. C. C. Z. Zhao, M. Werner, S. Taylor, and P. Chalker, 'Dielectric relaxation of high- k oxides.', *Nanoscale Res. Lett.*, vol. 8, no. 1, p. 456, Jan. 2013.
- [51] C. Z. Zhao, S. Taylor, M. Werner, P. R. Chalker, R. T. Murray, J. M. Gaskell, and A. C. Jones, 'Dielectric relaxation of lanthanum doped zirconium oxide', *J. Appl. Phys.*, vol. 105, no. 4, 2009.
- [52] K. Ellmer, A. Klein, and B. Rech, *Transparent Conductive Zinc Oxide*, vol. 104. 2008.
- [53] Z. Zhang, C. Shao, X. Li, L. Zhang, H. Xue, C. Wang, and Y. Liu, 'Electrospun Nanofibers of ZnO–SnO₂ Heterojunction with High Photocatalytic Activity', *J. Phys. Chem. C*, vol. 114, no. 17, pp. 7920–7925, May 2010.
- [54] L. Zheng, Y. Zheng, C. Chen, Y. Zhan, X. Lin, Q. Zheng, K. Wei, and J. Zhu, 'Network Structured SnO₂/ZnO Heterojunction Nanocatalyst with High Photocatalytic Activity', *Inorg. Chem.*, vol. 48, no. 5, pp. 1819–1825, Mar. 2009.

6. Niobium Aluminate $\text{Nb}_{1-x}\text{Al}_x\text{O}_y$ Thin Films

6.1 Introduction

Over the last years there has been an extensive interest in the implementation of transition metal oxides (TMOs) as gate dielectrics in the microelectronic industry. Typical examples of well-studied TMOs that attracted much scientific interest are Y_2O_3 [1]–[4], ZrO_2 [5]–[10] and HfO_2 [11]–[16].

Niobium oxide (NbO_x) is another TMO. NbO_x thin films have been deposited by a large number of deposition methods, including vacuum and solution based techniques [17], [18], [27]–[36], [19], [37]–[45], [20]–[26]. A comprehensive review of the physical properties of niobium oxides and niobates were reported by Nico et. al., [46]. The major drawback of niobium oxide is that it exhibits polymorphism. There are three stable niobium oxides i.e. niobium monoxide (NbO), niobium dioxide (NbO_2) and niobium pentoxide (Nb_2O_5) with different electrical properties. Niobium monoxide is a conductor, niobium dioxide is a semiconductor and niobium pentoxide is an insulator [47]. It has also been reported that NbO_x thin films deposited at moderate temperatures ($<400^\circ\text{C}$) are amorphous [18], [21]. In the microelectronics industry, amorphous dielectric metal oxides are preferable over their crystalline counterparts, as they better conform with the semiconductors used today, eliminating electrical defects at the interface which deteriorate the performance of devices. As an alternative, perfectly lattice matched, epitaxial oxide layers should be considered.

Amorphous dielectrics that simultaneously are of a high dielectric constant (k) and wide band gap are of great scientific interest. This is because by increasing the dielectric constant of a material, the geometric capacitance per unit area (C_{ox}) at a given film thickness (t_{ox}) is also increased ($C_{\text{ox}}=k/t_{\text{ox}}$), while a wide band gap ensures good insulating properties. Unfortunately, there is a trade-off between the dielectric constant and the optical band gap (Figure 2-6). Wide band gap materials are of low dielectric constant, while materials of high dielectric constant exhibit narrow optical band gap. An empirical relationship that describes the trade-off between static dielectric constant and band gap has been reported [48].

Narrow band gap materials (<4 eV) are not suitable to be implemented as gate dielectrics in TFTs employing wide band gap semiconductors (>3 eV), as the band offset

criterion dictates that there must be an energy difference of >1 eV between valence and conduction band of the dielectric and the active channel material ones, in order for the leakage current to be minimized, due to injection into their bands [50].

As previously mentioned, NbO_x films deposited at substrate temperatures up to 400°C are amorphous, while the dielectric constant of NbO_x was found to be in the range between 10 and 100 depending on the deposition conditions. However, like other high- k metal oxides, NbO_x has a relatively narrow band gap (E_g) of 3.3-3.6 eV. Besides the high dielectric constant of NbO_x and the relatively small E_g does not make it a suitable gate dielectric material in ZnO-based TFTs. However, it has been reported that ternary metal oxides in the form of $\text{M}_{1-x}\text{Al}_x\text{O}_y$ where M is a transition metal (TM), seem to be amorphous and exhibit at the same time wide band gap and high dielectric constant [51], [52], [61], [62], [53]–[60]. This is mainly because of the combination of the Al_2O_3 's wide band gap ($E_g \sim 9$ eV) with the TM's high dielectric constant.

The aim of this work is to investigate the structural, optical and electrical properties of a novel ternary metal oxide that consists of high- k niobium oxide and the wide band gap aluminum oxide which possesses at the same time a high dielectric constant, a wide band gap, low leakage current, and high dielectric strength. Moreover, such a dielectric should enhance the performance of a ZnO-based TFT when it is implemented as gate dielectric.

6.2 Experimental

6.2.1 Precursor and Solutions

The precursor materials that have been used in this study were AlCl_3 (Alfa Aesar, 99%), NbCl_5 (Alfa Aesar, 99.9%) and $\text{Zn}(\text{O}_2\text{C}_2\text{H}_3)_2 \cdot 2\text{H}_2\text{O}$ (Alfa Aesar, ACS, 98-101%). All the precursor materials were used as received without any further purification. In this study ethanol ($\text{C}_2\text{H}_5\text{OH}$, VWR, ACS, $\geq 99.8\%$) was used as solvent. However, ethanol has low boiling point ($\sim 65^\circ\text{C}$) and evaporates rapidly. To slow down solvent evaporation, and thereby hinder particle formation, ethanol was mixed with

acetylacetone ($\text{CH}_3\text{COCH}_2\text{COCH}_3$, Alfa Aesar, 99%) a high boiling point ($\sim 140^\circ\text{C}$) solvent [63].

For the preparation of the niobium-aluminate precursor solutions, two ethanol-based solutions of AlCl_3 and NbCl_5 at a concentration of 0.1 M were prepared. Acetylacetone (AcAc) was added in both solutions at $\text{C}_2\text{H}_5\text{OH}:\text{AcAc}$ molar ratio of 5:1. The solutions were left under continuous stirring for at least 1h prior deposition, ensuring complete dissolution. The stoichiometry of aluminum to niobium atomic ratio was controlled by simple blending of the appropriate amount of the precursor's solutions.

The ZnO precursor solution was prepared by dissolving $\text{Zn}(\text{O}_2\text{C}_2\text{H}_3)_2 \cdot 2\text{H}_2\text{O}$ in methanol at a concentration of 0.1 M [64].

6.2.2 Device Fabrication

Metal-insulator-metal (MIM) 2-terminal devices (Figure 6-1.a) were fabricated by spraying the precursor solution onto glass ITO coated glass substrates, followed by deposition of thermally evaporated gold (Au) contacts (~ 100 nm) through a shadow mask. The niobium-aluminate's precursor solution was sprayed onto the glass/ITO substrates at 400°C employing a pneumatic airbrush, held at a vertical distance of about 30 cm. Aerosols of the precursors and blends were spray-coated for 30 s while the spray coating process was interrupted for 20 s to allow the vapours to settle. The cycle was repeated until films of typical thickness of ~ 100 nm, were obtained.

BG-TC transistors (Figure 6-1.b) were fabricated by spray coating the glass/ITO/ $\text{Nb}_{1-x}\text{Al}_x\text{O}_y$ stack with the ZnO precursor solution, followed by deposition of thermally evaporated gold (Au) source and drain (S/D) electrodes (~ 60 nm) through a shadow mask. The ZnO precursor solution was sprayed onto the glass/ITO substrates at 400°C , employing the same experimental conditions as previously, until a film of typical thickness of ~ 30 nm was obtained.

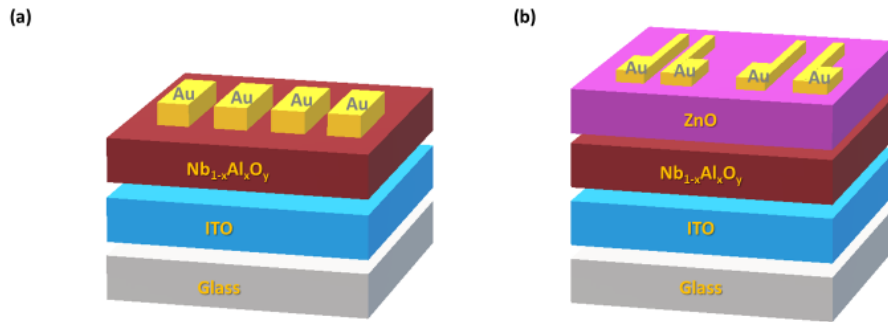


Figure 6-1: (a) MIM capacitor and (b) Bottom gate-top contact (BG-TC) ZnO-based TFT structures used in this study, implementing $Nb_{1-x}Al_xO_y$ thin film dielectric.

6.2.3 Thin Film & Device Characterisation Techniques

The thermal properties of the precursor materials were investigated by thermal gravimetric analysis (TGA) and differential scanning calorimetry (DSC). The microstructure of the spray deposited $Ti_{1-x}Al_{2x}O_y$ thin films were characterised by X-ray diffraction. The optical properties of the $Nb_{1-x}Al_xO_y$ films were investigated by Fourier transform infrared (FTIR) and UV-Vis-NIR spectroscopy. The dielectric properties of the $Nb_{1-x}Al_xO_y$ films were investigated by impedance spectroscopy and current-voltage (I-V) measurements. Finally, the performance of $Nb_{1-x}Al_xO_y$ as the gate dielectric in TFTs was investigated utilising a bottom-gate, top-contact BG-TC TFT architecture (Figure 6-1.b) employing spray coated ZnO as the channel semiconductor. The electron mobility was extracted from the transfer characteristics at linear and saturation using the gradual channel approximation [65].

6.3 Results and Discussion

6.3.1 Precursor thermal properties

The thermal properties of $AlCl_3$ were studied in a previous chapter. In Figure 6-2 the TGA and DSC of $NbCl_5$ are presented. There is a negligible mass loss at a temperature range of 100-130 °C due to the dehydration of the absorbed water molecules in $(NbCl_5)$. In the temperature range between 150 and 350 °C there is a significant mass loss (>80%) which is related to the decomposition of HCl fragments, a product of the interaction of $NbCl_5$ and the atmospheric moisture [66]. As shown in Figure 6-2, there is a set of exothermic peaks within this temperature (150-350 °C) with a discontinuity at about 210 °C where the melting point of $NbCl_5$ is.

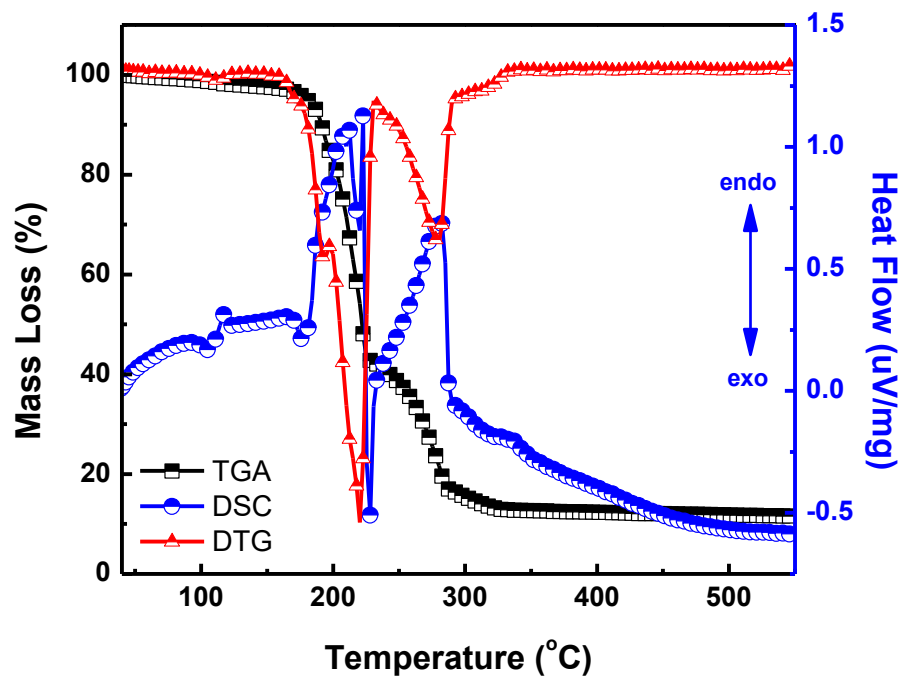


Figure 6-2: TGA and DSC data of niobium (V) chloride. TGA and DSC measurements conducted under nitrogen at a scan rate of 10K/min

6.3.2 UV-Vis-NIR Spectroscopy

The UV-Vis-NIR spectra of $\text{Nb}_{1-x}\text{Al}_x\text{O}_y$ films with varying $[\text{Nb}^{5+}]$ to $[\text{Al}^{3+}]$ atomic ratio were recorded in transmission mode in the range of 190-1000 nm. The Tauc plots [67] of selected $\text{Nb}_{1-x}\text{Al}_x\text{O}_y$ films are illustrated in Figure 6-3. The optical band gap as a function of the $[\text{Nb}^{5+}]/([\text{Al}^{3+}]+[\text{Nb}^{5+}])$ atomic ratio is shown in Figure 6-4.

The optical band gap shows a monotonic decrease with increase of the $[\text{Nb}^{5+}]/([\text{Al}^{3+}]+[\text{Nb}^{5+}])$ atomic ratio between the 4.2 eV for NbO_x and the 6.5 eV for Al_2O_3 , respectively. It should be noticed that a band gap of 4.2 eV for niobium oxide thin films is quite high. Such high band gap for niobium oxide has been reported by Agarwal and Reddy [68], and has been attributed to an amorphous/highly-disordered structure of the film.

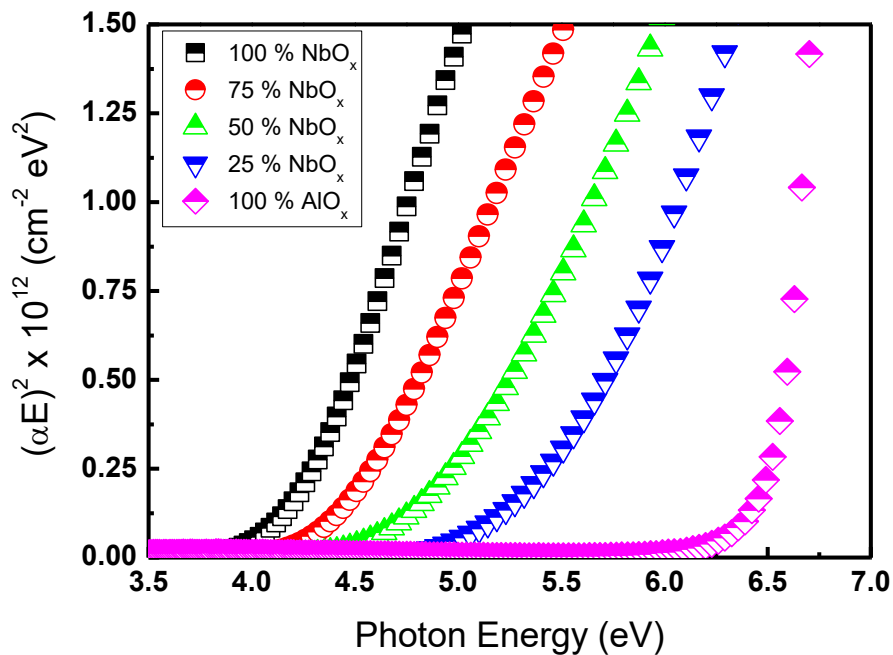


Figure 6-3: Tauc plots of selected $\text{Nb}_{1-x}\text{Al}_x\text{O}_y$ films of different $[\text{Nb}^{5+}]/([\text{Nb}^{5+}]+[\text{Al}^{3+}])$ ratios.

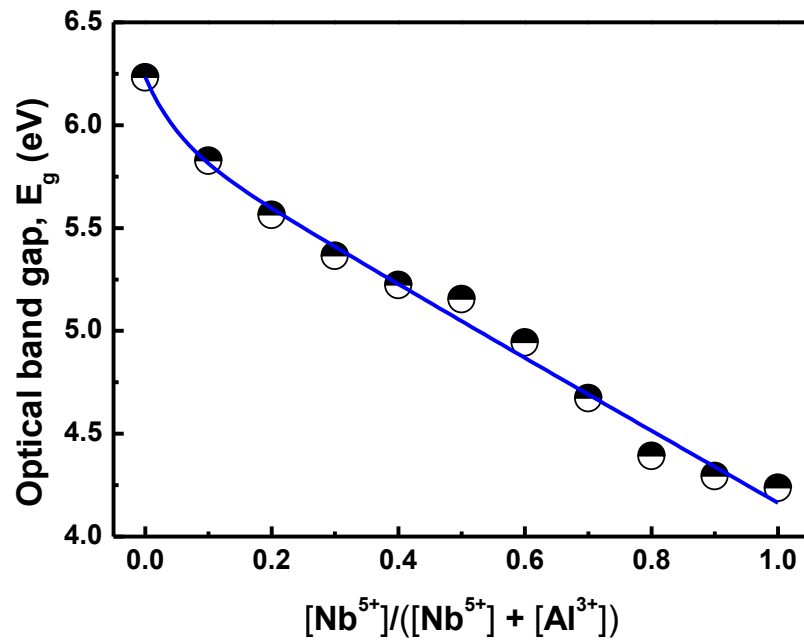


Figure 6-4: Optical band gap of $\text{Nb}_{1-x}\text{Al}_x\text{O}_y$ thin films as a function of the $[\text{Nb}^{5+}]/([\text{Nb}^{5+}] + [\text{Al}^{3+}])$ ratio. The solid line is a guide to the eye.

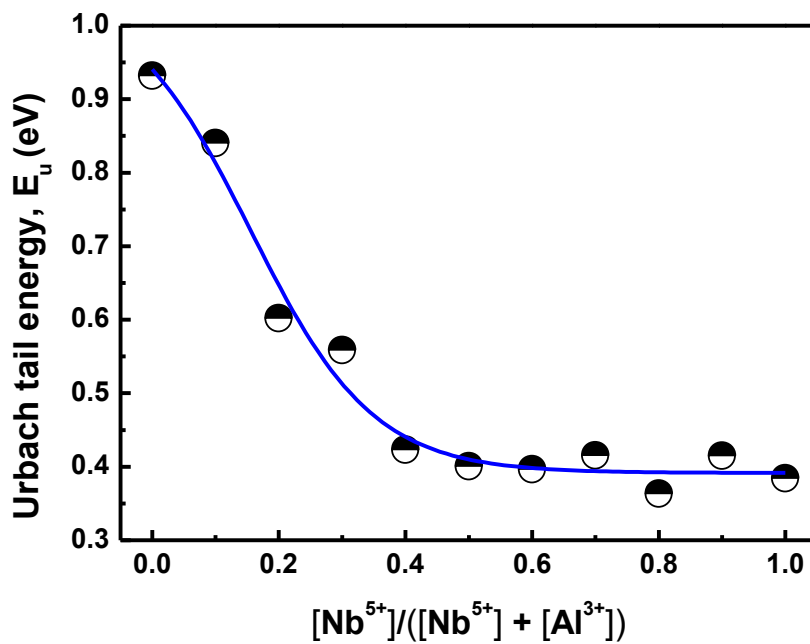


Figure 6-5: Urbach tail energy (E_u) as a function of the $[\text{Nb}^{5+}]/([\text{Nb}^{5+}] + [\text{Al}^{3+}])$ ratio. The solid line guides the eye.

The Urbach tail energy (E_u) has been proven to be a widespread tool for the study of disorder systems and is associated to the width of the tails of localised states

in the band gap [69], [70]. As shown in Figure 6-5, the Urbach tail energy of $\text{Nb}_{1-x}\text{Al}_x\text{O}_y$ films primarily exhibits a decrease as the $[\text{Nb}^{5+}]/([\text{Al}^{3+}]+[\text{Nb}^{5+}])$ ratio increases and reaches a saturation level of 400 meV at $[\text{Nb}^{5+}]/([\text{Al}^{3+}]+[\text{Nb}^{5+}]) \sim 0.7$ and beyond.

6.3.3 FTIR Spectroscopy

The complete decomposition of the precursors was studied by FTIR. Figure 6-6 illustrates the FTIR absorption spectra of $\text{Nb}_{1-x}\text{Al}_x\text{O}_y$ films deposited on (KBr) substrates with varying the $[\text{Nb}^{5+}]/([\text{Al}^{3+}]+[\text{Nb}^{5+}])$ ratio.

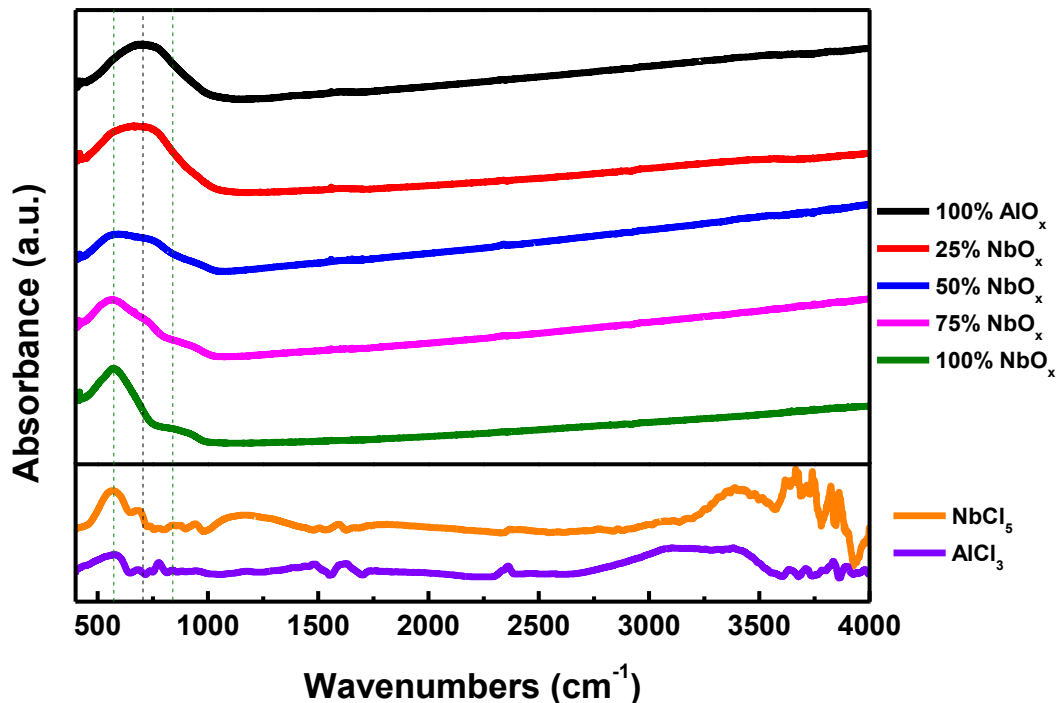


Figure 6-6: FTIR spectra of selected $\text{Nb}_{1-x}\text{Al}_x\text{O}_y$ films and NbCl_5 and AlCl_3 precursors deposited on KBr substrates.

The FTIR spectra clearly show the complete decomposition of the precursor, as features associated to the precursors and the solvents are absent from the spectra.

The spectrum of NbO_x shows a predominant broad peak at $\sim 570 \text{ cm}^{-1}$ as well as a shoulder centred at $\sim 840 \text{ cm}^{-1}$. These peaks are attributed to the asymmetric Nb-O stretching mode (570 cm^{-1}) and to the collinear Nb-O-Nb bridging stretching mode (840 cm^{-1}) of amorphous NbO_x [71].

Moreover, the AlO_x FTIR spectrum is dominated by a broad absorption band in the range between 400 and 1000 cm^{-1} . Such broad bands have been attributed to amorphous materials where, disordered distribution of vacancies and the continuous distribution of bond lengths are realised [72].

$\text{Nb}_{1-x}\text{Al}_x\text{O}_y$ FTIR spectra show broad peaks which could be considered as a convolution of the FTIR spectra of the NbO_x and AlO_x . Increasing the $[\text{Nb}^{5+}]/([\text{Al}^{3+}]+[\text{Nb}^{5+}])$ ratio there is an evident transition from the spectrum of AlO_x to that of NbO_x .

6.3.4 X-Ray Diffraction (XRD)

In order to scrutinise the microstructure of the spray deposited $\text{Nb}_{1-x}\text{Al}_x\text{O}_y$ thin films, grazing incidence XRD (GIXRD) experiments were performed. The GIXRD patterns of AlO_x , NbO_x and selected $\text{Nb}_{1-x}\text{Al}_x\text{O}_y$ films are depicted in Figure 6-7. The diffraction patterns lack any diffraction peaks associated with either of AlO_x , NbO_x and $\text{Nb}_{1-x}\text{Al}_x\text{O}_y$, suggesting amorphous films.

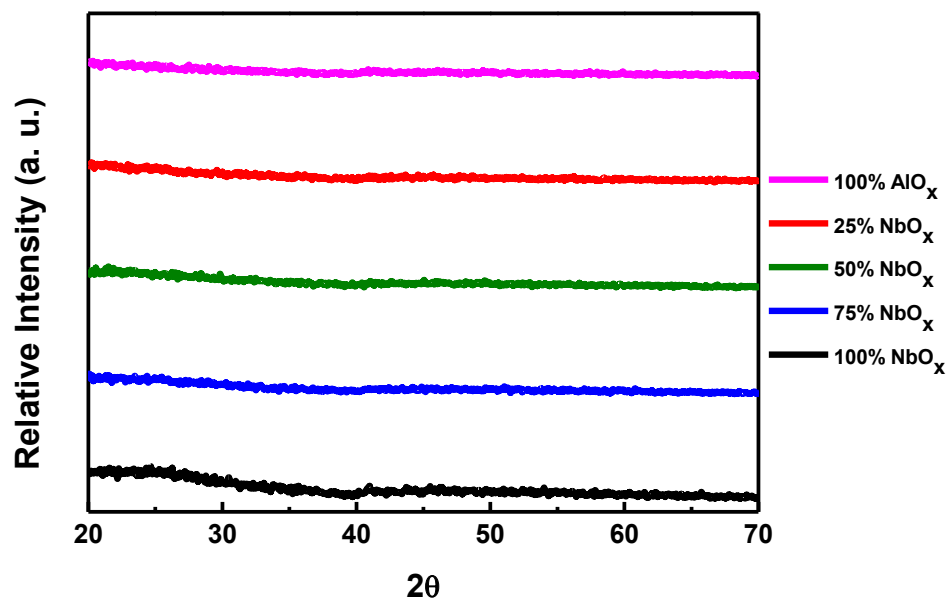


Figure 6-7: GIXRD patterns of selected $\text{Nb}_{1-x}\text{Al}_x\text{O}_y$ films of different $[\text{Nb}^{5+}]/([\text{Nb}^{5+}]+[\text{Al}^{3+}])$ ratios.

These results are consistent with the high Urbach tail energy, that is related to the degree of the disorder of a material, as well as, the broad bands present in the FTIR spectra. Additionally, the amorphous nature of the spray deposited $\text{Nb}_{1-x}\text{Al}_x\text{O}_y$ films renders them potential candidates for high-performance dielectrics.

6.3.5 Atomic Force Microscopy (AFM)

The surface morphologies of the spray deposited $\text{Nb}_{1-x}\text{Al}_x\text{O}_y$ films were investigated by atomic force microscopy (AFM). Representative images of spray deposited AlO_x , NbO_x and stoichiometric $\text{Nb}_{1-x}\text{Al}_x\text{O}_y$ films on silicon substrates are illustrated in Figure 6-8.

The topography images of the spray deposited $\text{Nb}_{1-x}\text{Al}_x\text{O}_y$ films that are illustrated in Figure 6-8, demonstrate films of low roughness ($<1\text{nm}$). It has been reported that such smooth film surfaces, is a desired characteristic for the implementation of $\text{Nb}_{1-x}\text{Al}_x\text{O}_y$ thin films deposited by the spray pyrolysis technique into high-performance electronic devices.

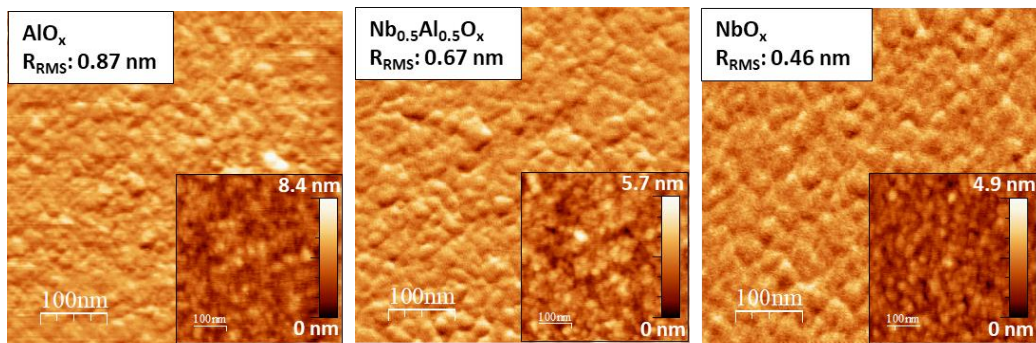


Figure 6-8: Friction and topography (inset) images (RMS roughness inset) of solution-processed AlO_x , stoichiometric $\text{Nb}_{0.5}\text{Al}_{0.5}\text{O}_y$, and (c) NbO_x films on silicon substrates.

6.3.6 Impedance Spectroscopy

The impedance characteristics of $\text{Nb}_{1-x}\text{Al}_x\text{O}_y$ thin films deposited by spray pyrolysis was measured using metal-insulator-metal (MIM) devices (Figure 6-1.a).

Figure 6-9 presents, the dispersions of the static dielectric constant (k). A characteristic feature of the static dielectric constant is the shift of the onset of the dielectric loss at higher frequencies for the stoichiometric NbAlO_x , compared to the rest of the $\text{Nb}_{1-x}\text{Al}_x\text{O}_y$ composites. The shift of the onset of the dielectric relaxation at lower frequencies has been related to a degradation in the insulating performance of the dielectrics [61], [73].

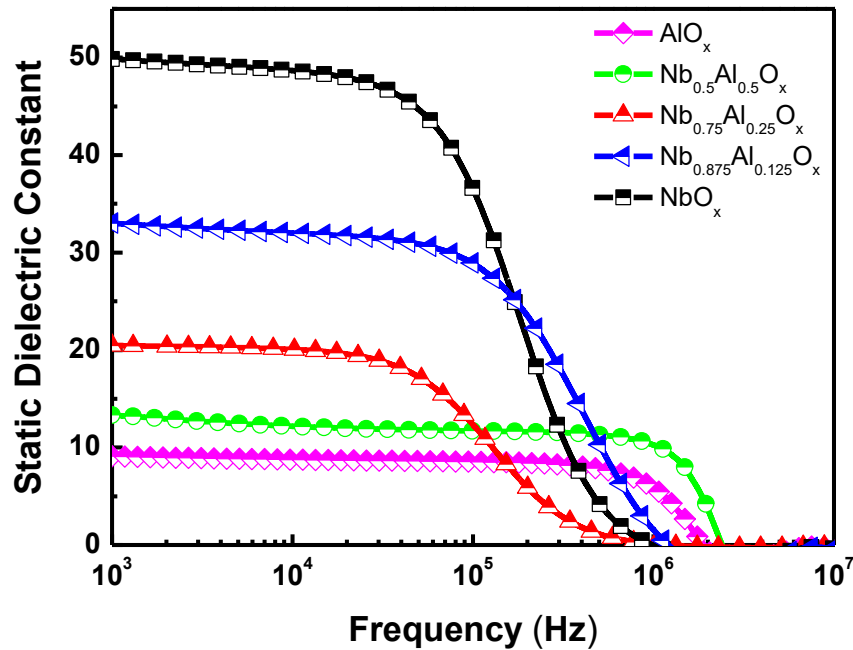


Figure 6-9: Static dielectric constant (k) dispersion of selected $\text{Nb}_{1-x}\text{Al}_x\text{O}_y$ films in the frequency range of 1 kHz-10 MHz

In Figure 6-10 the static dielectric constant of $\text{Nb}_{1-x}\text{Al}_x\text{O}_y$ films as a function of the $[\text{Nb}^{5+}]/([\text{Al}^{3+}]+[\text{Nb}^{5+}])$ ratio, is illustrated. As can be seen, there is a monotonic increase of the static dielectric constant with increase in the niobium content.

It is known that the static dielectric constant of gate dielectrics, varies inversely with the band gap [49], [50], [74]–[76]. Such trend is equally evidenced for spray coated $\text{Nb}_{1-x}\text{Al}_x\text{O}_y$ as shown in Figure 6-11.

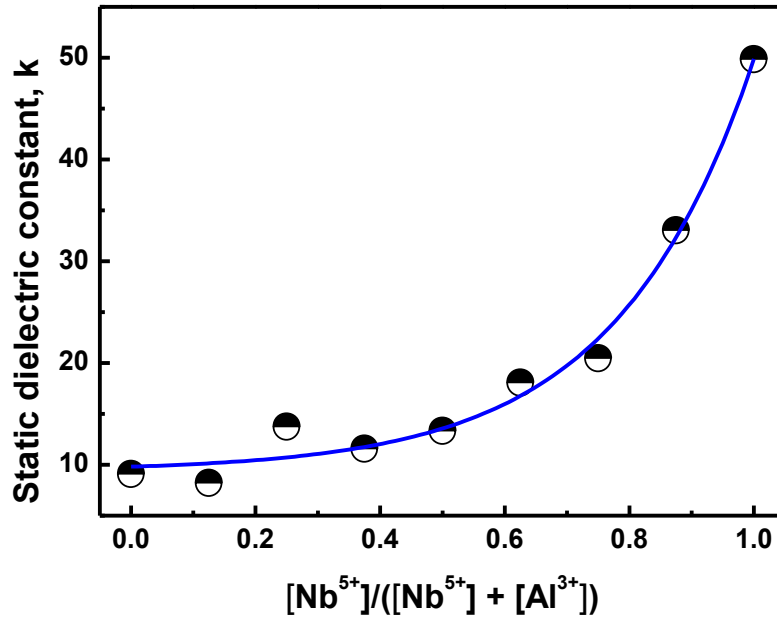


Figure 6-10: Dielectric constant of $\text{Nb}_{1-x}\text{Al}_x\text{O}_y$ films as a function of the $[\text{Nb}^{5+}]/([\text{Nb}^{5+}] + [\text{Al}^{3+}])$ ratio. The solid line is a guide to the eye.

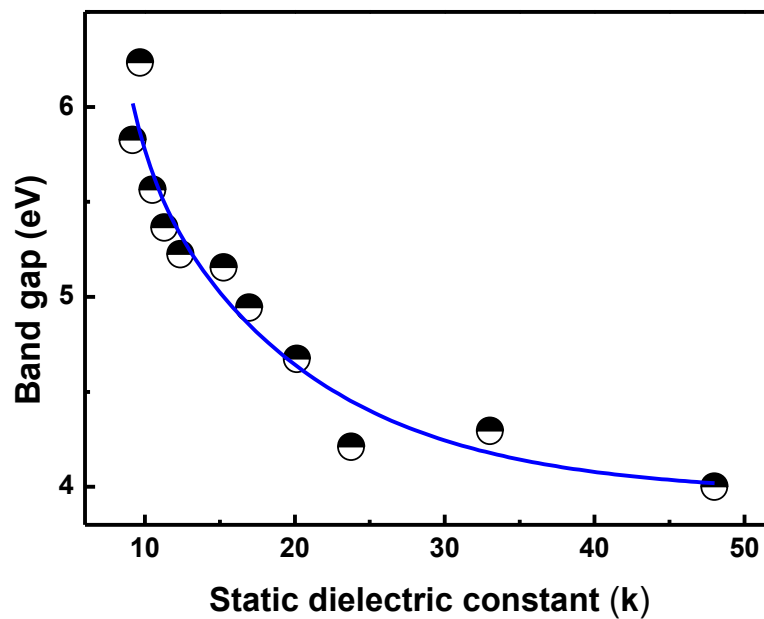


Figure 6-11: Static dielectric constant (k) vs band gap for $\text{Nb}_{1-x}\text{Al}_x\text{O}_y$ dielectrics grown by spray pyrolysis. The solid line is a guide to the eye.

6.3.7 Leakage Currents

The current-voltage characteristics of the $\text{Nb}_{1-x}\text{Al}_x\text{O}_y$ films were investigated by employing the same device architecture (Figure 6-1.a) as for impedance measurements. $\text{Nb}_{1-x}\text{Al}_x\text{O}_y$ films of thickness of ~ 100 nm were sandwiched between ITO and Au electrodes. All the measurements were performed under dark conditions at room temperature.

Figure 6-12 shows the leakage current density-electric field characteristics of selected $\text{Nb}_{1-x}\text{Al}_x\text{O}_y$ dielectrics of films with different $[\text{Nb}^{5+}]/([\text{Al}^{3+}]+[\text{Nb}^{5+}])$ ratio.

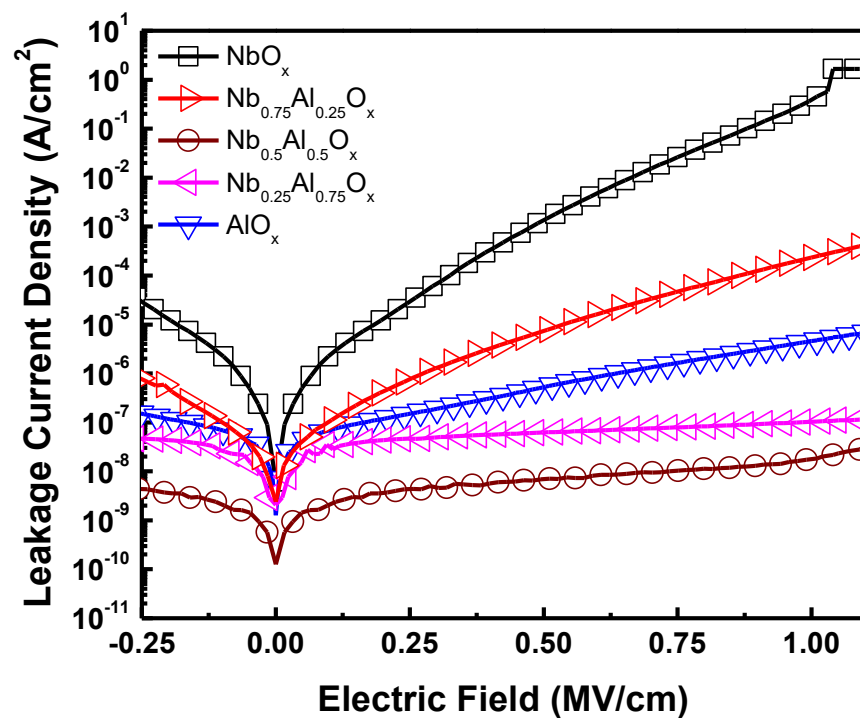


Figure 6-12: Leakage current density-electric field characteristics of selected $\text{Nb}_{1-x}\text{Al}_x\text{O}_y$ spray deposited dielectrics as a function of the $[\text{Nb}^{5+}]/([\text{Nb}^{5+}]+[\text{Al}^{3+}])$ atomic ratio (in the solution).

The leakage current density of solution processed $\text{Nb}_{1-x}\text{Al}_x\text{O}_y$ dielectrics at 0.5 and 1 MV/cm as a function of the $[\text{Nb}^{5+}]/([\text{Al}^{3+}]+[\text{Nb}^{5+}])$ ratio is shown in Figure 6-13. The stoichiometric $\text{Nb}_{1-x}\text{Al}_x\text{O}_y$ exhibits the lower leakage currents at both 0.5 MV/cm and 1 MV/cm. When a field of 0.5 MV/cm applied a density of leakage

current of $\sim 7 \text{ nA/cm}^2$ was measured. For an electrical field of 1 MV/cm the leakage current density was less than 20 nA/cm^2 .

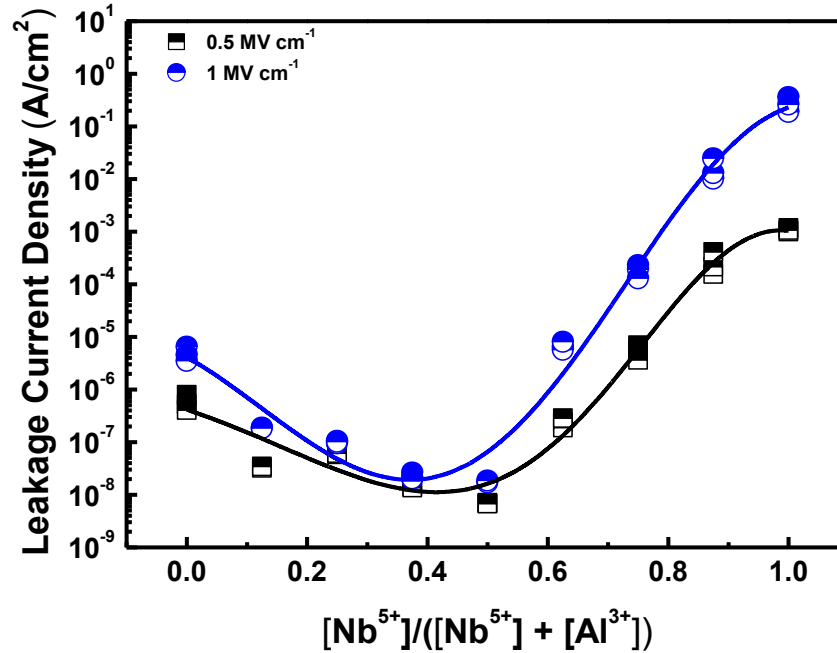
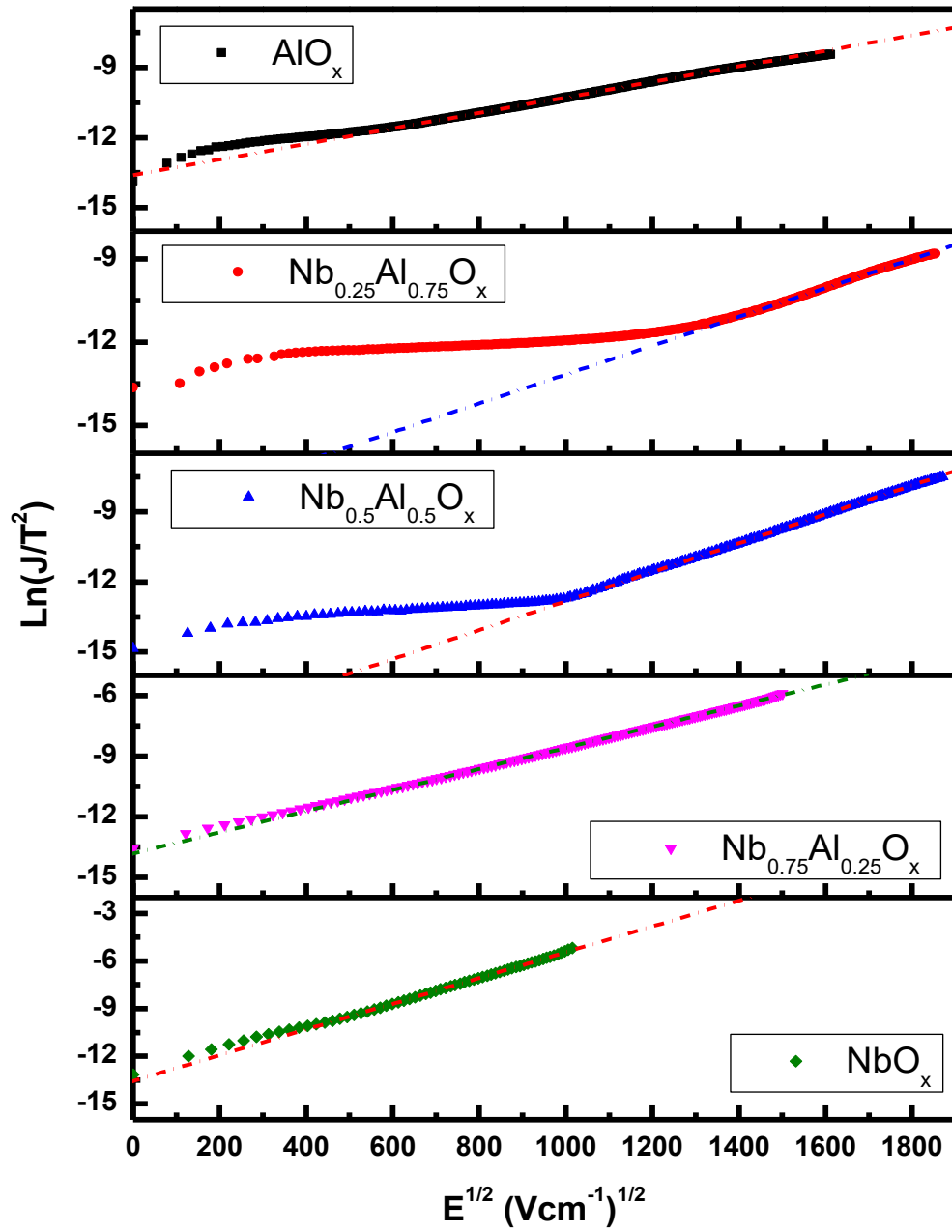
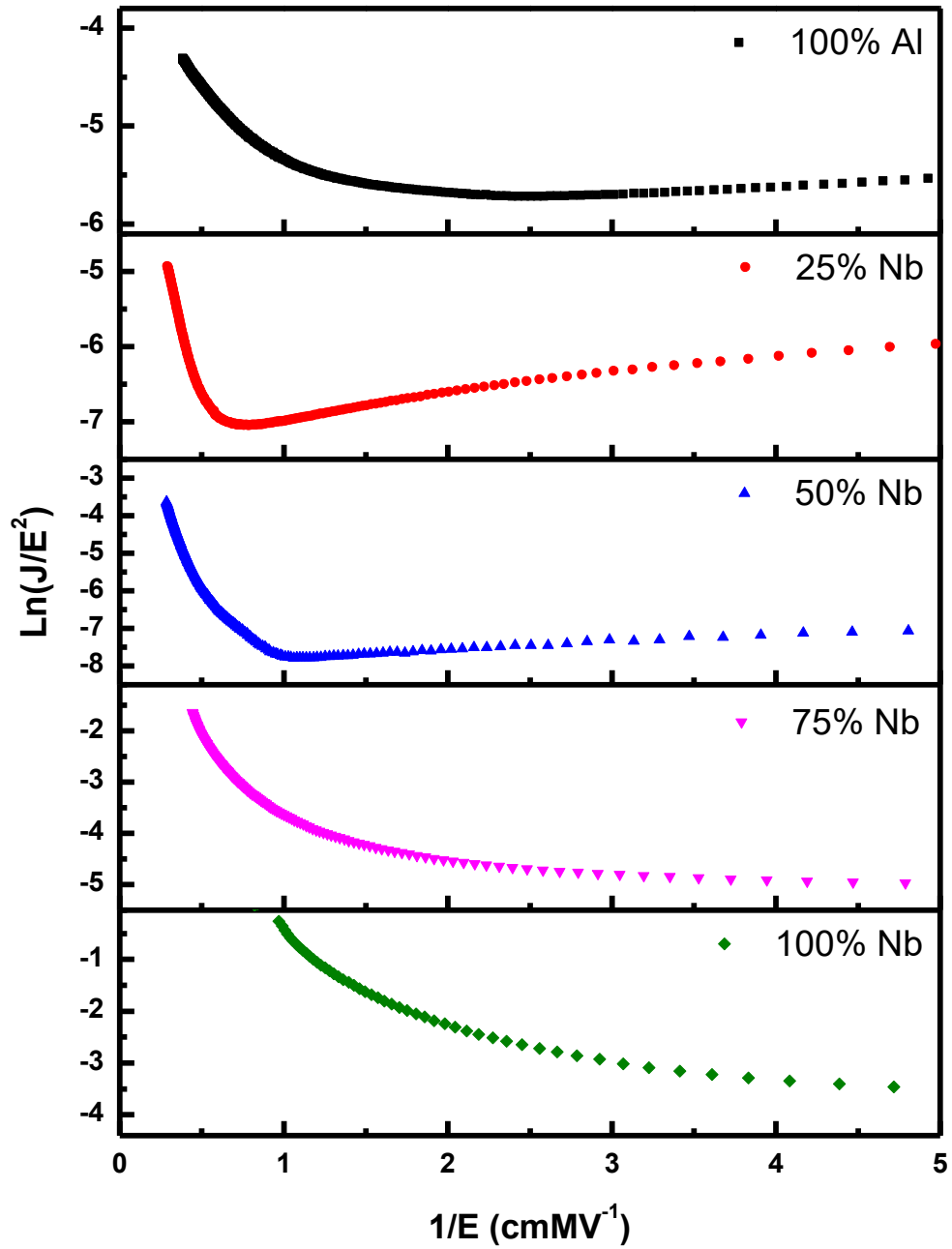


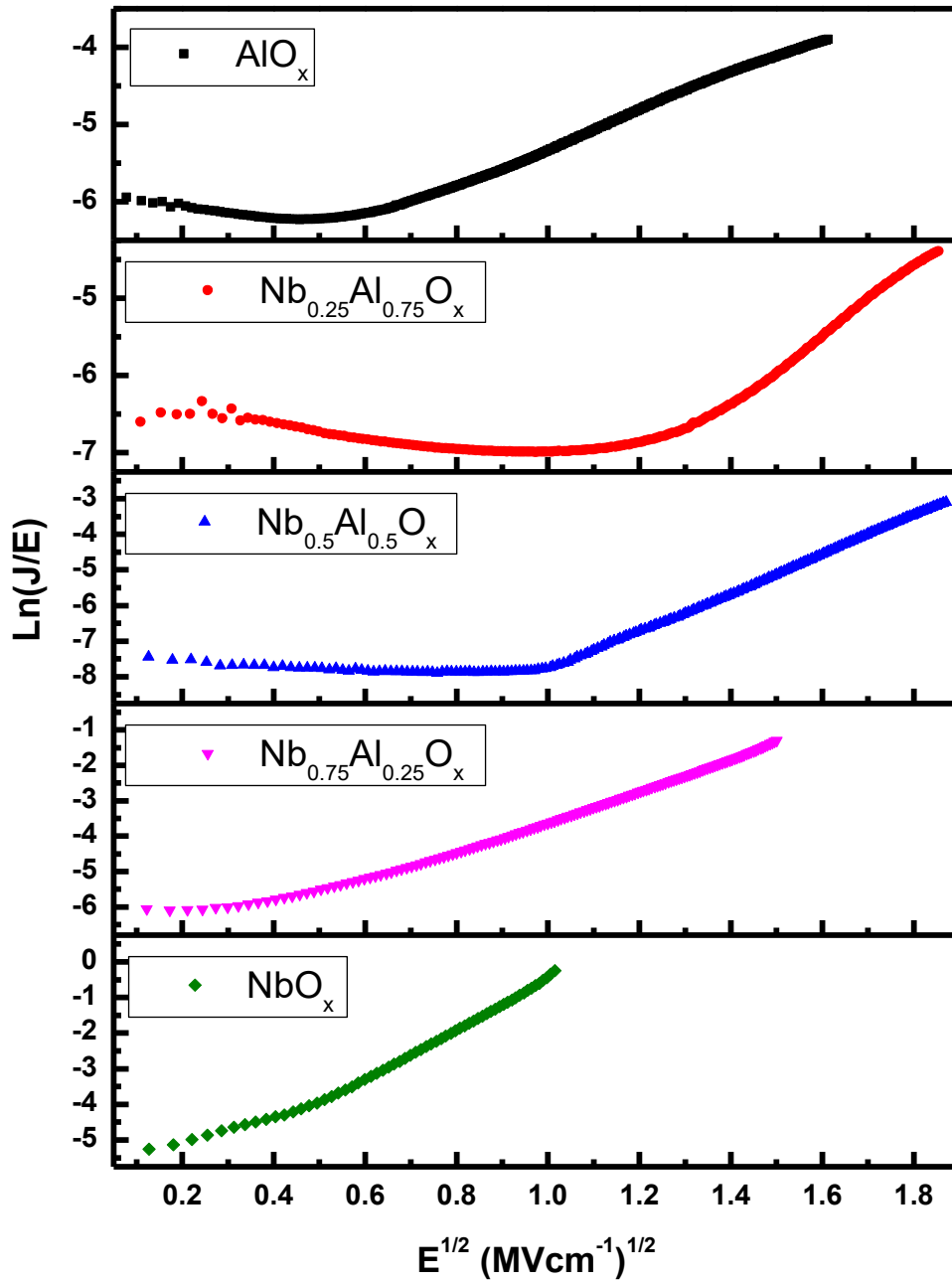
Figure 6-13: Leakage current density of solution processed $\text{Nb}_{1-x}\text{Al}_x\text{O}_y$ gate dielectrics at 0.5 and 1 MV/cm as a function of the $[\text{Nb}^{5+}]/([\text{Nb}^{5+}] + [\text{Al}^{3+}])$ atomic ratio in the solutions. The solid lines are guides to the eye.

The leakage currents of dielectric films strongly depend on material's composition, film processing, traps energy level and traps density in the films [77]. To elucidate the origin of the leakage current, the conduction mechanisms for the $\text{Nb}_{1-x}\text{Al}_x\text{O}_y$ thin films were further scrutinised.

In Figure 6-14, Figure 6-15 and Figure 6-16 the Schottky, Fowler-Nordheim and Poole-Frenkel plots for selected $\text{Nb}_{1-x}\text{Al}_x\text{O}_y$ thin films are illustrated [78].

Figure 6-14: Schottky emission (SE) plots of selected $Nb_{1-x}Al_xO_y$ films.

Figure 6-15: Fowler-Nordheim (FN) plots of selected $Nb_{1-x}Al_xO_y$ films.

Figure 6-16: Poole-Frenkel (PF) plots of selected $\text{Nb}_{1-x}\text{Al}_x\text{O}_y$ films.

Evidently, the Schottky emission (SE) constitutes the dominant conduction mechanism for all the $\text{Nb}_{1-x}\text{Al}_x\text{O}_y$ -based devices. This could be explained considering that the measurements were conducted at room temperature. At this temperature, the electrons have enough energy to overcome the potential barrier at the metal-dielectric interface and be diffused in the dielectric (Figure 6-17).

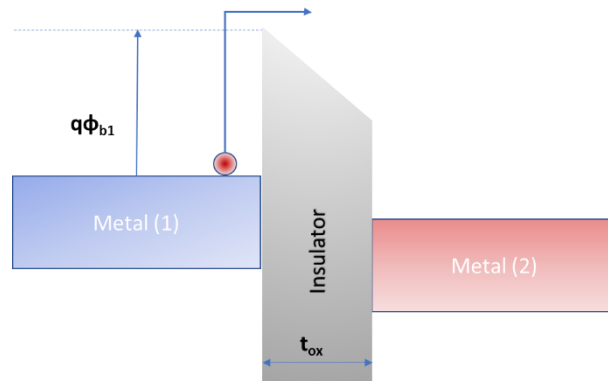


Figure 6-17: Schematic energy-band diagram of Schottky emission in a MIM structure.

Further analysis of SE plots provides more details on the barrier height at the metal-dielectric interface as well as the electron effective mass in the dielectric [79]. Figure 6-18 shows both the electron effective mass as well as the potential barrier height at the $\text{Au}/\text{Nb}_{1-x}\text{Al}_x\text{O}_y$ interfaces as a function of the $[\text{Nb}^{5+}]/([\text{Al}^{3+}]+[\text{Nb}^{5+}])$ ratio. In the case of the stoichiometric $\text{Nb}_{1-x}\text{Al}_x\text{O}_y$ film, both the electron effective mass (m^*) and the interface potential barrier height (Φ_{int}) at the metal-dielectric interface, reach a maximum of $0.37m_0$ and 0.734 eV respectively. Similar values have been reported and for other high- k metal oxides [79], [80].

Both the increased interfacial potential barrier height and the increased electron effective mass, of stoichiometric $\text{Nb}_{1-x}\text{Al}_x\text{O}_y$ ($x=0.5$) could also explain the low leakage currents (Figure 6-19).

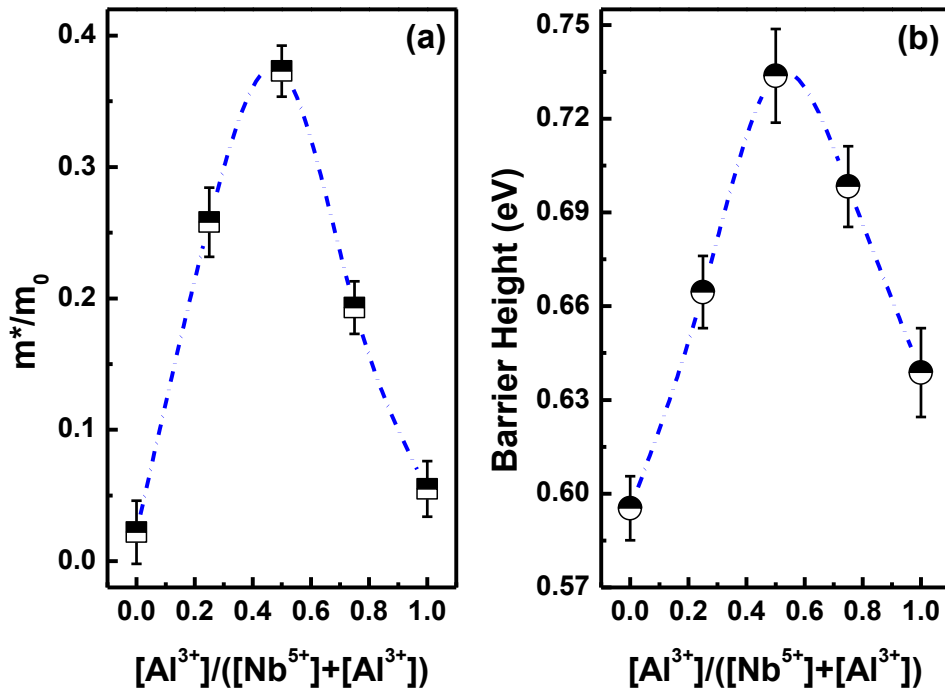


Figure 6-18: a) Electron effective mass in the $Nb_{1-x}Al_xO_y$ and b) barrier height at the Au/ $Nb_{1-x}Al_xO_y$ interface as a function of the $[Al^{3+}]/([Nb^{5+}]+[Al^{3+}])$ ratio. The lines are guides to the eye.

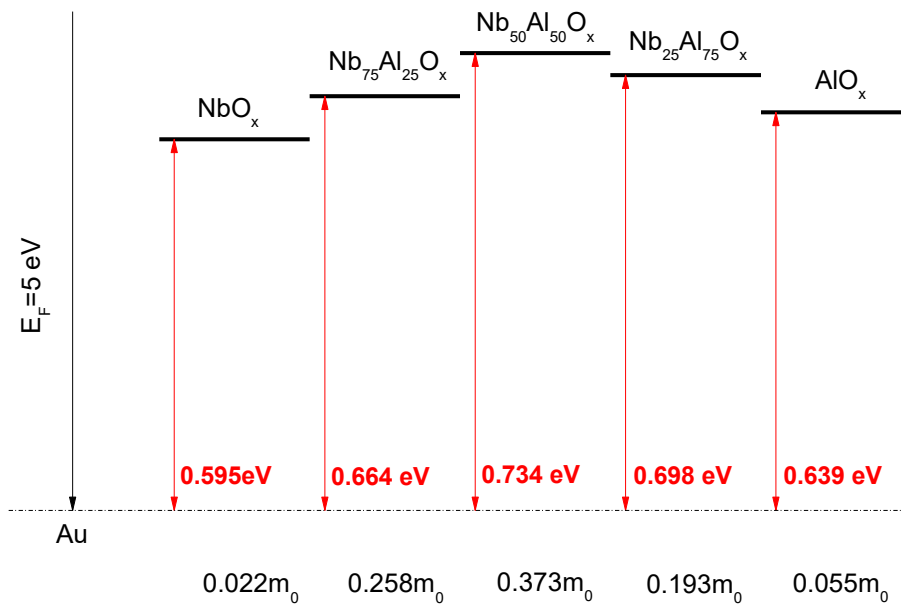


Figure 6-19: Energy band diagrams of selected $Nb_{1-x}Al_xO_y$ films. The conduction bands (black solid lines) are presented in respect to gold's fermi energy (E_F). The calculated effective masses included as well.

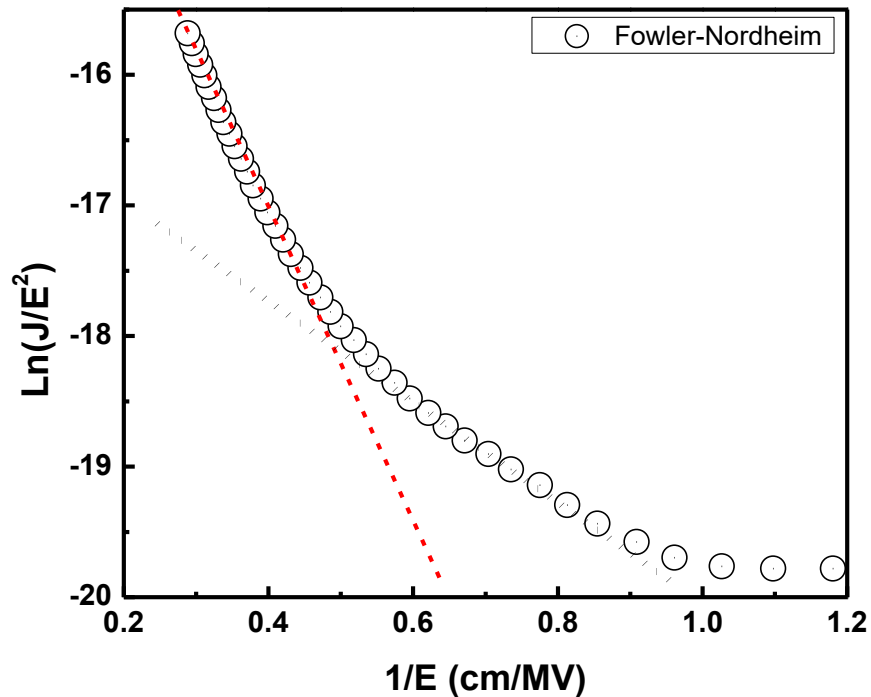


Figure 6-20: Fowler-Nordheim plot of the stoichiometric $\text{Nb}_{1-x}\text{Al}_x\text{O}_y$ film.

A more detailed analysis of the electrode-limited leakage current mechanism of $\text{Nb}_{1-x}\text{Al}_x\text{O}_y$ ($x=0.5$), where the lowest leakage current found, revealed a nonlinearity in Fowler-Nordheim plots (Figure 6-20). Such nonlinearity has been reported to be attributed to a transition from thermionic emission (SE) to field emission as the applied field increases [81].

It has been reported that oxide dielectrics have inherently a high density of charge carrier trap levels [49]. These trap levels play an important role in the conduction of such materials, especially at high electric fields. To investigate whether the conductivity of the $\text{Nb}_{1-x}\text{Al}_x\text{O}_y$ dielectrics is due to the charge carrier trap levels, the validity of Poole-Frenkel (PF) emission mechanism was investigated (Figure 6-16). As shown in Figure 6-16, conduction PF emission was the dominant mechanism for the niobium rich $\text{Nb}_{1-x}\text{Al}_x\text{O}_y$ ($0.5 < x < 1$) thin films.

6.3.8 Field effect measurements

The performance of the spray deposited $Nb_{1-x}Al_xO_y$ thin films as gate dielectrics was investigated in BG-TC TFTs (Figure 6-1.b) employing a spray coated ZnO semiconducting channel.

Figure 6-21 and Figure 6-22 show a representative set of transfer and output characteristics obtained from TFTs ($L = 20 \mu\text{m}$, $W = 1000 \mu\text{m}$) with a $\sim 105 \text{ nm}$ thick AlO_x , 125 nm thick stoichiometric $Nb_{1-x}Al_xO_y$ dielectric, respectively.

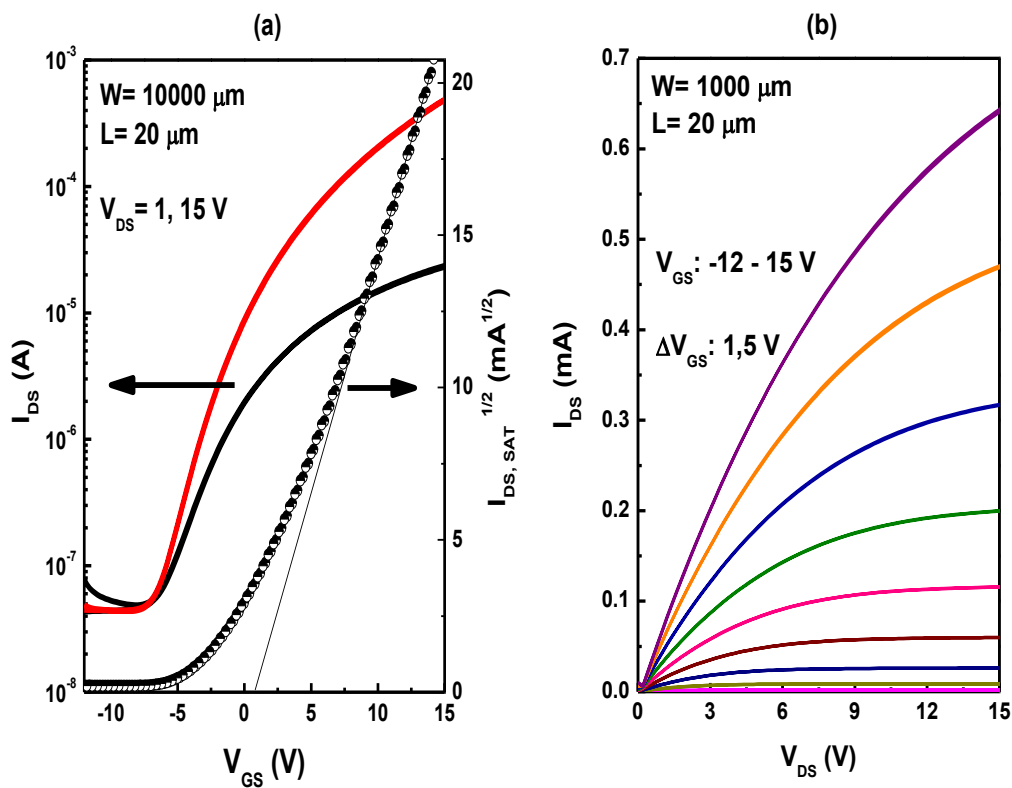


Figure 6-21: a) Transfer and b) output characteristics of ZnO-based TFTs employing spray coated AlO_y gate dielectric.

ZnO-based TFTs implementing AlO_x and $Nb_{1-x}Al_xO_y$ gate dielectrics, show excellent operating characteristics such as high ($> 10^5$) on/off current ratios, negligible hysteresis and high electron mobilities. More importantly, the implementation of stoichiometric $Nb_{1-x}Al_xO_y$ as a gate dielectric doesn't affect the electron mobility ($\sim 1 \text{ cm}^2/\text{Vs}$), however, the current modulation ratio was notably

improved by 1 order of magnitude ($\sim 10^4$ for AlO_x and $> 10^5$ for stoichiometric $\text{Nb}_{1-x}\text{Al}_x\text{O}_y$). In Figure 6-23 the field effect mobility and the on/off current modulation ratio of ZnO-based TFTs employing $\text{Nb}_{1-x}\text{Al}_x\text{O}_y$ gate dielectrics as a function of aluminum content, are presented.

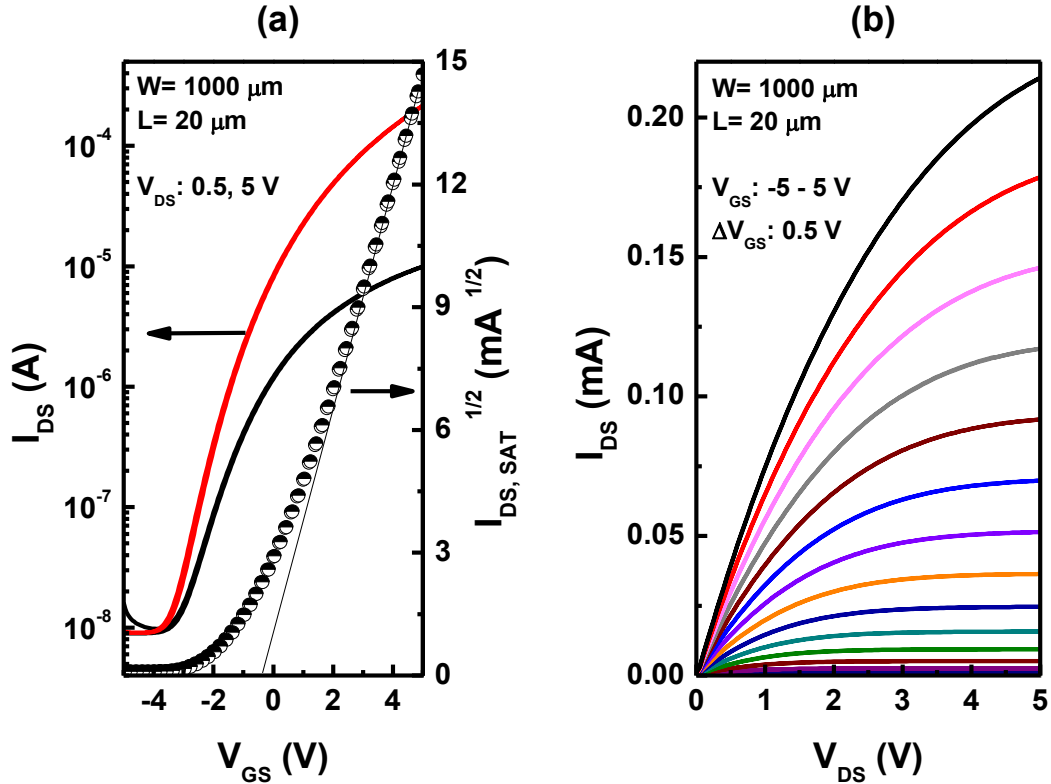


Figure 6-22: a) Transfer and b) output characteristics of ZnO-based TFTs employing stoichiometric $\text{Nb}_{0.5}\text{Al}_{0.5}\text{O}_y$ gate dielectric.

In this study, the ZnO-based TFTs implementing $\text{Nb}_{1-x}\text{Al}_x\text{O}_y$ gate dielectrics exhibited electron mobilities of about $1 \text{ cm}^2/\text{Vs}$. However, studies regarding the implementation of other transition metal-aluminates in ZnO-based TFT devices demonstrated TFTs exhibiting electron mobilities of about $10 \text{ cm}^2/\text{Vs}$ [55], [61]. The relatively low electron mobility of devices is attributed to the source/drain (S/D) gold contacts used in this study. Adamopoulos et al., have shown that the electron mobility is strongly depended on the work function of the S/D metal electrodes [82]. They concluded that because of the energy difference between the conduction band of ZnO and the work-function of Au, an energy barrier of 0.7 eV limits the carrier injection from the metal (Au) to semiconductor (ZnO).

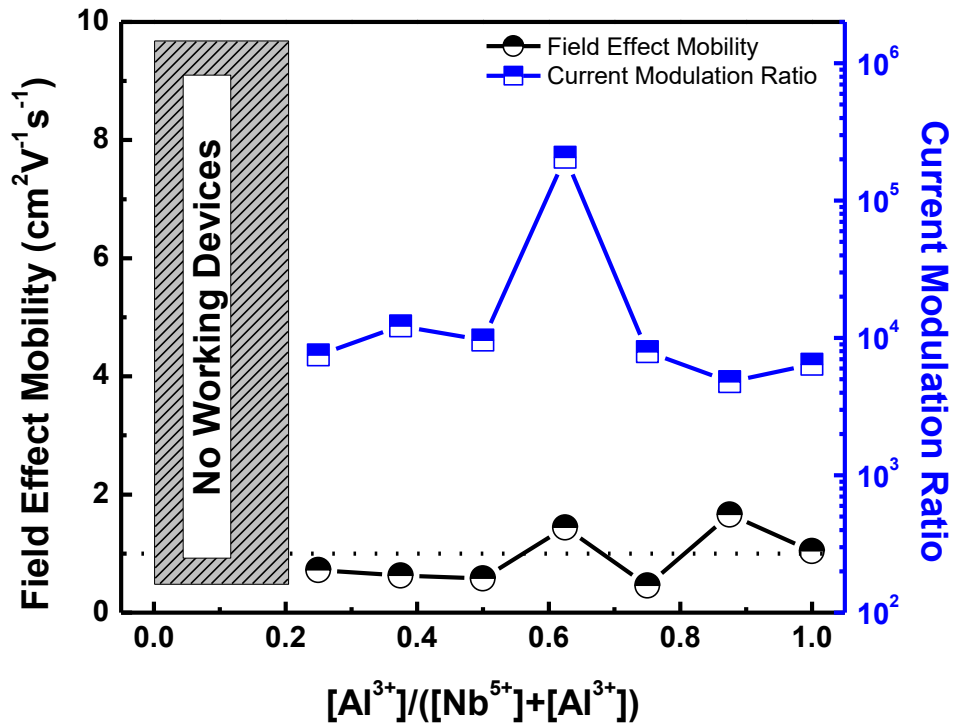


Figure 6-23: Field effect mobility (left Y-axis) and on/off current modulation ratio (right Y-axis) of ZnO-based TFTs employing spray coated $\text{Nb}_{1-x}\text{Al}_x\text{O}_y$ gate dielectrics.

Another point that should be discussed is that no working devices were realised for TFTs employing $\text{Nb}_{1-x}\text{Al}_x\text{O}_y$ gate dielectrics at the niobium rich compositional region, i.e., $[\text{Nb}^{5+}]/([\text{Al}^{3+}]+[\text{Nb}^{5+}]) > 0.8$. Considering the electron affinity (χ_e) and the work function (W_{ZnO}) of ZnO ($\chi_e=4.3\text{eV}$, $W_{\text{ZnO}}=5.2\text{eV}$, measured from vacuum level)[83] and assuming, that the Fermi energy level (E^f) of dielectrics lies in the middle of their respected band gaps ($E_{\text{Nb}_{1-x}\text{Al}_x\text{O}_y}^f = E_g/2$) and further assuming that both the Fermi energy levels are aligned ($E_{\text{ZnO}}^f = E_{\text{Nb}_{1-x}\text{Al}_x\text{O}_y}^f$), a schematic of their band alignment could be drawn as it is presented as an insert in Figure 6-24. The energy difference (ΔE_c) between the conduction bands of $\text{Nb}_{1-x}\text{Al}_x\text{O}_y$ and ZnO, provides an estimation of the effective conduction band offset.

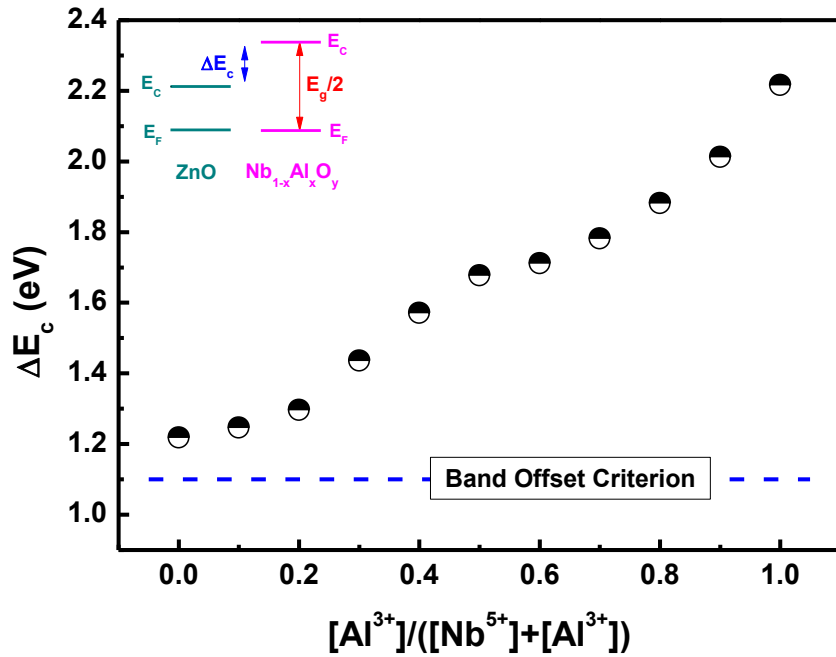


Figure 6-24: Conduction band offsets (ΔE_c) of spray coated $\text{Nb}_{1-x}\text{Al}_x\text{O}_y$ gate dielectrics with ZnO.

Figure 6-24 presents the calculated conduction band offsets between the ZnO and the $\text{Nb}_{1-x}\text{Al}_x\text{O}_y$ dielectrics. The Fermi level of ZnO was placed 0.9 eV below its conduction band as the difference in energy values of ZnO's electron affinity and work function. Considering the above assumptions, the band offset criterion is satisfied for all the $\text{Nb}_{1-x}\text{Al}_x\text{O}_y$ stoichiometries. However, the assumption that the $\text{Nb}_{1-x}\text{Al}_x\text{O}_y$ Fermi level lies at the midgap ($E_g/2$) is not valid. It could be considered that for the case of the niobium rich ($x < 0.8$) composition of $\text{Nb}_{1-x}\text{Al}_x\text{O}_y$ thin films, the Fermi level is transpositioned to a level closer to conduction band minima (E_c). This transposition could be related to gap states close to conduction band minima due to the disordered nature of the films.

In Figure 6-25, proposed band diagrams and offset of dielectric without (ΔE_c) and with gap states ($\Delta E'_c$) estimated, are presented. The lowering of the conduction band offset is due to the transposition (ΔE_{F2}) of the Fermi energy level. According to the findings (Figure 6-23 and Figure 6-24), it could be assumed that there must be a minimum transposition of 0.2 eV of Fermi level from midgap towards the conduction band minima for niobium-rich ($x < 0.2$) $\text{Nb}_{1-x}\text{Al}_x\text{O}_y$ dielectrics.

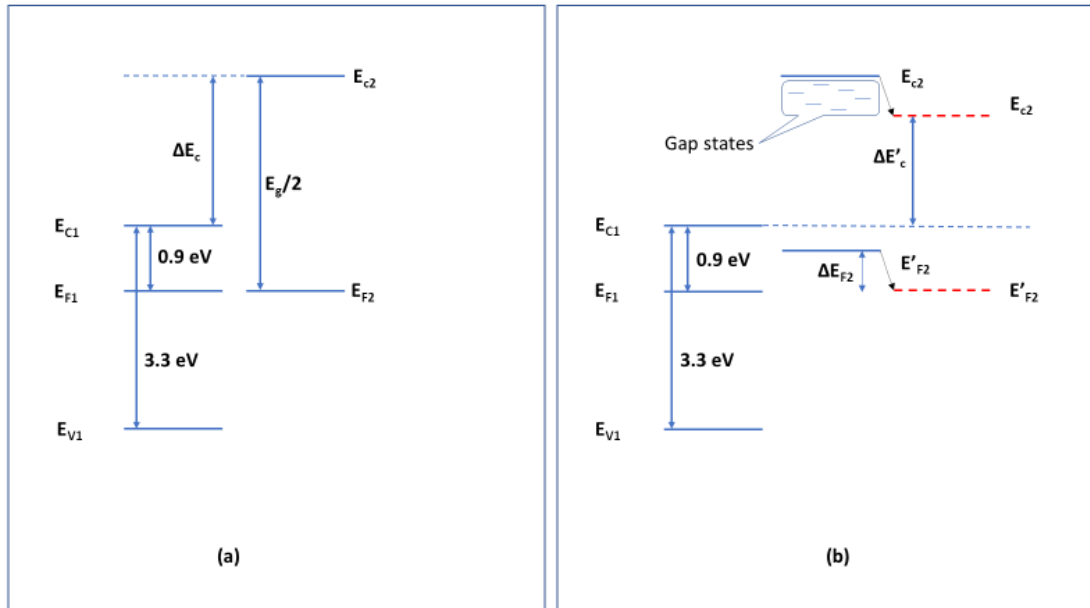


Figure 6-25: Band diagrams of conduction band offsets for dielectric (a) without gap states, (b) with gap states close to conduction band minimum. (E_{c1} : conduction band minimum of zinc oxide, E_{v1} : valence band maximum of ZnO, E_{c2} : Conduction band minimum of a dielectric, $E_{F2}(=E_g/2)$: Fermi level of dielectric assuming no gap states in its band gap, E'_{F2} : Fermi level of dielectric assuming gap states in its band gap, ΔE_{F2} : the transposition (in eV) of Fermi level from midgap, ΔE_c : conduction band offset for dielectrics without gap states, $\Delta E'_c = \Delta E_c - \Delta E_{F2}$: conduction band offset for dielectrics with gap states).

6.4 Summary

In this study, the properties of solution processed $\text{Nb}_{1-x}\text{Al}_x\text{O}_y$ films as a function of the $[\text{Nb}^{5+}]/([\text{Al}^{3+}] + [\text{Nb}^{5+}])$ atomic ratio were investigated. The thin films were spray deposited in air at moderate substrate temperatures (400 °C) and were implemented as gate dielectrics in TFTs employing spray coated ZnO semiconducting channels.

The $\text{Nb}_{1-x}\text{Al}_x\text{O}_y$ films were characterised using a wide range of experimental techniques. Analyses revealed amorphous $\text{Nb}_{1-x}\text{Al}_x\text{O}_y$ films with very smooth surfaces ($R_{\text{rms}} < 0.1$ nm), high dielectric constants ($9 < k < 50$), wide band gaps (4.2-6.5 eV) and low leakage currents (< 20 nA/cm²).

Analysis of the electron transport mechanisms revealed that at least two conduction mechanisms exist for each ratio. In all the cases the conduction of the dielectrics fits well the Schottky conduction mechanism. The electron effective mass of the stoichiometric $\text{Nb}_{1-x}\text{Al}_x\text{O}_y$ ($x=0.5$) and the effective barrier height at the Au/ $\text{Nb}_{0.5}\text{Al}_{0.5}\text{O}_y$ interface, were found to be of $0.37 m_0$ and 0.73 eV respectively, and

both are high enough to explain the low leakage currents at this ratio. For niobium-rich ($x < 0.2$) $\text{Nb}_{1-x}\text{Al}_x\text{O}_y$ dielectrics, Poole-Frenkel conduction dominated. That could be explained by the existence of localised gap states in the band gap close to the conduction band.

The stoichiometric $\text{Nb}_{1-x}\text{Al}_x\text{O}_y$ showed high dielectric constant (~ 13.5), wide band gap (5.15 eV), and very low leakage currents ($< 10 \text{ nA/cm}^2$). ZnO-based TFTs employing stoichiometric $\text{Nb}_{1-x}\text{Al}_x\text{O}_y$ dielectrics showed excellent characteristics, i.e., hysteresis-free operation, high electron mobilities ($1 \text{ cm}^2/\text{Vs}$) and high on/off current modulation ratio ($> 10^5$).

6.5 References

- [1] F. Xu, A. Liu, G. Liu, B. Shin, and F. Shan, 'Solution-processed yttrium oxide dielectric for high-performance IZO thin-film transistors', *Ceram. Int.*, vol. 41, no. 41, pp. S337–S343, Jul. 2015.
- [2] G. Alarcón-Flores, M. Aguilar-Fruti, M. García-Hipolito, J. Guzmán-Mendoza, M. A. Canseco, and C. Falcony, 'Optical and structural characteristics of Y_2O_3 thin films synthesized from yttrium acetylacetonate', *J. Mater. Sci.*, vol. 43, no. 10, pp. 3582–3588, May 2008.
- [3] S.-Y. Wang and Z.-H. Lu, 'Preparation of Y_2O_3 thin films deposited by pulse ultrasonic spray pyrolysis', *Mater. Chem. Phys.*, vol. 78, no. 2, pp. 542–545, Feb. 2003.
- [4] G. Adamopoulos, S. Thomas, D. D. C. Bradley, M. a. McLachlan, and T. D. Anthopoulos, 'Low-voltage ZnO thin-film transistors based on Y_2O_3 and Al_2O_3 high-k dielectrics deposited by spray pyrolysis in air', *Appl. Phys. Lett.*, vol. 123503, no. 12, pp. 1–4, Mar. 2011.
- [5] M. Hasan, M.-C. Nguyen, H. Kim, S.-W. You, Y.-S. Jeon, D.-T. Tong, D.-H. Lee, J. K. Jeong, and R. Choi, 'High performance solution processed zirconium oxide gate dielectric appropriate for low temperature device application', *Thin Solid Films*, vol. 589, pp. 90–94, Aug. 2015.
- [6] S. J. Wang, C. K. Ong, S. Y. Xu, P. Chen, W. C. Tjiu, J. W. Chai, A. C. H. Huan, W. J. Yoo, J. S. Lim, W. Feng, and W. K. Choi, 'Crystalline zirconia oxide on silicon as alternative gate dielectrics', *Appl. Phys. Lett.*, vol. 78, no. 11, pp. 1604–1606, Mar. 2001.
- [7] R. Engel-Herbert, Y. Hwang, J. Cagnon, and S. Stemmer, 'Metal-oxide-semiconductor capacitors with ZrO_2 dielectrics grown on $\text{In}_{0.53}\text{Ga}_{0.47}\text{As}$ by chemical beam deposition', *Appl. Phys. Lett.*, vol. 95, no. 6, pp. 1–4, 2009.

- [8] B. G. Son, S. Y. Je, H. J. Kim, C. K. Lee, C. K. Lee, A. Y. Hwang, J. Y. Won, J. H. Song, R. Choi, and J. K. Jeong, 'High-performance In-Zn-O thin-film transistors with a soluble processed ZrO_2 gate insulator', *Phys. Status Solidi - Rapid Res. Lett.*, vol. 7, no. 7, pp. 485–488, Jul. 2013.
- [9] G. Adamopoulos, S. Thomas, P. H. Wöbkenberg, D. D. C. Bradley, M. a. McLachlan, and T. D. Anthopoulos, 'High-Mobility Low-Voltage ZnO and Li-Doped ZnO Transistors Based on ZrO_2 High- k Dielectric Grown by Spray Pyrolysis in Ambient Air', *Adv. Mater.*, vol. 23, no. 16, pp. 1894–1898, Apr. 2011.
- [10] A. Liu, G. X. Liu, H. H. Zhu, F. Xu, E. Fortunato, R. Martins, and F. K. Shan, 'Fully Solution-Processed Low-Voltage Aqueous In_2O_3 Thin-Film Transistors Using an Ultrathin ZrO_x Dielectric', *ACS Appl. Mater. Interfaces*, vol. 6, no. 20, pp. 17364–17369, Oct. 2014.
- [11] J. H. Choi, Y. Mao, and J. P. Chang, 'Development of hafnium based high- k materials - A review', *Mater. Sci. Eng. R Reports*, vol. 72, no. 6, pp. 97–136, 2011.
- [12] M. Casse, L. Thevenod, B. Guillaumot, L. Tosti, F. Martin, J. Mitard, O. Weber, F. Andrieu, T. Ernst, G. Reimbold, T. Billon, M. Mouis, and F. Boulanger, 'Carrier transport in HfO_2 metal gate MOSFETs: physical insight into critical parameters', *IEEE Trans. Electron Devices*, vol. 53, no. 4, pp. 759–768, Apr. 2006.
- [13] W.-K. Lin, K.-C. Liu, S.-T. Chang, and C.-S. Li, 'Room temperature fabricated transparent amorphous indium zinc oxide based thin film transistor using high- k HfO_2 as gate insulator', *Thin Solid Films*, vol. 520, no. 7, pp. 3079–3083, Jan. 2012.
- [14] M. Lukosius, C. Walczyk, M. Fraszke, D. Wolansky, H. Richter, and C. Wenger, 'High performance metal–insulator–metal capacitors with atomic vapor deposited HfO_2 dielectrics', *Thin Solid Films*, vol. 518, no. 15, pp. 4380–4384, May 2010.
- [15] M. M. Frank, G. D. Wilk, D. Starodub, T. Gustafsson, E. Garfunkel, Y. J. Chabal, J. Grazul, and D. A. Muller, ' HfO_2 and Al_2O_3 gate dielectrics on GaAs grown by atomic layer deposition', *Appl. Phys. Lett.*, vol. 86, no. 15, p. 152904, Apr. 2005.
- [16] M. Caymax, S. Van Elshocht, M. Houssa, A. Delabie, T. Conard, M. Meuris, M. M. Heyns, A. Dimoulas, S. Spiga, M. Fanciulli, J. W. Seo, and L. V. Goncharova, ' HfO_2 as gate dielectric on Ge: Interfaces and deposition techniques', *Mater. Sci. Eng. B Solid-State Mater. Adv. Technol.*, vol. 135, no. 3, pp. 256–260, Dec. 2006.
- [17] D. C. Bharti and S.-W. Rhee, 'Dielectric properties and X-ray photoelectron spectroscopic studies of niobium oxide thin films prepared by direct liquid injection chemical vapor deposition method', *Thin Solid Films*, vol. 548, pp. 195–201, Dec. 2013.
- [18] T. Blanquart, J. Niinistö, M. Heikkilä, T. Sajavaara, K. Kukli, E. Puukilainen, C. Xu, W. Hunks, M. Ritala, and M. Leskelä, 'Evaluation and Comparison of Novel Precursors for Atomic Layer Deposition of Nb_2O_5 Thin Films', *Chem. Mater.*, vol. 24, no. 6, pp. 975–980, Mar. 2012.

- [19] M. Kovendhan, D. P. Joseph, P. Manimuthu, S. Ganesan, S. Sambasivam, P. Maruthamuthu, S. A. Suthanthiraraj, C. Venkateswaran, and R. Mohan, 'Spray deposited Nb_2O_5 thin film electrodes for fabrication of dye sensitized solar cells', *Trans. Indian Inst. Met.*, vol. 64, no. 1–2, pp. 185–188, Feb. 2011.
- [20] S. H. Mujawar, A. I. Inamdar, C. A. Betty, R. Cerc Korošec, and P. S. Patil, 'Electrochromism in composite $WO_3-Nb_2O_5$ thin films synthesized by spray pyrolysis technique', *J. Appl. Electrochem.*, vol. 41, no. 4, pp. 397–403, Apr. 2011.
- [21] R. Romero, E. A. Dalchiele, F. Martín, D. Leinen, and J. R. Ramos-Barrado, 'Electrochromic behaviour of Nb_2O_5 thin films with different morphologies obtained by spray pyrolysis', *Sol. Energy Mater. Sol. Cells*, vol. 93, no. 2, pp. 222–229, Feb. 2009.
- [22] H. Störmer, A. Weber, V. Fischer, E. Ivers-Tiffée, and D. Gerthsen, 'Anodically formed oxide films on niobium: Microstructural and electrical properties', *J. Eur. Ceram. Soc.*, vol. 29, no. 9, pp. 1743–1753, Jun. 2009.
- [23] V. A. Matylitskaya, W. Bock, and B. O. Kolbesen, 'Nitridation of niobium oxide films by rapid thermal processing', *Anal. Bioanal. Chem.*, vol. 390, no. 6, pp. 1507–1515, Mar. 2008.
- [24] M. Serényi, T. Lohner, P. Petrik, Z. Zolnai, Z. E. Horváth, and N. Q. Khánh, 'Characterization of sputtered and annealed niobium oxide films using spectroscopic ellipsometry, Rutherford backscattering spectrometry and X-ray diffraction', *Thin Solid Films*, vol. 516, no. 22, pp. 8096–8100, Sep. 2008.
- [25] S. H. Mujawar, A. I. Inamdar, C. A. Betty, V. Ganesan, and P. S. Patil, 'Effect of post annealing treatment on electrochromic properties of spray deposited niobium oxide thin films', *Electrochim. Acta*, vol. 52, no. 15, pp. 4899–4906, Apr. 2007.
- [26] S. Mujawar, A. Inamdar, S. Patil, and P. Patil, 'Electrochromic properties of spray-deposited niobium oxide thin films', *Solid State Ionics*, vol. 177, no. 37–38, pp. 3333–3338, Dec. 2006.
- [27] F. Lai, L. Lin, Z. Huang, R. Gai, and Y. Qu, 'Effect of thickness on the structure, morphology and optical properties of sputter deposited Nb_2O_5 films', *Appl. Surf. Sci.*, vol. 253, no. 4, pp. 1801–1805, Dec. 2006.
- [28] H. Habazaki, T. Ogasawara, H. Konno, K. Shimizu, S. Nagata, K. Asami, K. Takayama, P. Skeldon, and G. E. Thompson, 'Suppression of Field Crystallization of Anodic Niobia by Oxygen', *J. Electrochem. Soc.*, vol. 153, no. 5, p. B173, May 2006.
- [29] J.-P. Masse, H. Szymanowski, O. Zabeida, A. Amassian, J. E. Klemberg-Sapieha, and L. Martinu, 'Stability and effect of annealing on the optical properties of plasma-deposited Ta_2O_5 and Nb_2O_5 films', *Thin Solid Films*, vol. 515, no. 4, pp. 1674–1682, Dec. 2006.

- [30] S. Venkataraj, D. Severin, S. H. Mohamed, J. Ngaruiya, O. Kappertz, and M. Wuttig, 'Towards understanding the superior properties of transition metal oxynitrides prepared by reactive DC magnetron sputtering', *Thin Solid Films*, vol. 502, no. 1–2, pp. 228–234, Apr. 2006.
- [31] P. S. Patil, A. R. Patil, S. H. Mujawar, and S. B. Sadale, 'Properties of spray deposited niobium oxide thin films', *J. Mater. Sci. Mater. Electron.*, vol. 16, no. 1, pp. 35–41, Jan. 2005.
- [32] H. Szymanowski, O. Zabeida, J. E. Klemberg-Sapieha, and L. Martinu, 'Optical properties and microstructure of plasma deposited Ta_2O_5 and Nb_2O_5 films', *J. Vac. Sci. Technol. A Vacuum, Surfaces, Film.*, vol. 23, no. 2, pp. 241–247, Mar. 2005.
- [33] R. L. Karlinsey, 'Preparation of self-organized niobium oxide microstructures via potentiostatic anodization', *Electrochem. commun.*, vol. 7, no. 12, pp. 1190–1194, Dec. 2005.
- [34] R. Romero, J. R. Ramos-Barrado, F. Martin, and D. Leinen, ' Nb_2O_5 thin films obtained by chemical spray pyrolysis', *Surf. Interface Anal.*, vol. 36, no. 8, pp. 888–891, Aug. 2004.
- [35] C.-C. Lee, C.-L. Tien, and J.-C. Hsu, 'Internal stress and optical properties of Nb_2O_5 thin films deposited by ion-beam sputtering', *Appl. Opt.*, vol. 41, no. 10, p. 2043, Apr. 2002.
- [36] B. Hunsche, M. Vergöhl, H. Neuhäuser, F. Klose, B. Szyszka, and T. Mattheé, 'Effect of deposition parameters on optical and mechanical properties of MF- and DC-sputtered Nb_2O_5 films', *Thin Solid Films*, vol. 392, no. 2, pp. 184–190, Jul. 2001.
- [37] M. A. Aegerter, 'Sol-gel niobium pentoxide: A promising material for electrochromic coatings, batteries, nanocrystalline solar cells and catalysis', *Sol. Energy Mater. Sol. Cells*, vol. 68, no. 3–4, pp. 401–422, Jun. 2001.
- [38] M. Strømme, G. A. Niklasson, M. Ritala, M. Leskelä, and K. Kukli, '($Ta_{1-x}Nb_x$) $_2O_5$ films produced by atomic layer deposition: Temperature dependent dielectric spectroscopy and room-temperature I–V characteristics', *J. Appl. Phys.*, vol. 90, no. 9, pp. 4532–4542, Nov. 2001.
- [39] K. Kukli, M. Ritala, M. Leskelä, and R. Lappalainen, 'Niobium Oxide Thin Films Grown by Atomic Layer Epitaxy', *Chem. Vap. Depos.*, vol. 4, no. 1, pp. 29–34, Jan. 1998.
- [40] M. Maček and B. Orel, 'Electrochromism of sol-gel derived niobium oxide films', *Sol. Energy Mater. Sol. Cells*, vol. 54, no. 1–4, pp. 121–130, Jul. 1998.
- [41] M. Schmitt, S. Heusing, M. A. Aegerter, A. Pawlicka, and C. Avellaneda, 'Electrochromic properties of Nb_2O_5 sol-gel coatings', *Sol. Energy Mater. Sol. Cells*, vol. 54, no. 1–4, pp. 9–17, Jul. 1998.

- [42] K. Yoshimura, 'Electrochromic Properties of Niobium Oxide Thin Films Prepared by DC Magnetron Sputtering', *J. Electrochem. Soc.*, vol. 144, no. 9, p. 2982, Sep. 1997.
- [43] A. Pawlicka, M. Atik, and M. . Aegerter, 'Synthesis of multicolor Nb_2O_5 coatings for electrochromic devices', *Thin Solid Films*, vol. 301, no. 1–2, pp. 236–241, Jun. 1997.
- [44] N. Özer, D.-G. Chen, and C. M. Lampert, 'Preparation and properties of spin-coated Nb_2O_5 films by the sol-gel process for electrochromic applications', *Thin Solid Films*, vol. 277, no. 1–2, pp. 162–168, May 1996.
- [45] L. Young, 'Anodic oxide films on niobium: thickness, dielectric constant, dispersion, reflection minima, formation field strength, and surface area', *Can. J. Chem.*, vol. 38, no. 7, pp. 1141–1147, Jul. 1960.
- [46] C. Nico, T. Monteiro, and M. P. F. Graça, 'Niobium oxides and niobates physical properties: Review and prospects', *Progress in Materials Science*, vol. 80. Pergamon, pp. 1–37, 01-Jul-2016.
- [47] K. Tanabe, 'Catalytic application of niobium compounds', *Catal. Today*, vol. 78, no. 1–4, pp. 65–77, Feb. 2003.
- [48] S. A. Campbell, D. C. Gilmer, Xiao-Chuan Wang, Ming-Ta Hsieh, Hyeon-Seag Kim, W. L. Gladfelter, and Jinhua Yan, 'MOSFET transistors fabricated with high permittivity TiO_2 dielectrics', *IEEE Trans. Electron Devices*, vol. 44, no. 1, pp. 104–109, 1997.
- [49] J. Robertson and R. M. Wallace, 'High- k materials and metal gates for CMOS applications', *Mater. Sci. Eng. R Reports*, vol. 88, pp. 1–41, Feb. 2015.
- [50] J. Robertson, 'Electronic Structure and Band Offsets of High-Dielectric-Constant Gate Oxides', *MRS Bull.*, vol. 27, no. 03, pp. 217–221, Mar. 2002.
- [51] K. Kukli, M. Ritala, and M. Leskelä, 'Development of Dielectric Properties of Niobium Oxide, Tantalum Oxide, and Aluminum Oxide Based Nanolayered Materials', *J. Electrochem. Soc.*, vol. 148, no. 2, p. F35, Feb. 2001.
- [52] P. N. Plassmeyer, K. Archila, J. F. Wager, and C. J. Page, 'Lanthanum Aluminum Oxide Thin-Film Dielectrics from Aqueous Solution', *ACS Appl. Mater. Interfaces*, vol. 7, no. 3, pp. 1678–1684, Jan. 2015.
- [53] G. Tilloca, 'Thermal stabilization of aluminium titanate and properties of aluminium titanate solid solutions', *J. Mater. Sci.*, vol. 26, no. 10, pp. 2809–2814, 1991.
- [54] L. Shi, Y. D. Xia, B. Xu, J. Yin, and Z. G. Liu, 'Thermal stability and electrical properties of titanium-aluminum oxide ultrathin films as high- k gate dielectric materials', *J. Appl. Phys.*, vol. 101, no. 3, p. 034102, Feb. 2007.

- [55] M. Esro, R. Mazzocco, G. Vourlias, O. Kolosov, A. Krier, W. I. Milne, and G. Adamopoulos, 'Solution processed lanthanum aluminate gate dielectrics for use in metal oxide-based thin film transistors', *Appl. Phys. Lett.*, vol. 106, no. 20, p. 203507, May 2015.
- [56] R. Guo, A. S. Bhalla, J. Sheen, F. W. Ainger, S. Erdei, E. C. Subbarao, and L. E. Cross, 'Strontium aluminum tantalum oxide and strontium aluminum niobium oxide as potential substrates for HTSC thin films', *J. Mater. Res.*, vol. 10, no. 01, pp. 18–25, Jan. 1995.
- [57] O. Rico-Fuentes, J. C. Alonso, G. Santana, and A. Ortiz, 'Ultrasonic Spray Pyrolysis Deposition and Characterization of Tantalum–Aluminum Oxide Thin Films', *J. Electrochem. Soc.*, vol. 154, no. 12, p. G277, 2007.
- [58] P. De Rouffignac and R. G. Gordon, 'Atomic layer deposition of praseodymium aluminum oxide for electrical applications', *Chem. Vap. Depos.*, vol. 12, no. 2–3, pp. 152–157, 2006.
- [59] A. N. Meza-Rocha, E. Zaleta-Alejandre, R. Balderas, Z. Rivera, M. L. Perez-Arrieta, and C. Falcony, 'Structural, Optical and Electrical Properties of Thin Films of Lanthanum Aluminum Oxide Synthesized by Spray Pyrolysis', in *ECS Transactions*, 2011, vol. 41, no. 3, pp. 183–191.
- [60] D. . Kuo and K. . Tzeng, 'Growth and properties of titania and aluminum titanate thin films obtained by r.f. magnetron sputtering', *Thin Solid Films*, vol. 420–421, no. 1, pp. 497–502, Dec. 2002.
- [61] D. Afouxenidis, R. Mazzocco, G. Vourlias, P. J. Livesley, A. Krier, W. I. Milne, O. Kolosov, and G. Adamopoulos, 'ZnO-based Thin Film Transistors Employing Aluminum Titanate Gate Dielectrics Deposited by Spray Pyrolysis at Ambient Air', *ACS Appl. Mater. Interfaces*, vol. 7, no. 13, pp. 7334–7341, Apr. 2015.
- [62] G. Ya-Na, L. Xi-Feng, Z. Jian-Hua, and Z. J.-H. Gao Ya-Na, Li Xi-Feng, 'Solution-processed high performance HIZO thin film transistor with AZO gate dielectric', *ACTA Phys. Sin.*, vol. 63, no. 11, p. 118502, Jun. 2014.
- [63] D. Perednis, O. Wilhelm, S. E. Pratsinis, and L. J. Gauckler, 'Morphology and deposition of thin yttria-stabilized zirconia films using spray pyrolysis', *Thin Solid Films*, vol. 474, no. 1–2, pp. 84–95, Mar. 2005.
- [64] G. Adamopoulos, A. Bashir, W. P. Gillin, S. Georgakopoulos, M. Shkunov, M. A. Baklar, N. Stingelin, D. D. C. Bradley, and T. D. Anthopoulos, 'Structural and Electrical Characterization of ZnO Films Grown by Spray Pyrolysis and Their Application in Thin-Film Transistors', *Adv. Funct. Mater.*, vol. 21, no. 3, pp. 525–531, Feb. 2011.
- [65] D. Hong, G. Yerubandi, H. Q. Chiang, M. C. Spiegelberg, and J. F. Wager, 'Electrical Modeling of Thin-Film Transistors', *Crit. Rev. Solid State Mater. Sci.*, vol. 33, no. 2, pp. 101–132, May 2008.

- [66] S. Harjanto, A. Shibayama, K. Sato, G. Suzuki, T. Otomo, Y. Takasaki, and T. Fujita, 'Thermal Decomposition of $NbCl_5$ in Reductive Atmosphere by Using Hydrogen Gas', *Resour. Process.*, vol. 52, no. 3, pp. 113–121, 2005.
- [67] J. Tauc, 'Optical properties and electronic structure of amorphous Ge and Si', *Mater. Res. Bull.*, vol. 3, no. 1, pp. 37–46, Jan. 1968.
- [68] G. Agarwal and G. B. Reddy, 'Study of surface morphology and optical properties of Nb_2O_5 thin films with annealing', *J. Mater. Sci. Mater. Electron.*, vol. 16, no. 1, pp. 21–24, Jan. 2005.
- [69] F. Urbach, 'The Long-Wavelength Edge of Photographic Sensitivity and of the Electronic Absorption of Solids', *Phys. Rev.*, vol. 92, no. 5, pp. 1324–1324, Dec. 1953.
- [70] D. J. Dunstan, 'Evidence for a common origin of the Urbach tails in amorphous and crystalline semiconductors', *J. Phys. C Solid State Phys.*, vol. 15, no. 13, p. 008, May 1982.
- [71] B. Orel, M. Maček, J. Grdadolnik, and A. Meden, 'In situ UV-Vis and ex situ IR spectroelectrochemical investigations of amorphous and crystalline electrochromic Nb_2O_5 films in charged/discharged states', *J. Solid State Electrochem.*, vol. 2, no. 4, pp. 221–236, Jun. 1998.
- [72] C. H. Shek, J. K. L. Lai, T. S. Gu, and G. M. Lin, 'Transformation evolution and infrared absorption spectra of amorphous and crystalline nano- Al_2O_3 powders', *Nanostructured Mater.*, vol. 8, no. 5, pp. 605–610, Aug. 1997.
- [73] C. C. C. Z. Zhao, M. Werner, S. Taylor, and P. Chalker, 'Dielectric relaxation of high-k oxides.', *Nanoscale Res. Lett.*, vol. 8, no. 1, p. 456, Jan. 2013.
- [74] P. W. Peacock and J. Robertson, 'Band offsets and Schottky barrier heights of high dielectric constant oxides', *J. Appl. Phys.*, vol. 92, no. 8, pp. 4712–4721, 2002.
- [75] J. Robertson, 'Band offsets of wide-band-gap oxides and implications for future electronic devices', *J. Vac. Sci. Technol. B Microelectron. Nanom. Struct.*, vol. 18, no. 3, p. 1785, May 2000.
- [76] M. Esro, G. Vourlias, C. Somerton, W. I. Milne, and G. Adamopoulos, 'High-mobility ZnO thin film transistors based on solution-processed hafnium oxide gate dielectrics', *Adv. Funct. Mater.*, vol. 25, no. 1, pp. 134–141, Jan. 2015.
- [77] B. L. Yang, P. T. Lai, and H. Wong, 'Conduction mechanisms in MOS gate dielectric films', *Microelectron. Reliab.*, vol. 44, no. 5, pp. 709–718, May 2004.
- [78] H. Wong, 'The Current Conduction Issues in High-k Gate Dielectrics', in *2007 IEEE Conference on Electron Devices and Solid-State Circuits*, 2007, no. CityU 121707, pp. 31–36.
- [79] F. C. Chiu, 'Interface characterization and carrier transportation in metal/ HfO_2 /silicon structure', *J. Appl. Phys.*, vol. 100, no. 11, p. 114102, Dec. 2006.

- [80] Y.-C. Yeo, T.-J. King, and C. Hu, 'Direct tunneling leakage current and scalability of alternative gate dielectrics', *Appl. Phys. Lett.*, vol. 81, no. 11, pp. 2091–2093, Sep. 2002.
- [81] N. S. Xu, J. Chen, and S. Z. Deng, 'Physical origin of nonlinearity in the Fowler–Nordheim plot of field-induced emission from amorphous diamond films: Thermionic emission to field emission', *Appl. Phys. Lett.*, vol. 76, no. 17, pp. 2463–2465, Apr. 2000.
- [82] G. Adamopoulos, A. Bashir, P. H. Wöbkenberg, D. D. C. Bradley, and T. D. Anthopoulos, 'Electronic properties of ZnO field-effect transistors fabricated by spray pyrolysis in ambient air', *Appl. Phys. Lett.*, vol. 95, no. 13, p. 133507, Sep. 2009.
- [83] Z. Zhang, C. Shao, X. Li, L. Zhang, H. Xue, C. Wang, and Y. Liu, 'Electrospun Nanofibers of ZnO–SnO₂ Heterojunction with High Photocatalytic Activity', *J. Phys. Chem. C*, vol. 114, no. 17, pp. 7920–7925, May 2010.

7. Solution Processed Crystalline Indium Zinc Oxide (c-IZO) for High Performance Thin Film Transistors

7.1 Introduction

Oxide semiconductors is a class of materials that have attracted attention as materials of choice to replace hydrogenated amorphous silicon (a-Si:H) in electronic and optoelectronic applications. This class of materials possesses advantageous properties over the a-Si:H, where their low carrier mobility, ($<1 \text{ cm}^2\text{V}^{-1}\text{s}^{-1}$) originated from its structural properties, and optical opacity, limit their use in applications where high transparency and fast switching properties are required, such as in flat panel displays (FPDs) [1]. In contrast, metal oxide based semiconductors exhibit wide optical band gaps ($>3 \text{ eV}$) that favour their use in applications where optical transparency is a prerequisite, while their electrical properties are not significantly affected by structural distortions that limit their performance [2]–[4].

In covalent semiconductors such as Si, the conduction band minimum (CBM) and the valence band maximum (VBM) are attributed to the anti-bonding ($sp^3 \sigma^*$) and bonding ($sp^3 \sigma$) states of Si hybridised orbitals, that are spatially directional. So, any bond angle fluctuation significantly alters the electronic levels, leading to high density of deep tail states within their band gap that significantly degrade their performance [5]. In contrast, the CBM of the metal oxides used in microelectronics consists of overlapping spherical ns orbitals, while the VBM consists mainly of oxygen 2p orbitals. The overlap between close ns orbitals forms a conduction pathway for free electrons. Therefore, good carrier transport properties can be achieved which are not significantly affected from crystal distortions [6], [7].

In Figure 7-1, a schematic orbital contour indicating the charge transport pathways in the conduction band of both crystalline and highly disordered covalent as well as metal oxide semiconductors is presented. As can be seen, the large overlapping ns orbitals, in metal oxides, are merely affected from structural disorder.

Among the various metal oxides that have been extensively studied as potential alternatives to a-Si:H, indium oxide (In_2O_3) and zinc oxide (ZnO) are two well characterised binary semiconductors, and a high number of studies have been reported based on their implementation as channel materials in TFTs [8]–[21]. TFTs

implementing In_2O_3 or ZnO exhibit excellent performance characteristics, such as high on/off current modulation ratio and high electron mobility [8], [9], [15], [22], [23].

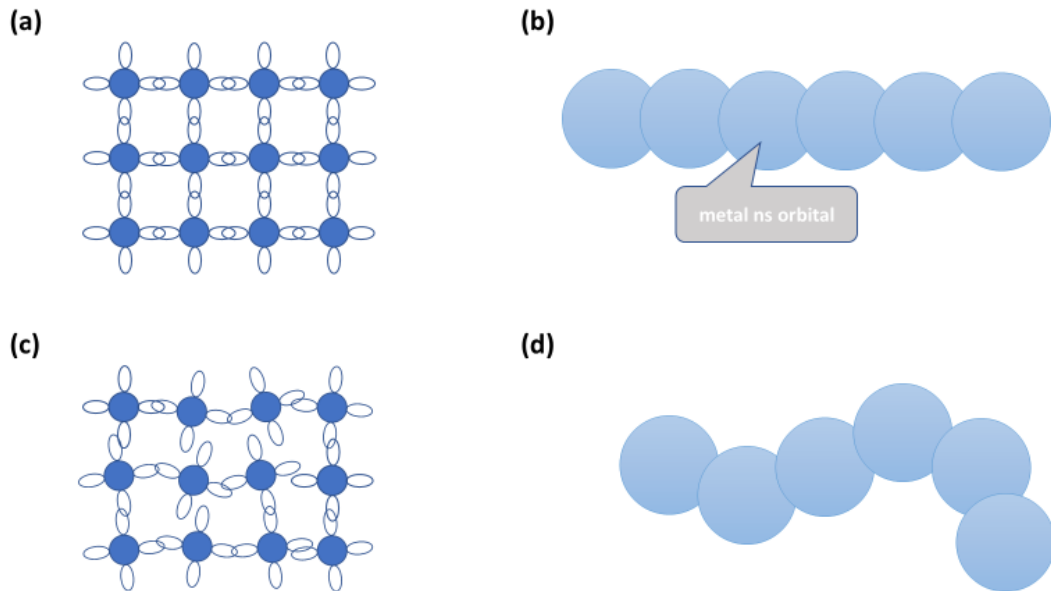


Figure 7-1: Schematic orbital contours for charge transport pathways in the conduction band of crystalline a) covalent semiconductor, b) metal oxide semiconductor, disorder c) covalent semiconductor and d) metal oxide semiconductor.

In addition to the binary In_2O_3 and ZnO , the composite oxide consisting of both indium and zinc, the ternary indium-zinc oxide (IZO), has been the subject of study, basically in its amorphous state (a-IZO). Depending on the $[\text{In}^{3+}]:[\text{Zn}^{3+}]$ ratio and oxygen content, a-IZO could be considered either as transparent conductor or, if the conductivity is reduced, as semiconductor [3].

a-IZO-based TFTs have been fabricated and extensively studied by several groups employing various deposition techniques [24]–[42]. In these reports a-IZO based TFTs exhibited remarkable performance characteristics such as high field effect mobilities and high on/off ratios. For instance, Paine et al. reported on the fabrication and performance of a-IZO TFTs fabricated by dc-magnetron sputtering techniques from a sintered IZO (In_2O_3 — 10 wt.% ZnO) sputter target [35]. The a-IZO based TFTs exhibited a threshold voltage of -5 V, field effect mobility of $15 \text{ cm}^2/\text{Vs}$, an on-off ratio of $> 10^6$ and, a subthreshold slope of 1.2 V/decade . Also, a persistent photoconductivity of the channel under UV illumination was reported. Fortunato et al.,

reported on TFTs employing a-IZO both as active channel layer and as source/drain electrodes, processed at room temperature by rf sputtering [39]. The best a-IZO based TFTs exhibited saturation mobilities higher than $100 \text{ cm}^2/\text{Vs}$, threshold voltages lower than 6 V, subthreshold slopes of 0.8 V/dec and on/off current ratios of 10^7 . Choi et al., reported on solution processed a-IZO based transparent TFTs [29]. The spin-coated a-IZO TFTs were amorphous and of high transparency. The spin-coated a-IZO based TFTs exhibited high field-effect mobility ($7.3 \text{ cm}^2/\text{Vs}$), threshold voltage of 2.5 V, an on/off current ratio in excess of 10^7 , and a subthreshold slope of about 0.47 V/dec. As a last example, Itagaki et al. studied the dependence of TFT characteristics based on the a-IZO composition [34]. According to their findings, both the performance of IZO-TFTs and IZO film properties are highly dependent on the $[\text{In}^{3+}]:[\text{Zn}^{2+}]$ atomic ratio, while the best TFT characteristics were obtained when $[\text{In}^{3+}]:[\text{Zn}^{2+}]=4:6$. The optimised TFTs exhibited high field effect mobility ($26.5 \text{ cm}^2/\text{Vs}$), low subthreshold slope (0.24 V/dec.), and very high $I_{\text{on}}/I_{\text{off}}$ current ratio (10^{10}).

Besides the admittedly high performance of a-IZO based TFTs, it has been reported that fundamentally a-IZO based TFTs suffer from instability issues, such as degradation under illumination, under bias stress or even under thermal stress [43]. The instability issue is related to the shift of threshold voltage (V_{TH}), which originates from the trapping of the charge carriers, oxygen vacancies, at the interface of the oxide semiconductor with the gate dielectric, or from the oxide semiconductor itself [4], [44], [45]. A lot of research has been conducted to overcome the instability issues in amorphous oxide semiconductor based TFTs [46]–[48]. Among the different approaches regarding the enhanced stability, post deposition induced crystallisation through high temperature annealing seems to become the dominant treatment regarding the stability enhancement.

In fact, after Yamazaki's pioneering work on the so called c-axis aligned crystal indium-gallium-zinc-oxide [49]–[51], crystalline semiconductors reattract both scientific and industrial interest; SHARP already commercialises the use of crystalline IGZO (c-IGZO) [52]. This is because, c-IGZO possesses a lower density of defect states compared to the amorphous one, resulting in higher reliability and lower off-state

leakage current [53]. In Figure 7-2 the (a) single-crystal InGaZnO_4 , (b) plane, and (c) cross-section transmission electron microscopy (TEM) images of a c-axis-aligned indium gallium zinc oxide (CAAC IGZO) thin film ($\text{In}:\text{Ga}:\text{Zn}=1:1:1$) are presented.

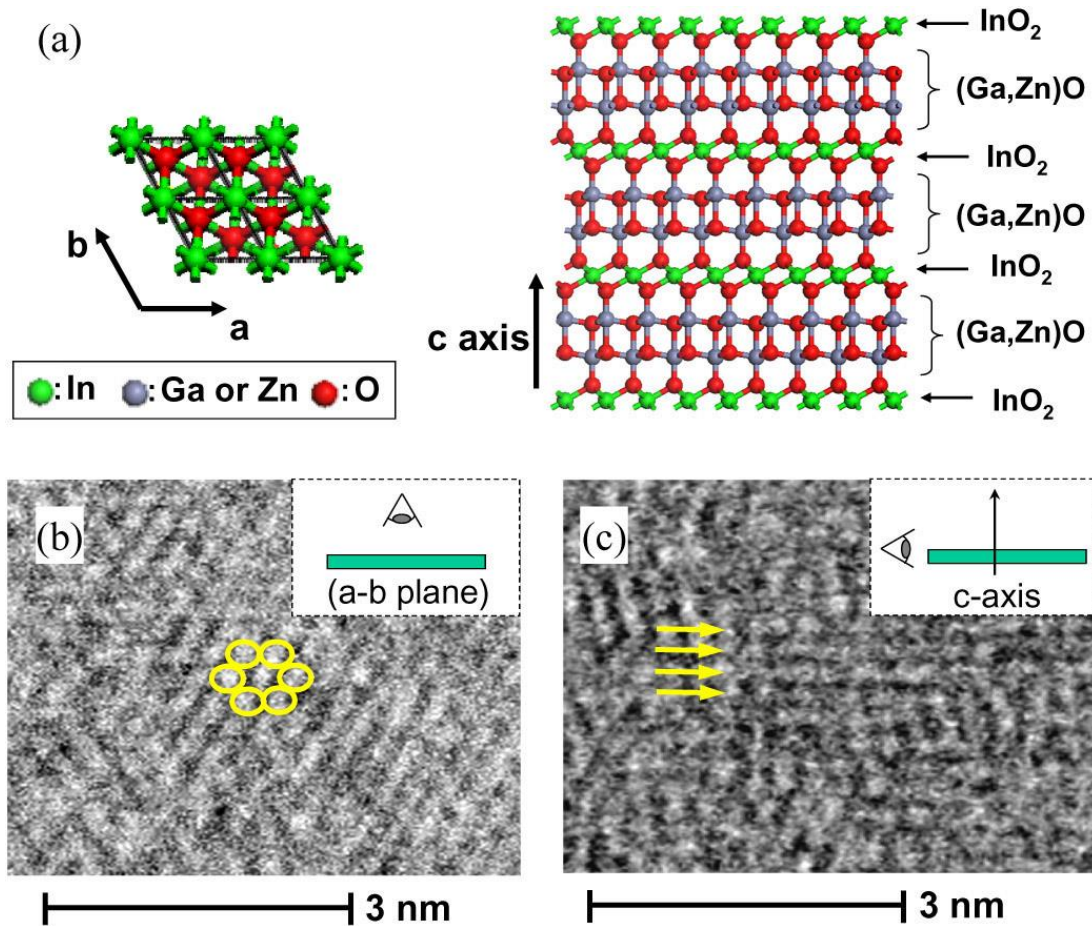


Figure 7-2: (a) Single-crystal InGaZnO_4 , (b) plane, and (c) cross-section transmission electron microscopy (TEM) images of a c-axis-aligned indium gallium zinc oxide (CAAC IGZO) thin film ($\text{In}:\text{Ga}:\text{Zn}=1:1:1$). The InO_2 layer has a compositional ratio of $\text{In}:\text{O}=1:2$ and the (Ga,Zn)O layer has a compositional ratio of $\text{Ga}:\text{Zn}:\text{O}=0.5:0.5:1$. In: Indium. Ga: Gallium. Zn: Zinc. O: Oxygen. Reprinted from [49]

Park et al., investigated the effect of c-IGZO thin films on device performance, while they further evaluated the c-IGZO based TFT reliability under bias stress and illumination [54]. The c-IGZO based TFTs exhibited lower carrier mobility, compared with amorphous IGZO (a-IGZO) TFTs, but there was a remarkable improvement of the device stability under the bias stress with illumination for the c-IGZO based TFTs. They attributed the enhanced stability to the reduced defect density of c-IGZO compared to a-IGZO ones.

Similarly, Kim et al. [55], investigated c-IZO-based TFTs. The c-IZO TFTs were fabricated at room temperature by RF sputtering with $[\text{In}^{3+}]:[\text{Zn}^{2+}]=7:3$. The as deposited films were amorphous. Post-deposition annealing at 800°C promoted the crystallinity of the films. In their study, the field effect mobility of the c-IZO-based TFTs was in excess of $50\text{ cm}^2/\text{Vs}$ in comparison to the $12\text{ cm}^2/\text{Vs}$ for the case of a-IZO. Equally, the bias stress stability even under illumination was greatly improved. The stability of the devices implementing c-IZO has been attributed to the reduction of the defect states related to the oxygen vacancy near the conduction band edge. Finally, it has been proposed that even in highly disordered semiconductors the crystallisation through post deposition annealing could be an effective way towards stability and electrical performance enhancement.

Besides the post deposition annealing of vacuum deposited a-IZO thin films at room temperature, there are no reports on directly deposited c-IZO thin films. In this chapter the structural, optical and electronic properties of c-IZO films grown by spray pyrolysis of indium chloride and zinc acetate solution with different $[\text{In}^{3+}]:[\text{Zn}^{2+}]$ atomic ratios are reported. The primary aim of this work was the study of the role of $[\text{Zn}^{2+}]$ content in IZO films and its impact on the electronic properties of IZO based TFTs. The film microstructure was investigated using a wide range of characterization techniques including X-ray diffraction, UV-Vis and FTIR spectroscopy and AFM. Finally, the electron mobility of the IZO films was investigated using an optimised bottom-gate, top-contact transistor architecture. It is the first time that direct deposition of c-IZO films and their structural and optical properties, as well as the performance of TFTs employing solution processed c-IZO, are reported.

7.2 Experimental

7.2.1 Precursor Solution Chemistry

The precursor materials that have been used in this study were aluminum 2,4-pentanedionate ($\text{Al}(\text{C}_5\text{H}_7\text{O}_2)_3$, Alfa Aesar, 99%), indium chloride (InCl_3 , Alfa Aesar, 98+%) and zinc acetate dihydrate ($\text{Zn}(\text{O}_2\text{C}_2\text{H}_3)_2 \cdot 2\text{H}_2\text{O}$, Alfa Aesar, ACS, 98-101%). All the precursor materials were used as received without any further purification. In this study, methanol (CH_3OH , VWR, ACS, $\geq 99.8\%$) was used as the solvent. However, methanol has low boiling point ($\sim 64.6^\circ\text{C}$) and evaporates rapidly. To slow down solvent evaporation, and thereby hinder particle formation, methanol was mixed with 2,4-pentanedione ($\text{C}_5\text{H}_8\text{O}_2$, Alfa Aesar, 99%) which possesses a high boiling point ($\sim 140^\circ\text{C}$) [56].

For the preparation of the indium-zinc oxide ($\text{In}_{1-x}\text{Zn}_x\text{O}_y$) precursor solutions, two methanol-based solutions of InCl_3 and $\text{Zn}(\text{O}_2\text{C}_2\text{H}_3)_2 \cdot 2\text{H}_2\text{O}$ at a concentration of 0.1 M were prepared. 2,4-pentanedione was added in both the precursor solutions at $\text{CH}_3\text{OH}:\text{C}_5\text{H}_8\text{O}_2$ molar ratio of 10:1. The solutions were left under continuous stirring for at least 1 h prior deposition, ensuring complete dissolution. The stoichiometry of indium to zinc atomic ratio was controlled by simple blending of the appropriate amount of the precursors solutions.

7.2.2 Device Fabrication

For this study, bottom gate-top contact (BG-TC) transistors (Figure 7-3) were fabricated. Commercially available indium tin oxide (ITO) coated glasses (sheet resistivity $R_s \sim 15 \Omega/\text{sq}$) were used as substrates and ITO served as gate electrode of the TFT devices. The ITO substrates were ultrasonically cleaned in acetone, rinsed with deionized water, washed with isopropanol, and dried at room temperature. On top of the ITO coated glass, Al_2O_3 of about 150 nm, serving as gate dielectric, was deposited by spray pyrolysis from methanol based aluminum 2,4-pentanedionate solution, as described elsewhere [57].

The IZO thin films were deposited on top of the glass/ITO/ Al_2O_3 stack at 400 °C using a pneumatic airbrush at ambient atmosphere. The stoichiometry of the $[\text{Zn}^{2+}]/([\text{In}^{3+}]+[\text{Zn}^{2+}])$ atomic ratio (x, hereafter) was controlled by simple blending of the appropriate amount of the precursor solutions. Finally, aluminium (Al) contacts were deposited on top of the glass/ITO/ Al_2O_3 /IZO stacks as source and drain electrodes by thermal evaporation through a shadow mask and a number of TFTs with different L/W ratios were fabricated. In Figure 7-3 the device fabrication routine employed in this study, is illustrated.

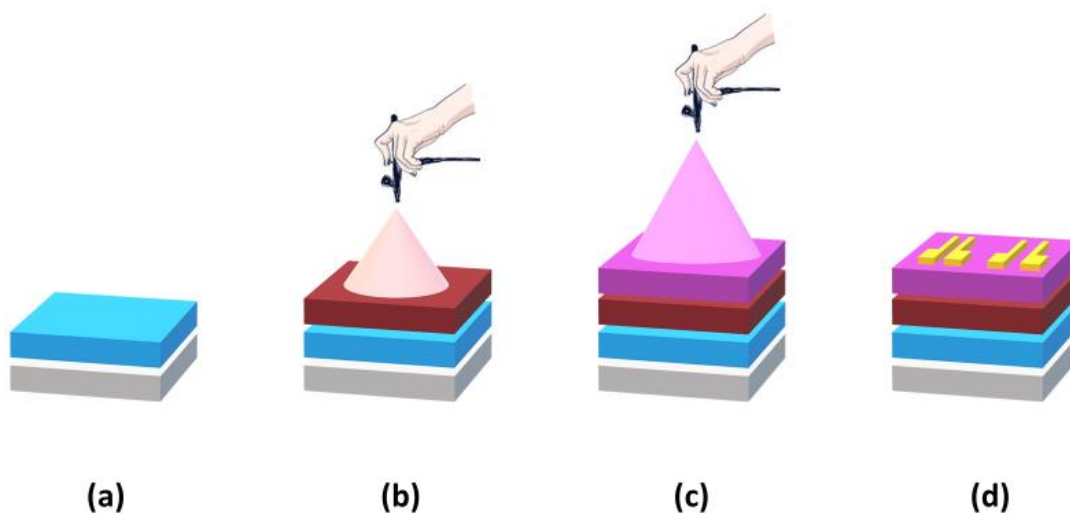


Figure 7-3: TFT fabrication routine followed in this study: a) ultrasonically clean glass/ITO substrate, b) heated glass/ITO substrates were spray coated with the Al_2O_3 precursor solution, c) deposition of IZO semiconducting channel by spray pyrolysis and d) deposition of source and drain electrodes by thermal evaporation.

7.2.3 Thin Film & Device Characterisation Techniques

The thermal properties of the precursors were investigated by thermal gravimetric analysis (TGA) and differential scanning calorimetry (DSC). The microstructure of the spray deposited thin films was characterised by X-ray diffraction. The optical properties of the films were investigated by Fourier transform infrared (FTIR) and UV-Vis absorption spectroscopy. Finally, the performance of IZO as channel material was investigated utilising a BG-TC TFT architecture (Figure 7-3.d). The

electron mobility was extracted from the transfer characteristics in both the linear and saturation regime using the gradual channel approximation [65].

7.3 Results

7.3.1 Thermal Analysis of Precursor Compounds

In Figure 7-4 the thermal analysis of indium (III) chloride (InCl_3) is shown. The TGA curve shows an initial weight loss between 80 °C and 120 °C which is attributed to the release of the absorbed water molecules due to the high hygroscopic nature of InCl_3 . Karakaya et al., studied the sublimation of InCl_3 at atmospheric pressure [58]. They showed that at high temperatures ($T > 370$ °C) the remaining product is identified as being In_2O_3 , while for the temperature region in the range between 300 °C and 370 °C, the product had been identified as being InOCl . In all cases, it has been shown that during the sublimation process of InCl_3 the inevitably absorbed H_2O had a major impact on the final products at each temperature range.

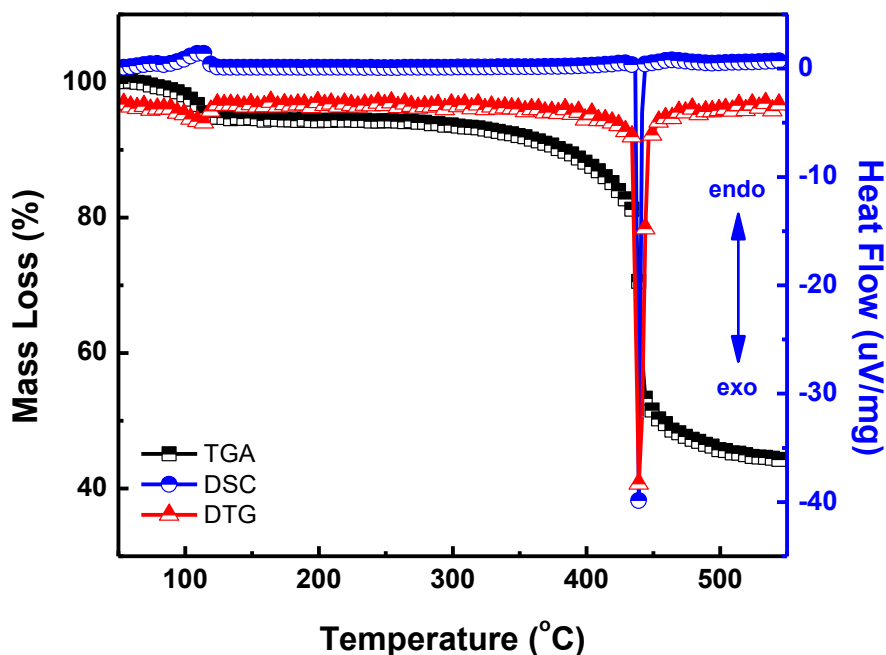


Figure 7-4: TGA (black line) and weight loss rate (red line) and DSC (right Y axis) data of 30 mg indium (III) chloride powder. TGA and DSC measurements conducted under nitrogen at a heating rate of 10 K/min.

Figure 7-5 illustrates the TGA and DSC data of $\text{Zn}(\text{O}_2\text{C}_2\text{H}_3)_2 \cdot 2\text{H}_2\text{O}$. Evidently, there is an initial mass loss in the temperature range of 80-150 °C which is attributed to the loss of the water molecules of the precursor. It has been reported that, in the temperature range 200-350 °C, a collapse of the intralayer structure that releases a variety of products that include acetic acid, acetone, water, as well as carbon dioxide, resulting from thermo-oxidation of organic species, takes place [10]. Moreover and taking into account the DSC and DTG data, it could be anticipated that for temperatures >350 °C the $\text{Zn}(\text{O}_2\text{C}_2\text{H}_3)_2 \cdot 2\text{H}_2\text{O}$ is fully decomposed while as had been reported elsewhere, polycrystalline zinc oxide is formed at about 400 °C [59], [60].

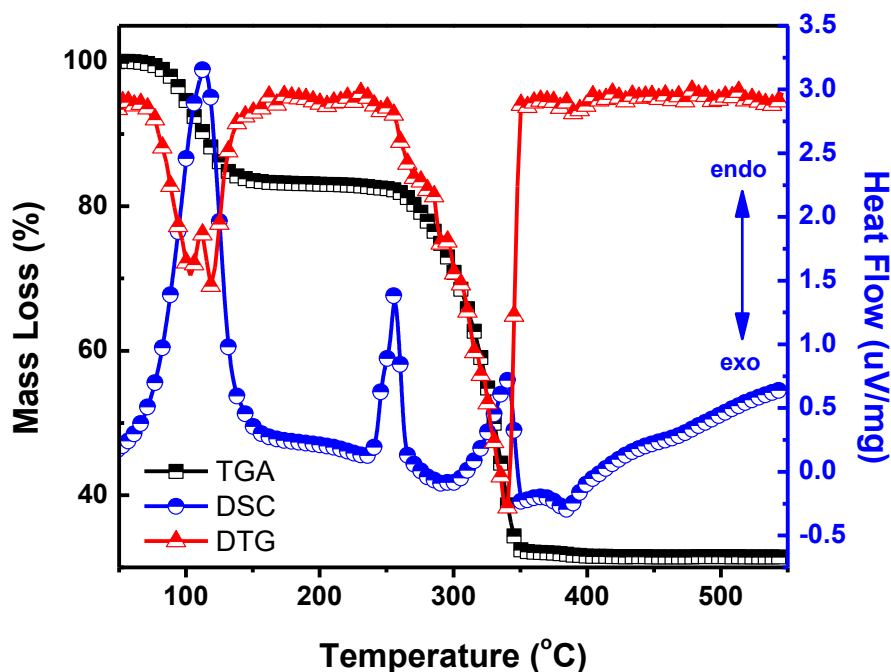


Figure 7-5: TGA (black line) and weight loss rate (red line) and DSC (right Y axis) data of 15 mg zinc acetate dihydrate powder. TGA and DSC measurements conducted under nitrogen at a heating rate of 10 K/min.

The above thermal analysis indicates that 350 °C constitutes the lowest substrate temperature for the complete precursors decomposition that can be achieved.

7.3.2 Solution Processed Indium Oxide (In_2O_3)

Firstly, the structural, optical and electronic properties of In_2O_3 films grown by spray pyrolysis of a methanol based InCl_3 solution at different substrate temperatures were investigated. The aim of this work was the study of the growth mechanism of In_2O_3 films and its impact on the electronic properties of In_2O_3 -based TFTs. The film microstructure was investigated using a UV-Vis and FTIR spectroscopy while the performance of In_2O_3 -based TFTs were evaluated as a function of deposition temperature.

7.3.2.1 Optical Properties

The optical properties of In_2O_3 films deposited at different temperatures were investigated by UV-Vis-NIR spectroscopy. In Figure 7-6 the Tauc plots of the spray deposited In_2O_3 films are presented [61].

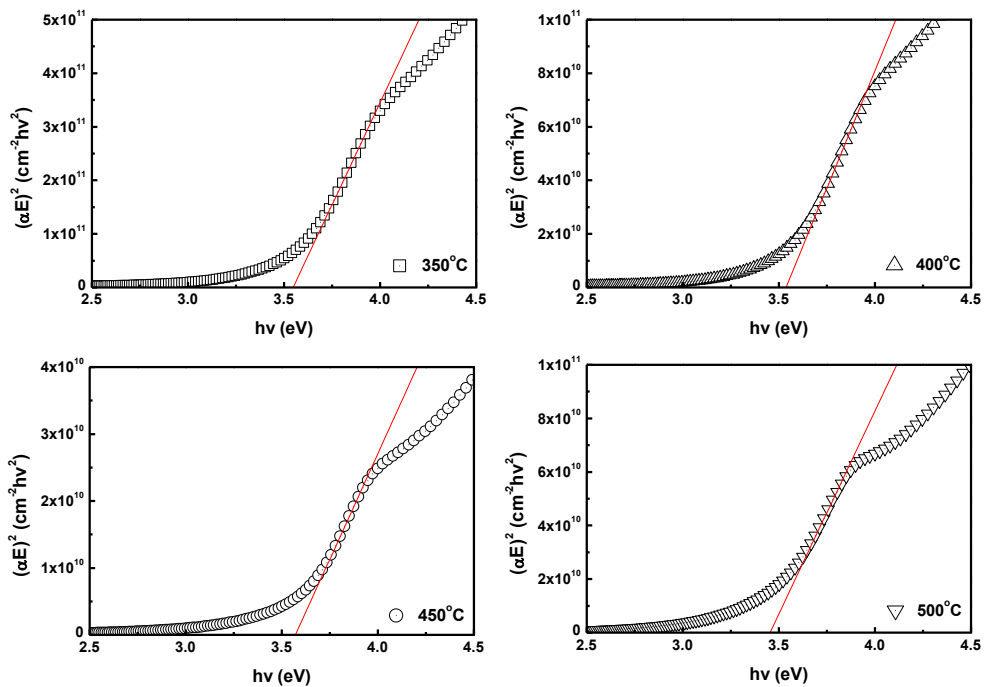


Figure 7-6: Tauc plots of spray deposited In_2O_3 films, for different deposition temperatures.

The optical band gap of the spray-deposited In_2O_3 films were derived by the Tauc plots assuming direct electronic transitions. In Figure 7-7 the calculated band gap and Urbach tail energy for spray deposited In_2O_3 films as a function of the deposition temperatures are presented. The films' band gap shows a negligible increase up to 400 °C following a sharp decrease for higher substrate temperatures. Such a decrease could be attributed to the existence of localised states in the forbidden band gap of In_2O_3 . Urbach tail energy is related to the width of the tails of localised states in the band gap of disordered materials where, the existence of localised states in the band structure is responsible for the narrowing of the optical band gap. An increase of the Urbach tail energy denotes the increase of the density of defect states, perturbation of the parabolic density of states at the band edge, loss of stoichiometry or the change in the valence state of the doping element [62]. In Figure 7-7, a decrease of Urbach tail energy was observed up to 400 °C followed by a sharp increase for substrate temperatures in excess of 500 °C. The latter explains the band gap narrowing of In_2O_3 films in the temperature range between 400 °C and 500 °C.

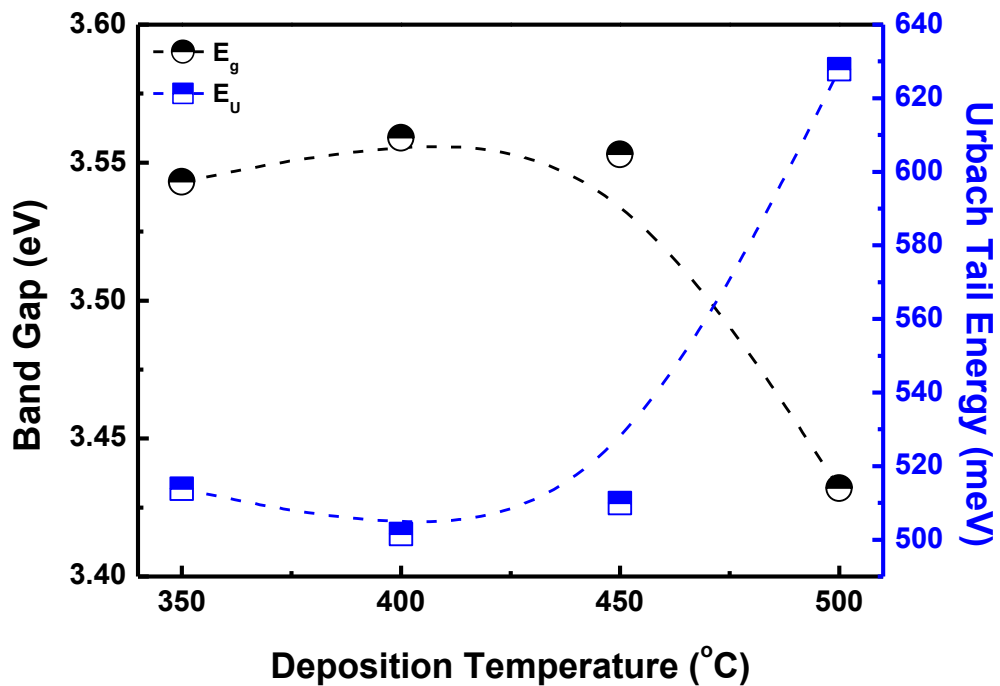


Figure 7-7: Variation of band gap (left Y axis) and Urbach tail energy (right Y axis) with deposition temperature of In_2O_3 films.

To investigate the origin of the structural disorder of In_2O_3 films, vibrational FTIR measurements were conducted for samples deposited at different substrate temperatures, as shown in Figure 7-8. Three main intense peaks centred at about 598 cm^{-1} , 562 cm^{-1} and 537 cm^{-1} were observed for all the samples deposited in the temperature range of $350\text{--}500\text{ }^\circ\text{C}$. The peak at 598 cm^{-1} has been attributed to asymmetric In-O stretching mode while the peak centred at 562 cm^{-1} has been attributed to the asymmetric stretching of O-In-O bond. A symmetric stretching of O-In-O bond is responsible for the peak centred at 537 cm^{-1} existed. Also, a peak centred at about 412 cm^{-1} (not shown) has been reported to be the characteristic In-O in plane bending mode. All the aforementioned vibration modes have been reported to be of the cubic In_2O_3 phase [63]–[65].

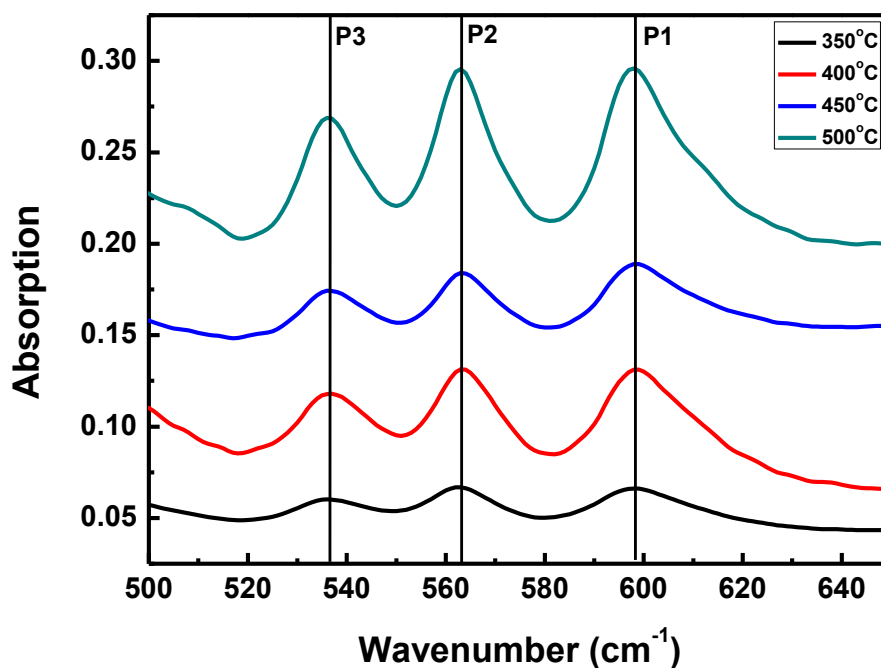


Figure 7-8: FT-IR spectra of spray deposited In_2O_3 thin films at different substrate temperatures.

A structure describing the In_2O_3 molecule, without In-In bonds, has been proposed by Panneerdoss et al., [66]. The molecule that they proposed exhibited a V-shape structure where an O was centred and two In and O atoms coupled symmetrically with equal internuclear distance. The In and O atoms were coupled

linearly and form the chain structure. According to their computational studies, the In-O bond lengths in the chain were reported to be of 1.87 and 1.96 Å, while the bond angle In-O-In was of 129°. In Figure 7-9 the proposed molecular structure of In_2O_3 by Panneerdoss et al., is depicted.

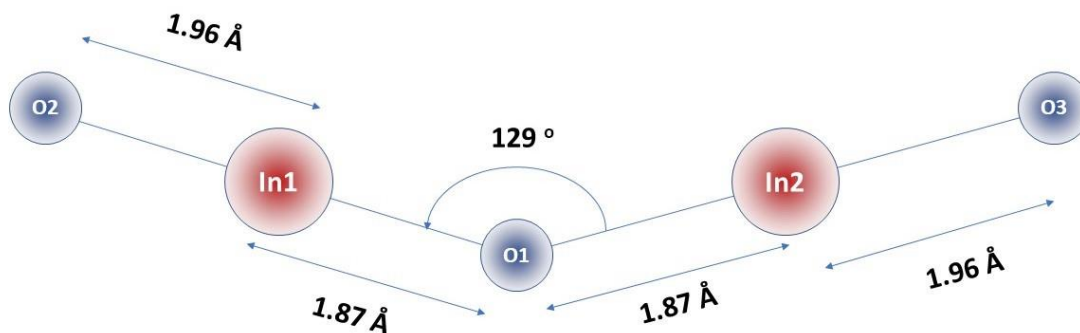


Figure 7-9: Molecular structure of In_2O_3 [66].

7.3.2.2 TFTs

The electron transport properties of spray deposited In_2O_3 thin films deposited at different substrate temperatures were investigated by their implementation as semiconducting channels in TFTs employing a BG-TC architecture (Figure 7-3d). In Figure 7-10 the transfer characteristics ($I_{\text{DS}}-V_{\text{GS}}$) of the spray-deposited In_2O_3 thin films for different substrate temperatures are presented. The impact of deposition temperature on the electronic transport properties of the spray deposited In_2O_3 TFTs, was assessed. To this end, the deposition temperature dependence of the field-effect mobility in saturation regime ($\mu_{\text{e,sat}}$), the off-state current (I_{off}), the threshold voltage (V_{T}) and the subthreshold voltage (SS) were investigated (Figure 7-11).

In_2O_3 -based TFTs deposited at 350 °C exhibit an off-state current of about 100 nA, a current modulation ratio of 10^4 , a threshold voltage of -2.87 V, an electron mobility of about $9 \text{ cm}^2\text{V}^{-1}\text{s}^{-1}$ and a subthreshold voltage swing of 2.19 V/dec. The TFTs deposited at 400 °C show the lowest off-state current of 1 nA, the highest current modulation in excess of 10^5 , threshold voltage of about 8 V, the highest electron

mobility in excess of $9.5 \text{ cm}^2\text{V}^{-1}\text{s}^{-1}$ and the lowest subthreshold voltage swing of about 1.67 V/dec. At higher deposition temperatures, the performance of the In_2O_3 -based TFTs deteriorated, as the TFTs exhibited higher off-state currents, reduced on to off current modulation ratios, decreased field effect mobilities and higher subthreshold voltage swing. The operational characteristics of the In_2O_3 based TFTs are summarised in Table 7-1.

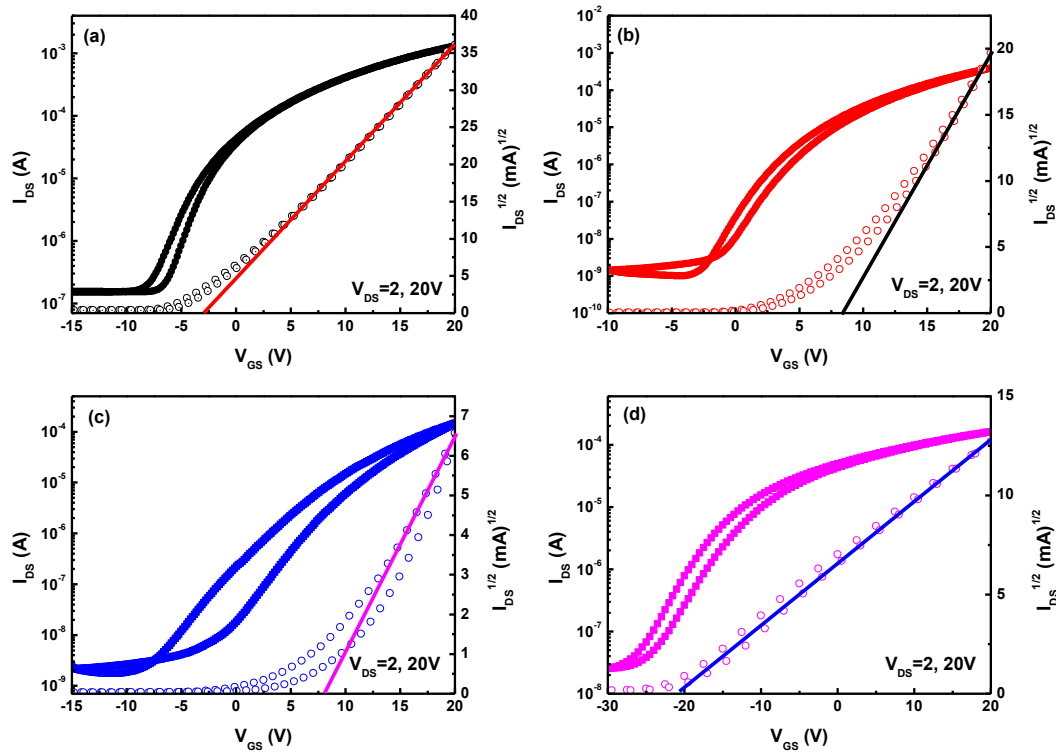


Figure 7-10: I_{DS} (left axis) and $I_{DS}^{1/2}$ (right axis) versus V_{GS} curves of spray deposited In_2O_3 -based TFTs for different In_2O_3 deposition temperatures (a) 350°C, (b) 400°C, (c) 450°C and (d) 500°C. The channel length (L) and width (W) were 100 and 1000 μm respectively.

Table 7-1: Operational characteristics of spray deposited In_2O_3 based TFTs, for different deposition temperatures.

T_d (°C)	V_t (V)	ΔV_t (V)	I_{off} (A)	I_{on} (A)	I_{on}/I_{off}	μ_{sat} (cm^2/Vs)	SS (V/dec)
350	-2.87	0.8	1.51×10^{-7}	1.30×10^{-3}	8.65×10^3	9.13	2.19
400	8.27	1.1	1.01×10^{-9}	3.87×10^{-4}	3.85×10^5	9.63	1.67
450	7.62	3.6	1.75×10^{-9}	1.47×10^{-4}	8.38×10^4	3.76	3.58
500	-21.09	3.63	2.53×10^{-8}	1.62×10^{-4}	6.40×10^3	0.45	4.41

The extracted operational characteristics of spray deposited In_2O_3 -based TFTs for different deposition temperature could be interpreted considering also the results from the optical measurements. By increasing the deposition temperature from 350 °C to 400 °C, an initial increase in the band gap could be seen while the Urbach energy was reduced. Considering that Urbach energy refers to the width of the tails of localised states in the band gap, it could be associated to the decrease of the conductivity of the films. Since the density of localised states is reduced, the density of the donor like traps close to conduction band of In_2O_3 should be reduced. That is the reason of the observed decrease of the off-state current, by increasing the deposition temperature up to 400 °C. Also, the positive shift of threshold voltage originates from the decrease of the carrier concentration in the film.

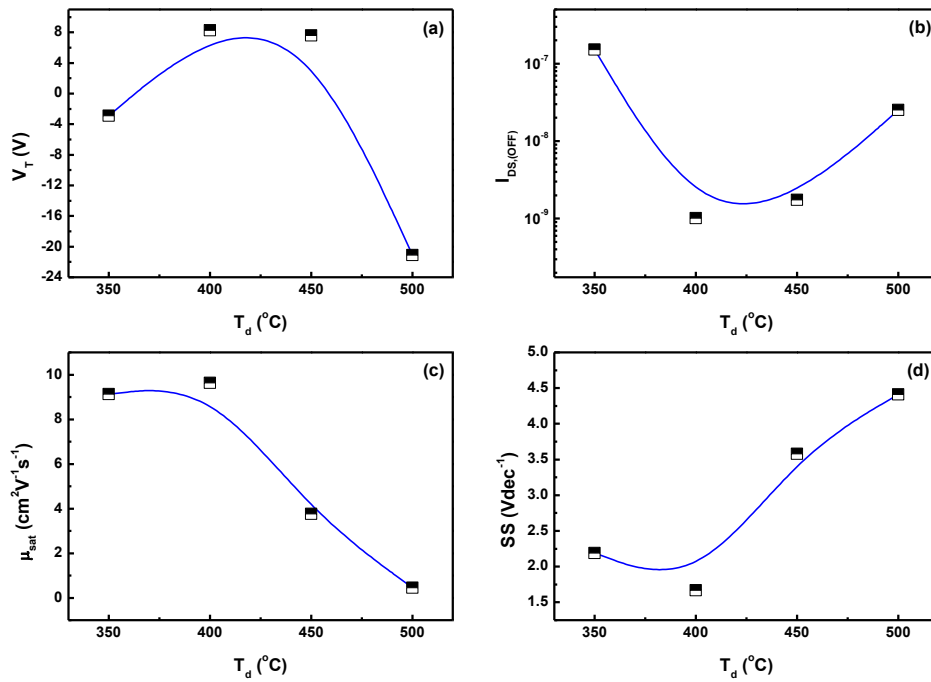


Figure 7-11: Extracted operational characteristics of spray deposited In_2O_3 -based TFTs for different deposition temperatures. a) threshold voltage, b) off-state current, c) field effect mobility in saturation regime and d) subthreshold swing. (The lines are guides to the eyes)

Further increase of deposition temperature, from 400 °C to 500 °C, resulted in an increase of the Urbach energy. It could be expected that such increase in the width of the localised states result to an increase of the conductivity of the films due to the

band gap narrowing. The latter is reflected in the off-state current of TFTs, as it was found to increase as the deposition temperature was increased from 400 °C to 500 °C.

Finally, a decrease in the field effect mobility as the deposition temperature increased, is depicted in Figure 7-11.c. Considering that the carrier mobility in oxide semiconductors is not band tail limited, the decrease in mobility could be attributed to increased interface trap density (D_{it}). D_{it} is proportional to subthreshold swing (SS), ($D_{it}=C_i[(SS/2.3ek_B T)-1/e^2]$) where C_i is the geometric capacitance of the dielectric, e is the elementary charge, k_B is Boltzmann constant, and T the temperature. As can be seen from Figure 7-11(d), an increase of SS as the deposition temperature increased, is realised. The reason of this increase is not entirely clear, but it could be attributed to a deterioration of the dielectric-semiconductor interface quality which further deteriorates the field effect mobility.

Among the devices, TFTs based on In_2O_3 deposited at 400 °C showed the best performance which could result from the fact that structural distortions, such as oxygen vacancies, are minimised at this temperature. The latter is associated with the minimum of Urbach energy at this deposition temperature.

7.3.3 Solution Processed Indium Zinc Oxide (IZO)

In this section, spray deposited IZO thin films as potential TFTs semiconducting channel, are studied. In order for an all-around characterisation to be performed, IZO films were prepared onto a number of substrates for optical, structural and electronic characterisation. IZO films were deposited at 400 °C, as it was found to be the optimum deposition temperature of In_2O_3 , in respect to the TFT characteristics.

7.3.3.1 Optical Properties

Figure 7-12 illustrates the transmission spectra of the IZO films with varying the $[Zn^{2+}]/([Zn^{2+}]+[In^{3+}])$ ratio. Figure 7-12 reveals IZO films of excellent optical quality and high optical transparency on the order of 85 % in the visible spectrum.

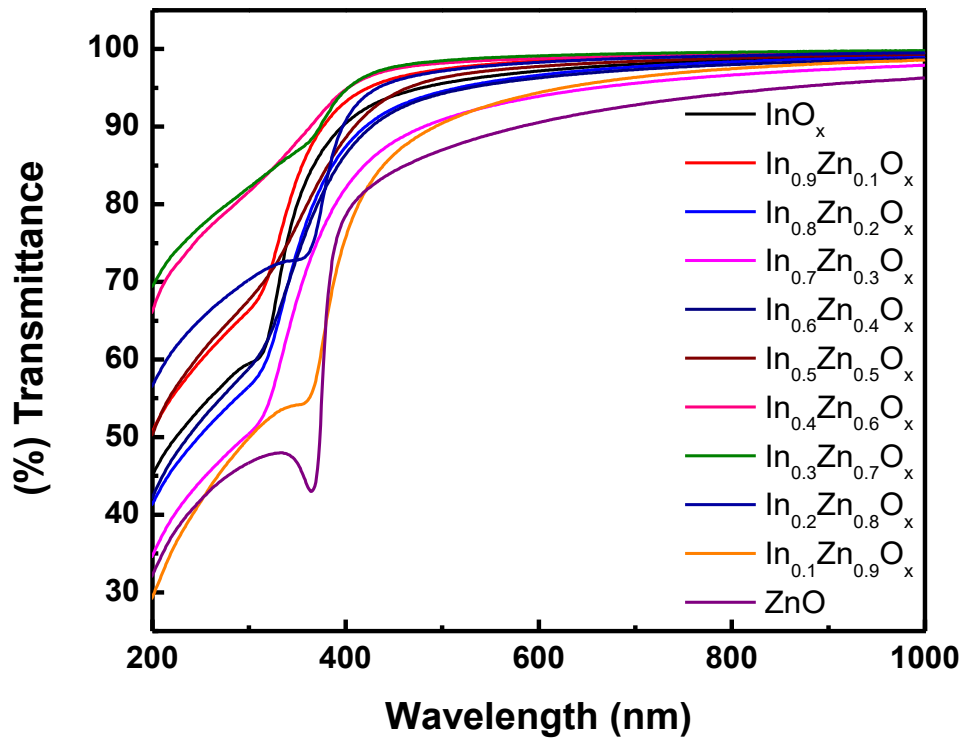


Figure 7-12: Optical transmittance of IZO thin films deposited by spray pyrolysis on fused silica substrates

The optical band gap of IZO films were derived using the Tauc plots. Figure 7-13 shows the Tauc plots of IZO films with varying the $[Zn^{2+}]/([Zn^{2+}]+[In^{3+}])$ atomic ratio. The optical band gap as well as the Urbach tail energy as a function of the $[Zn^{2+}]/([Zn^{2+}]+[In^{3+}])$ atomic ratio are illustrated in Figure 7-14.

The optical band gap (E_g) shows a monotonic decrease with the increase of the $[Zn^{2+}]/([Zn^{2+}]+[In^{3+}])$ ratio in the solution and ranges between 3.6 eV and 3.2 eV. These results clearly demonstrate the band gap engineering of solution processed metal oxides by means of physical blending of the precursor solutions [67], [68].

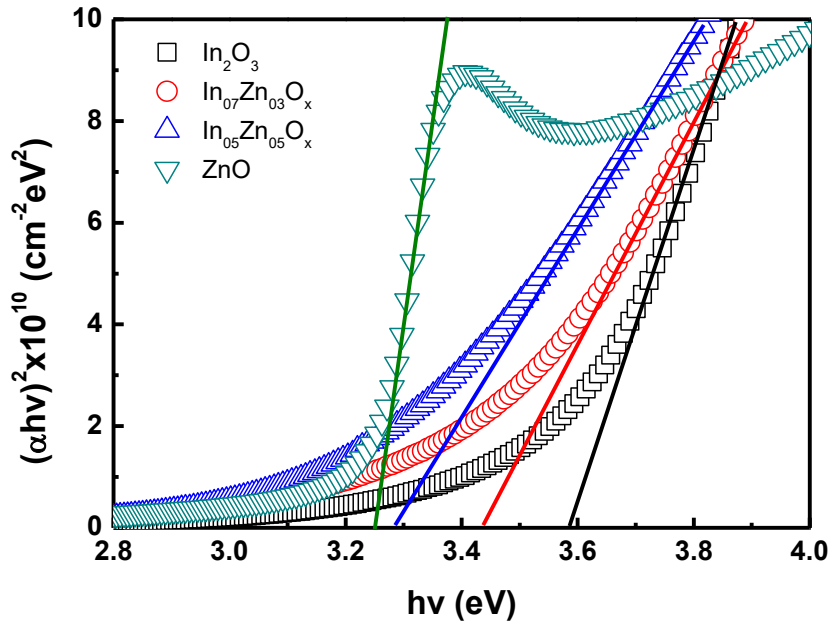


Figure 7-13: Tauc Plots of selected IZO spray deposited thin films.

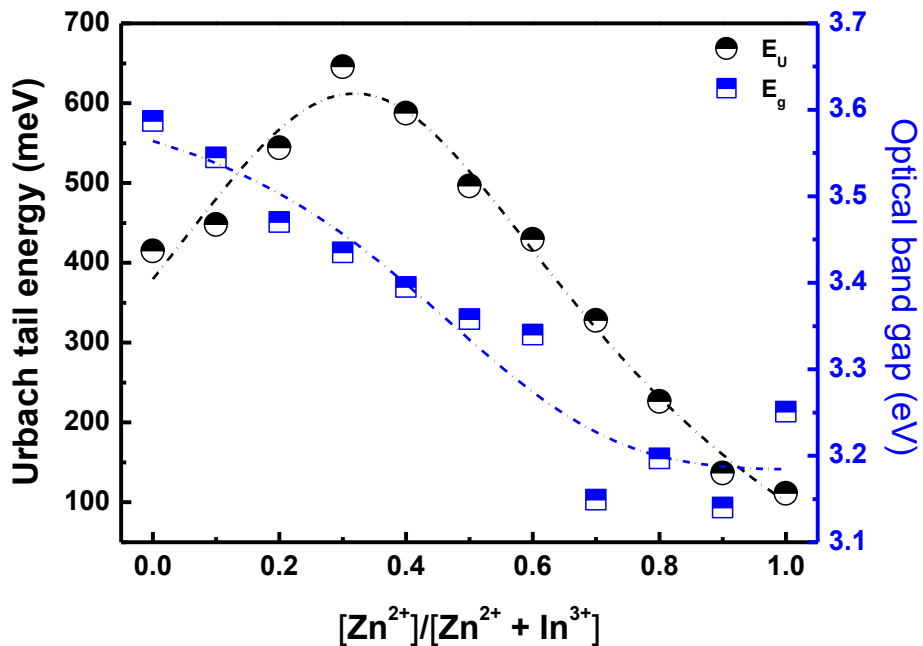


Figure 7-14: Urbach tail energy E_u (left axis) and optical band gap energy (right axis) of spray deposited IZO thin films as a function of $[Zn^{2+}]/([Zn^{2+}]+[In^{3+}])$ in the solution. The lines are guides to the eye.

Figure 7-14 shows the Urbach tail energy (E_u) of IZO thin films as a function of the $[Zn^{2+}]/([Zn^{2+}]+[In^{3+}])$ ratio, which peaks at $[Zn^{2+}]/([Zn^{2+}]+[In^{3+}]) \sim 0.3$

($[\text{In}^{3+}]:[\text{Zn}^{2+}]=7:3$). From this stoichiometry and beyond the Urbach tail energy showed a monotonic decrease, reaching a minimum of 100 meV for ZnO. Urbach tail energy is associated with the degree of the structural distortion in both crystalline and amorphous materials [69]. It is well known that defects, such as vacancies and interstitials as well as changes in bond lengths and bond angles between atoms in a crystal structure, induce localised states in the band gap.

To further investigate the origin of the Urbach energy dependence on $[\text{Zn}^{2+}]/([\text{Zn}^{2+}]+[\text{In}^{3+}])$ atomic ratio the films were characterised by FTIR spectroscopy. Besides the evolution of bond lengths and angles between the atoms, FTIR could provide useful information related to the precursors' decomposition and their conversion to the related oxides.

The FTIR spectra of IZO films deposited on KBr substrates were conducted in absorption mode in the range of 400-4000 cm^{-1} . Figure 7-15(a), shows the FTIR spectra of IZO films in the range of 400-450 cm^{-1} , while Figure 7-15(b) shows the range between 500 and 650 cm^{-1} . The FTIR spectra clearly demonstrate the complete decomposition of the precursor materials as bands attributed to the precursors do not contribute to the spectra (Figure 7-23 in this chapter's Appendixes).

As it can be seen from Figure 7-15(a) and Figure 7-15(b) there is a peak centred at 419 cm^{-1} followed by a set of peaks in the range between 520 and 650 cm^{-1} . As already mentioned these peaks are the characteristic vibration modes of In-O bonds signature of cubic In_2O_3 [63]–[65]. The peak at 598 cm^{-1} is attributed to asymmetric In-O bond stretching while the peak centred at 562 cm^{-1} is attributed to the asymmetric stretching of O-In-O. Moreover, from the symmetric stretching of O-In-O the peak centred at 537 cm^{-1} existed. Also, a peak centred at about 412 cm^{-1} (not shown) has been reported to be the characteristic In-O in plane bending mode.

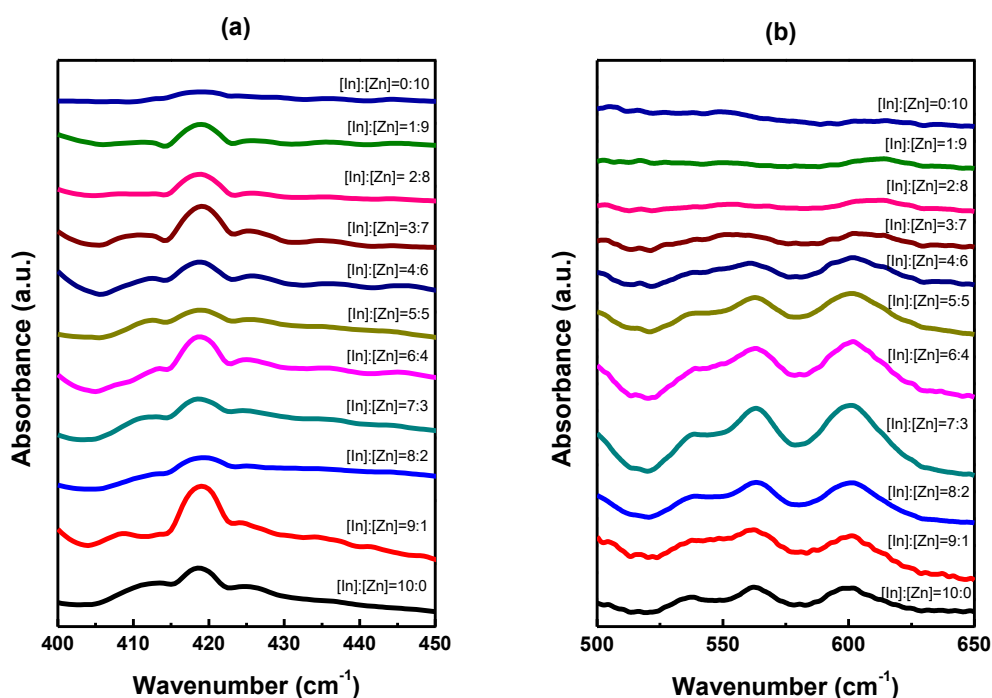


Figure 7-15: FTIR spectra of spray deposited IZO films on KBr substrates for different wavenumber regions.

Increasing the $[Zn^{2+}]/([In^{3+}]+[Zn^{2+}])$ ratio results in a decrease of the peak intensity as well as a noticeable broadening. It is known that the broadening of a FTIR peak is related to the structural disorder. Because of the broadening of the FTIR peaks, it could be assumed that increase of the $[Zn^{2+}]$ content in the films results in a structural distortion. However, this distortion could not be related neither with the change of In-O bond lengths nor with the change in In-O-In bond angle (Figure 7-9), as there was no remarkable peak shift, as the $[Zn^{2+}]/([In^{3+}]+[Zn^{2+}])$ ratio increased. It could be assumed that either $[Zn^{2+}]$ substitute $[In^{3+}]$ atoms in its crystal lattice, or $[Zn^{2+}]$ is an interstitial in a host In_2O_3 lattice.

To elucidate the crystallographic structure of the IZO and further investigate the role of $[Zn^{2+}]$ atoms into the In_2O_3 crystal structure, supplementary structural analysis was conducted, by XRD.

7.3.3.2 Structural Properties

The diffraction patterns of IZO films on silicon substrates are shown in Figure 7-16. Evidently, IZO films show distinct crystalline features for a $[\text{Zn}^{2+}]/([\text{Zn}^{2+}]+[\text{In}^{3+}])$ atomic ratio of up to 0.7. Pattern indexing is based on the bixbyite In_2O_3 structure (JCPDS 06-0416) [55].

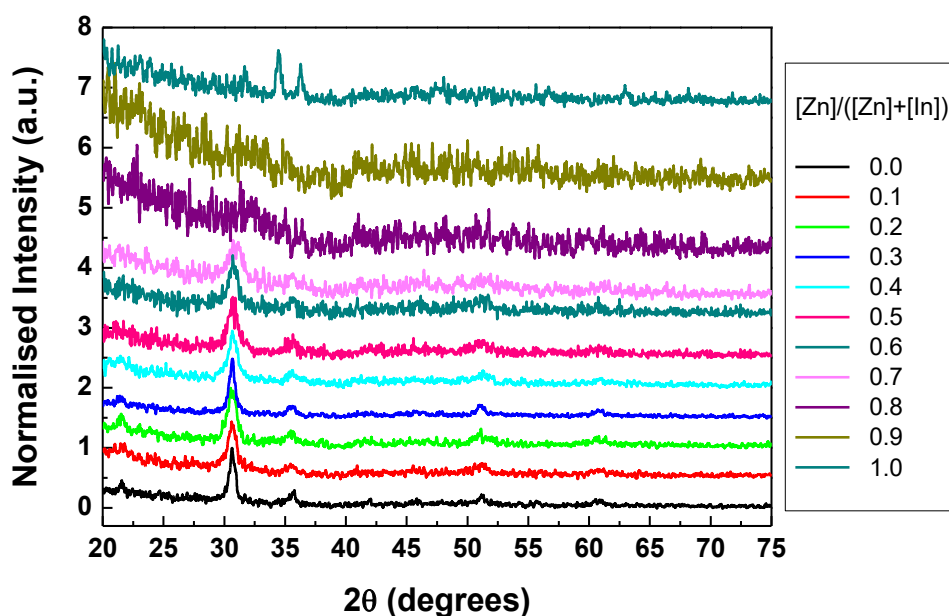


Figure 7-16: X-ray diffraction of spray deposited IZO films on Si substrates for different $[\text{Zn}^{2+}]/([\text{Zn}^{2+}]+[\text{In}^{3+}])$

The strong (222) diffraction peak indicates highly textured films along this crystallographic orientation. Besides this, a less predominant reflection that appears at $2\theta=35.5^\circ$ is the (400) reflection of cubic bixbyite-type In_2O_3 [19], [55], [70].

For the case of ZnO films, diffraction peaks at $2\theta=31.8^\circ$, 34.54° and 36.5° were shown in XRD patterns. These peaks are the (100), (002) and (101) reflections of hexagonal ZnO (JCPDS 89–1397) [71]–[73].

It is however noticed that for the case of the spray deposited IZO thin films where $[\text{Zn}^{2+}]/([\text{Zn}^{2+}]+[\text{In}^{3+}])>0.7$, i.e. $[\text{In}^{3+}]:[\text{Zn}^{2+}]>3:7$, there were no diffraction peaks that could be attributed to any zinc or indium-related compound. The absence of any zinc related compound diffraction peaks demonstrates that the $[\text{Zn}^{2+}]$ influences the

In_2O_3 crystal structure without forming any IZO compound. This is consistent with the results obtained from FTI. The broadening of the characteristic vibration modes in the range between 520 and 650 cm^{-1} could be explained by the existence of amorphous structure, as it is well known that high structural distortion increases the FWHM of the peaks.

To further investigate the effects of $[\text{Zn}^{2+}]$ of the structural properties of IZO films in the range of $0 \leq [\text{Zn}^{2+}]/([\text{Zn}^{2+}] + [\text{In}^{3+}]) \leq 0.7$, the average crystallite size, interplanar spacing, lattice constant and lattice volume were calculated using the (222) reflection. The average crystal size was derived from the Scherer formula while interplanar spacing d_{hkl} was calculated from the Bragg law [74].

In Figure 7-17 the average crystal size, the interplanar spacing, the lattice constant and the lattice volume of the spray deposited IZO thin films in the range of $0 \leq [\text{Zn}^{2+}]/([\text{Zn}^{2+}] + [\text{In}^{3+}]) \leq 0.7$ as they were calculated from the (222) reflection peak, are presented.

The average crystal size of the spray deposited IZO films in the range of $0 \leq [\text{Zn}^{2+}]/([\text{Zn}^{2+}] + [\text{In}^{3+}]) \leq 0.7$ decreases monotonically with increasing the $[\text{Zn}^{2+}]/([\text{Zn}^{2+}] + [\text{In}^{3+}])$ ratio. The average crystal size of In_2O_3 thin film was found to be 13.34 nm while for the case of IZO film possessing a stoichiometry of $[\text{Zn}^{2+}]/([\text{Zn}^{2+}] + [\text{In}^{3+}]) = 0.7$ the average crystal size was found to be of about 4.86 nm. The interplanar spacing d_{222} showed an initial increase from 2.91413 Å for the case of In_2O_3 to 2.91685 Å for the case of IZO film with stoichiometry of $[\text{Zn}^{2+}]/([\text{Zn}^{2+}] + [\text{In}^{3+}]) = 0.2$, following by a decrease to 2.89288 Å for $[\text{Zn}^{2+}]/([\text{Zn}^{2+}] + [\text{In}^{3+}]) = 0.7$.

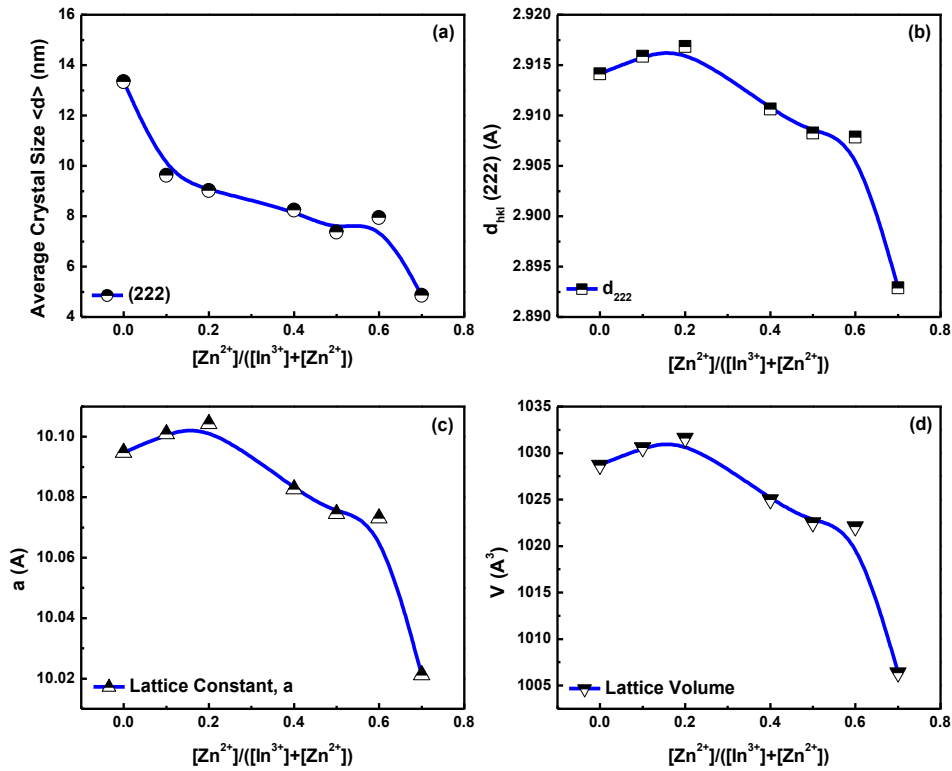


Figure 7-17: (a) average crystallite size, calculated from (222) diffraction peaks, (b) interplanar spacing d_{hkl} calculated for (222) plane, (c) lattice parameter a calculated from the (222) diffraction peak and (d) the corresponding lattice volume assuming the cubic bixbyite cubic In_2O_3 structure.

Considering the results of Figure 7-17, it can be assumed that in the indium rich region (i.e. $[\text{Zn}^{2+}]/([\text{Zn}^{2+}]+[\text{In}^{3+}]) < 0.3$), $[\text{In}^{3+}]$ has not been replaced by $[\text{Zn}^{2+}]$. This is because a substitution of $[\text{Zn}^{2+}]$ in $[\text{In}^{3+}]$ should cause a contraction of the lattice due to the difference on the size of the ions. $[\text{Zn}^{2+}]$ has an atomic radius of 142 pm while the atomic radius of $[\text{In}^{3+}]$ is 156 pm. In contrast, assuming that $[\text{Zn}^{2+}]$ acts as an interstitial in the In_2O_3 structure, a lattice expansion can be expected.

A further increase of the $[\text{Zn}^{2+}]$ content in the films, results in further substitution of $[\text{In}^{3+}]$ atoms. Since the atomic radius of $[\text{Zn}^{2+}]$ is smaller than that of $[\text{In}^{3+}]$ a shrinkage of the lattice is expected. Indeed, when the $[\text{Zn}^{2+}]/([\text{Zn}^{2+}]+[\text{In}^{3+}])$ is higher than 0.3, the lattice constant of the IZO films was reduced indicating a lattice contraction. In Figure 7-18 a schematic representation of deformation in In_2O_3 crystal structure due to Zn^{2+} interstitials and substitutions in In^{3+} sites, is illustrated.

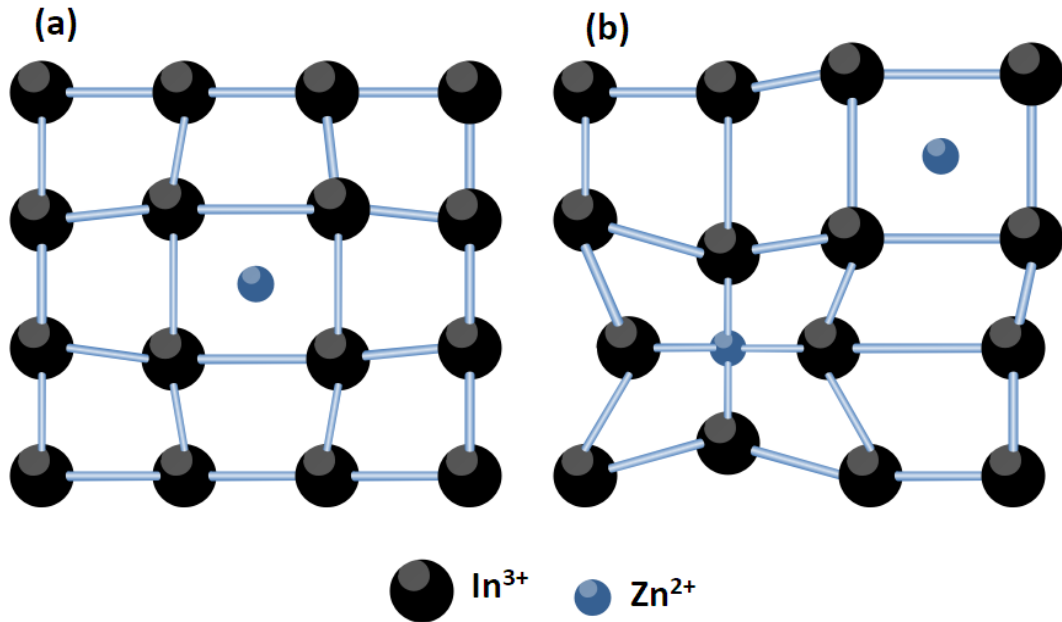


Figure 7-18: Representation of In_2O_3 lattice structure assuming a) Zn^{2+} interstitials and b) Zn^{2+} interstitials and substitutions in In^{3+} site.

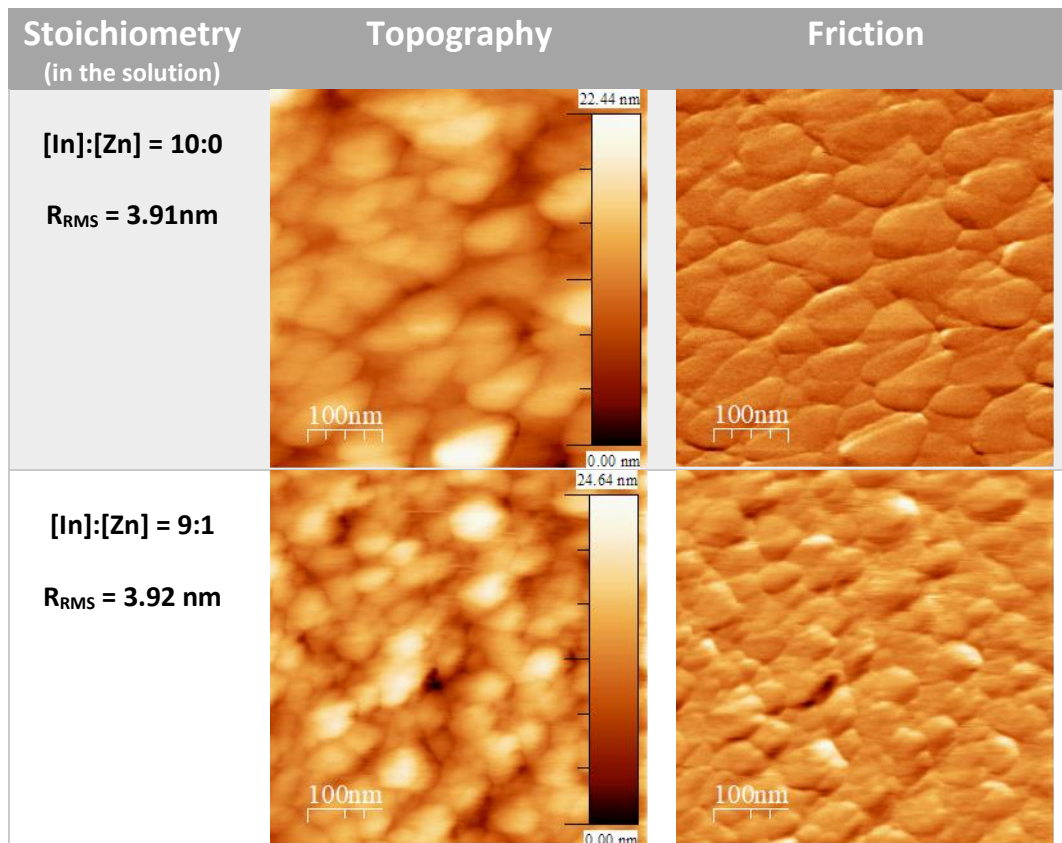
The lattice expansion or contraction as a function of $[\text{Zn}^{2+}]/([\text{Zn}^{2+}]+[\text{In}^{3+}])$ affects the Urbach energy. Following Cody et al., [75] the total disorder can be anticipated as the sum of two terms; thermal disorder and static disorder. The thermal disorder yields from excitations of phonon modes while the static disorder is due to structural disorder. Cody et al., proposed a generalised equation to summarise both the contributions of static and dynamic disorder, as

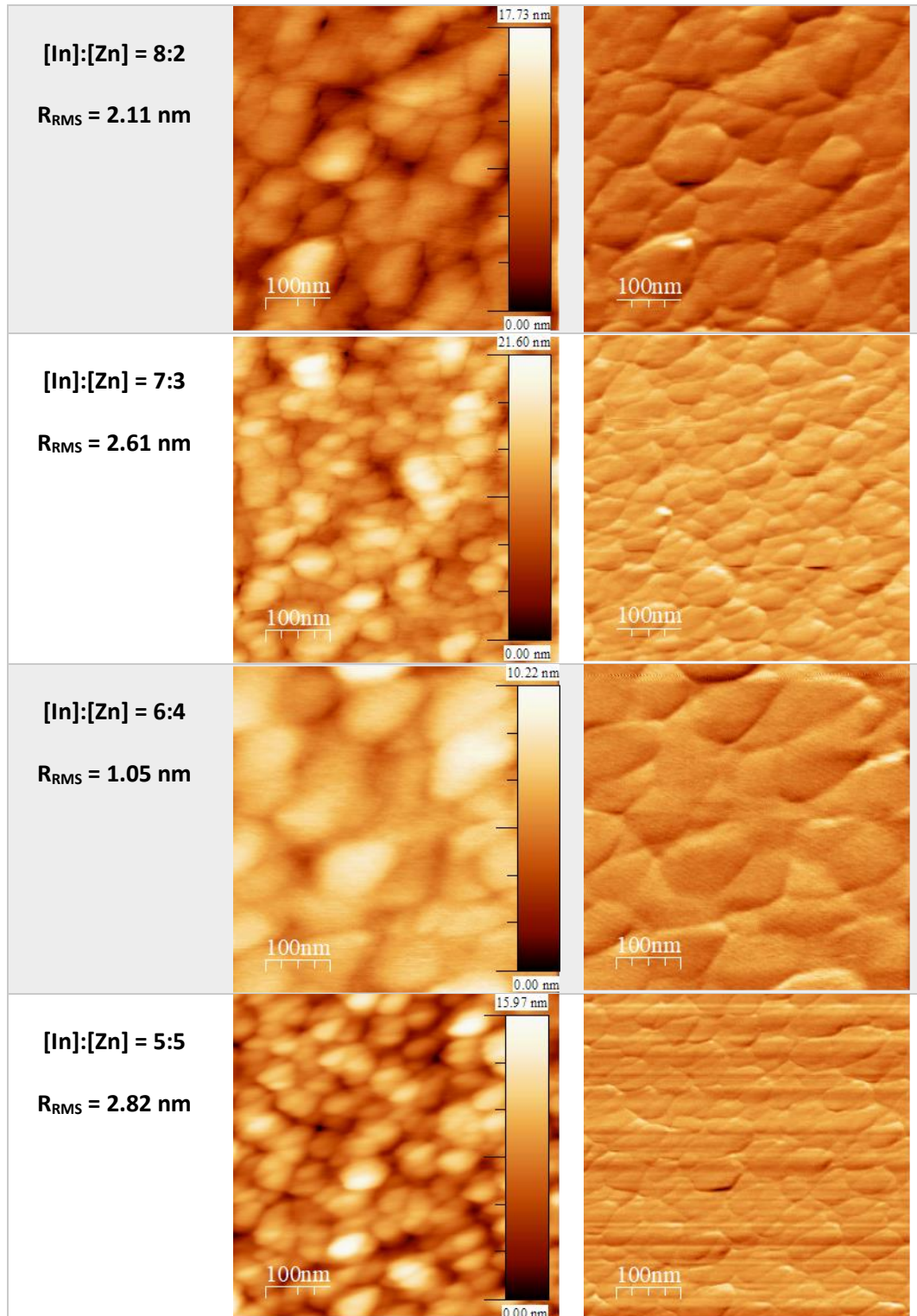
$$E_u(T,X)=K(\langle U^2 \rangle_T + \langle U^2 \rangle_X) \quad (7-1)$$

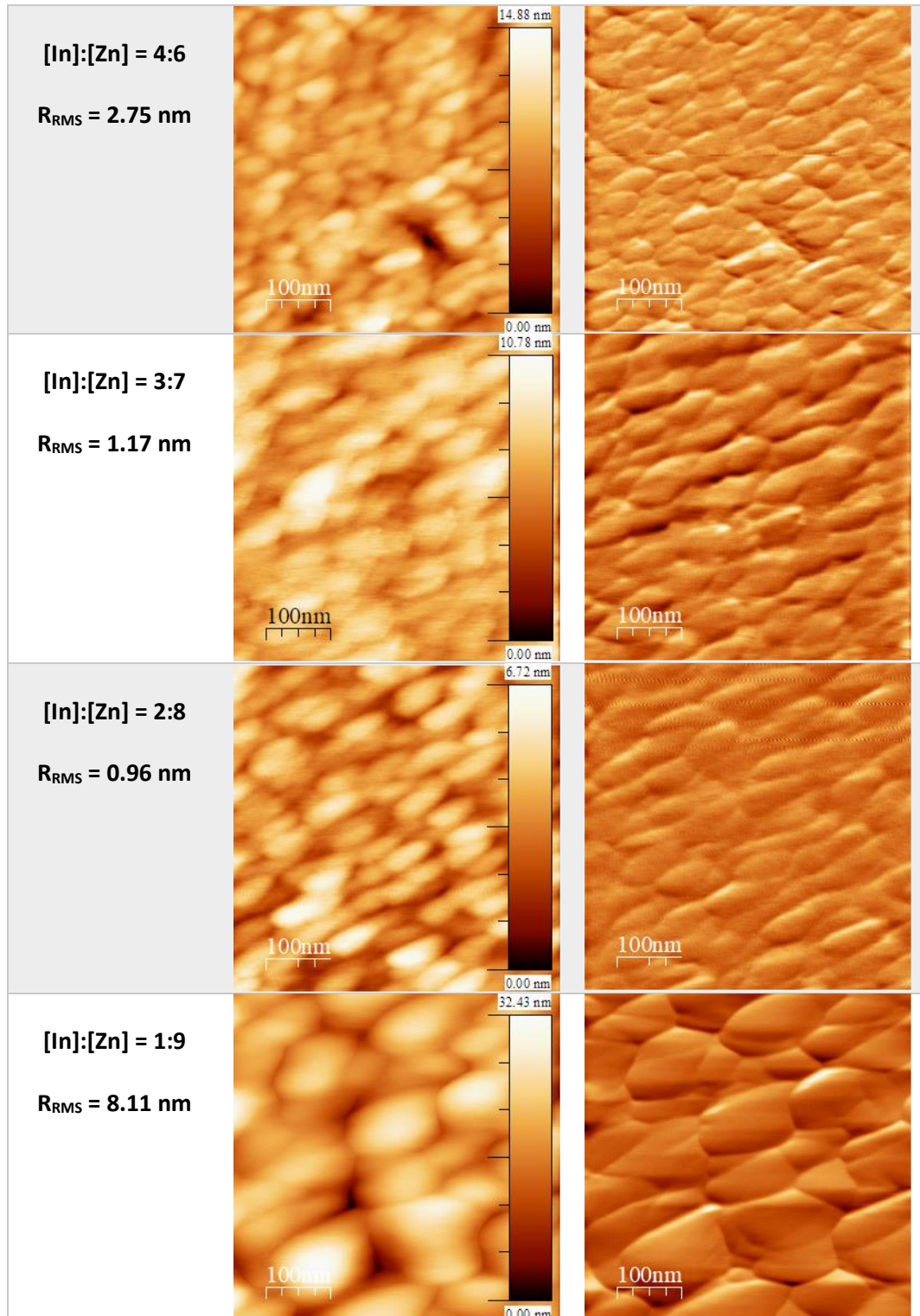
where, $\langle U^2 \rangle_T$ is related to the mean square displacement of atoms and $\langle U^2 \rangle_X$ is the static inherent structural disorder. Considering the impact of the dynamic disorder component, it could be assumed that Zn^{2+} interstitials increase the dynamic disorder due to the increased displacement among the atoms, while the substitution of In^{3+} atoms by Zn^{2+} reduces the Urbach tail as the interatomic distances become shorter reducing the impact of dynamic disorder in Urbach energy.

7.3.3.3 Surface Analysis on IZO thin films

The surface morphologies of IZO films as a function of $[Zn^{2+}]/([Zn^{2+}]+[In^{3+}])$ were investigated by AFM. In Figure 7-19 both topography and friction images of the spray deposited IZO films are illustrated. The surface friction characteristics are of particular interest because they provide not only an insight of homogeneity but additionally topography images with enhanced edges [76]. The latter is a useful feature as it allows the investigation on the density of the grain boundaries. It is well known that grain boundaries have a major impact on the carrier transport, as they are scattering centres that degrade the carrier mobility.







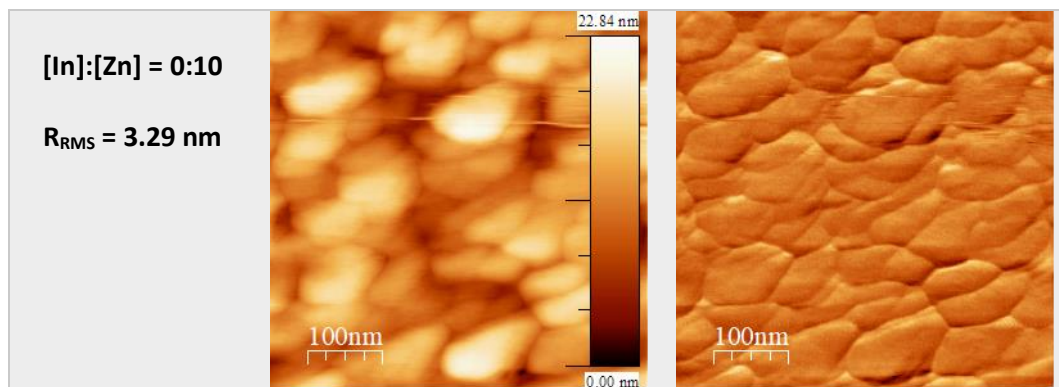


Figure 7-19: Atomic force images of spray deposited IZO films on Si substrates for different $[\text{In}^{3+}]:[\text{Zn}^{2+}]$ ratios.

The topography images analysis revealed films of low roughness ($R_{\text{rms}} < 10 \text{ nm}$). Films of low roughness values have been reported to exhibit high performance as TFT, channel materials [72], [77], [78]. Besides Coulombic and phonon scattering, interface roughness is an important scattering mechanism that limits the carrier mobility [79]. Moreover, from the friction images, it could be seen that there is an initial decrease of the concentration of grain boundaries which seems that for the case of $[\text{In}^{3+}]:[\text{Zn}^{2+}] = 6:4$, is reduced to a minimum level. This is attributed to an increase in grain size which could be resulted by the increase of the lattice volume of the films

7.3.3.4 TFT characteristics

The electron transport properties of IZO films were investigated by their implementation as semiconducting channels in TFTs employing a BG-TC TFT architecture and equally spray coated Al_2O_3 gate dielectric. In this study, all the devices were of $100 \mu\text{m}$ and $1000 \mu\text{m}$ channel length (L) and width (W) respectively.

Figure 7-20 illustrates the transfer characteristics, at saturation of the TFTs employing spray deposited IZO films as semiconducting channel for different $[\text{In}]:[\text{Zn}]$ ratios. The TFT parameters are also summarised in Table 7-2.

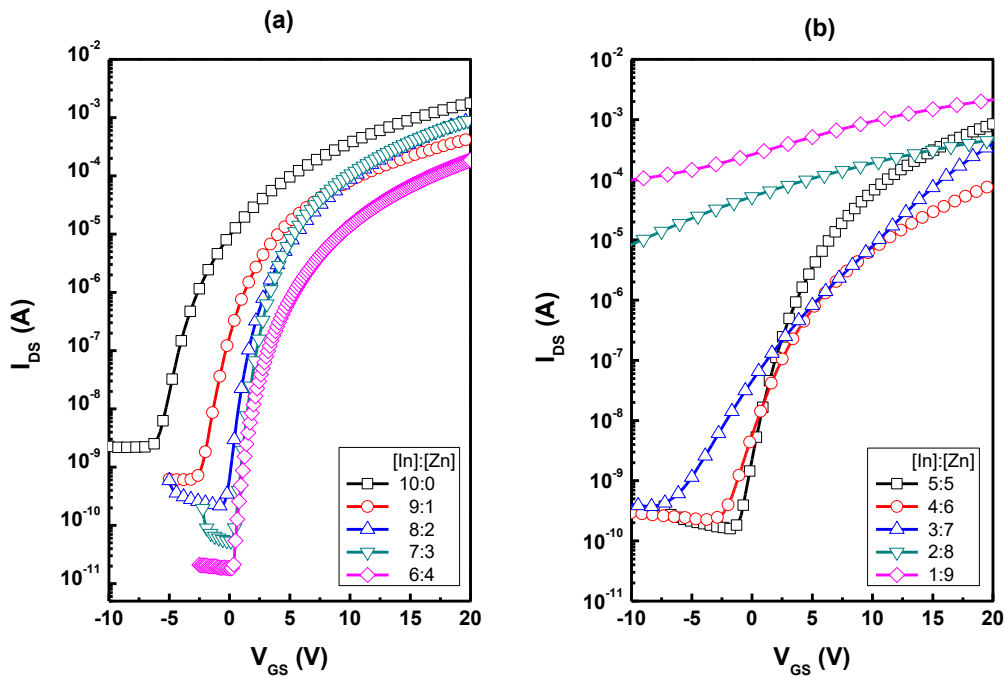


Figure 7-20: Transfer characteristics (I_{DS} - V_{GS}), in saturation regime ($V_{DS}=20$ V), of the spray deposited IZO thin films for different [In]:[Zn] atomic ratios. (a) Indium rich region, (b) zinc rich region.

The effects of the IZO composition on the off-state current, current modulation, field-effect mobility and subthreshold voltage swing as a function of $[Zn^{2+}]$ content in the IZO-films, are presented in Figure 7-21.

As it can be seen from Figure 7-20, Figure 7-21 and Table 7-2 the off-state current (I_{off}) showed an initial decrease from about 2 nA for the case of In_2O_3 channel, down to about 18 pA for $[In]:[Zn] = 6:4$ followed by an increase up to about 1 nA for the case of ZnO. The initial decrease of the I_{off} is due to a decrease of the free carrier concentration induced by the inclusion of $[Zn^{2+}]$ atoms as lattice interstitials into the lattice of In_2O_3 . Naghavi et al., reported that increase in the content of $[Zn^{2+}]$ into In_2O_3 host matrix, led to a decrease in the carrier concentration in their IZO thin films [80]. Considering the results based on the I_{off} , it can be assumed that $[Zn^{2+}]$ suppress the oxygen vacancies of In_2O_3 , which are the source of free carriers.

Table 7-2: Summary of operational characteristics of the spray deposited IZO thin films for different [In]:[Zn] atomic ratios.

[In]:[Zn]	V_{on} (V)	I_{off} (A)	I_{on} (A)	I_{on}/I_{off}	μ_{sat} ($cm^2V^{-1}s^{-1}$)	SS (Vdec $^{-1}$)
10:0	-6.91	2.2×10^{-9}	1.7×10^{-3}	7.7×10^5	8.50	1.02
9:1	-3.01	6.1×10^{-10}	4.3×10^{-4}	7.1×10^5	7.95	0.87
8:2	-0.55	2.2×10^{-10}	9.1×10^{-4}	4.1×10^6	7.67	0.60
7:3	0.182	5.3×10^{-11}	9.6×10^{-4}	1.8×10^7	6.58	0.45
6:4	1.91	1.8×10^{-11}	1.8×10^{-4}	1.0×10^7	4.80	0.30
5:5	-1.62	1.6×10^{-10}	8.3×10^{-4}	5.2×10^6	3.51	0.92
4:6	-2.61	2.3×10^{-10}	8.2×10^{-5}	3.4×10^5	1.18	1.58
3:7	-8.01	5.3×10^{-10}	3.9×10^{-4}	7.4×10^5	8.30	2.93
2:8	No TFT characteristics					
1:9	No TFT characteristics					
0:10	-3.8	9.5×10^{-10}	2.5×10^{-4}	2.6×10^5	5.30	1.77

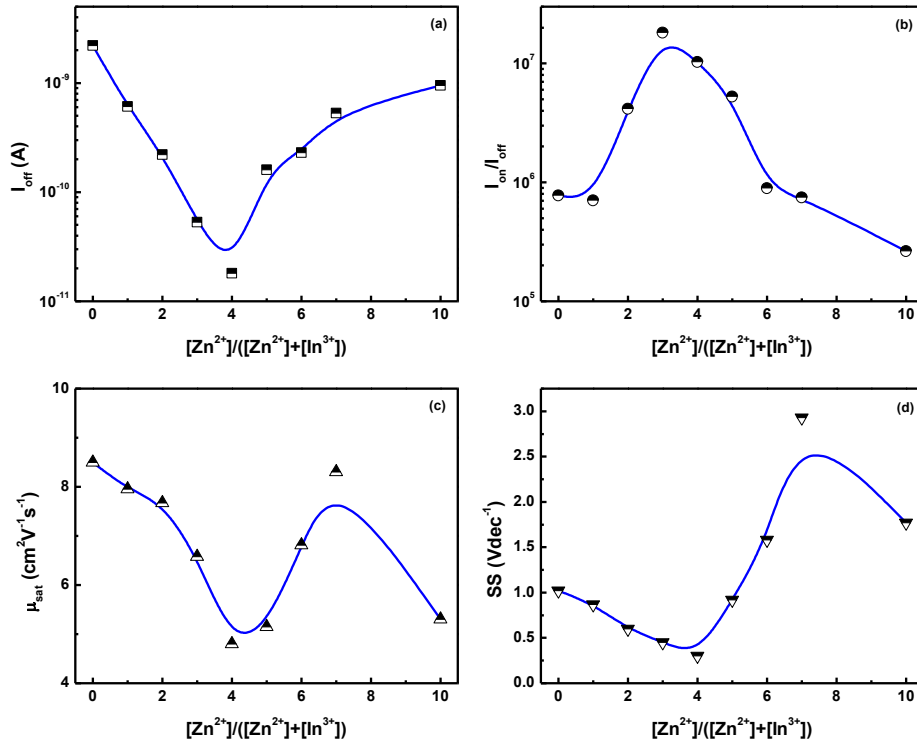


Figure 7-21: (a) off-state current, (b) current modulation, (c) field effect mobility, (d) subthreshold voltage swing. The lines are guides to the eye.

The increase of conductivity of Zn-rich IZO is shown by the increase of I_{off} and it is attributed to an increase of free carriers, possibly originated from oxygen vacancies induced by the excess of Zn atoms that substitute the indium [77], [80].

Indium atoms can coordinate 6 oxygens, while Zn can coordinate 4. Based on this, when an In atom is substituted by a Zn atom, a formation of a pair of oxygen vacancies may result. The higher the substituted Zn content, the higher the oxygen vacancy concentration in the In_2O_3 crystal.

A similar trend, was observed for the SS as a function of the $[\text{In}^{3+}]:[\text{Zn}^{2+}]$ ratio. The SS value showed a decrease from 1 V/dec for undoped In_2O_3 -based TFTs down to about 300 mV/dec for the films with a ratio of $[\text{In}^{3+}]:[\text{Zn}^{2+}]=6:4$ followed by an increase up to about 1.8 V/dec for In-free ZnO. The SS has been used to extract the maximum trap density per unit energy ($D_{\text{tr}}=C_{\text{ox}}[(\text{SS}/2.3ek_{\text{B}}T)-1/e^2]$) at the semiconductor/dielectric interface [81]. Therefore, for IZO films of a $[\text{In}^{3+}]:[\text{Zn}^{2+}]$ ratio of 6:4, with the lowest SS, the maximum trap density was found to be as low as $D_{\text{tr}}=1.38 \times 10^{12} \text{ eV}^{-1}\text{cm}^{-2}$. Such low trap density is acceptable for oxide/oxide interfaces [82]. The semiconductor-dielectric interface is of great importance regarding TFT operation since it manifests the carrier transport within the channel of the TFT. An interface free of trap centres will allow smoother carrier pathways free of scattering centres that degrade performance.

Finally, the field effect mobility (μ_{sat}) of the IZO-based TFTs was found to be decreased with increasing the $[\text{Zn}^{2+}]$ content. The highest field effect mobility of about ($8.5 \text{ cm}^2\text{V}^{-1}\text{s}^{-1}$) was achieved for the devices employing In_2O_3 . Martins et. al., reported that, in contrast to covalent semiconductors, in oxide semiconductors the carrier mobility is not band-tail limited, therefore is not affected by structural disorder and the carrier transport properties highly depend on the oxygen vacancies, the source of free carriers [82]. Additionally, Adamopoulos et. al., reported that average crystal size $\langle d \rangle$, of the oxide semiconductor, strongly affects the field effect mobility of ZnO-based TFTs [10], [83]. According to their findings larger crystals reduce the effect of grain boundary limited transport. Therefore, the decrease of the μ_{sat} originates from both the decrease of the carrier concentration with the increase of $[\text{Zn}^{2+}]$ content in the films as well as the decrease of the average crystal size (Figure 7-17a). Assuming that low $[\text{Zn}^{2+}]$ concentration in In_2O_3 , i.e. $[\text{Zn}^{2+}]/([\text{Zn}^{2+}]+[\text{In}^{3+}]) < 0.4$, considered to be a metal interstitial, that immobilises the oxygen vacancies, the decrease in I_{off} and μ_{sat}

could be explained. Further increase of the $[Zn^{2+}]$ content in the IZO, enhanced channel conductivity that it was hard to be depleted, even when high voltages were applied.

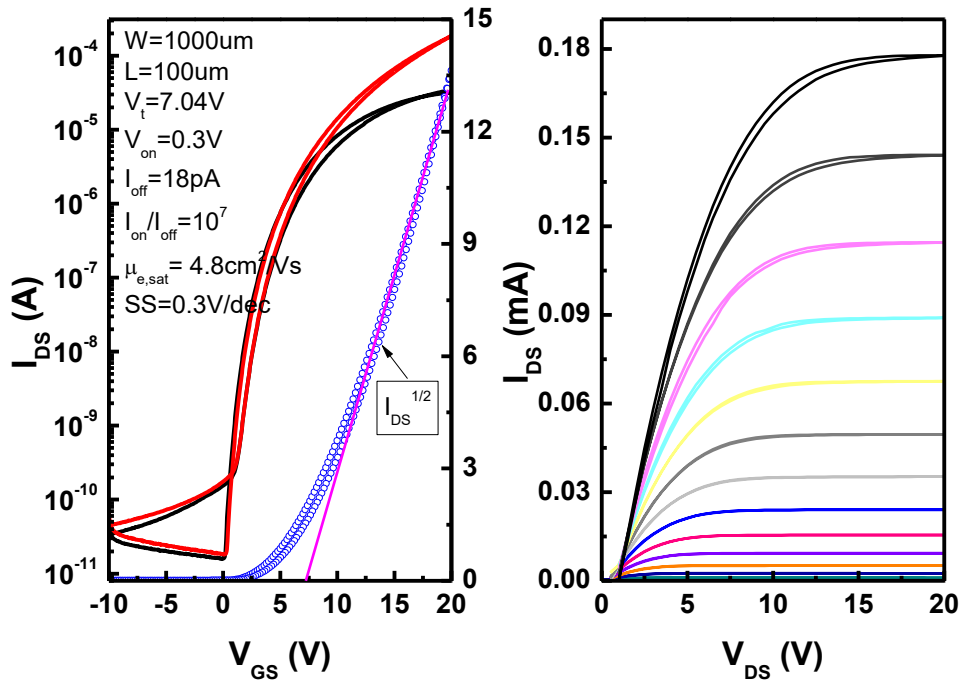


Figure 7-22: Transfer (left) and output (right) characteristics of the spray deposited IZO based thin film transistor possessing a $[In^{3+}]:[Zn^{2+}]=6:4$ stoichiometry.

A representative set of the transfer and output characteristics for an optimised TFT ($L=100\mu m$, $W=1000\mu m$) based on IZO with the optimum ratio of $[Zn^{2+}]/([Zn^{2+}]+[In^{3+}])=0.4$, i.e $[In^{3+}]:[Zn^{2+}]=6:4$, is shown in Figure 7-22.

7.4 Summary

In this chapter the role of $[Zn^{2+}]$ on the structural, optical and charge carrier transport properties of spray deposited crystalline IZO was investigated. Thin films were deposited from methanol-based solution of the respected metal precursors. $InCl_3$ and $Zn(O_2C_2H_3)_2 \cdot 2H_2O$ were used in this study as source of In and Zn respectively. The thermal properties both of precursors, were investigated by TGA/DSC. A substrate temperature higher than $370\text{ }^\circ C$ was found to be sufficient for the complete decomposition of $InCl_3$ to In_2O_3 , while a temperature slightly higher than $350\text{ }^\circ C$ was

found to be sufficient for the complete decomposition of $\text{Zn}(\text{O}_2\text{C}_2\text{H}_3)_2 \cdot 2\text{H}_2\text{O}$ and its transformation to ZnO.

Firstly, the impact of deposition temperature, on the optical and charge carrier transport properties of the spray deposited In_2O_3 thin films was investigated. Optical characterisation, by UV-Vis spectroscopy, revealed a negligible increase of the In_2O_3 band gap, 3.56 eV for substrate temperature of 400 °C, followed by a sharp decrease for higher deposition temperatures, i.e. 3.43 eV for deposition at 500 °C. Such a decrease was attributed to the existence of localised states in the band gap of In_2O_3 as was further confirmed from the Urbach energy. FTIR confirmed the complete conversion of the precursor to indium oxide, while further analysis revealed the molecular structure of In_2O_3 . Furthermore, the impact of deposition temperature on the electron transport properties of In_2O_3 thin films was also investigated. Among the devices, In_2O_3 -based TFTs deposited at 400 °C showed the best performance exhibiting low off-state current (~ 2 nA), high on-off current ratio ($\sim 10^5$), high field-effect electron mobility (9.63 cm^2/Vs) and low subthreshold swing (1.67 V/dec). The origin of the improved characteristics at this temperature was interpreted considering the reduced width of the localised tails in the band gap that slightly increased the band gap, and the improved oxide-dielectric interface quality as confirmed by SS.

Considering the optimum deposition temperature for In_2O_3 films, a series of IZO films were deposited as a function of $[\text{Zn}^{2+}]/([\text{Zn}^{2+}]+[\text{In}^{3+}])$ ratio. The impact of $[\text{Zn}^{2+}]$ on optical, structural and electrical properties of the IZO was investigated by a wide range of experimental techniques. Optical experiments (UV-Vis transmission spectroscopy and FTIR) revealed films of high optical quality and transparency on the order of 85 % in the visible spectrum. The optical band gap decreased as the $[\text{Zn}^{2+}]/([\text{Zn}^{2+}]+[\text{In}^{3+}])$ ratio was increased and ranged between 3.6 eV for In_2O_3 and 3.2 eV for ZnO. To elucidate the impact of $[\text{Zn}^{2+}]$ content on the band structure of $\text{In}_{1-x}\text{Zn}_x\text{O}_y$, further analysis based on Urbach energy was carried out. Urbach energy of IZO thin films, showed an initially increase as the $[\text{Zn}^{2+}]/([\text{Zn}^{2+}]+[\text{In}^{3+}])$ ratio was increased. The increase of the Urbach energy peaked at $[\text{Zn}^{2+}]/([\text{Zn}^{2+}]+[\text{In}^{3+}]) \sim 0.3$, (i.e., $[\text{In}^{3+}]:[\text{Zn}^{2+}] = 7:3$). From this stoichiometry and beyond the Urbach tail energy showed

a decrease with increasing the $[Zn^{2+}]/([Zn^{2+}]+[In^{3+}])$ ratio, reaching a minimum of 100 meV for ZnO. To elucidate the origin of this trend of the Urbach energy, further analysis based on FTIR spectroscopy was conducted. By FTIR spectra analysis it was found that $[Zn^{2+}]$ (at low $[Zn^{2+}]/([Zn^{2+}]+[In^{3+}])$ ratios), could act as an interstitial in a In_2O_3 host, while for higher ratios it was concluded that $[Zn^{2+}]$ substitutes $[In^{3+}]$ atoms in their lattice. The latter was confirmed by XRD analysis, as it was found that, both the lattice constant and interplanar spacing, were initially increased by increasing the $[Zn^{2+}]/([Zn^{2+}]+[In^{3+}])$ ratio leading to a lattice expansion while for higher $[Zn^{2+}]/([Zn^{2+}]+[In^{3+}])$ ratios a lattice shrinkage was observed. The change of structural characteristics as a function of $[Zn^{2+}]/([Zn^{2+}]+[In^{3+}])$ ratio affected the carrier transport characteristics of IZO based TFTs. The lattice expansion (result of $[Zn^{2+}]$ interstitial), led to a reduction of the I_{off} current, which was assumed to be originated from the suppression of intrinsic oxygen vacancies of In_2O_3 by $[Zn^{2+}]$. Further increase of the $[Zn^{2+}]$ content of In_2O_3 led to an increase in I_{off} which was assumed to originate from the substitution of $[In^{3+}]$ atoms by $[Zn^{2+}]$. Since $[Zn^{2+}]$ coordinates 4 oxygen, in contrast to $[In^{3+}]$ (which coordinates 6), a substitution of $[In^{3+}]$ by $[Zn^{2+}]$ could induce 2 oxygen vacant places in the In_2O_3 host matrix. Finally, the field-effect mobility was found to depend on both the carrier concentration and the average crystal size.

It was found that, for the optimum c-IZO, of ratio $[Zn^{2+}]/([Zn^{2+}]+[In^{3+}])=0.4$, i.e. $[In^{3+}]:[Zn^{2+}]=6:4$, the c-IZO based TFTs showed the highest performance, exhibiting low off-state currents (18 pA), high on/off current ratio (10^7), high field-effect mobility of about $5\text{ cm}^2/Vs$, and low subthreshold swing of 0.3 V/dec.

7.5 References

- [1] M. Klasen-Memmer and H. Hirschmann, *Handbook of Visual Display Technology*. Berlin, Heidelberg: Springer Berlin Heidelberg, 2012.
- [2] A. Facchetti and T. J. Marks, *Transparent Electronics*. Chichester, UK: John Wiley & Sons, Ltd, 2010.
- [3] P. Barquinha, R. Martins, L. Pereira, E. Fortunato, and L. P. and E. F. Pedro Barquinha, Rodrigo Martins, *Transparent Oxide Electronics*. Chichester, UK: John Wiley & Sons, Ltd, 2012.
- [4] A. Nathan, S. Lee, S. Jeon, and J. Robertson, 'Amorphous Oxide Semiconductor TFTs for Displays and Imaging', *J. Disp. Technol.*, vol. 10, no. 11, pp. 917–927, Nov. 2014.
- [5] K. Nomura, H. Ohta, A. Takagi, T. Kamiya, M. Hirano, and H. Hosono, 'Room-temperature fabrication of transparent flexible thin-film transistors using amorphous oxide semiconductors.', *Nature*, vol. 432, no. November, pp. 488–492, Nov. 2004.
- [6] E. Fortunato, P. Barquinha, and R. Martins, 'Oxide Semiconductor Thin-Film Transistors: A Review of Recent Advances', *Adv. Mater.*, vol. 24, no. 22, pp. 2945–2986, Jun. 2012.
- [7] J. S. Park, W.-J. Maeng, H.-S. Kim, and J.-S. Park, 'Review of recent developments in amorphous oxide semiconductor thin-film transistor devices', *Thin Solid Films*, vol. 520, no. 6, pp. 1679–1693, Jan. 2012.
- [8] Joo Hyon Noh, Seung Yoon Ryu, Sung Jin Jo, Chang Su Kim, Sung-Woo Sohn, P. D. Rack, Dong-Joo Kim, and Hong Koo Baik, 'Indium Oxide Thin-Film Transistors Fabricated by RF Sputtering at Room Temperature', *IEEE Electron Device Lett.*, vol. 31, no. 6, pp. 567–569, Jun. 2010.
- [9] H. Faber, Y.-H. Lin, S. R. Thomas, K. Zhao, N. Pliatsikas, M. a. McLachlan, A. Amassian, P. a. Patsalas, and T. D. Anthopoulos, 'Indium Oxide Thin-Film Transistors Processed at Low Temperature via Ultrasonic Spray Pyrolysis', *ACS Appl. Mater. Interfaces*, vol. 7, no. 1, pp. 782–790, Jan. 2015.
- [10] G. Adamopoulos, A. Bashir, W. P. Gillin, S. Georgakopoulos, M. Shkunov, M. A. Baklar, N. Stingelin, D. D. C. Bradley, and T. D. Anthopoulos, 'Structural and Electrical Characterization of ZnO Films Grown by Spray Pyrolysis and Their Application in Thin-Film Transistors', *Adv. Funct. Mater.*, vol. 21, no. 3, pp. 525–531, Feb. 2011.
- [11] P. Barquinha, E. Fortunato, A. Gonçalves, A. Pimentel, A. Marques, L. Pereira, and R. Martins, 'A Study on the Electrical Properties of ZnO Based Transparent TFTs', *Mater. Sci. Forum*, vol. 514–516, pp. 68–72, 2006.

- [12] J.-S. Park, J. K. Jeong, Y.-G. Mo, H. D. Kim, and C.-J. Kim, 'Control of threshold voltage in ZnO-based oxide thin film transistors', *Appl. Phys. Lett.*, vol. 93, no. 3, p. 033513, Jul. 2008.
- [13] Ü. Özgür, Y. I. Alivov, C. Liu, A. Teke, M. A. Reshchikov, S. Doğan, V. Avrutin, S.-J. J. Cho, H. Morkoç, U. Özgür, Y. I. Alivov, C. Liu, A. Teke, M. A. Reshchikov, S. Doğan, V. Avrutin, S.-J. J. Cho, H. Morkoç, Ü. Özgür, Y. I. Alivov, C. Liu, A. Teke, M. A. Reshchikov, S. Doğan, V. Avrutin, S.-J. J. Cho, and H. Morkoç, 'A comprehensive review of ZnO materials and devices', *J. Appl. Phys.*, vol. 98, no. 4, p. 041301, Aug. 2005.
- [14] P. K. Nayak, M. N. Hedhili, D. Cha, and H. N. Alshareef, 'High performance In₂O₃ thin film transistors using chemically derived aluminum oxide dielectric', *Appl. Phys. Lett.*, vol. 103, no. 3, p. 033518, Jul. 2013.
- [15] H. S. Kim, P. D. Byrne, A. Facchetti, and T. J. Marks, 'High Performance Solution-Processed Indium Oxide Thin-Film Transistors', *J. Am. Chem. Soc.*, vol. 130, no. 38, pp. 12580–12581, Sep. 2008.
- [16] A. Liu, G. X. Liu, H. H. Zhu, F. Xu, E. Fortunato, R. Martins, and F. K. Shan, 'Fully Solution-Processed Low-Voltage Aqueous In₂O₃ Thin-Film Transistors Using an Ultrathin ZrO_x Dielectric', *ACS Appl. Mater. Interfaces*, vol. 6, no. 20, pp. 17364–17369, Oct. 2014.
- [17] G. Jiang, A. Liu, G. Liu, C. Zhu, Y. Meng, B. Shin, E. Fortunato, R. Martins, and F. Shan, 'Solution-processed high-*k* magnesium oxide dielectrics for low-voltage oxide thin-film transistors', *Appl. Phys. Lett.*, vol. 109, no. 18, p. 183508, Oct. 2016.
- [18] S.-Y. Y. Han, G. S. Herman, and C. H. Chang, 'Low-Temperature, High-Performance, Solution-Processed Indium Oxide Thin-Film Transistors', *J. Am. Chem. Soc.*, vol. 133, no. 14, pp. 5166–5169, Apr. 2011.
- [19] K. Choi, M. Kim, S. Chang, T.-Y. Oh, S. W. Jeong, H. J. Ha, and B.-K. Ju, 'High-Performance Amorphous Indium Oxide Thin-Film Transistors Fabricated by an Aqueous Solution Process at Low Temperature', *Jpn. J. Appl. Phys.*, vol. 52, no. 6R, p. 060204, Jun. 2013.
- [20] B. Walker, A. K. Pradhan, and B. Xiao, 'Low temperature fabrication of high performance ZnO thin film transistors with high-*k* dielectrics', *Solid. State. Electron.*, vol. 111, pp. 58–61, Sep. 2015.
- [21] R. L. Hoffman, 'ZnO-channel thin-film transistors: Channel mobility', *J. Appl. Phys.*, vol. 95, no. 10, pp. 5813–5819, May 2004.

- [22] G. Adamopoulos, A. Bashir, S. Thomas, W. P. Gillin, S. Georgakopoulos, M. Shkunov, M. a. Baklar, N. Stingelin, R. C. Maher, L. F. Cohen, D. D. C. Bradley, and T. D. Anthopoulos, 'Spray-Deposited Li-Doped ZnO Transistors with Electron Mobility Exceeding 50 cm²/Vs', *Adv. Mater.*, vol. 22, no. 42, pp. 4764–4769, Nov. 2010.
- [23] G. Adamopoulos, A. Bashir, P. H. Wöbkenberg, D. D. C. Bradley, and T. D. Anthopoulos, 'Electronic properties of ZnO field-effect transistors fabricated by spray pyrolysis in ambient air', *Appl. Phys. Lett.*, vol. 95, no. 13, p. 133507, Sep. 2009.
- [24] H.-C. Cheng and C.-Y. Tsay, 'Flexible a-IZO thin film transistors fabricated by solution processes', *J. Alloys Compd.*, vol. 507, no. 1, pp. L1–L3, Sep. 2010.
- [25] B. G. Son, S. Y. Je, H. J. Kim, C. K. Lee, C. K. Lee, A. Y. Hwang, J. Y. Won, J. H. Song, R. Choi, and J. K. Jeong, 'High-performance In-Zn-O thin-film transistors with a soluble processed ZrO₂ gate insulator', *Phys. Status Solidi - Rapid Res. Lett.*, vol. 7, no. 7, pp. 485–488, Jul. 2013.
- [26] W.-K. Lin, K.-C. Liu, S.-T. Chang, and C.-S. Li, 'Room temperature fabricated transparent amorphous indium zinc oxide based thin film transistor using high-κ HfO₂ as gate insulator', *Thin Solid Films*, vol. 520, no. 7, pp. 3079–3083, Jan. 2012.
- [27] K. Song, C. Young Koo, T. Jun, D. Lee, Y. Jeong, and J. Moon, 'Low-temperature soluble InZnO thin film transistors by microwave annealing', *J. Cryst. Growth*, vol. 326, no. 1, pp. 23–27, Jul. 2011.
- [28] J. Lee, H. Seul, and J. K. Jeong, 'Solution-processed ternary alloy aluminum yttrium oxide dielectric for high performance indium zinc oxide thin-film transistors', *J. Alloys Compd.*, vol. 741, pp. 1021–1029, 2018.
- [29] C. G. Choi, S.-J. Seo, and B.-S. Bae, 'Solution-Processed Indium-Zinc Oxide Transparent Thin-Film Transistors', *Electrochem. Solid-State Lett.*, vol. 11, no. 1, p. H7, 2008.
- [30] C. Y. Koo, K. Song, T. Jun, D. Kim, Y. Jeong, S.-H. Kim, J. Ha, and J. Moon, 'Low Temperature Solution-Processed InZnO Thin-Film Transistors', *J. Electrochem. Soc.*, vol. 157, no. 4, p. J1111, 2010.
- [31] D. H. Lee, S. M. Park, J. Il Yang, D. K. Cho, S. H. Woo, Y. S. Lim, D. K. Kim, and M. Yi, 'Effect of Chloride Precursors on the Stability of Solution-Processed Indium Zinc Oxide Thin-Film Transistors', *Jpn. J. Appl. Phys.*, vol. 52, no. 10S, p. 10MA02, Oct. 2013.
- [32] S. Y. Park, J. H. Song, C. K. Lee, B. G. Son, C. K. Lee, H. J. Kim, R. Choi, Y. J. Choi, U. K. Kim, C. S. Hwang, H. J. Kim, and J. K. Jeong, 'Improvement in photo-bias stability of high-mobility indium zinc oxide thin-film transistors by oxygen high-pressure annealing', *IEEE Electron Device Lett.*, vol. 34, no. 7, pp. 894–896, 2013.

- [33] X. Han, J. Jiang, B. Zhou, J. Sun, W. Dou, H. Liu, and Q. Wan, 'Low-voltage indium-zinc-oxide thin film transistors gated by solution-processed chitosan-based proton conductors', in *2011 IEEE International Conference of Electron Devices and Solid-State Circuits*, 2011, pp. 1–2.
- [34] N. Itagaki, T. Iwasaki, H. Kumomi, T. Den, K. Nomura, T. Kamiya, and H. Hosono, 'Zn-In-O based thin-film transistors: Compositional dependence', *Physica Status Solidi (A) Applications and Materials Science*, 2008, vol. 205, no. 8, pp. 1915–1919.
- [35] D. C. Paine, B. Yaglioglu, Z. Beiley, and S. Lee, 'Amorphous IZO-based transparent thin film transistors', *Thin Solid Films*, vol. 516, no. 17, pp. 5894–5898, Jul. 2008.
- [36] F. Xu, A. Liu, G. Liu, B. Shin, and F. Shan, 'Solution-processed yttrium oxide dielectric for high-performance IZO thin-film transistors', *Ceram. Int.*, vol. 41, no. 41, pp. S337–S343, Jul. 2015.
- [37] B.-Y. Su, S.-Y. Chu, Y.-D. Juang, and H. Lee, 'Improved Negative Bias Stress Stability of IZO Thin Film Transistors via Post-Vacuum Annealing of Solution Method', *ECS J. Solid State Sci. Technol.*, vol. 2, no. 7, pp. Q99–Q103, May 2013.
- [38] W. H. Jeong, J. H. Bae, and H. J. Kim, 'High-performance oxide thin-film transistors using a volatile nitrate precursor for low-temperature solution process', *IEEE Electron Device Lett.*, vol. 33, no. 1, pp. 68–70, 2012.
- [39] E. Fortunato, P. Barquinha, A. Pimentel, L. Pereira, G. Gonçalves, and R. Martins, 'Amorphous IZO TFTs with saturation mobilities exceeding 100 cm²/Vs', *Phys. status solidi – Rapid Res. Lett.*, vol. 1, no. 1, pp. R34–R36, Jan. 2007.
- [40] P. Barquinha, G. Gonçalves, L. Pereira, R. Martins, and E. Fortunato, 'Effect of annealing temperature on the properties of IZO films and IZO based transparent TFTs', *Thin Solid Films*, vol. 515, no. 24, pp. 8450–8454, Oct. 2007.
- [41] E. Fortunato, P. Barquinha, G. Gonçalves, L. Pereira, and R. Martins, 'High mobility and low threshold voltage transparent thin film transistors based on amorphous indium zinc oxide semiconductors', *Solid. State. Electron.*, vol. 52, no. 3, pp. 443–448, Mar. 2008.
- [42] S. Lee, B. Bierig, and D. C. Paine, 'Amorphous structure and electrical performance of low-temperature annealed amorphous indium zinc oxide transparent thin film transistors', in *Thin Solid Films*, 2012, vol. 520, no. 10, pp. 3764–3768.
- [43] J. F. Conley, 'Instabilities in Amorphous Oxide Semiconductor Thin-Film Transistors', *IEEE Trans. Device Mater. Reliab.*, vol. 10, no. 4, pp. 460–475, Dec. 2010.

- [44] J. K. Jeong, H. Won Yang, J. H. Jeong, Y.-G. Mo, and H. D. Kim, 'Origin of threshold voltage instability in indium-gallium-zinc oxide thin film transistors', *Appl. Phys. Lett.*, vol. 93, no. 12, p. 123508, Sep. 2008.
- [45] B. Ryu, H.-K. Noh, E.-A. Choi, and K. J. Chang, 'O-vacancy as the origin of negative bias illumination stress instability in amorphous In-Ga-Zn-O thin film transistors', *Appl. Phys. Lett.*, vol. 97, no. 2, p. 022108, Jul. 2010.
- [46] Y.-H. Kim, K.-H. Kim, and S. K. Park, 'Effects of Annealing Conditions on the Dielectric Properties of Solution-Processed Al₂O₃ Layers for Indium-Zinc-Tin-Oxide Thin-Film Transistors', *J. Nanosci. Nanotechnol.*, vol. 13, no. 11, pp. 7779–7782, Nov. 2013.
- [47] P. K. Nayak, J. V. Pinto, G. Goncalves, R. Martins, and E. Fortunato, 'Environmental, Optical, and Electrical Stability Study of Solution-Processed Zinc-Tin-Oxide Thin-Film Transistors', *J. Disp. Technol.*, vol. 7, no. 12, pp. 640–643, Dec. 2011.
- [48] Y. Jeong, K. Song, T. Jun, S. Jeong, and J. Moon, 'Effect of gallium content on bias stress stability of solution-deposited Ga-Sn-Zn-O semiconductor transistors', *Thin Solid Films*, vol. 519, no. 18, pp. 6164–6168, 2011.
- [49] S. Yamazaki, 'New crystalline structure yields reliable thin-film transistors', *SPIE Newsroom*, 2012.
- [50] S. Yamazaki, J. Koyama, Y. Yamamoto, and K. Okamoto, '15.1: Research, Development, and Application of Crystalline Oxide Semiconductor', *SID Symp. Dig. Tech. Pap.*, vol. 43, no. 1, pp. 183–186, Jun. 2012.
- [51] K. Tsutsui, D. Matsubayashi, N. Ishihara, T. Takasu, S. Matsuda, and S. Yamazaki, 'Mobility enhancement in crystalline In-Ga-Zn-oxide with In-rich compositions', *Appl. Phys. Lett.*, vol. 107, no. 26, 2015.
- [52] 'Sharp Corporation website <http://www.sharp-world.com/igzo/>'.
- [53] Y. Sekine, K. Furutani, Y. Shionoiri, K. Kato, J. Koyama, and S. Yamazaki, 'Success in Measurement the Lowest Off-state Current of Transistor in the World', in *ECS Transactions*, 2011, vol. 37, no. 1, pp. 77–88.
- [54] K. Park, H. W. Park, H. S. Shin, J. Bae, K. S. Park, I. Kang, K. B. Chung, and J. Y. Kwon, 'Reliability of Crystalline Indium-Gallium-Zinc-Oxide Thin-Film Transistors under Bias Stress with Light Illumination', *IEEE Trans. Electron Devices*, vol. 62, no. 9, pp. 2900–2905, Sep. 2015.
- [55] H. Kim, D. Choi, S. Park, K. Park, H.-W. Park, K.-B. Chung, and J.-Y. Kwon, 'Impact of bias stability for crystalline InZnO thin-film transistors', *Appl. Phys. Lett.*, vol. 110, no. 23, p. 232104, Jun. 2017.

- [56] D. Perednis, O. Wilhelm, S. E. Pratsinis, and L. J. Gauckler, 'Morphology and deposition of thin yttria-stabilized zirconia films using spray pyrolysis', *Thin Solid Films*, vol. 474, no. 1–2, pp. 84–95, Mar. 2005.
- [57] G. Adamopoulos, S. Thomas, D. D. C. Bradley, M. a. McLachlan, and T. D. Anthopoulos, 'Low-voltage ZnO thin-film transistors based on Y₂O₃ and Al₂O₃ high-*k* dielectrics deposited by spray pyrolysis in air', *Appl. Phys. Lett.*, vol. 123503, no. 12, pp. 1–4, Mar. 2011.
- [58] C. Karakaya, S. Ricote, D. Albin, E. Sánchez-Cortezón, B. Linares-Zea, and R. J. Kee, 'Thermogravimetric analysis of InCl₃ sublimation at atmospheric pressure', *Thermochim. Acta*, vol. 622, pp. 55–63, Dec. 2015.
- [59] A. V. Ghule, K. Ghule, C.-Y. Chen, W.-Y. Chen, S.-H. Tzing, H. Chang, and Y.-C. Ling, 'In situ thermo-TOF-SIMS study of thermal decomposition of zinc acetate dihydrate', *J. Mass Spectrom.*, vol. 39, no. 10, pp. 1202–1208, Oct. 2004.
- [60] A. Vithal Ghule, B. Lo, S.-H. Tzing, K. Ghule, H. Chang, and Y. Chien Ling, 'Simultaneous thermogravimetric analysis and in situ thermo-Raman spectroscopic investigation of thermal decomposition of zinc acetate dihydrate forming zinc oxide nanoparticles', *Chem. Phys. Lett.*, vol. 381, no. 3–4, pp. 262–270, Nov. 2003.
- [61] J. Tauc, 'Optical properties and electronic structure of amorphous Ge and Si', *Mater. Res. Bull.*, vol. 3, no. 1, pp. 37–46, Jan. 1968.
- [62] M. Esro, S. Georgakopoulos, H. Lu, G. Vourlias, A. Krier, W. I. Milne, W. P. Gillin, and G. Adamopoulos, 'Solution processed SnO₂:Sb transparent conductive oxide as an alternative to indium tin oxide for applications in organic light emitting diodes', *J. Mater. Chem. C*, vol. 4, no. 16, pp. 3563–3570, 2016.
- [63] C. Manoharan, M. Jothibas, S. J. Jeyakumar, and S. Dhanapandian, 'Structural, optical and electrical properties of Zr-doped In₂O₃ thin films', *Spectrochim. Acta - Part A Mol. Biomol. Spectrosc.*, vol. 145, pp. 47–53, 2015.
- [64] I. J. Panneerdoss, S. J. Jeyakumar, S. Ramalingam, and M. Jothibas, 'Characterization of prepared In₂O₃ thin films: The FT-IR, FT-Raman, UV–Visible investigation and optical analysis', *Spectrochim. Acta Part A Mol. Biomol. Spectrosc.*, vol. 147, pp. 1–13, Aug. 2015.
- [65] M. Jothibas, C. Manoharan, S. Ramalingam, S. Dhanapandian, S. Johnson Jeyakumar, and M. Bououdina, 'Preparation, characterization, spectroscopic (FT-IR, FT-Raman, UV and visible) studies, optical properties and Kubo gap analysis of In₂O₃ thin films', *J. Mol. Struct.*, vol. 1049, pp. 239–249, Oct. 2013.
- [66] J. Panneerdoss I, 'Preparation, Characterization, Spectroscopic (FT-IR, FT-Raman, UV and Visible) Investigation, Optical and Physico Chemical Property Analysis on In₂O₃ Thin Films', *J. Theor. Comput. Sci.*, vol. 02, no. 02, 2015.

- [67] M. Esro, R. Mazzocco, G. Vourlias, O. Kolosov, A. Krier, W. I. Milne, and G. Adamopoulos, 'Solution processed lanthanum aluminate gate dielectrics for use in metal oxide-based thin film transistors', *Appl. Phys. Lett.*, vol. 106, no. 20, p. 203507, May 2015.
- [68] D. Afouxenidis, R. Mazzocco, G. Vourlias, P. J. Livesley, A. Krier, W. I. Milne, O. Kolosov, and G. Adamopoulos, 'ZnO-based Thin Film Transistors Employing Aluminum Titanate Gate Dielectrics Deposited by Spray Pyrolysis at Ambient Air', *ACS Appl. Mater. Interfaces*, vol. 7, no. 13, pp. 7334–7341, Apr. 2015.
- [69] D. J. Dunstan, 'Evidence for a common origin of the Urbach tails in amorphous and crystalline semiconductors', *J. Phys. C Solid State Phys.*, vol. 15, no. 13, p. 008, May 1982.
- [70] R. M. Pasquarelli, D. S. Ginley, and R. O'Hayre, 'Solution processing of transparent conductors: from flask to film', *Chem. Soc. Rev.*, vol. 40, no. 11, p. 5406, 2011.
- [71] M. Esro, G. Vourlias, C. Somerton, W. I. Milne, and G. Adamopoulos, 'High-mobility ZnO thin film transistors based on solution-processed hafnium oxide gate dielectrics', *Adv. Funct. Mater.*, vol. 25, no. 1, pp. 134–141, Jan. 2015.
- [72] S. Jongthammanurak, T. Cheawkul, and M. Witana, 'Morphological differences in transparent conductive indium-doped zinc oxide thin films deposited by ultrasonic spray pyrolysis', *Thin Solid Films*, vol. 571, no. P1, pp. 114–120, Nov. 2014.
- [73] K. Ravichandran, N. Jabena Begum, S. Snega, and B. Sakthivel, 'Properties of Sprayed Aluminum-Doped Zinc Oxide Films—A Review', *Mater. Manuf. Process.*, vol. 31, no. 11, pp. 1411–1423, Aug. 2016.
- [74] I. Hargittai, 'Christopher Hammond: The basics of crystallography and diffraction. Third edition', *Struct. Chem.*, vol. 20, no. 4, pp. 751–751, Aug. 2009.
- [75] G. D. Cody, T. Tiedje, B. Abeles, B. Brooks, and Y. Goldstein, 'Disorder and the Optical-Absorption Edge of Hydrogenated Amorphous Silicon', *Phys. Rev. Lett.*, vol. 47, no. 20, pp. 1480–1483, Nov. 1981.
- [76] 'BRUKER <https://www.bruker.com/products/surface-and-dimensional-analysis/atomic-force-microscopes/modes/modes/specialized-modes/lfm.html>'.
- [77] C.-K. Chen, H.-H. Hsieh, J.-J. Shyue, and C.-C. Wu, 'The Influence of Channel Compositions on the Electrical Properties of Solution-Processed Indium-Zinc Oxide Thin-Film Transistors', *J. Disp. Technol.*, vol. 5, no. 12, pp. 509–514, Dec. 2009.

- [78] U. Betz, M. Kharrazi Olsson, J. Marthy, M. F. Escolá, and F. Atamny, 'Thin films engineering of indium tin oxide: Large area flat panel displays application', *Surf. Coatings Technol.*, vol. 200, no. 20–21, pp. 5751–5759, May 2006.
- [79] J. Robertson and R. M. Wallace, 'High-*k* materials and metal gates for CMOS applications', *Mater. Sci. Eng. R Reports*, vol. 88, pp. 1–41, Feb. 2015.
- [80] N. Naghavi, L. Dupont, C. Marcel, C. Maugy, B. Laïk, A. Rougier, C. Guéry, and J. . Tarascon, 'Systematic study and performance optimization of transparent conducting indium–zinc oxides thin films', *Electrochim. Acta*, vol. 46, no. 13–14, pp. 2007–2013, Apr. 2001.
- [81] P. Pattanasattayavong, S. Thomas, G. Adamopoulos, M. a. McLachlan, and T. D. Anthopoulos, 'P-channel thin-film transistors based on spray-coated Cu₂O films', *Appl. Phys. Lett.*, vol. 102, no. 2013, pp. 0–4, 2013.
- [82] R. Martins, P. Barquinha, I. Ferreira, L. Pereira, G. Gonçalves, and E. Fortunato, 'Role of order and disorder on the electronic performances of oxide semiconductor thin film transistors', *J. Appl. Phys.*, vol. 101, no. 4, p. 044505, Feb. 2007.
- [83] G. Adamopoulos, S. Thomas, P. H. Wöbkenberg, D. D. C. Bradley, M. a. McLachlan, and T. D. Anthopoulos, 'High-Mobility Low-Voltage ZnO and Li-Doped ZnO Transistors Based on ZrO₂ High-*k* Dielectric Grown by Spray Pyrolysis in Ambient Air', *Adv. Mater.*, vol. 23, no. 16, pp. 1894–1898, Apr. 2011.

7.6 Appendix

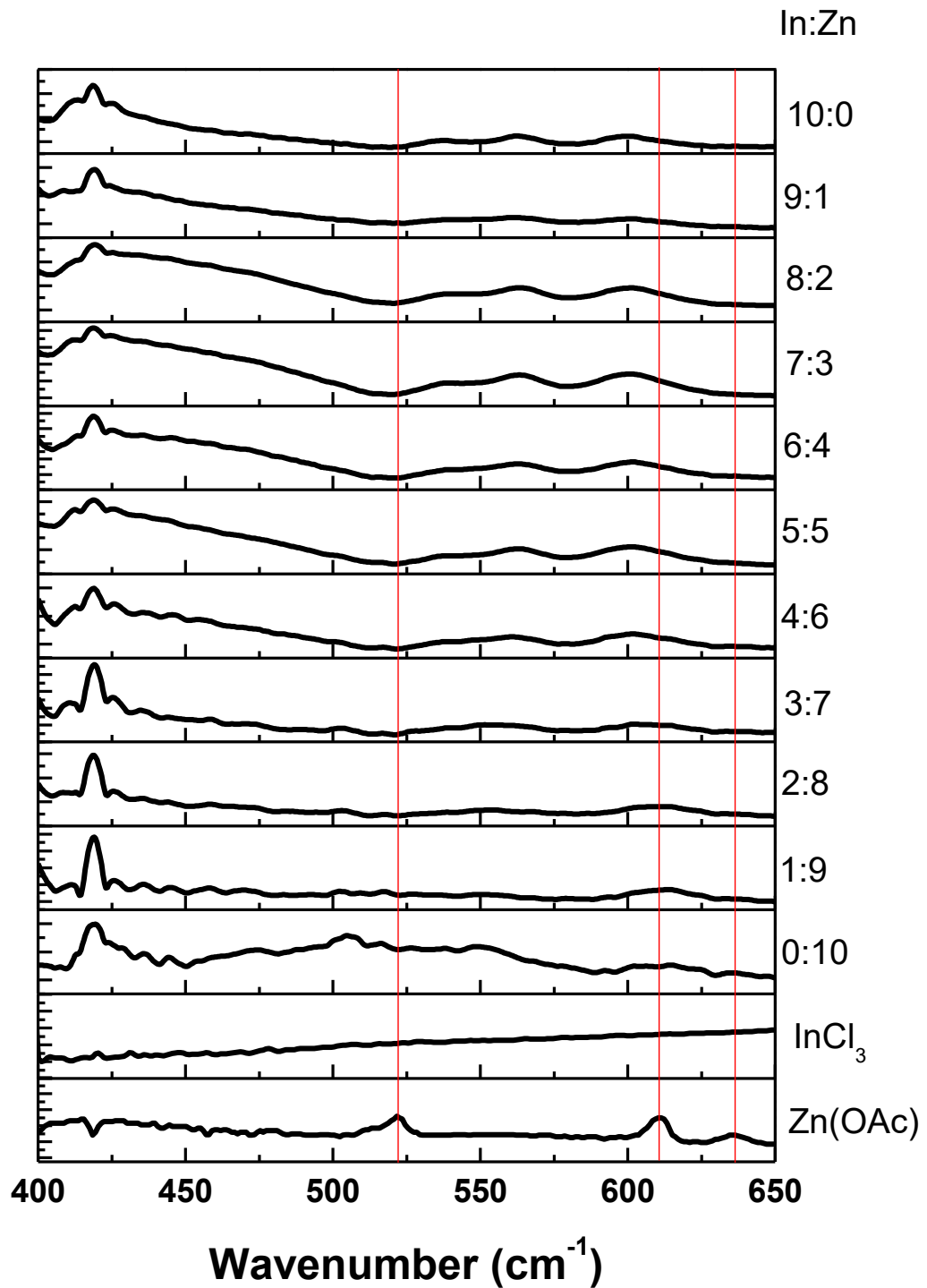


Figure 7-23: FTIR spectra of IZO thin films and the InCl₃ and Zn(O₂C₂H₃)₂·2H₂O precursors demonstrating the complete decomposition of the precursors.

8. High-Performance TFTs based on Indium Zinc Oxide (c-IZO:X) TFTs

8.1 Introduction

In the previous chapter, solution-processed c-IZO films were deposited at substrate temperatures of 400 °C. In this chapter, the investigation of selected dopants (Ga^{3+} , Y^{3+} , Zr^{4+} , Nb^{5+}), and their role in IZO films and TFTs is investigated. The TFTs' characteristics such as the off-state current (I_{off}), the current modulation ratio ($I_{\text{off}}/I_{\text{on}}$), the field effect mobility (μ) and the subthreshold voltage swing (SS) are studied as function of the physical characteristics of the metal cations.

Gallium has for long been considered as an additive to amorphous indium-zinc oxide (a-IZO) in order to suppress the carrier concentration of a-IZO [1]–[4]. The suppressing efficiency of Ga has been attributed to its higher electronegativity (1.81) in contrast to Zn (1.65) and In (1.78) [5]. Over the last decade, several other metal cations have been proposed as alternatives to Ga^{3+} in a-IZO, as effective carrier suppressors [6]. For instance, Hf and Zr have been selected due to their stronger bonding strength with oxygen [7], [8]. Hennek et al., suggested that oxide lattice formation enthalpy (ΔH_L) and metal ionic radius are the properties ruling the oxygen getter efficacy of metal cations towards their carrier suppression efficiency in a-IZO films [9]. Benwadih et al., reported that dopants possessing high electronegativity and ionic radii close to that of In and Zn exhibited low interface trap density that favours high TFT mobilities [10].

In contrast, other studies argued that metal cations of low electronegativity are needed. For instance, Kim et al., reported on Ba doped IZO TFTs [11]. They suggested that low electronegativity of Ba (0.89) favours it because it could be oxidised more readily. In another study, Kim et al., fabricated Mg-doped IZO TFTs [12]. According to their findings Mg, which possesses low standard electrode potential (-2.37 V) and high optical band gap when oxidised (7.9 eV), was found to decrease the carrier concentration of the films.

Parthiban et al., suggested that the Lewis acid strength (L), which is related to the charge number (Z) of the atomic core and ionic radius (r) along with the electronegativity (χ_z) of the doping elements, and the bonding strength of M-O (M: metal dopant) are important key parameters towards high performance TFTs [6].

However, so far there is not a clear methodology for selection of an appropriate metal cation as an effective dopant towards high performance TFTs. In this study the metal dopant selection was based on a) the ionic radius of the metal and b) the oxidation number along with the electronegativity. Therefore, Ga, a well-established metal dopant in IZO films, was studied. Ga is of an oxidation number of +3 and an ionic radius of 76 pm. In the next stage, Y was selected because it possesses the same oxidation number with Ga, i.e. +3, but a significantly bigger ionic radius (104 pm). Next, Zr was studied due to its higher oxidation number of +4, but a smaller ionic radius of 86 pm in contrast to Y one but similar to that of Ga. Lastly, Nb with an oxidation number of +5 with an ionic radius of 78 pm. Additionally, the electronegativity of the selected dopants was increased in the series of Y^{3+} (1.22), Zr^{4+} (1.33), Nb^{5+} (1.6), Ga^{3+} (1.81).

8.2 Experimental

8.2.1 Precursor Solution Chemistry

The precursor materials that have been used in this study were aluminum 2,4-pentanedionate ($Al(C_5H_7O_2)_3$, Alfa Aesar, 99%), indium (III) chloride ($InCl_3$, Alfa Aesar, 98+%), zinc acetate dihydrate ($Zn(O_2C_2H_3)_2 \cdot 2H_2O$, Alfa Aesar, ACS, 98-101%), gallium (III) chloride ($GaCl_3$, Alfa Aesar, ultra-dry, 99.999%), zirconium (IV) acetylacetonate ($Zr(C_5H_7O_2)_4$, Sigma-Aldrich, 97%), yttrium (III) 2,4-pentanedionate hydrate ($Y(C_5H_7O_2)_3 \cdot 2H_2O$, Alfa Aesar, 99.9%) and niobium (IV) chloride ($NbCl_5$, Alfa Aesar, 99.9%). All the precursors were used as received without any further purification. In this study methanol (CH_3OH , VWR, ACS, $\geq 99.8\%$) was used as the solvent of choice due to the high solubility of the precursors in it. However, methanol has low boiling point (64.6 °C) and evaporates rapidly. To slow down solvent evaporation, and thereby hinder particle formation, methanol was mixed with 2,4-pentanedione ($C_5H_8O_2$, Alfa Aesar, 99%) which possesses a high boiling point (~ 140 °C) [13].

Solutions of 0.1 M IZO:X (X=Ga, Y, Zr, Nb), for each metal composition, were produced by dissolving the precursors into a mixture of methanol and acetylacetonate

at CH₃OH: C₅H₈O₂ molar ratio of 10:1. The atomic ratio of the X varied from 0 to 20 atomic percent (at.%) of In. The atomic ratio of [In³⁺]:[Zn²⁺] was kept constant at 3:2, as that was found to be the optimum [In³⁺]:[Zn²⁺] atomic ratio, in terms of the performance of c-IZO based TFTs, from the previous chapter. The doping level of [X]:[In]:[Zn] was achieved by simple blending of the appropriate amount of precursor solutions.

8.2.2 Device Fabrication

For this study, bottom gate-top contact (BG-TC) transistors were fabricated in the same way as illustrated in Figure 7-3.

8.2.3 Thin Film & Device Characterisation Techniques

The thermal properties of the precursor materials were investigated by thermal gravimetric analysis (TGA) and differential scanning calorimetry (DSC). The microstructure of the spray deposited thin films was characterised by X-ray diffraction. The optical properties of the films were investigated by Fourier transform infrared (FTIR) and UV-Vis absorption spectroscopy. Finally, the performance of IZO as semiconductor was investigated utilising a bottom-gate, top-contact (BG-TC) TFT architecture. The electron mobility was extracted from the transfer characteristics (I_{DS} - V_{GS}) in saturation regime using the gradual channel approximation [14].

8.3 Results

8.3.1 Thermal Analysis of Precursor Compounds

The thermogravimetric (TG) and differential scanning calorimetric (DSC) data of InCl₃ and Zn(CH₃COO)₂.2H₂O and their interpretation have been presented in the previous chapter. In this chapter, the TG and DSC data of Y(C₅H₇O₂)₃.xH₂O, Zr(C₅H₇O₂)₄ and GaCl₃ are investigated. In Figure 8-1, the TG and DSC data of the Y(C₅H₇O₂)₃.xH₂O, are presented. The initial mass loss, taking place in the temperature

range between 80 and 130 °C, is due to the dehydration of the precursor. The dehydration process is a highly endothermic process as can be seen from the DSC data. On the next endothermic process at around 240 °C, the observed mass loss has been attributed, by Alarcón-Flores et al. [15], to the loss of one of the β -ketone molecules ($C_5H_7O_2$), leaving an $Y(C_5H_7O_2)_2$ complex. Finally, in the temperature range between 380 and 550 °C two endothermic processes are taking place while further mass loss is observed. This mass loss probably results from the partially thermal decomposition of the remaining $Y(C_5H_7O_2)_2$ complex [15]. It has been reported that the $Y(C_5H_7O_2)_2$ complex tends to slowly be degraded to form yttrium oxide (Y_2O_3) and organic residues at temperature of about 600 °C [15].

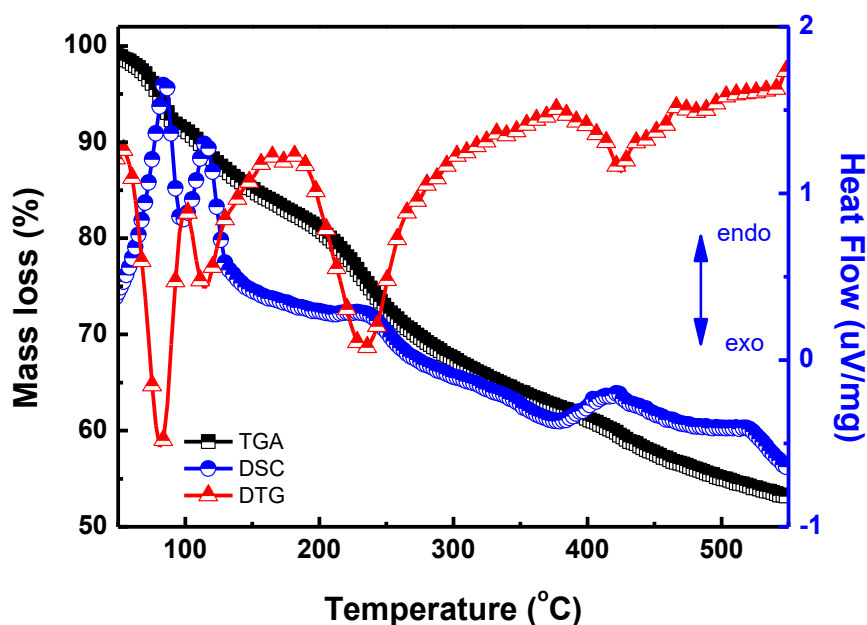


Figure 8-1: TGA (black line) and weight loss rate (red line) and DSC (right Y axis) data of 20 mg yttrium (III) acetylacetonate hydrate powder. TGA and DSC measurements conducted under nitrogen flow at a heating rate of 10 K/min.

The TG and DSC data of zirconium (IV) acetylacetonate ($Zr(C_5H_7O_2)_4$) in N_2 , are depicted in Figure 8-2. Primarily, it consists of an endothermic decomposition at 195 °C prior to a drastic decomposition where about 40 % of the total mass loss occurs. This process ends up at about 250 °C, where the end of the endothermic peak is observed. Similar results were reported by Petit et al., [16]. Ismail, reported that in the temperature, between 150 and 200 °C, there is a release of two moles of C_3H_4

indicating that the decomposition of $\text{Zr}(\text{C}_5\text{H}_7\text{O}_2)_4$ starts by the formation of a complex of acetate and acetoacetate of zirconium, $\text{Zr}(\text{C}_5\text{H}_7\text{O}_2)_2(\text{CH}_3\text{COO})_2$ [17]. The decomposition process is followed by two progressive steps in the temperature range of 300-500 °C. The exothermic process in the temperature region between 325 and 400 °C has been attributed to the decomposition of $\text{Zr}(\text{C}_5\text{H}_7\text{O}_2)_2(\text{CH}_3\text{COO})_2$ to $\text{ZrO}(\text{CH}_3\text{COO})_2$, while the endothermic process in the temperature region between 400 and 500 °C has been attributed to the decomposition of $\text{ZrO}(\text{CH}_3\text{COO})_2$ to ZrOCO_3 [17]. Petit et al., associated the last exothermic peak at about 535 °C, with the onset of crystallization of ZrOCO_3 [16].

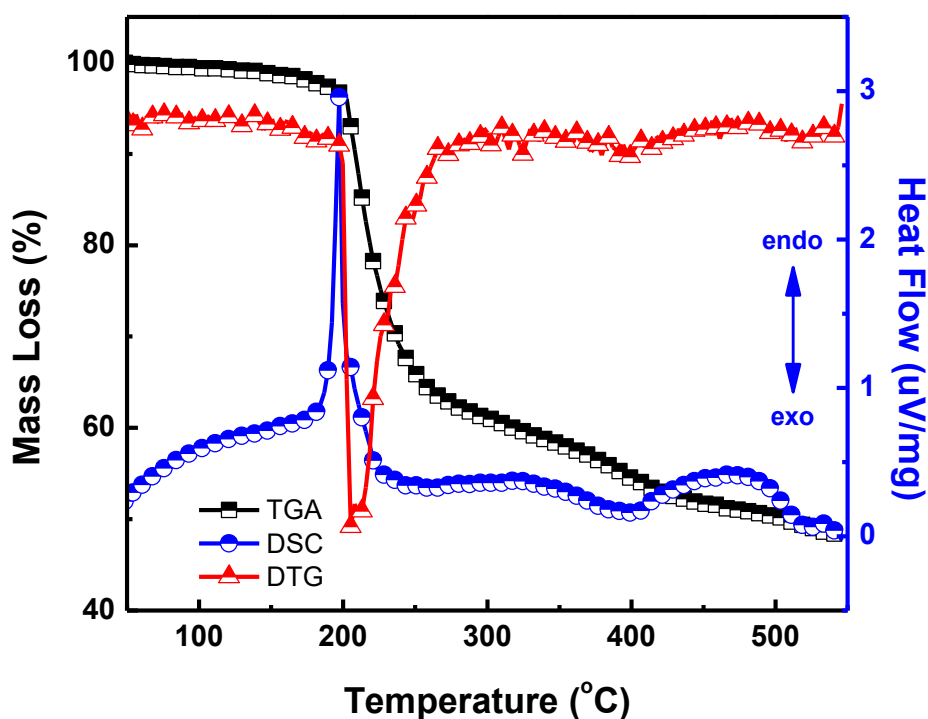


Figure 8-2: TGA (black line) and weight loss rate (red line) and DSC (right Y axis) data of 15 mg zirconium (IV) acetylacetonate powder. TGA and DSC measurements conducted under nitrogen flow at a heating rate of 10 K/min.

In Figure 8-3, the the TG and DSC data of GaCl_3 are presented. Considering the hygroscopic nature of GaCl_3 it could be assumed that because of the reaction of GaCl_3 with the atmospheric moisture, prior the measurement, part of GaCl_3 turned into $\text{Ga}(\text{OH})_3$ according to the reaction $\text{GaCl}_3 + 3 \cdot \text{H}_2\text{O} \rightarrow \text{Ga}(\text{OH})_3 + 3 \cdot \text{HCl}$. As can be seen there is a constant decrease in mass in the temperature range between 50 and 150 °C.

Considering the high hygroscopic nature of GaCl_3 , it could be assumed that this initial mass loss is attributed to released of the absorbed water. The small endothermic peak around 80 °C is attributed to the melting point of GaCl_3 (MP=78 °C), while the endothermic peak at around 180 °C accompanied with a significant mass loss, could be due to the boiling point of GaCl_3 (BP=201 °C).

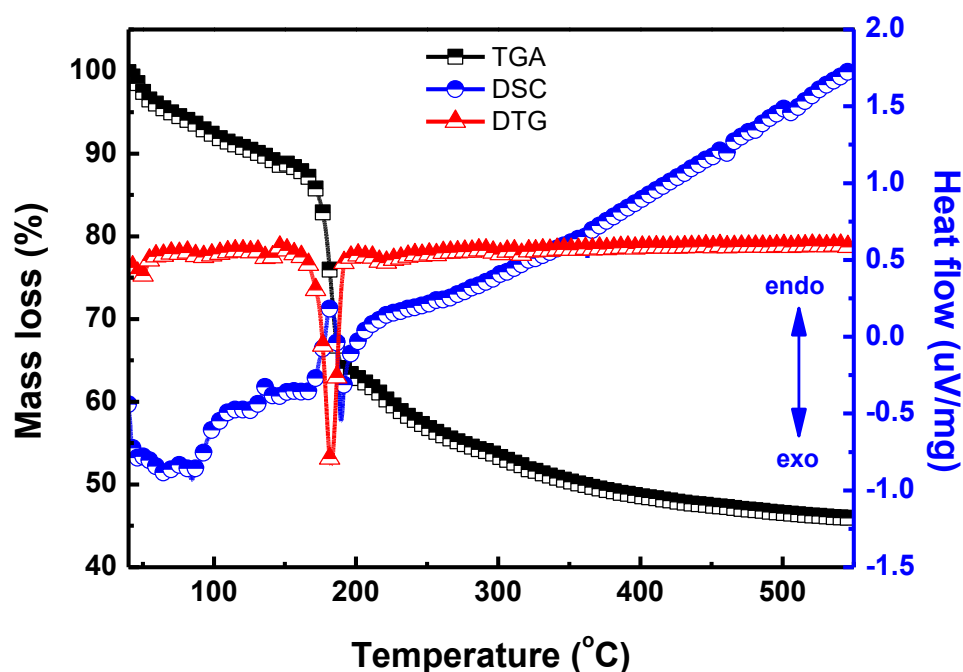


Figure 8-3: TGA (black line) and weight loss rate (red line) and DSC (right Y axis) data of 15 mg gallium (III) chloride powder. TGA and DSC measurements conducted under nitrogen flow at a heating rate of 10 K/min.

8.3.2 Optical & structural properties of c-IZO:X thin films

The optical properties of the c-IZO:X (X: Ga, Y, Zr, Nb) films as a function of the doping ratios were investigated by UV-Vis-NIR absorption spectroscopy while information about bonding configuration were investigated by FTIR. Films were deposited at a temperature of 400 °C and film thickness was estimated to be approximately 15 nm by single wavelength ellipsometry.

8.3.2.1 Ga-doped c-IZO

In Figure 8-4.a, the optical transmittance of spray deposited IZO:Ga films for different Ga concentrations (5, 10, 20 at. %) are presented. The Tauc plots [18] that show the onset of optical transitions near the band edge are illustrated in Figure 8-4.b. The optical band gap as well as the Urbach tail energy of films with different Ga doping concentrations are illustrated in Figure 8-5.

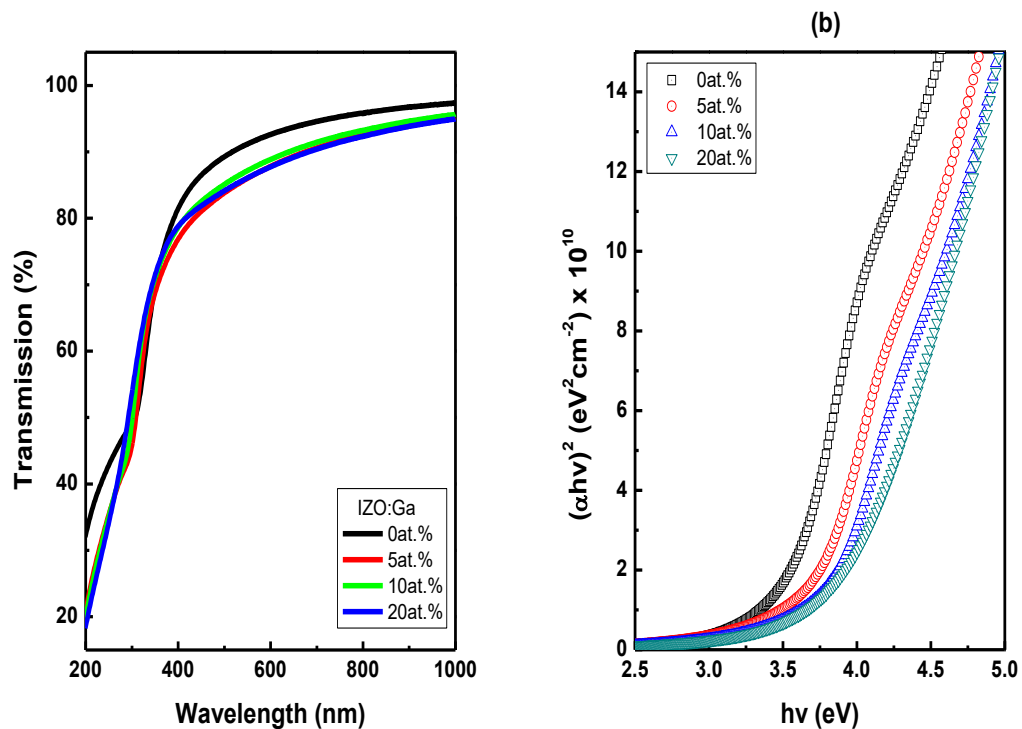


Figure 8-4: a) Transmittance spectra and b) Tauc plots of the IZO:Ga thin films for different Ga doping concentration.

As can be seen from Figure 8-5, the optical band gap of the IZO:Ga films is becoming wider as the Ga fraction in the films is increasing. The increase in band gap could be attributed to Burstein-Moss effect [19], [20]. According to the Burstein–Moss effect, the blue-shift of the onset of optical transitions of the films near the band edge is due to an increase in carrier concentration. Therefore, Ga doping in c-IZO films could be assumed to increase carrier concentration in the c-IZO films.

Considering the increase in Urbach energy (Figure 8-5) with the increase in Ga doping concentration, it is postulated that the increase in carrier concentration with

the increase of the Ga doping concentration is due to the fact that Ga forms a shallow donor level close to the conduction band of IZO. Moreover, the increase in Urbach energy has been related to the increase in density of defect states. The origin of defect states could be attributed to Ga interstitials in the IZO host matrix and or Ga_{Zn} antisite defects. Also, an increase in carrier concentration due to an increase in structural distortion induced by the increase in Ga content in IZO could be assumed. Oxygen vacancies and antisite defects have for long been considered as the origin of free carriers in metal oxide based semiconductors [21], [22].

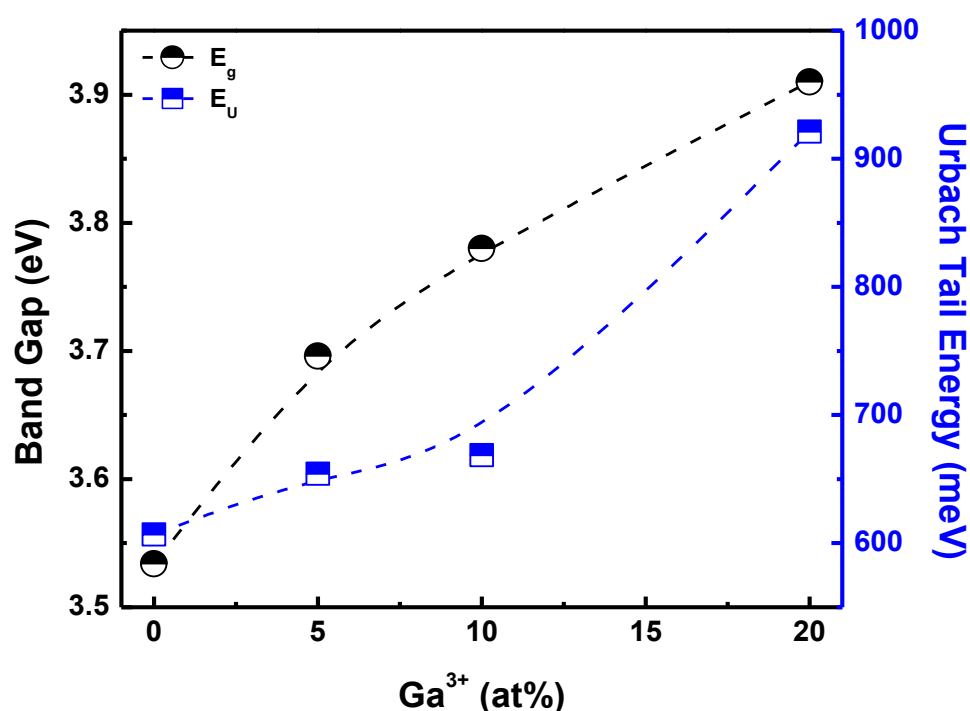


Figure 8-5: Optical band gap and Urbach tail energy of IZO:Ga films as a function of Ga doping levels. Lines are guides to the eye.

To further investigate the role of Ga doping concentration on the structural properties of IZO:Ga films and their impact on the electrical properties, FTIR measurements were conducted. In Figure 8-6 the FTIR absorption spectra of Ga-doped IZO on KBr substrates for thin films of varying Ga doping ratios are presented. Evidently, increasing the Ga doping level results in a shift towards higher wavenumbers as well as a widening of the main peaks associated with c-IZO. It has been shown that when amorphous oxides crystallise, the absorption peaks shift to

lower frequencies and their width becomes narrower [23]. Considering the results from FTIR it could be further supported that Ga inclusion in the c-IZO crystal structure induced structural disorder, while considering the lack of peaks at the very high doping level (20% at.), it could be assumed that the c-IZO:Ga crystal becomes amorphous. This is in full agreement with the XRD patterns presented in Figure 8-7. Evidently, increasing the Ga content in the film, there is a shift of the main peaks previously assigned to cubic In_2O_3 , while it could further explain the monotonic increase in Urbach energy with increase in Ga doping level. Therefore, considering that Urbach energy is associated with the width of the localised states in the band gap, it could be assumed that by increasing the Ga content in the c-IZO films there was an increase in the density of localised states in the c-IZO band gap which could be further attributed to the phase transformation from crystalline IZO to amorphous.

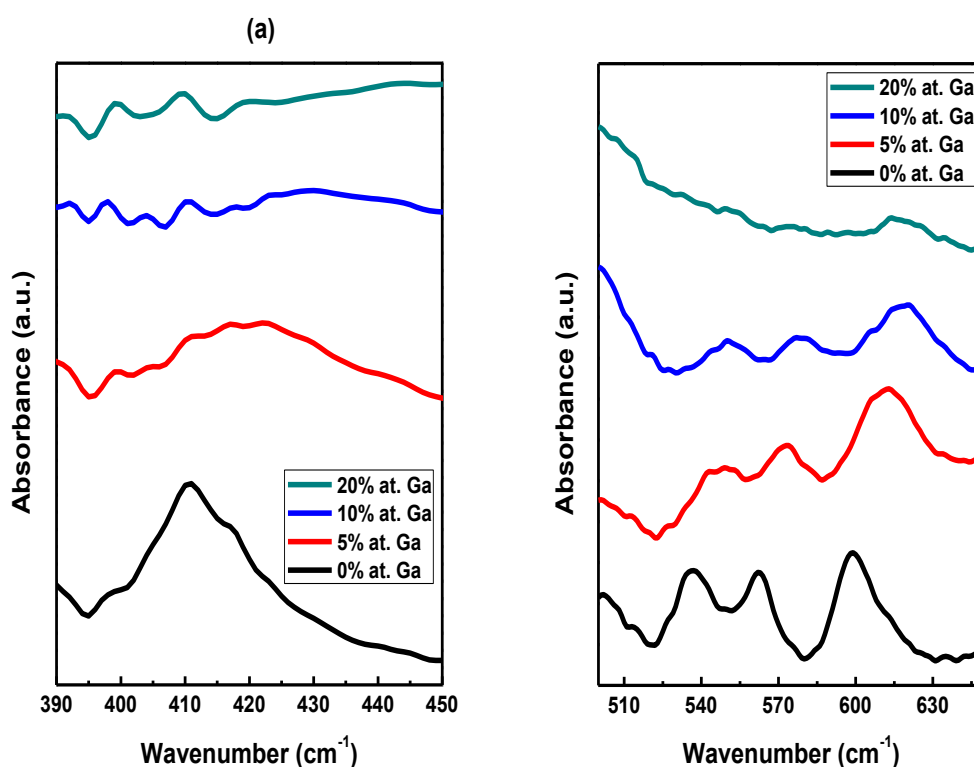


Figure 8-6: FTIR absorption spectra of Ga -doped IZO, at two different spectra regions, on KBr substrates for thin films of varying Ga doping ratios.

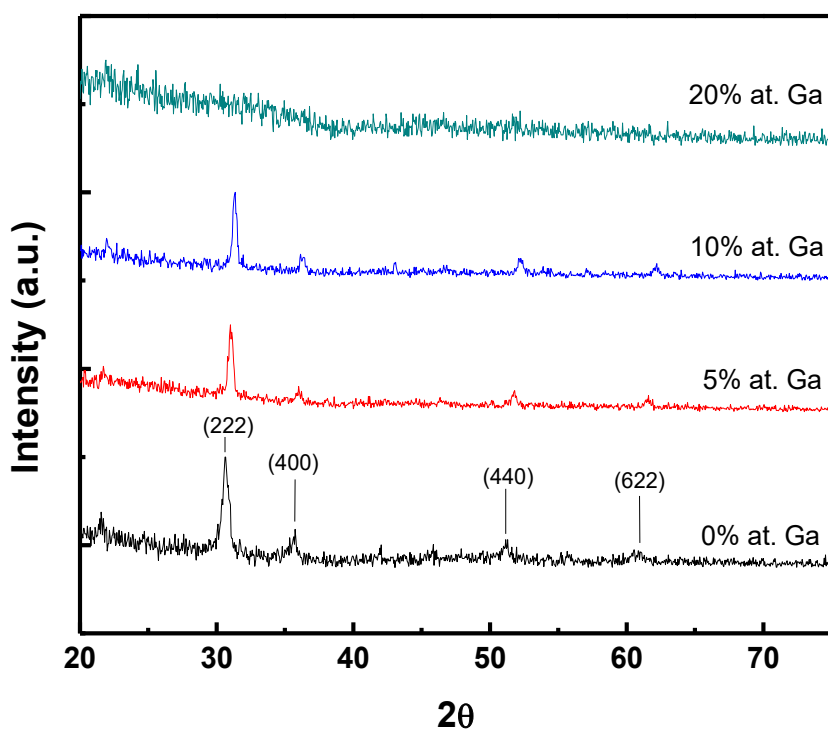


Figure 8-7: GIXRD diffraction patterns of Ga-doped c-IZO films for varying Ga doping ratios.

8.3.2.2 Y-doped c-IZO

In Figure 8-8.a, the optical transmittance of spray deposited IZO:Y films for different Y concentrations (5, 10, 20 at. %) are presented. The Tauc plots [18] are illustrated in Figure 8-8b. The optical band gap energy and Urbach tail energy of IZO:Y thin films as a function of the Y doping concentration as extracted from the Tauc plots, are depicted in Figure 8-9.

As can be seen from Figure 8-9, increase in Y doping level slightly affected the optical band gap of IZO while it decreases the Urbach energy. At first glance, considering the decrease in Urbach energy it could be assumed that Y doping resulted a less disordered crystal structure by either enhancing the crystallisation of c-IZO possibly due to an increase of the crystal size or bridging the non-bridged oxygens in the c-IZO structure. In both cases, the increase of the Y content in c-IZO films reduced the density of localised states in the band gap, as is denoted by the decrease in Urbach energy.

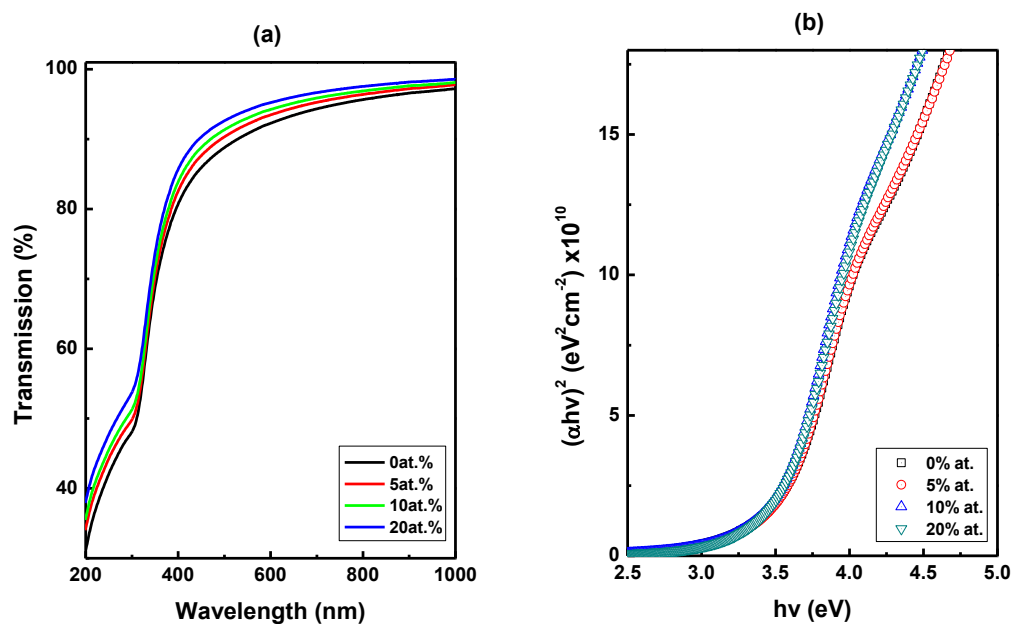


Figure 8-8: a) Transmittance spectra and b) Tauc plots of the IZO:Y thin films for different Y doping concentration

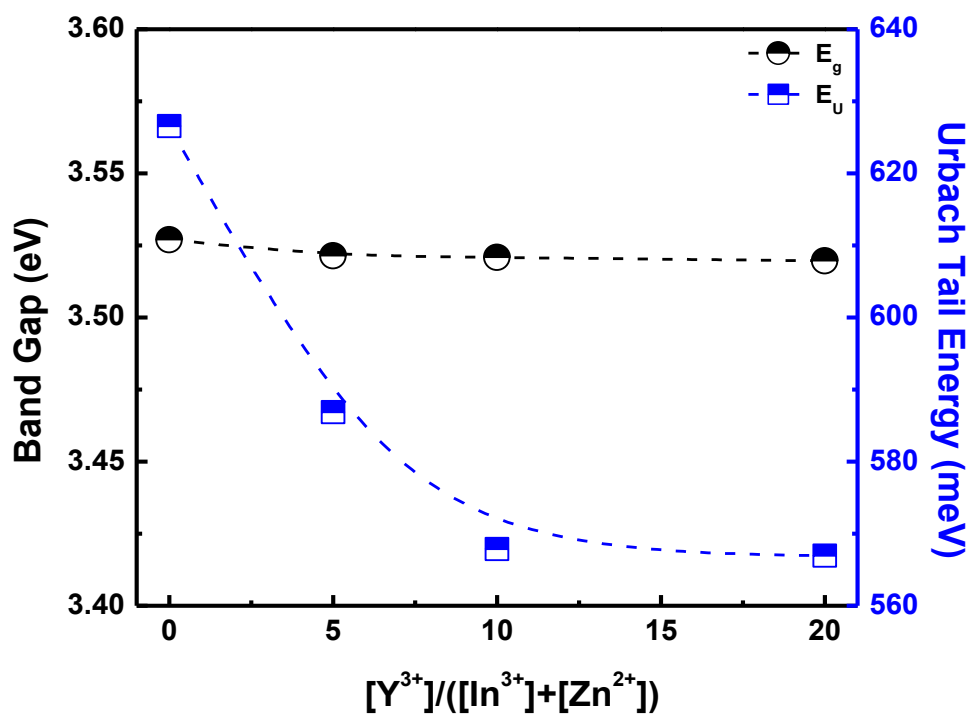


Figure 8-9: Optical band gap and Urbach tail energy of IZO:Y thin films as a function of Y fraction. Lines are guides to the eye.

To investigate the origin of the decrease in Urbach energy, the structural properties were investigated by GIXRD (Figure 8-10). Considering the GIXRD patterns, all films exhibit strong diffraction peaks centred at 30.7° and less intense peaks at 21.5° , 35.6° , 51° and 60.9° . These peaks are the (211), (222), (400), (440) and (622) reflections, signature of cubic In_2O_3 (JCPDS-PDF 06-0416).

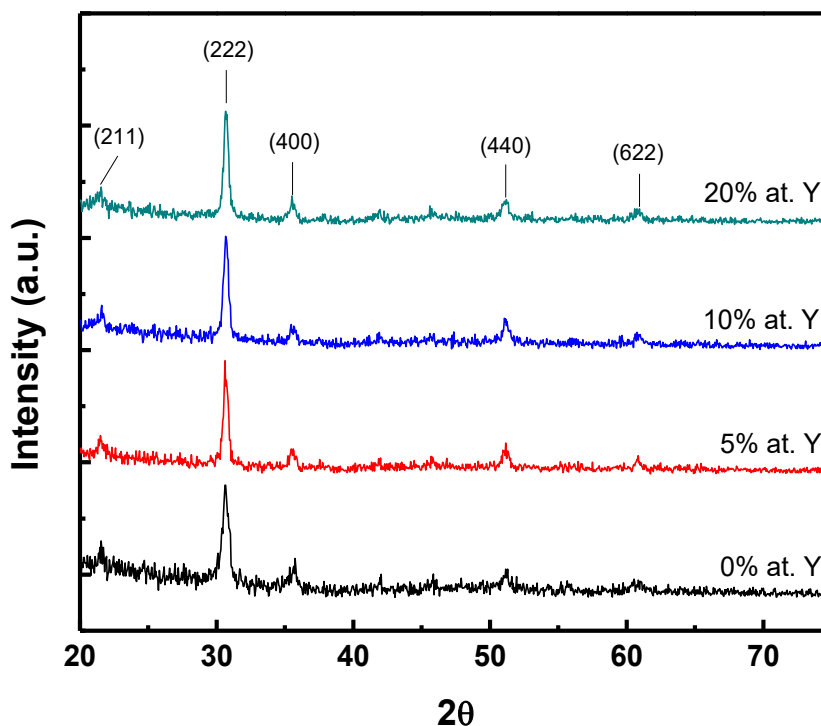


Figure 8-10: GIXRD diffraction patterns of Y-doped c-IZO films for varying Y doping ratios.

The crystal size of Y-doped IZO thin films was obtained by using Debye-Scherrer formula, while the lattice strain of all the thin films were calculated using the tangent formula, $\varepsilon = \beta/4\tan\theta$, where β the full width at half maximum of the diffraction peak and θ the diffraction angle [24]. In Figure 8-11 the average crystal size (a) and the calculated lattice strain (b) calculated from the (222) plane of reflection are depicted.

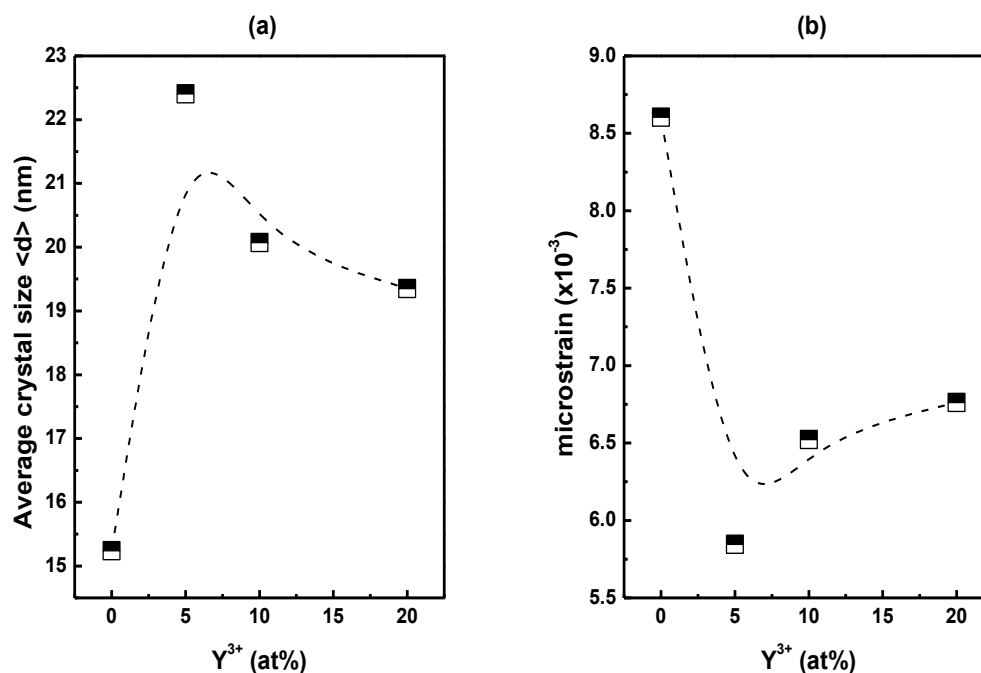


Figure 8-11: (a) average crystal size and (b) lattice strain calculated from (222) plane of IZO:Y thin films as a function of Y fraction. The lines are guides to the eye.

As can be seen from Figure 8-11, increase in Y concentration induced a strain relief in c-IZO crystal structure. This strain relief could be attributed to the increase in crystallinity as the increase in average crystal size denotes. Moreover, the decrease in lattice strain could be attributed to the decrease in lattice defects which is reflected in the decrease of Urbach energy with the increase of Y content in c-IZO films. Furthermore, considering that Y possesses lower electronegativity (1.22) and standard electrode potential (-2.372 V), it has been shown that it can act as carrier suppressor in IZO system [25]. Here, it is postulated that the increase in Y doping concentration suppressed the concentration of oxygen vacancies in c-IZO crystal structure, therefore a less distorted c-IZO structure was emerged, in accordance to the observed decrease both in Urbach energy and lattice strain.

8.3.2.3 Zr-doped c-IZO

Figure 8-12 presents the optical transmittance spectra of spray deposited IZO:Zr films and the Tauc plots for different Zr doping concentrations (5, 10, 20 at. %). The optical band gap as well as the Urbach tail energy of films with different Zr doping concentrations are illustrated in Figure 8-13.

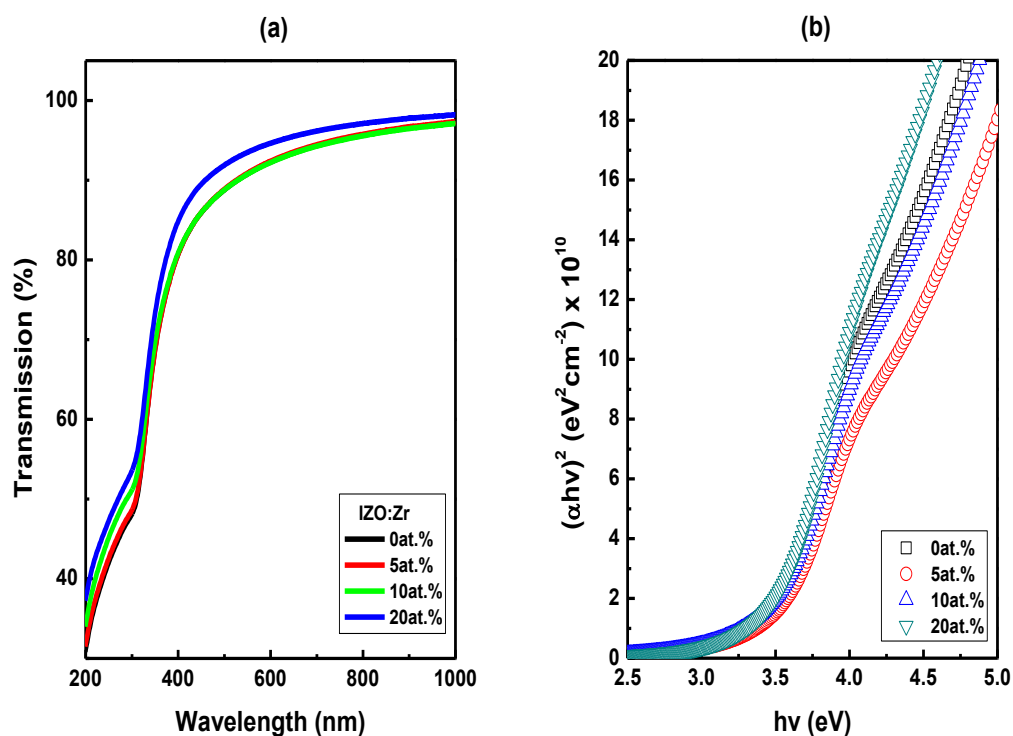


Figure 8-12: a) Transmittance spectra and b) Tauc plots of the IZO:Zr thin films for different Zr doping concentration

Evidently, the increase of the Zr content in the c-IZO the optical band gap of the spray deposited IZO:Zr thin films, initially showed a monotonic decrease for a concentration up to 10at.%. Such decrease can be attributed to the formation of defect sites like oxygen vacancies or metal interstitials. The initial increase of the Urbach tail energy for a concentration up to 10at.% could further support the hypothesis about the formation of defect sites. As it has been already mentioned, the Urbach tail energy constitutes a qualitative measure of disorder in solids [26]. Therefore, it is postulated that Zr(10 at.%) -doped IZO thin films are more disordered.

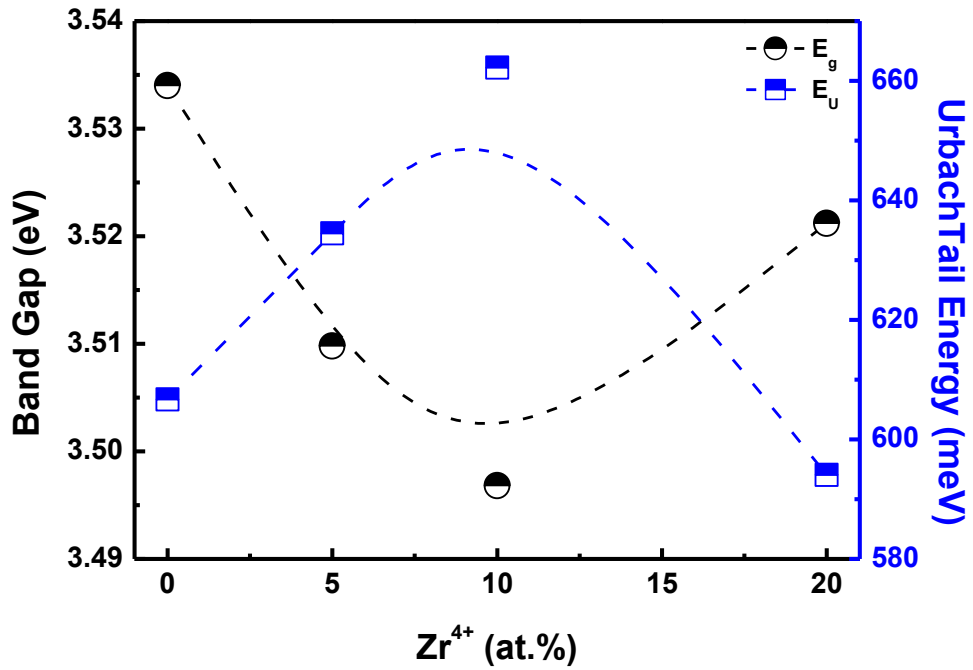


Figure 8-13: Optical band gap and Urbach tail energy of IZO:Zr thin films as a function of Zr content. The lines are guides to the eye.

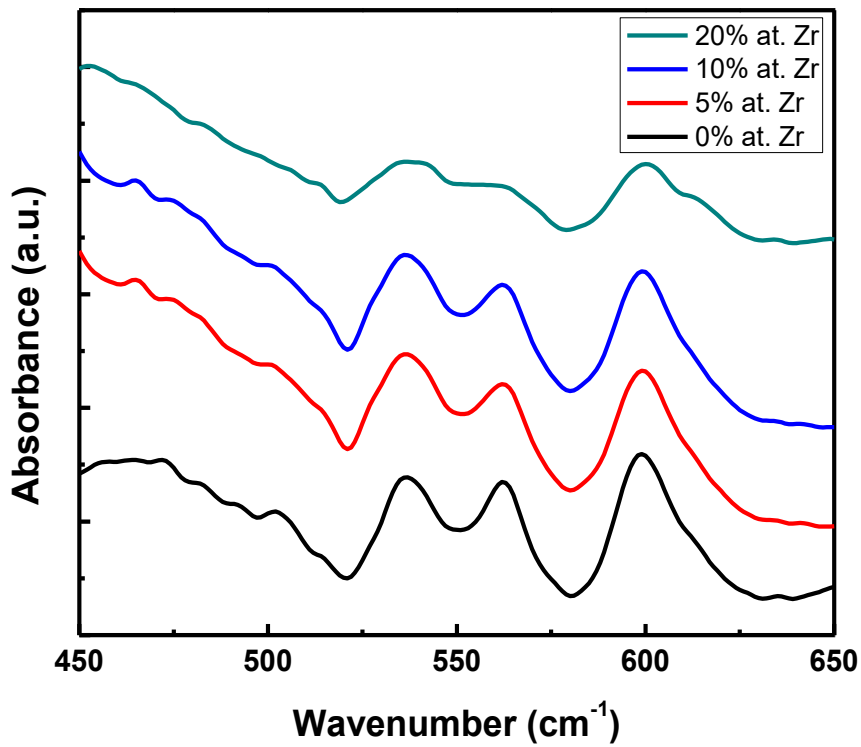


Figure 8-14: FTIR absorption spectra of Zr-doped IZO on KBr substrates for thin films of varying Zr doping ratios.

To investigate the origin of the increase of the structural distortion, FTIR measurements were conducted. In Figure 8-14 the FTIR spectra of Zr-doped IZO films are shown. Considering the FTIR spectra we can assume that an increase in Zr content in the IZO film, did not affect significantly the position of the three main peaks at 536 cm^{-1} , 562 cm^{-1} and 599 cm^{-1} . However, for high Zr doping level (20 at.%) a broadening of the peaks can be observed. This could be related to an increase of the structural distortion of the Zr-doped IZO films for high Zr concentration. Interestingly, the latter was not reflected in the Urbach energy, where for higher Zr doping level, a decrease in Urbach energy was observed. Here, it is postulated that, for Zr doping concentration up to 10 at%, the contribution of structural disorder due to complex defects that Zr addition in IZO films induced dominated the Urbach energy.

8.3.2.4 *Nb-doped c-IZO*

The transmission spectra and the Tauc plots of the Nb-doped IZO deposited on fused silica substrates are presented in Figure 8-15. In Figure 8-16 the band gap and Urbach tail energy for the Nb-doped IZO films are shown. One can be seen, for a Nb content of up to 5 at.% the optical band gap slightly decreases whereas the Urbach tail energy slightly increases. The initial decrease of the band gap along with the increase of the Urbach tail energy could be attributed to an initial formation of defect states as a result of the Nb doping level. Further increase of the Nb content results in an equally negligible increase of the band gap, while the Urbach energy was decreased. To investigate the origin of the decrease of the Urbach energy, FTIR measurements were conducted. In Figure 8-17 the FTIR spectra of Nb-doped IZO films in the spectra region of 500-650 cm^{-1} are presented.

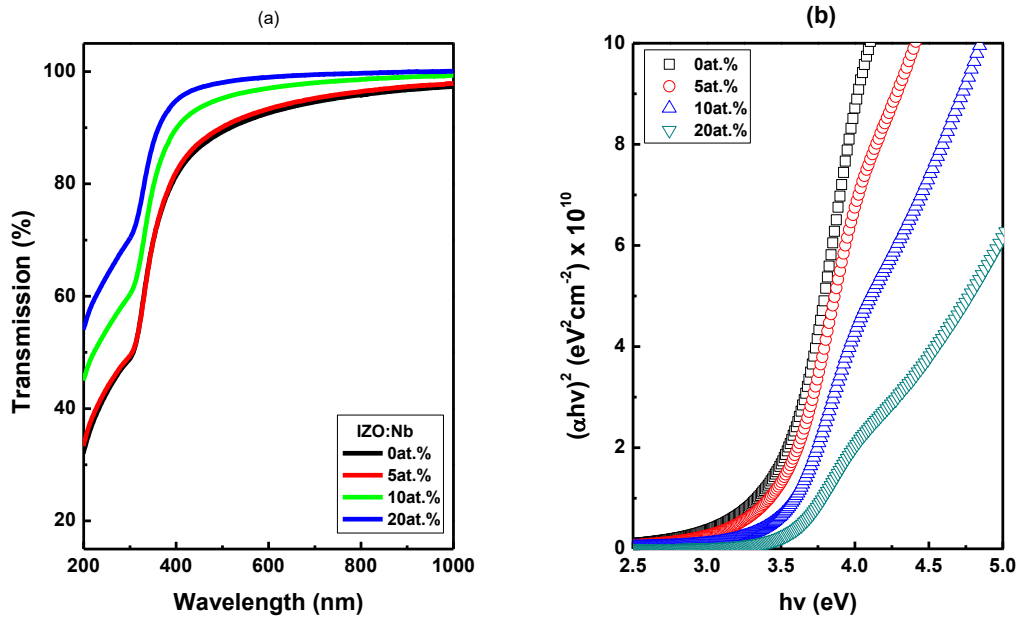


Figure 8-15: a) Transmittance spectra and b) Tauc plots of the IZO:Nb thin films for different Nb doping concentration

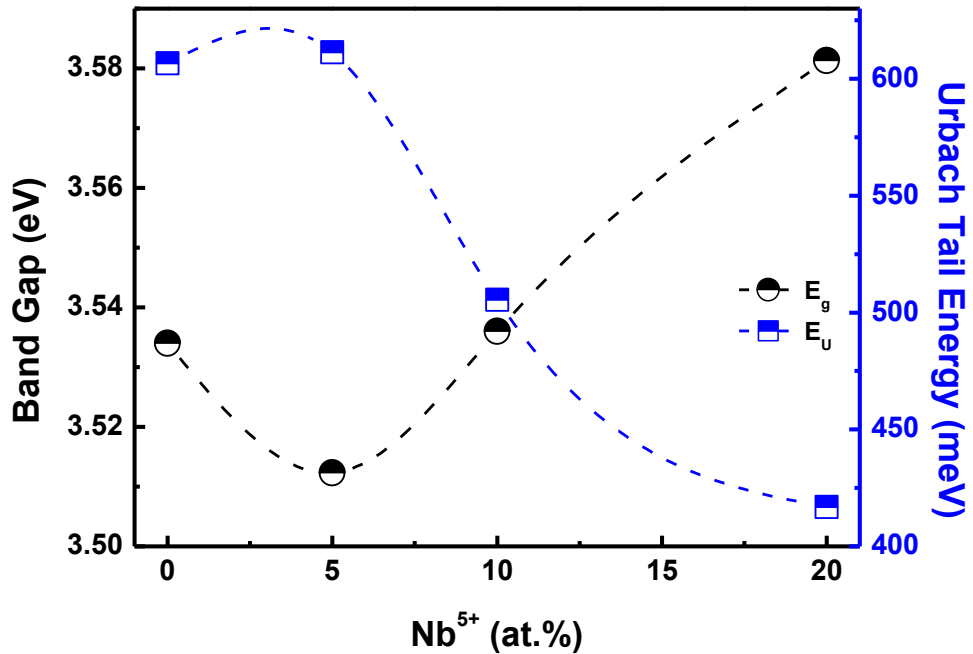


Figure 8-16: Optical band gap and Urbach tail energy of IZO:Nb thin films as function of Nb⁵⁺ content. The lines are guides to the eye.

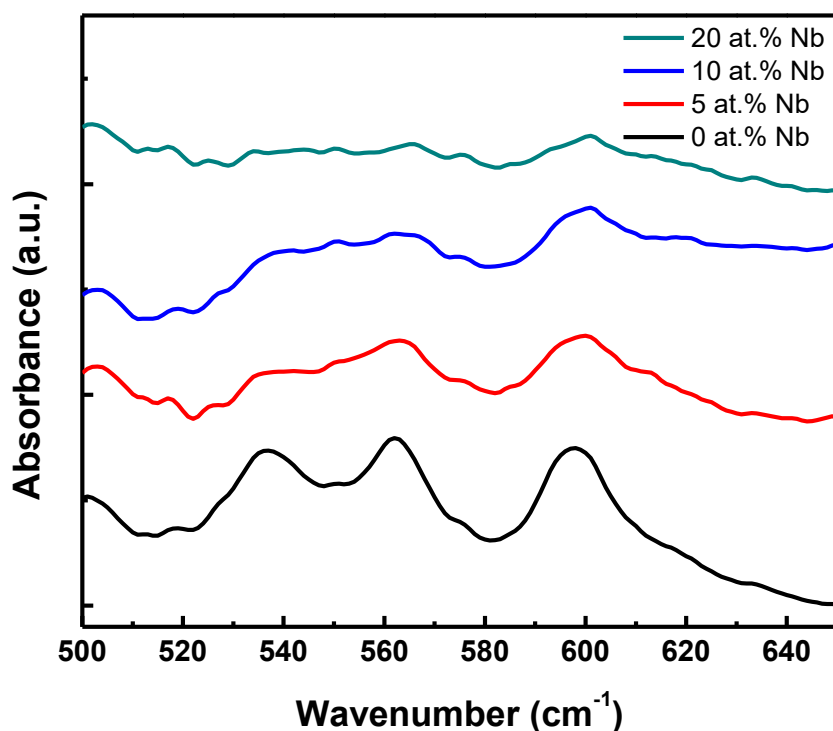


Figure 8-17: FTIR absorption spectra of Nb-doped IZO on KBr substrates for thin films of varying Nb doping ratios.

Evidently, there is a broadening of the FTIR peaks previously associated to In-O stretching bonds in the crystal. This could be related to a change from an order to a less ordered crystal structure. Considering the Urbach energy, this is quite interesting. The Urbach energy is related to the width of localised states in the band gap as result of structural distortion [27]. In crystalline materials the disorder can be both static and dynamic. Static structural disorder can be due to the presence of complex defects, while dynamic disorder arises due to electron-phonon coupling [27]. Considering the results from FTIR a structural distortion due to increase in Nb content is postulated. This is reflected in the initial increase of the Urbach energy for a Nb doping concentration up to 5 at.%. Further increase in Nb content resulted in a significant decrease in dynamic disorder. The decrease of dynamic disorder is postulated that prevailed over the increase in static disorder, resulted to a total decrease in Urbach energy.

8.3.3 Field effect measurements

The charge carrier transport properties of X-IZO films, were investigated by the implementation of X-IZO films as semiconducting channels in bottom-gate top-contact TFTs.

Figure 8-18 depicts the transfer characteristics for c-IZO, X=Ga, Y, Zr, Nb, TFTs at $V_{DS}=20$ V with X to In ratio of 0 to 20 at.%. The extracted device parameters are summarised in Table 8-1 and are presented in, Figure 8-19, Figure 8-20 and Figure 8-21.

Table 8-1: Summary of c-IZO:X TFT parameters.

	X (at.%)	V_{TH} (V)	I_{off} (A)	I_{on} (A)	I_{on}/I_{off}	μ (cm^2/Vs)	SS (V/dec)
c-IZO	0	6.80	1.8×10^{-10}	6.1×10^{-4}	3.4×10^6	4.47	0.67
Ga	5	-7.90	4.4×10^{-5}	7.4×10^{-3}	1.7×10^2	18.48	7.60
	10	-7.50	9.7×10^{-6}	2.8×10^{-3}	2.9×10^2	14.31	5.77
	20	-0.95	1.1×10^{-6}	1.0×10^{-3}	9.3×10^2	5.90	3.16
Y	5	5.29	1.0×10^{-9}	2.2×10^{-3}	2.2×10^6	18.49	0.62
	10	3.77	6.7×10^{-11}	2.3×10^{-3}	3.5×10^7	20.20	0.67
	20	7.37	1.6×10^{-11}	3.8×10^{-6}	2.3×10^5	3.48	0.60
Zr	5	3.36	3.2×10^{-7}	3.1×10^{-3}	9.7×10^3	13.61	2.24
	10	4.10	1.8×10^{-7}	2.7×10^{-3}	1.5×10^4	12.85	2.13
	20	3.16	4.3×10^{-8}	7.7×10^{-4}	1.8×10^4	9.83	2.08
Nb	5	-1.04	2.8×10^{-6}	2.6×10^{-3}	9.3×10^2	10.64	4.24
	10	2.69	4.4×10^{-7}	2.1×10^{-3}	4.7×10^3	12.37	2.76
	20	3.53	1.0×10^{-7}	1.9×10^{-3}	1.8×10^4	12.65	1.75

For all the c-IZO:X thin films the inclusion of the metal cation initially resulted to an increase of the off-state current of the TFTs (Figure 8-19). For the case of Ga^{3+} the increase is of five orders of magnitude, for the case of Nb^{5+} four orders of magnitude, for Zr^{4+} three orders of magnitude while for Y^{3+} it is barely up to one order of magnitude. The origin of the increase in carrier concentration is not clear, but it is postulated that it could be due to metal interstitials (X_i), or substitutional antisite defects, e.g. X_{Zn} , X_{In} , (X=Ga, Y, Zr, Nb). Indeed, since the ionic radius of Ga^{3+} (76 pm), Zr^{4+} (86 pm) and Nb^{5+} (78 pm) is close to Zn^{2+} (88 pm), it could be assumed that such metal cations, substituted Zn atoms from its place leading to a more defective

structure as the Urbach energy increases. It has been reported, based on experimental and theoretical calculations, that antisite defects could act as shallow electron donors.

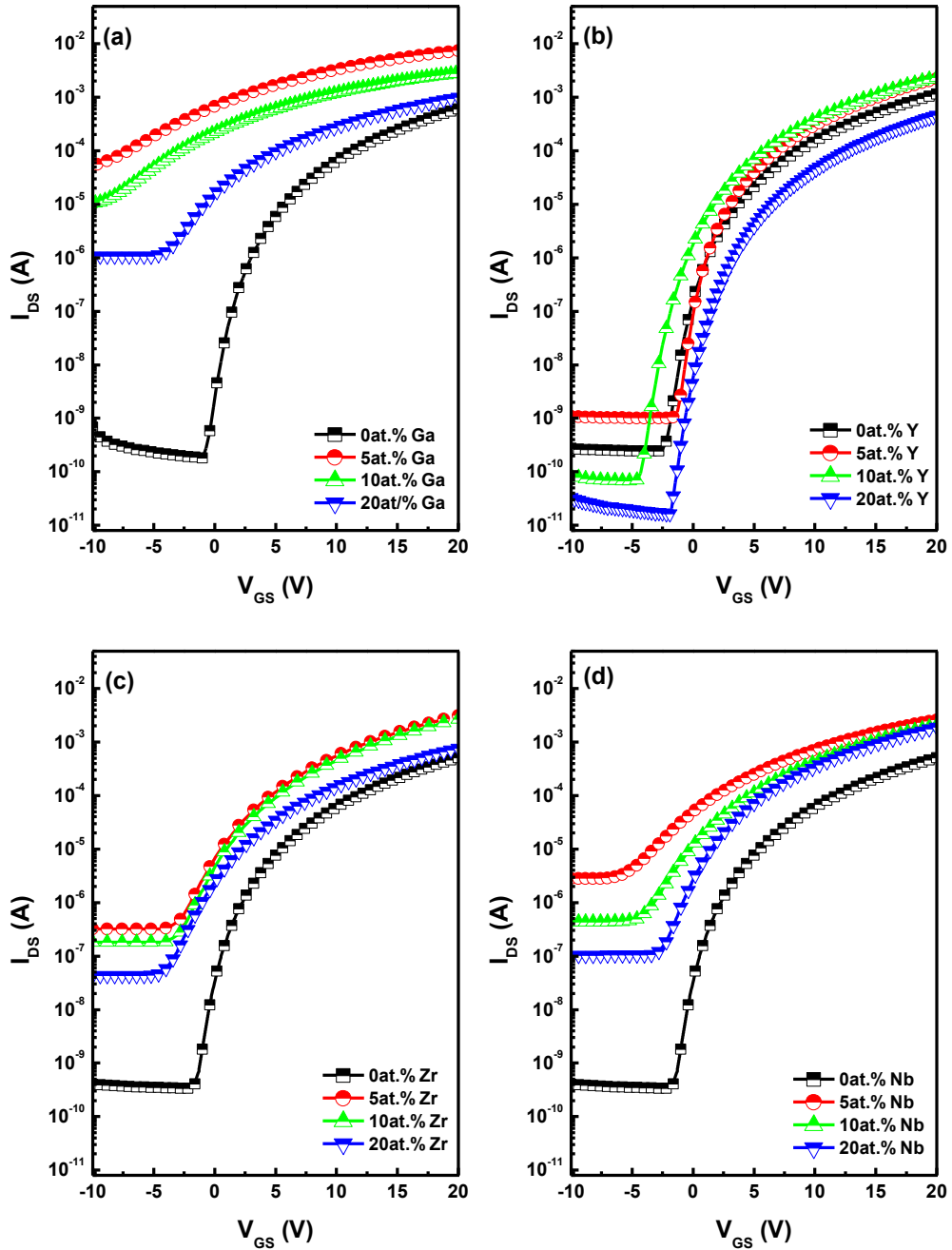


Figure 8-18: Transfer characteristic of (a) Ga -doped IZO, (b) Y -doped IZO, (c) Zr -doped IZO, (d) Nb -doped c-IZO thin films with different doping ratios.

On the other hand, Y^{3+} is of a relatively large ionic radius (104 pm). In this case, it is postulated that Y^{3+} acted as interstitial. Furthermore, due to its lower electronegativity (1.22) and standard electrode potential (the individual potential of a reversible electrode at standard state, -2.372) in contrast to the other dopants studied, Y^{3+} is of higher free carrier suppressing efficiency. The carrier suppressing efficiency of Y^{3+} has been previously reported [25], [28]–[30].

Besides the decrease of the off-state current, Y^{3+} doping significantly enhanced the field-effect mobility of TFTs, while the subthreshold swing has equally been improved. These two parameters, are of high importance as they are strongly related to the quality of dielectric/semiconductor interface. A high-field effect mobility enhances the performance of a TFT, while a small subthreshold swing is related with the reliability of the device. Subthreshold swing is a metric of the interface trap density and is directly related to it [31]. An important finding is that the decrease of the subthreshold swing follows the same trend as the Urbach energy. Since Urbach energy is related to the localised states in the band gap, it is postulated that the decrease of the subthreshold swing originated from the decrease of the localised states. Therefore, besides the other factors that limit the field-effect mobility, the decrease of the localised states in Y-doped IZO films, as the decrease of Urbach energy implies, could explain the increase in field effect mobility of the Y-doped IZO based TFTs.

The field effect mobility was also initially increased for the rest of the dopants, Ga^{3+} , Zr^{4+} , Nb^{5+} . Such increase of the field-effect mobility has not been followed by either an acceptable decrease of the off-state current or a decrease of the subthreshold swing. Also, considering the negative shift of the threshold voltage, it could be assumed that Ga^{3+} , Zr^{4+} and Nb^{5+} doping increases the carrier concentration, presumably due to an increase of the shallow donor levels close to conduction band edge. As already stated, this increase of the donor level could be related to the increase of antisite defects such as X_{Zn} or X_{In} that act as shallow donors. The latter is further supported by the increase of the Urbach energy in both Ga^{3+} and Zr^{4+} doped films. For the case of Nb^{5+} the decrease of the subthreshold slope could be attributed to the decrease of the interfacial states resulted from the decrease of trap energy levels in the band gap as Urbach energy revealed. Besides, the low on-off current ratio

and the high off-state current do not qualify Nb^{5+} as a suitable dopant, for improved performance c-IZO TFTs.

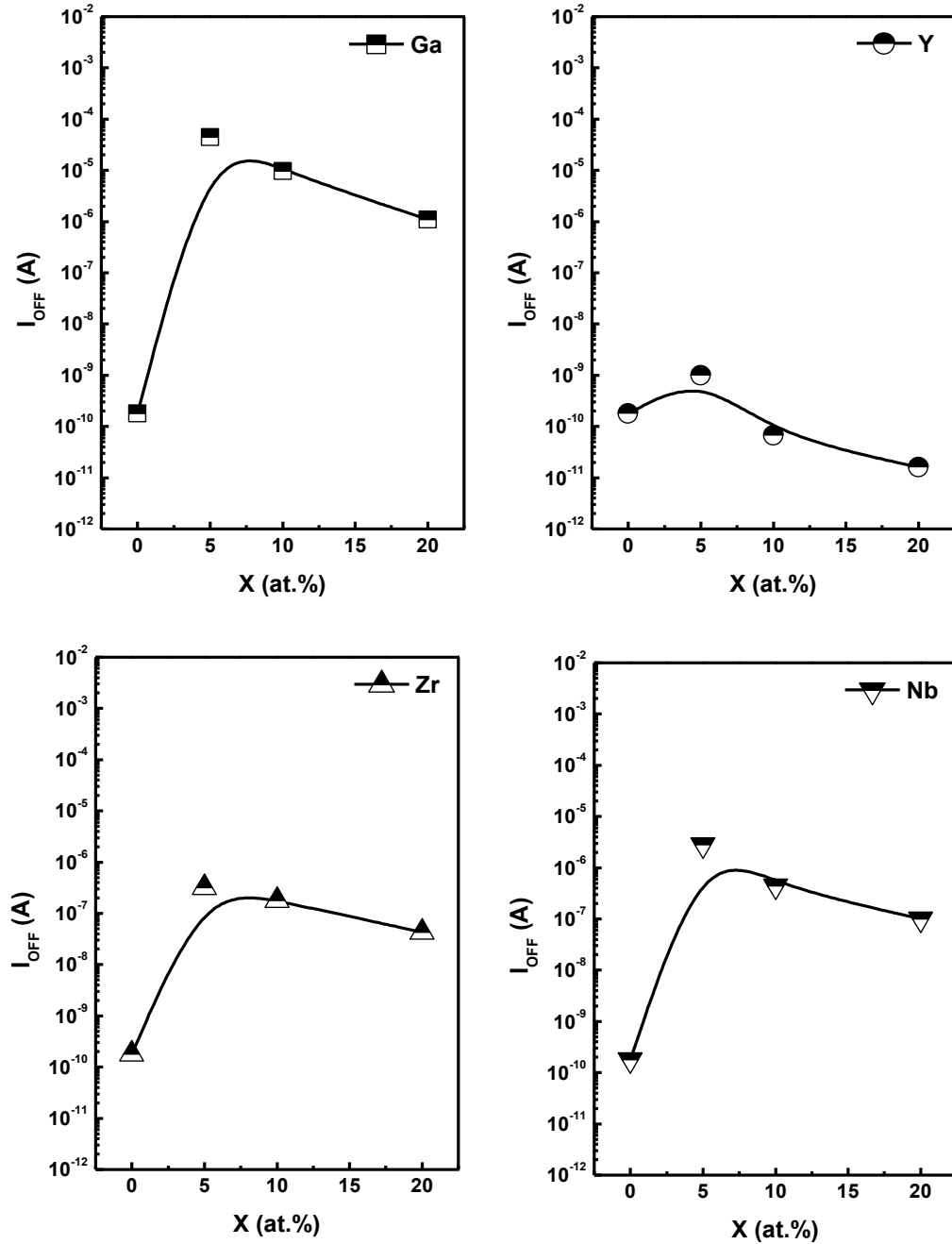


Figure 8-19: Off-state current (I_{off}) of c-IZO:X, (X=Ga, Y, Zr, Nb) based TFTs as a function of X content in the films.

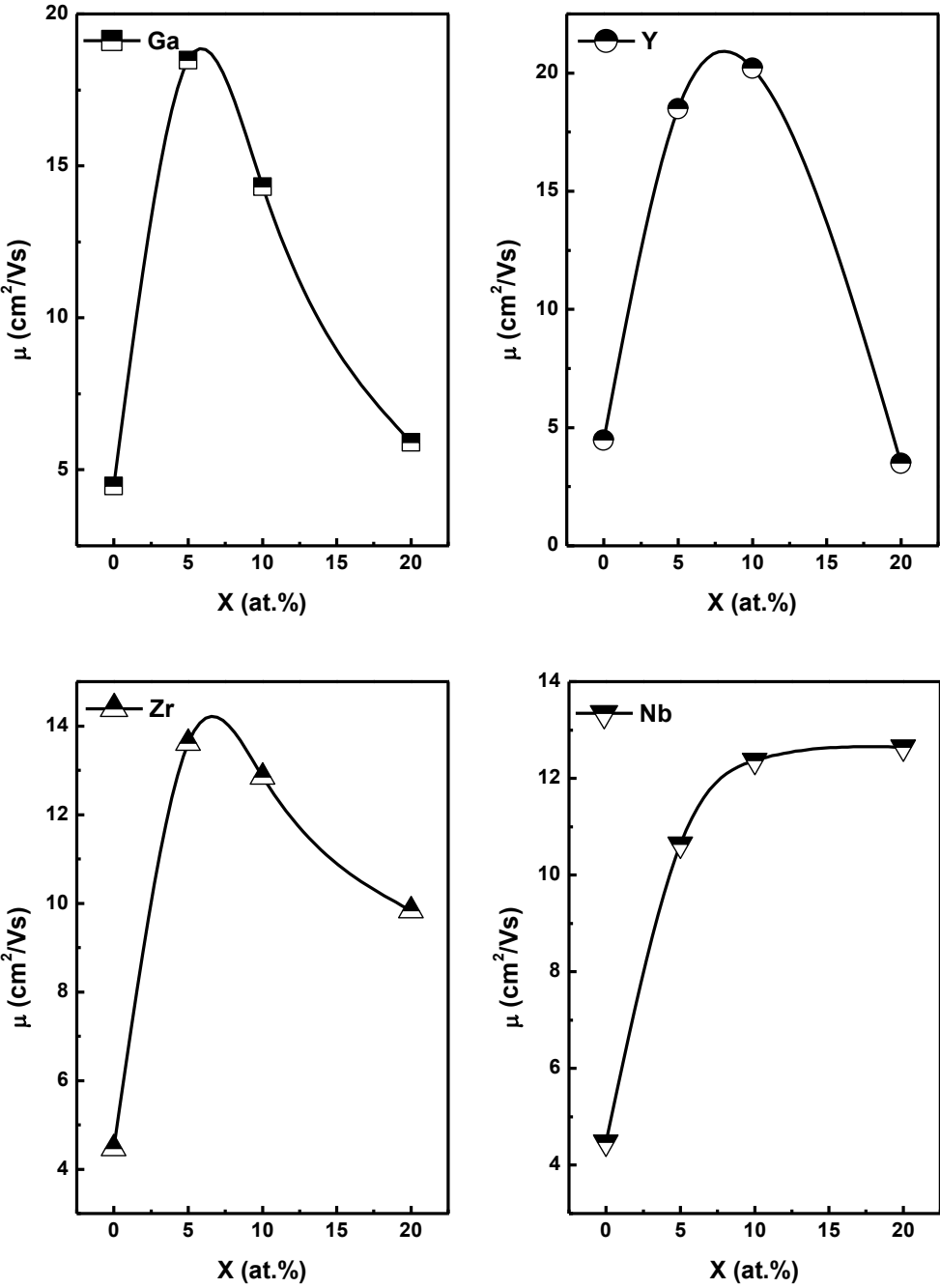


Figure 8-20: Field effect mobility (μ) of c-IZO:X, (X=Ga, Y, Zr, Nb) based TFTs as a function of X content in the films.

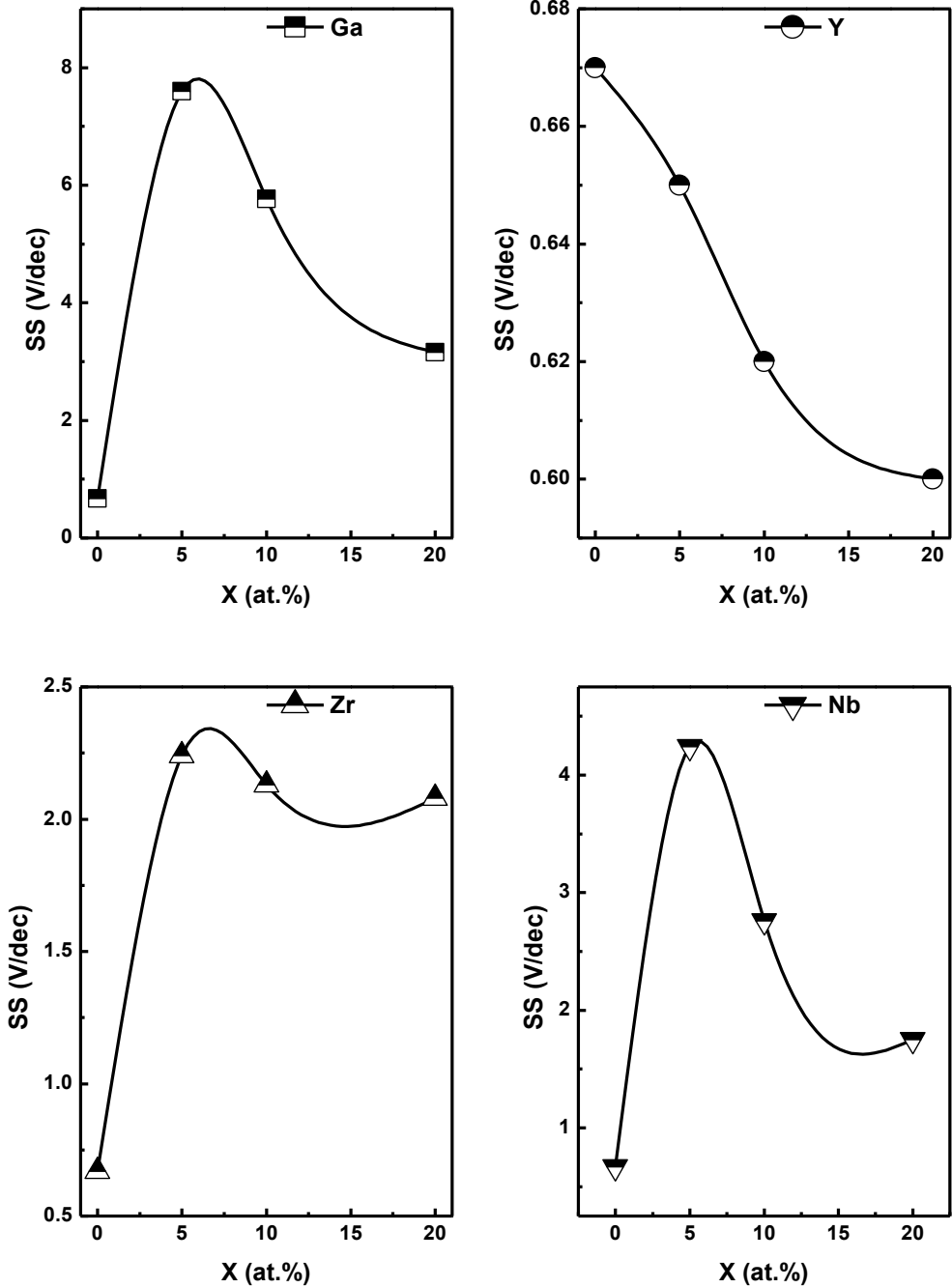


Figure 8-21: Subthreshold slope (SS) of c-IZO:X, (X=Ga, Y, Zr, Nb) based TFTs as a function of X content in the films.

8.3.4 Detailed study of IZO:Y.

The high performance c-IZO:Y based TFTs stimulated the interest to elucidate in more detail the optical, structural and electrical characteristics of the c-IZO:Y films as a function of Y content. The physical properties of c-IZO:Y films were investigated as a function of $[Y^{3+}]/([In^{3+}]+[Zn^{2+}])$ atomic ratio, keeping constant the $[In^{3+}]:[Zn^{2+}]$ ratio. In Figure 8-22, the Tauc plots of selected c-IZO:Y films and the calculated optical band gaps and Urbach tail energies of c-IZO:Y thin films for different $[Y^{3+}]/([In^{3+}]+[Zn^{2+}])$ ratio are illustrated.

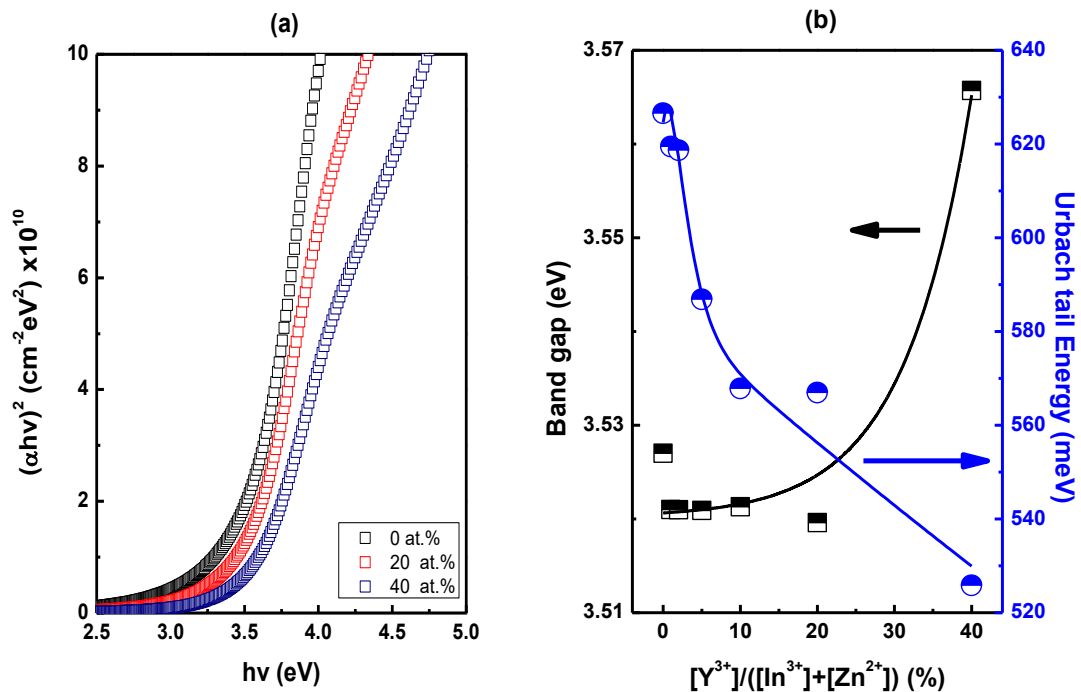


Figure 8-22: (a) Tauc plots of selected c-IZO:Y films, (b) optical band gap and Urbach energy as a function of the $[Y^{3+}]/([In^{3+}]+[Zn^{2+}])$ atomic ratio. The solid lines are guides to the eye.

Evidently, the increase of $[Y^{3+}]$ concentration in IZO:Y films didn't significantly affect the optical band gap for a doping concentration up to about 20%, while for higher doping concentrations a distinct increase of the optical band gap is obvious as shown in Figure 8-22.b. This increase of the band gap, of heavily doped IZO:Y is attributed to a blue shift due to Burstein-Moss effect [19], which in occurs due to an increased carrier concentration.

Interestingly, the Urbach tail energy showed a monotonic decrease with the increase in Y doping concentration. The Urbach energy is associated with the width of localised states in the band gap due to structural distortion [26], [32], [33]. Here, the increase in Y content seems to have a positive impact decreasing the width of localised states in the band gap of the c-IZO films. This could be due to an enhanced crystallinity of the films, and/or due to a decrease in lattice strain. To interpret the origin of the decrease of the Urbach energy, the structural properties of the IZO:Y films were investigated. Structural information of the IZO:Y films was obtained from XRD experiments. The GIXRD diffraction patterns of the IZO:Y with different $[Y^{3+}]/([In^{3+}]+[Zn^{2+}])$ ratios are presented in Figure 8-23.

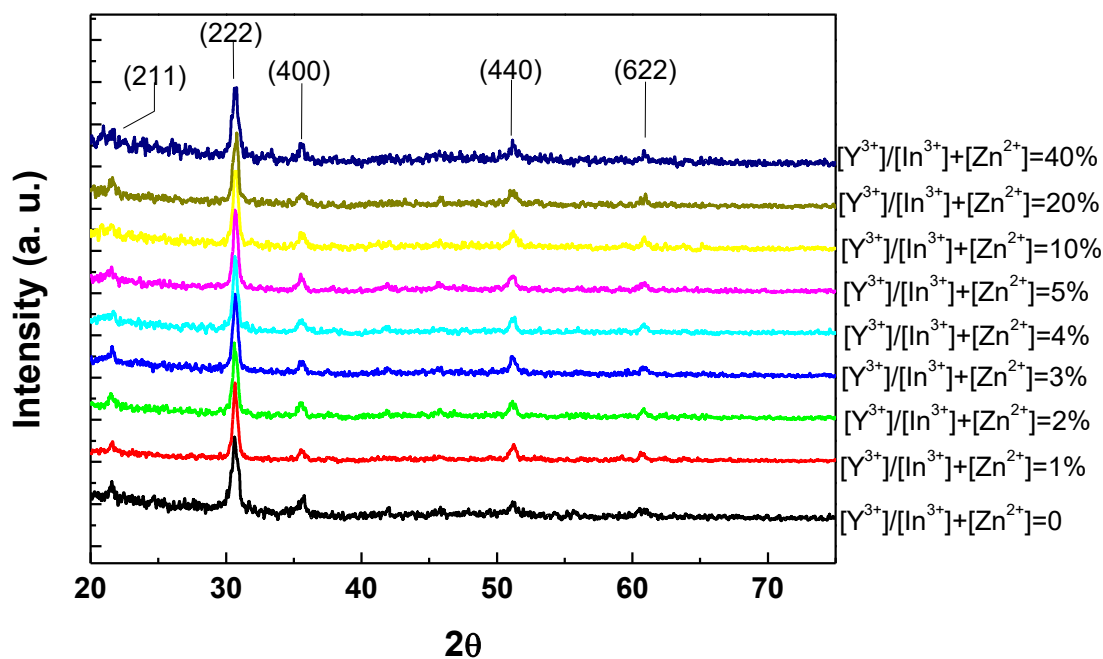


Figure 8-23: GIXRD diffraction patterns of Y-doped c-IZO films with different $[Y^{3+}]/([In^{3+}]+[Zn^{2+}])$ ratios.

All films exhibit a strong diffraction peak centred at 30.7° and less intense peaks at 21.5° , 35.6° , 51° and 60.9° . These peaks are the (211), (222), (400), (440) and (622) reflections, signature of polycrystalline cubic In_2O_3 (JCPDS-PDF 06-0416). It should be noted that for all Y-doped films there are no diffraction peaks associated to any yttrium compound.

In Figure 8-24, the average grain size $\langle d \rangle$, derived from the Debye-Scherrer formula and the interplanar spacing d_{hkl} from Bragg equation calculated from the (222) diffraction peak are presented [24].

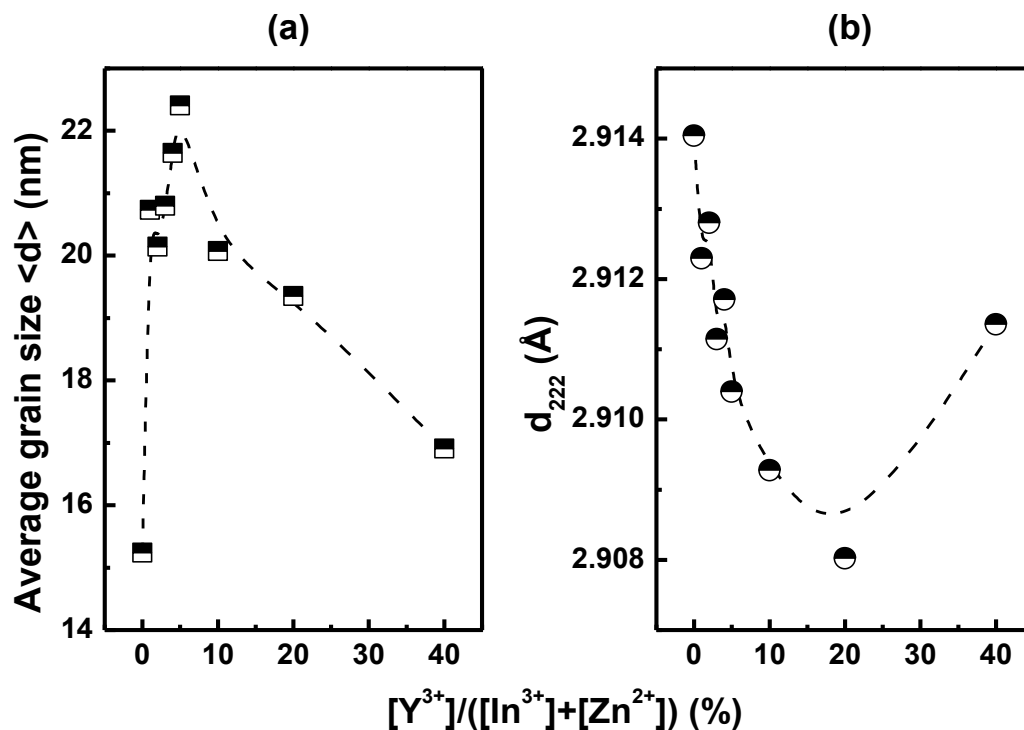


Figure 8-24: (a) Average grain size ($\langle d \rangle$) and (b) interplanar spacing (d_{hkl}) calculated from the (222) diffraction peak as a function of $[Y^{3+}]:[In^{3+}]$ atomic ratio (in the solution).

As shown in Figure 8-24, the average grain size increases with increasing the $[Y^{3+}]/([In^{3+}]+[Zn^{2+}])$ ratio and it reaches a maximum value of about 23 nm for $[Y^{3+}]/([In^{3+}]+[Zn^{2+}])=5\%$. Further increase of the $[Y^{3+}]/([In^{3+}]+[Zn^{2+}])$ atomic ratio results in a decrease of the average grain size. The opposite trend observed for the interplanar spacing d_{hkl} . The inclusion of $[Y^{3+}]$ reduces the interplanar spacing of (222) planes. Figure 8-25 depicts the calculated lattice constant for the spray deposited c-IZO:Y thin films as a function of $[Y^{3+}]/([In^{3+}]+[Zn^{2+}])$ atomic ratio.

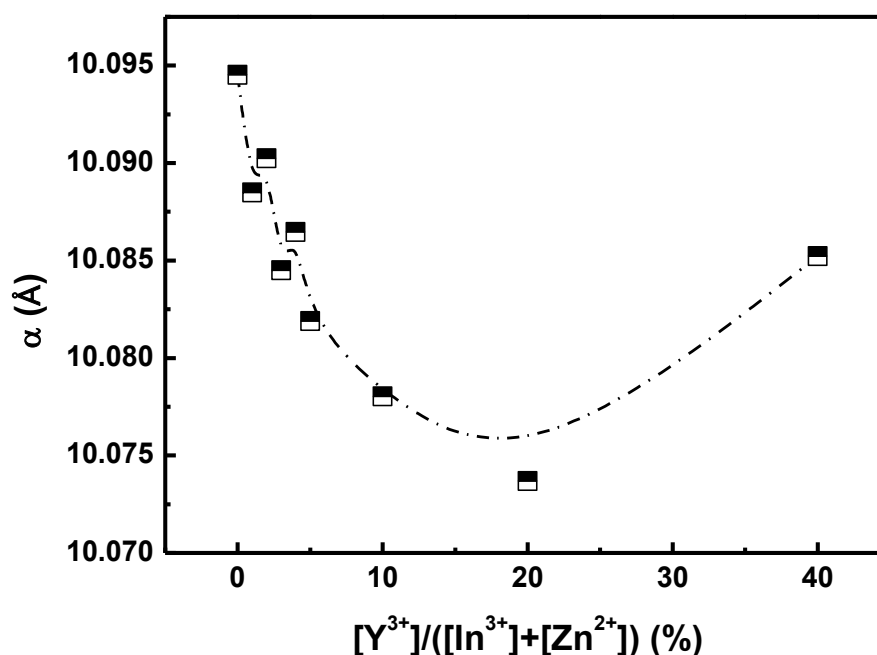


Figure 8-25: Lattice parameter a for Y-doped c-IZO thin films as a function of $[Y^{3+}]/([In^{3+}]+[Zn^{2+}])$ atomic ratio.

As the yttrium content increases, the lattice constant a decreases from 10.0945 Å for undoped c-IZO to 10.073 Å for 20% Y-doped IZO, while further increase in $[Y^{3+}]$ content results in an increase to 10.085 Å for 40% Y-doped IZO. Since $[Y^{3+}]$ is of higher ionic radius (104 pm) from both $[In^{3+}]$ and $[Zn^{2+}]$, it is anticipated that $[Y^{3+}]$ did not enter the c-IZO crystal but it was located at the grain boundaries of c-IZO, as interstitial “impurity”. The grain boundaries are postulated to act as the channel for $[Y^{3+}]$ migration. In this study, the grain boundaries are assumed that not only, would not degrade the carrier transport properties and it is postulated that it could also have a positive impact by further enhancing the carrier transportation, providing sufficient channel for ion migration. In Figure 8-26 the proposed $[Y^{3+}]$ induced channel formation at grain boundaries is illustrated. Charge carriers could diffuse via the channel at nanocrystalline domain boundaries in the polycrystalline grain, enhancing the conductivity of the films.

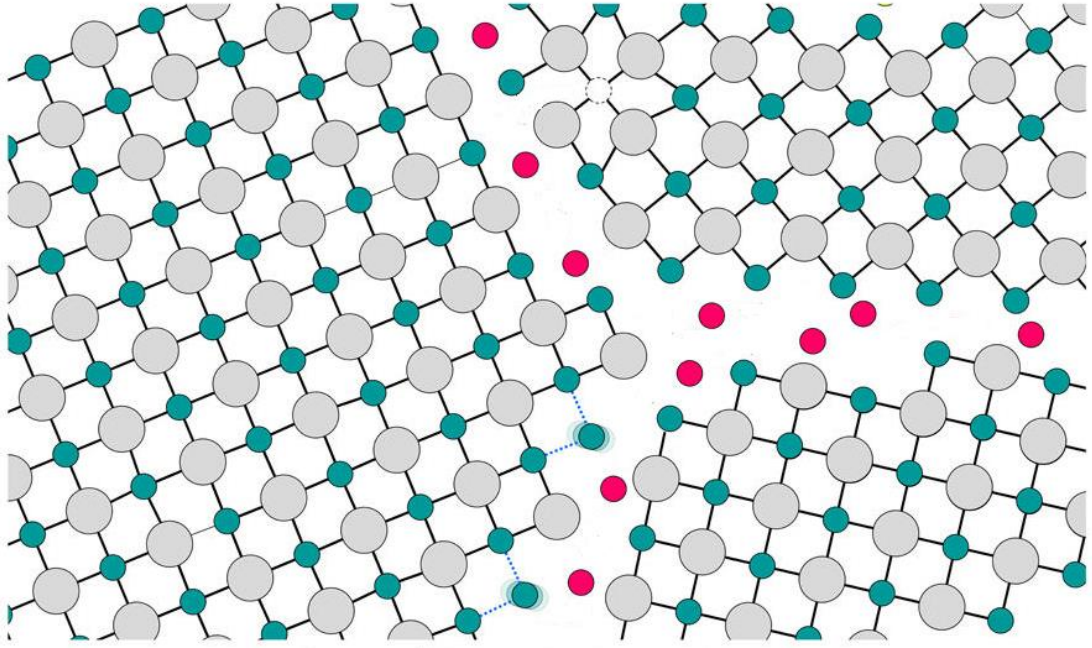


Figure 8-26: Channel formation at grain boundaries and carrier transport pathway [34].

The surface morphologies of films are of critical importance towards the implementation of thin films in TFTs. Smooth film surfaces enhance the performance of devices due to the better dielectric-semiconductor interfaces. Film roughness is one of the scattering mechanisms that degrade the carrier transport properties, such as the carrier mobility.

The impact of $[Y^{3+}]$ doping on the surface morphologies of the c-IZO thin films was investigated by AFM over a $0.5 \mu\text{m}^2$ area. Figure 8-27 shows topography and friction images of selected c-IZO:Y thin films. AFM analysis revealed smooth surfaces with RMS roughness less than 2 nm for all the c-IZO:Y films.

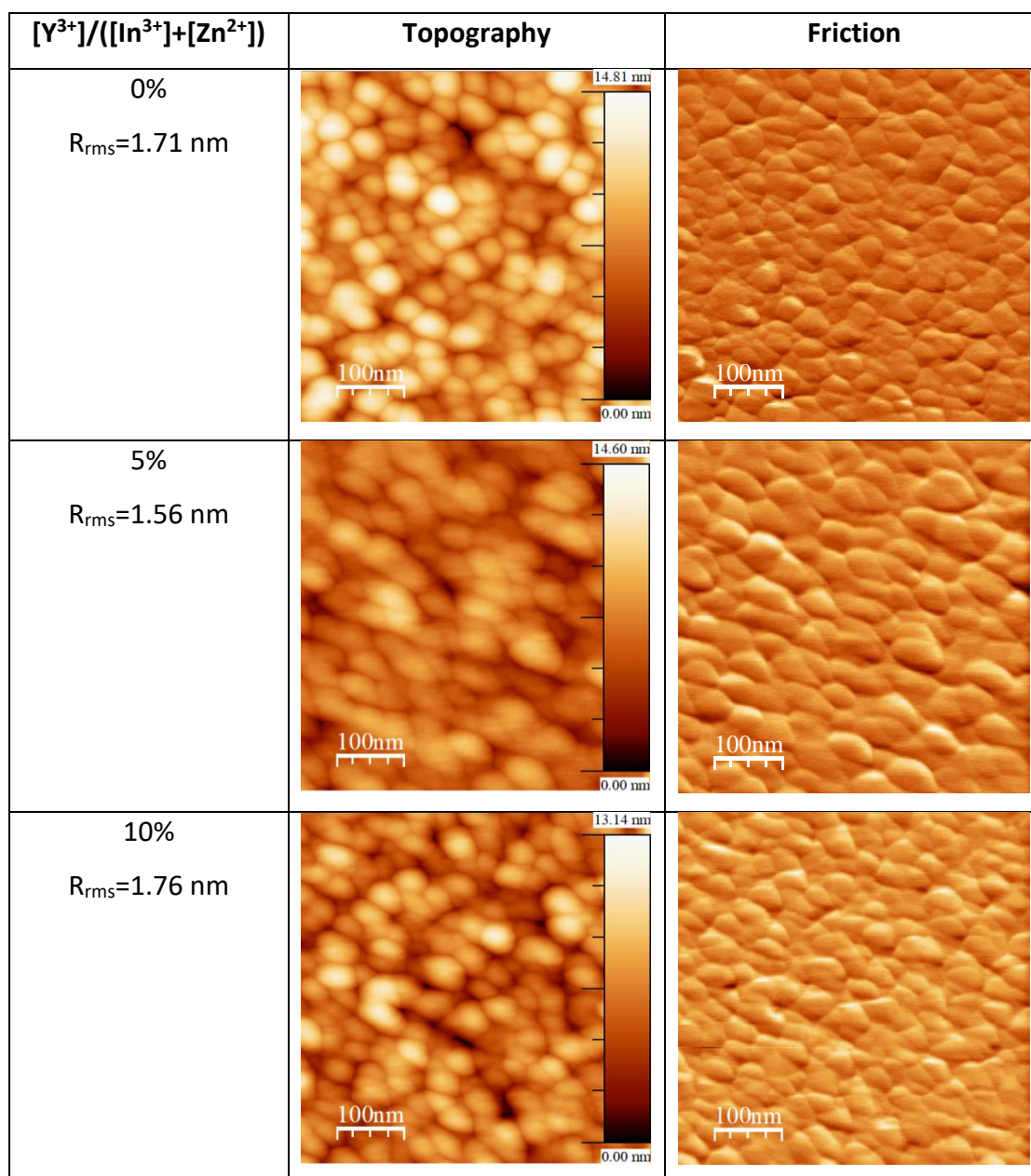


Figure 8-27: AFM (topography and friction) images of selected c-IZO:Y thin films.

Contact mode AFM provides images with enhanced edges of topographic features and is a useful tool towards the study of homogeneity of the film's surface. Evidently, films are homogeneous since there is not any secondary phase as there is no significant change in the intensity of friction images, while the grain boundaries are well delimited.

As become evident from both XRD and AFM measurements, there is an increase in the grain size for the 5% Y-doped c-IZO films. This results to a decrease of

the total length of grain boundaries. Therefore, it is expected that the increase of the grain size would reduce the density of grain boundaries minimising the impact of grain boundary limited carrier transport [35]. To investigate this hypothesis, the electronic transport properties of c-IZO:Y were investigated by field effect measurements. The TFT parameters of the of the c-IZO:Y-based TFTs are presented in Table 8-2. All the devices were exhibiting excellent switching properties with low off-state currents, high current modulation ratios, high electron mobilities and low subthreshold slopes.

Table 8-2: TFT operational characteristics of spray deposited c-IZO:Y based devices

$[Y^{3+}]/([In^{3+}]+[Zn^{2+}])$ (%)	I_{off} (A)	I_{on} (A)	I_{on}/I_{off}	μ (cm^2/Vs)	SS (V/dec)
0	2.79×10^{-10}	1.19×10^{-3}	4.27×10^6	8.4	0.71
3	9.93×10^{-10}	1.99×10^{-3}	2.00×10^6	18.82	0.66
4	1.12×10^{-9}	2.47×10^{-3}	2.21×10^6	19.93	0.62
5	1.03×10^{-9}	2.20×10^{-3}	2.20×10^6	20.87	0.63
10	6.68×10^{-11}	2.33×10^{-3}	3.49×10^7	19.52	0.68
20	1.63×10^{-11}	4.59×10^{-4}	2.82×10^7	4.54	0.62

Increasing the yttrium content of the films led to an increase in the off-state current was observed. Additionally, the maximum drain current was increased. It is postulated that yttrium doping increases the conductivity of the films by increasing the free carrier concentration. Indeed, it is considered that Y ions located at the grain boundaries are free to move via the characteristic channel as in Figure 8-26. Excess Y-doping though, could have a negative impact on the carrier transport (ion migration) via the grain boundaries. An overpopulation of Y ions results in an increase of scattering at grain boundaries degrading the carrier transport properties. An indication of the carrier transport in materials is the carrier mobility. In this study the TFT mobility at saturation was used to evaluate the carrier transport in the c-IZO:Y films. In Figure 8-28 the calculated field-effect mobility at saturation, of the c-IZO:Y based TFTs as a function of Y doping concentration is presented. Evidently, the field-effect mobility was enhanced as the Y doping level was increased up to $[Y^{3+}]/([In^{3+}]+[Zn^{2+}])=5\%$. The reason behind this enhancement is twofold. First, at this stoichiometry it was found that the crystal size has its maximum value. Therefore, at a given space, such as the TFT channel, the increase of the grain size results in a decrease of the grain boundaries

density across the TFT channel. Furthermore, the decrease of the density of grain boundaries is associated with the decrease of charge scattering centres for a carrier transport via the grain.

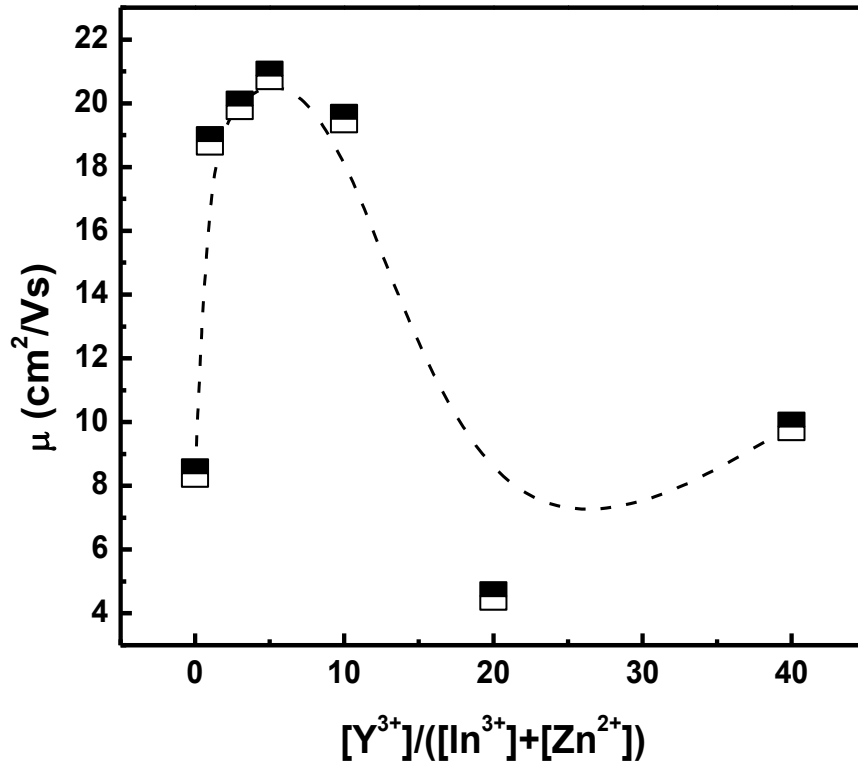


Figure 8-28: Field effect mobility of c-IZO:Y based TFTs as a function of $[Y^{3+}]/([In^{3+}]+[Zn^{2+}])$ atomic ratio.

The second reason is related to the high solubility of Y ions in the grain. Therefore, Y doping increases the film's conductivity because it decreases the energy barriers, by providing a carrier migration pathway, for the carrier transport through the polycrystalline grain. Indeed, this is also reflected in the off-state current (Figure 8-29), where an increase of the $[Y^{3+}]/([In^{3+}]+[Zn^{2+}])$ doping ratio resulted in an increase of the off-state current, presumably due to the increase of the free carriers in the c-IZO:Y film.

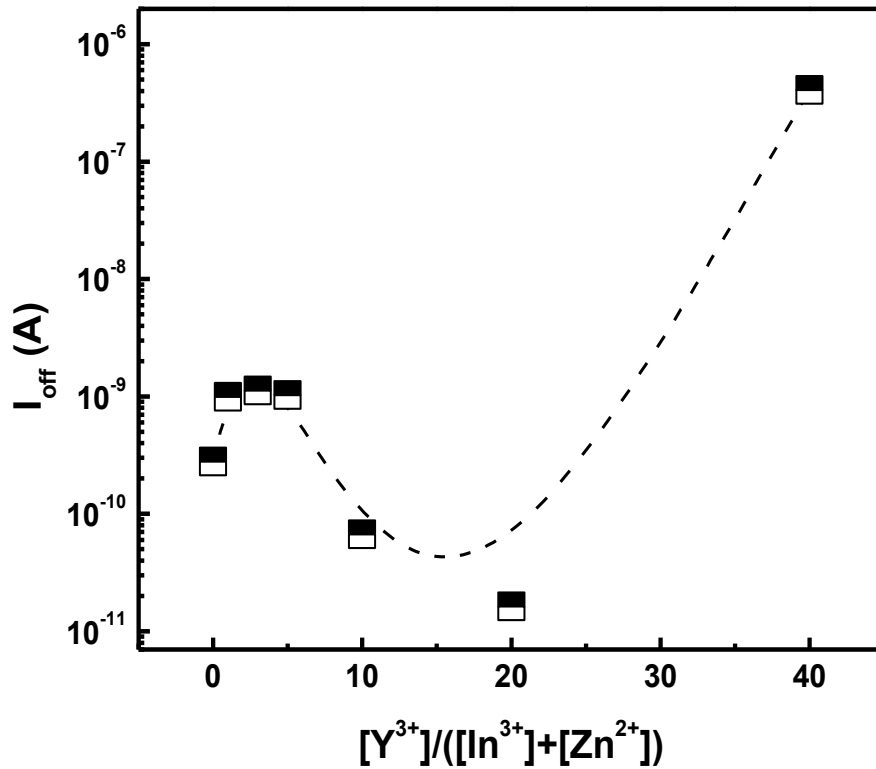


Figure 8-29: Off-state current of c-IZO:Y based TFTs as a function of $[Y^{3+}]/([In^{3+}]+[Zn^{2+}])$ atomic ratio.

For $[Y^{3+}]/([In^{3+}]+[Zn^{2+}])$ of 5%, a maximum drain current of about 2 mA, a high on-off current ratio of 10^6 , the highest field effect mobility in excess of $20 \text{ cm}^2/\text{Vs}$ and a subthreshold swing of 0.63 V/dec were extracted. On the other hand, the 10% Y-doped devices exhibited low off-state currents of about 70 pA, high on-state current of 2 mA, high current modulation ratio in excess of 10^7 , high field effect mobility of $20 \text{ cm}^2/\text{Vs}$ and low SS of 0.68 V/dec. Further increase of the yttrium content resulted in device deterioration as both significant mobility loss ($\mu_{\text{sat}} < 5 \text{ cm}^2/\text{Vs}$) and maximum drain current ($I_{\text{on}} < 0.5 \text{ mA}$) were observed. In Figure 8-30 the transfer and output TFT characteristics of the optimised c-IZO:Y (Y 10%) are presented.

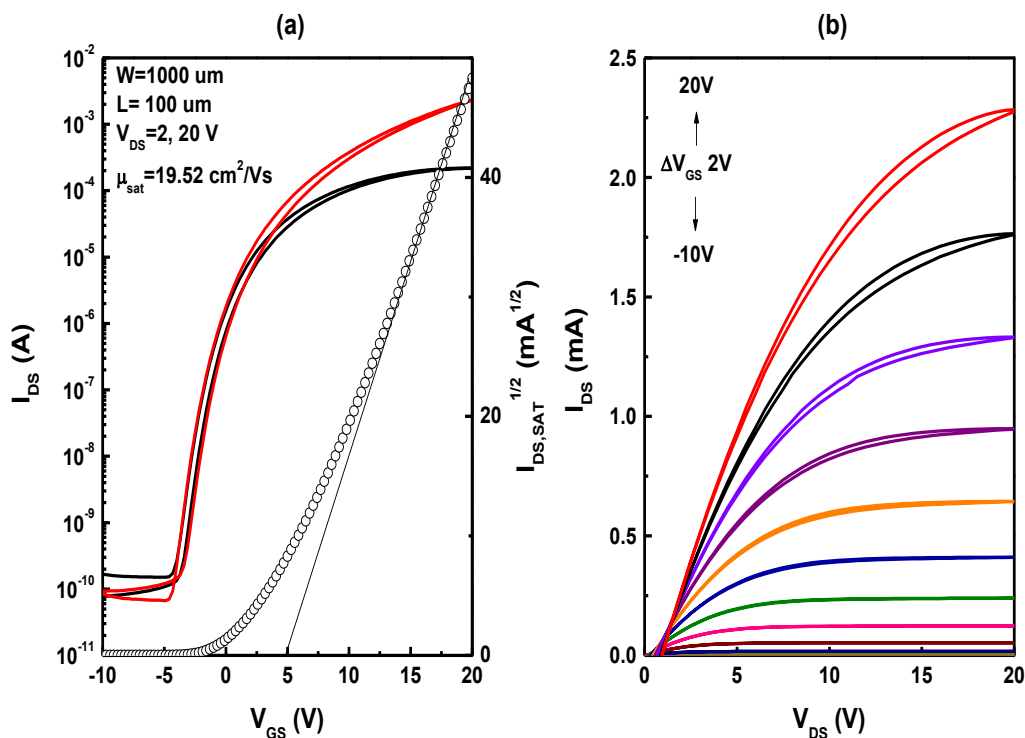


Figure 8-30: a) Transfer and b) output characteristics of 10% Y-doped c-IZO TFT.

8.4 Summary & Discussion

In this chapter, the optical, structural and electronic properties of c-IZO doped with Ga, Y, Zr, Nb were investigated. Gallium was chosen as dopant because it's been considered as the metal cation of choice for carrier suppression in amorphous indium-zinc oxide (a-IZO) due to its higher electronegativity (1.81) in contrast to the Zn (1.65) and In (1.78). Considering the increase of both the optical band gap and Urbach tail energy, it is postulated that the increase of Ga doping concentration resulted in a highly disorder-amorphous IGZO. In this study, Ga-doped c-IZO films showed higher conductivity than the undoped c-IZO, as the increase of the off-state current indicated. This is due to an increase of the carrier concentration as a result of Ga inclusion in the crystal lattice of c-IZO. Since Ga is of a small ionic radius (76 pm), it could create both interstitial and substitutional defects. Such defects could act as shallow donors increasing the films' conductivity.

Since the optical, structural and electronic properties of c-IZO are found to depend on the ionic radius of the doping element, another metal cation with higher ionic radius than Zn (88 pm) and In (94 pm) but with similar oxidation number was investigated. Yttrium has an ionic radius of 104 pm and is of the same oxidation number (+3) with Ga and much lower electronegativity (1.22). Y-doped c-IZO films exhibited wide band gap of about 3.53 eV, which was not significantly affected by the Y doping. Besides, the Urbach tail energy decreased with the increase of the Y concentration in the c-IZO films. Such decrease was further attributed to a higher crystallinity of the c-IZO:Y films, in terms of increase in crystal size. Furthermore, Y doping resulted in a decrease of the off-state current following by a significant enhancement of the field effect mobility. The decrease of the Urbach energy, which is related to structural distortion, along with the increase of the crystal size, which is related to the decrease of the density of the grain boundaries, are the reason for the enhanced performance of c-IZO:Y based TFTs.

Furthermore, Zr and Nb were studied as alternative dopants for performance enhancement of c-IZO based TFTs. These metal cations are of smaller ionic radii than Y^{3+} , but higher electronegativity. Zr^{4+} has an ionic radius of 86 pm and an electronegativity of 1.33. On the other hand, Nb^{5+} is of an ionic radius of 78 pm and an electronegativity of 1.6. Considering the performance of both c-IZO:Zr and c-IZO:Nb based TFTs, it could be seen that both dopants induced an increase of the off-state current which for the case of Nb^{5+} was more pronounced. Since Nb^{5+} is of smaller ionic radius it could be postulated that Nb^{5+} could more easily enter the crystal of c-IZO either as a substitute or interstitial increasing the free-carriers.

In this study, it was demonstrated the major impact of dopant size and electronegativity towards the performance of c-IZO based TFTs. Yttrium was found to be the most effective dopant. Among Ga, Y, Zr, Nb, cations Y^{3+} is of the larger ionic radius and the smaller electronegativity. It is believed that the larger ionic radius prevents Y^{3+} from entering the crystal of c-IZO but remain at the grain boundaries. Considering the mobility enhancement of the c-IZO:Y based TFTs, it is believed that the increase of the Y doping level reduced the energy barriers at the grain boundaries of the c-IZO:Y, therefore the carrier mobility in the grain was increased. In addition,

the increase of the grain size with Y doping reduced the number of grain boundaries across the device channel, so the impact of the grain boundary scattering of charge carriers was reduced.

Finally it was found that for $[Y^{3+}]/([In^{3+}]+[Zn^{2+}])$ of 10% the c-IZO:Y based TFTs exhibited the best performance i.e. a low threshold voltage of about 5 V, a low off-state current of 70 pA, a high current modulation ratio in excess of 10^7 , a high field-effect mobility of about $20 \text{ cm}^2/\text{Vs}$ and a low subthreshold swing of 0.68 V/dec. Such operational characteristics qualify the c-IZO:Y to be considered as a channel material of high performance TFTs.

8.5 References

- [1] M. S. Park, D. H. Lee, E. J. Bae, D.-H. Kim, J. G. Kang, D.-H. Son, and S. O. Ryu, 'Fabrication of Indium Gallium Zinc Oxide (IGZO) TFTs Using a Solution-Based Process', *Mol. Cryst. Liq. Cryst.*, vol. 529, no. 1, pp. 137–146, Oct. 2010.
- [2] H. Yabuta, M. Sano, K. Abe, T. Aiba, T. Den, H. Kumomi, K. Nomura, T. Kamiya, and H. Hosono, 'High-mobility thin-film transistor with amorphous $InGaZnO_4$ channel fabricated by room temperature rf-magnetron sputtering', *Appl. Phys. Lett.*, vol. 89, no. 11, p. 112123, Sep. 2006.
- [3] K. Nomura, H. Ohta, A. Takagi, T. Kamiya, M. Hirano, and H. Hosono, 'Room-temperature fabrication of transparent flexible thin-film transistors using amorphous oxide semiconductors.', *Nature*, vol. 432, no. November, pp. 488–492, Nov. 2004.
- [4] T. Kamiya, K. Nomura, and H. Hosono, 'Present status of amorphous $In-Ga-Zn-O$ thin-film transistors', *Sci. Technol. Adv. Mater.*, vol. 11, no. 4, p. 044305, Feb. 2010.
- [5] T. Kamiya, K. Nomura, and H. Hosono, 'Origins of High Mobility and Low Operation Voltage of Amorphous Oxide TFTs: Electronic Structure, Electron Transport, Defects and Doping', *J. Disp. Technol.*, vol. 5, no. 12, pp. 468–483, Dec. 2009.
- [6] S. Parthiban and J.-Y. Kwon, 'Role of dopants as a carrier suppressor and strong oxygen binder in amorphous indium-oxide-based field effect transistor', *J. Mater. Res.*, vol. 29, no. 15, pp. 1585–1596, Aug. 2014.
- [7] J.-S. Park, K. Kim, Y.-G. Park, Y.-G. Mo, H. D. Kim, and J. K. Jeong, 'Novel $ZrInZnO$ Thin-film Transistor with Excellent Stability', *Adv. Mater.*, vol. 21, no. 3, pp. 329–333, Jan. 2009.

- [8] E. Chong, K. C. Jo, and S. Y. Lee, 'High stability of amorphous hafnium-indium-zinc-oxide thin film transistor', *Appl. Phys. Lett.*, vol. 96, no. 15, p. 152102, Apr. 2010.
- [9] J. W. Hennek, J. Smith, A. Yan, M. Kim, W. Zhao, V. P. Dravid, A. Facchetti, and T. J. Marks, 'Oxygen "Getter" Effects on Microstructure and Carrier Transport in Low Temperature Combustion-Processed a-InXZnO (X=Ga, Sc, Y, La) Transistors', *J. Am. Chem. Soc.*, vol. 135, no. 29, pp. 10729–10741, Jul. 2013.
- [10] M. Benwadih, J. A. Chroboczek, G. Ghibaudo, R. Coppard, and D. Vuillaume, 'Impact of dopant species on the interfacial trap density and mobility in amorphous In-X-Zn-O solution-processed thin-film transistors', *J. Appl. Phys.*, vol. 115, no. 21, p. 214501, Jun. 2014.
- [11] S. J. Kim, D. Lim Kim, Y. Seung Rim, W. Hee Jeong, D. Na Kim, D. Hyun Yoon, and H. J. Kim, 'The formation of InZnO lattices incorporating Ba for thin-film transistors using a solution process', *J. Cryst. Growth*, vol. 326, no. 1, pp. 163–165, Jul. 2011.
- [12] G. H. Kim, W. H. Jeong, B. Du Ahn, H. S. Shin, H. J. Kim, H. J. Kim, M.-K. Ryu, K.-B. Park, J.-B. Seon, and S.-Y. Lee, 'Investigation of the effects of Mg incorporation into InZnO for high-performance and high-stability solution-processed thin film transistors', *Appl. Phys. Lett.*, vol. 96, no. 16, p. 163506, Apr. 2010.
- [13] D. Perednis, O. Wilhelm, S. E. Pratsinis, and L. J. Gauckler, 'Morphology and deposition of thin yttria-stabilized zirconia films using spray pyrolysis', *Thin Solid Films*, vol. 474, no. 1–2, pp. 84–95, Mar. 2005.
- [14] D. Hong, G. Yerubandi, H. Q. Chiang, M. C. Spiegelberg, and J. F. Wager, 'Electrical Modeling of Thin-Film Transistors', *Crit. Rev. Solid State Mater. Sci.*, vol. 33, no. 2, pp. 101–132, May 2008.
- [15] G. Alarcón-Flores, M. Aguilar-Frutis, M. García-Hipolito, J. Guzmán-Mendoza, M. A. Canseco, and C. Falcony, 'Optical and structural characteristics of Y_2O_3 thin films synthesized from yttrium acetylacetonate', *J. Mater. Sci.*, vol. 43, no. 10, pp. 3582–3588, May 2008.
- [16] S. Petit, S. Morlens, Z. Yu, D. Luneau, G. Pilet, J.-L. Soubeyroux, and P. Odier, 'Synthesis and thermal decomposition of a novel zirconium acetato-propionate cluster: $[Zr_{12}]$ ', *Solid State Sci.*, vol. 13, no. 3, pp. 665–670, Mar. 2011.
- [17] H. M. Ismail, 'Characterization of the decomposition products of zirconium acetylacetonate: nitrogen adsorption and spectrothermal investigation', *Powder Technol.*, vol. 85, no. 3, pp. 253–259, Dec. 1995.
- [18] J. Tauc, 'Optical properties and electronic structure of amorphous Ge and Si', *Mater. Res. Bull.*, vol. 3, no. 1, pp. 37–46, Jan. 1968.
- [19] E. Burstein, 'Anomalous optical absorption limit in InSb', *Physical Review*, vol. 93, no. 3. American Physical Society, pp. 632–633, 01-Feb-1954.

- [20] T. S. Moss, 'The interpretation of the properties of indium antimonide', *Proc. Phys. Soc. Sect. B*, vol. 67, no. 10, pp. 775–782, Oct. 1954.
- [21] E. Mitchell Hopper, H. Peng, S. A. Hawks, A. J. Freeman, and T. O. Mason, 'Defect mechanisms in the $\text{In}_2\text{O}_3(\text{ZnO})_k$ system ($k = 3, 5, 7, 9$)', *J. Appl. Phys.*, vol. 112, no. 9, p. 093712, Nov. 2012.
- [22] S. Lany and A. Zunger, 'Dopability, Intrinsic Conductivity, and Nonstoichiometry of Transparent Conducting Oxides', *Phys. Rev. Lett.*, vol. 98, no. 4, p. 045501, Jan. 2007.
- [23] K. Matsuo and K. Nakano, 'Characterization of semiconductor oxides by IR diffuse reflectance spectroscopy', *Appl. Surf. Sci.*, vol. 41–42, no. C, pp. 53–56, Jan. 1990.
- [24] I. Hargittai, 'Christopher Hammond: The basics of crystallography and diffraction. Third edition', *Struct. Chem.*, vol. 20, no. 4, pp. 751–751, Aug. 2009.
- [25] C.-C. Ting, S.-P. Chang, W.-Y. Li, and C.-H. Wang, 'Enhanced performance of indium zinc oxide thin film transistor by yttrium doping', *Appl. Surf. Sci.*, vol. 284, pp. 397–404, Nov. 2013.
- [26] J. A. Olley, 'Structural disorder and the Urbach edge', *Solid State Commun.*, vol. 13, no. 9, pp. 1437–1440, Nov. 1973.
- [27] I. Studenyak, M. Kranj, and M. Kurik, 'Urbach Rule in Solid State Physics', *Int. J. Opt. Appl.*, 2014.
- [28] Y.-J. Lee, J.-H. Kim, B.-Y. Oh, and K.-Y. Kim, 'Electrical and Optical Properties of Y-Doped Indium Zinc Oxide Films Grown by RF Magnetron Sputtering', *J. Nanosci. Nanotechnol.*, vol. 13, no. 9, pp. 6296–6299, Sep. 2013.
- [29] H. S. Shin, G. H. Kim, W. H. Jeong, B. Du Ahn, and H. J. Kim, 'Electrical Properties of Yttrium–Indium–Zinc-Oxide Thin Film Transistors Fabricated Using the Sol–Gel Process and Various Yttrium Compositions', *Jpn. J. Appl. Phys.*, vol. 49, no. 3, p. 03CB01, Mar. 2010.
- [30] Y.-J. Lee, J.-H. Kim, and J. Kang, 'Characteristics of Y_2O_3 -doped indium zinc oxide films grown by radio frequency magnetron co-sputtering system', *Thin Solid Films*, vol. 534, pp. 599–602, May 2013.
- [31] J.-S. Lyu, 'A New Method for Extracting Interface Trap Density in Short-Channel MOSFETs from Substrate-Bias-Dependent Subthreshold Slopes', *ETRI J.*, vol. 15, no. 2, pp. 10–25, Oct. 1993.
- [32] W. Sritrakool, V. Sa-yakanit, and H. R. Glyde, 'Band tails in disordered systems', *Phys. Rev. B*, vol. 33, no. 2, pp. 1199–1202, Jan. 1986.
- [33] K. Tanaka, 'Minimal Urbach energy in non-crystalline materials', *J. Non. Cryst. Solids*, vol. 389, pp. 35–37, Apr. 2014.
- [34] Y. Yuan and J. Huang, 'Ion Migration in Organometal Trihalide Perovskite and Its Impact on Photovoltaic Efficiency and Stability', *Acc. Chem. Res.*, vol. 49, no. 2, pp. 286–293, 2016.

- [35] G. Adamopoulos, A. Bashir, S. Thomas, W. P. Gillin, S. Georgakopoulos, M. Shkunov, M. a. Baklar, N. Stingelin, R. C. Maher, L. F. Cohen, D. D. C. Bradley, and T. D. Anthopoulos, 'Spray-Deposited Li-Doped ZnO Transistors with Electron Mobility Exceeding $50 \text{ cm}^2/\text{Vs}$ ', *Adv. Mater.*, vol. 22, no. 42, pp. 4764–4769, Nov. 2010.

9. Conclusions and Further Work

9.1 Conclusions

In this thesis, the physical properties of solution processed metal oxide dielectrics and semiconductors are reported. Aiming to develop low cost, high performance and low power consumption thin film transistors for large area applications, metal oxide thin films were deposited on by spray pyrolysis, a versatile and large area compatible technique.

Several analytical techniques such as thermal analysis, UV-Vis-NIR spectroscopy, Fourier-transform infrared spectroscopy, X-ray diffraction, atomic force microscopy, ellipsometry, impedance spectroscopy and field effect measurements were conducted to investigate the physical properties of the solution-processed metal oxide thin films.

The thesis presented here was organised in four parts. In the first part (chapters 2 and 3), an extensive literature review of solution-processed metal oxide thin as well as the related device principles are presented. The second part (chapter 4), reports on the films' deposition and characterisation methods. A description of the spray pyrolysis technique is also included.

The third part (chapter 5 and 6) reports on the investigation of high- k dielectrics for low power, high performance thin film transistors. The implementation of titanium aluminate ($\text{Ti}_{1-x}\text{Al}_{2x}\text{O}_y$) gate dielectrics in solution processed ZnO-based TFTs was studied. Similarly, the properties of niobium aluminate ($\text{Nb}_{1-x}\text{Al}_x\text{O}_y$) high- k , wide band gap dielectrics were also extensively studied.

The $\text{Ti}_{1-x}\text{Al}_{2x}\text{O}_y$ films but TiO_2 were amorphous. Further analysis showed (tetragonal) anatase phase of TiO_2 . Films exhibited very smooth surfaces (R_{rms} in the order of 1nm), high dielectric constants (between 9 and 45), wide band gaps (between 3.7 eV and 6.5 eV) and low leakage currents in the order of nA/cm^2 . Specifically, the stoichiometric $\text{Ti}_{1-x}\text{Al}_{2x}\text{O}_y$ ($\text{Al}_2\text{O}_3\cdot\text{TiO}_2$) showed high dielectric constant (~ 13), wide band gap (4.5 eV), and very low leakage currents ($\sim 5 \text{ nA/cm}^2$) at an electric field of 3 MV/cm. There was not dielectric breakdown for fields up to 3 MV/cm indicating dielectrics of high dielectric strength. The performance of the spray deposited

$Ti_{1-x}Al_{2x}O_y$ films as gate dielectrics was investigated as well. The ZnO-based TFTs employing stoichiometric $Ti_{1-x}Al_{2x}O_y$ ($Al_2O_3 \cdot TiO_2$) dielectrics, showed excellent characteristics, i.e., low operation voltage (10 V), hysteresis-free operation, high electron mobility ($\sim 10 \text{ cm}^2/\text{Vs}$), high on/off current modulation ratio ($>10^5$) and low subthreshold swing (549 mV/dec).

Equally, analyses of $Nb_{1-x}Al_xO_y$ films revealed amorphous $Nb_{1-x}Al_xO_y$ films with very smooth surfaces ($R_{rms} < 0.1 \text{ nm}$), high dielectric constants, (between 9 and 50) wide band gaps (4.2-6.5 eV) and low leakage currents ($< 20 \text{ nA/cm}^2$). Further analysis of the electron transport mechanisms revealed two dominant conduction mechanisms for films with varying the Nb to Al ratio. Based on the Schottky conduction mechanism, the electron effective mass of the stoichiometric $NbAlO_y$ and the effective barrier height at the Au/ $NbAlO_y$ interface, were found to be of $0.37 m_0$ and 0.73 eV respectively. For niobium-rich ($x < 0.2$) $Nb_{1-x}Al_xO_y$ dielectrics, Poole-Frenkel conduction dominated.

In the fourth part (chapters 7 and 8), solution processed metal-oxide semiconductors were investigated. In chapter 7, the optical, structural and electronic properties of crystalline indium-zinc-oxide films as a function of $[Zn^{2+}]/([Zn^{2+}]+[In^{3+}])$ were investigated. The properties of metal cation-doped c-IZO thin films, were further investigated in chapter 8. In chapter 7 more particularly, the role of $[Zn^{2+}]$ on the structural, optical and electron transport properties of crystalline IZO were investigated. IZO films were deposited as a function of the $[Zn^{2+}]/([Zn^{2+}]+[In^{3+}])$ ratio. Optical measurements (UV-Vis transmission spectroscopy and FTIR) revealed films of high transparency on the order of 85 % in the visible spectrum. The optical band gap decreased as the $[Zn^{2+}]/([Zn^{2+}]+[In^{3+}])$ ratio was increased and ranged between 3.6 eV for In_2O_3 and 3.2 eV for ZnO. To elucidate the impact of $[Zn^{2+}]$ content on the band structure of $In_{1-x}Zn_xO_y$, further analysis based on Urbach energy was carried out. Urbach energy of IZO thin films, showed an initially increase as the $[Zn^{2+}]/([Zn^{2+}]+[In^{3+}])$ ratio was increased. The increase of the Urbach energy peaked at $[Zn^{2+}]/([Zn^{2+}]+[In^{3+}]) \sim 0.3$, (i.e., $[In^{3+}]:[Zn^{2+}] = 7:3$). From this stoichiometry and beyond, the Urbach tail energy showed a decrease with increasing the $[Zn^{2+}]/([Zn^{2+}]+[In^{3+}])$ ratio, reaching a minimum of 100 meV for ZnO. To elucidate the origin of this trend of the Urbach energy, further analysis based on FTIR spectroscopy was conducted. It was

found that $[Zn^{2+}]$ low doping level acts as an interstitial in In_2O_3 , while for higher concentrations $[Zn^{2+}]$ substitutes $[In^{3+}]$ atoms in In_2O_3 lattice. The latter was confirmed by XRD analysis, as both the lattice constant and interplanar spacing, were initially increased by increasing the $[Zn^{2+}]/([Zn^{2+}]+[In^{3+}])$ ratio resulting in lattice expansion, while for higher $[Zn^{2+}]/([Zn^{2+}]+[In^{3+}])$ ratios a lattice shrinkage was observed. The change of structural characteristics as a function of $[Zn^{2+}]/([Zn^{2+}]+[In^{3+}])$ ratio affected the carrier transport characteristics of IZO based TFTs. The lattice expansion, resulted in a reduction of the I_{off} currents, which originates from the suppression of intrinsic oxygen vacancies of In_2O_3 by $[Zn^{2+}]$. Further increase of the $[Zn^{2+}]$ content resulted in an increase of I_{off} due to the substitution of $[In^{3+}]$ atoms by $[Zn^{2+}]$. Since $[Zn^{2+}]$ coordinates with 4 oxygen atoms, in contrast to $[In^{3+}]$ which coordinates 6, a substitution of $[In^{3+}]$ by $[Zn^{2+}]$ induces 2 oxygen vacant places in the In_2O_3 . Finally, the field-effect mobility was found to depend on both the carrier concentration and the average crystal size. It was found that, for the optimum c-IZO, of ratio $[Zn^{2+}]/([Zn^{2+}]+[In^{3+}])=0.4$, i.e. $[In^{3+}]:[Zn^{2+}]=6:4$, the c-IZO based TFTs showed the best performance in terms of low off-state currents (18 pA), high on/off current modulation ratio (10^7), high field-effect mobility of about $5 \text{ cm}^2/\text{Vs}$, and low subthreshold swing of 0.3 V/dec .

Finally, in chapter 8, the optical, structural and electronic properties of c-IZO doped with Ga, Y, Zr, Nb were investigated in relation to the electronegativity and doping element ionic radius. Among the Ga^{3+} , Y^{3+} , Zr^{4+} , Nb^{5+} cations, Y^{3+} is of the largest ionic radius and the smallest electronegativity. It is believed that the larger ionic radius prevents Y^{3+} from incorporated, the IZO lattice (either as interstitial or substitute) but occupies the grain boundaries. Considering the mobility increase of the c-IZO:Y based TFTs, it is believed that the increase of the Y content, reduces the energy barriers at the grain boundaries of the c-IZO:Y, therefore the carrier mobility in the grain was increased. In addition, the increase of the grain size with Y doping reduced the number of grain boundaries across the device channel, hence reduces the electrons grain boundary scattering. Moreover, it was found that for $[Y^{3+}]/([In^{3+}]+[Zn^{2+}])$ of 10% the c-IZO:Y based TFTs exhibited the best performance i.e. a low threshold voltage of about 5 V, a low off-state current of 70 pA, high current modulation ratio in excess of 10^7 ,

high field-effect mobility of about 20 cm²/Vs and a low subthreshold swing of 0.68 V/dec.

9.2 Further Work

Based on the results of this study, a number of complementary development steps could be performed. As per the dielectrics (Ti_{1-x}Al_{2x}O_y and Nb_{1-x}Al_xO_y), further investigation of conduction mechanisms, could provide further insights on the materials' electronic properties. Low temperature measurements (77 K), would provide a better insight on the dominant conduction mechanism so that to confirm the Fowler-Norheim or thermionic emission and consequently information about the electron effective mass and metal/metal-oxide barrier to be obtained.

Apart from a materials' angle, the quality of the high-*k* dielectric/semiconductor interface is of high importance as such interfaces determine the performance and the reliability of a TFT. There are numerous techniques employed for interface and trap density levels characterisation. Amongst them, the low frequency noise (1/f) is a non-destructive and powerful technique to evaluate the quality of electronic devices, and its behaviour is directly related to the dielectric interface quality by directly probing the pink noise. On the other hand, negative, positive and cycle bias stress measurements are essential as they provide with stability and reliability information most notably, the such threshold voltage shift as well as mobility and on-currents deterioration.

It should be noted that for such measurements, meticulous device fabrication is necessary. As this study was mostly focused on the materials properties investigation, the devices were fabricated on non-patterned substrates that resulted in higher leakage currents and consequently underestimated performance. For detailed analysis of the device performance, the TFTs have to be properly patterned, in terms of gate electrode and channels overlap.

Besides the remarkable results of the proposed high-*k* and dielectrics (Ti_{1-x}Al_{2x}O_y and Nb_{1-x}Al_xO_y), alternative binary metal oxides such as hafnium titanate/niobate (Ti_{1-x}Hf_xO_y, Nb_{2x}Hf_{1-x}O_y), zirconium titanate /niobate (Ti_{1-x}Zr_xO_y,

$\text{Nb}_{2x}\text{Zr}_{1-x}\text{O}_y$) could equally be investigated as they all combine a high-k metal oxide (TiO_2 , Nb_2O_5) along with a wide band gap one (HfO_2 , ZrO_2).

Finally, the fabrication of a metal-oxide based CMOS inverter, taking into account the recent results on intrinsically p-type oxides along with the already investigated nMOS based on c-YIZO, combined with the proposed high-k dielectrics ($\text{Ti}_{1-x}\text{Al}_{2x}\text{O}_y$, $\text{Nb}_{1-x}\text{Al}_x\text{O}_y$), constitutes the next step towards the all solution metal oxide-based electronics.